

**A Thesis Submitted for the Degree of PhD at the University of Warwick**

**Permanent WRAP URL:**

<http://wrap.warwick.ac.uk/175004>

**Copyright and reuse:**

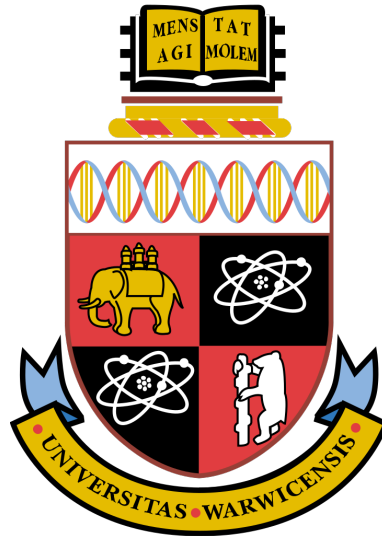
This thesis is made available online and is protected by original copyright.

Please scroll down to view the document itself.

Please refer to the repository record for this item for information to help you to cite it.

Our policy information is available from the repository home page.

For more information, please contact the WRAP Team at: [wrap@warwick.ac.uk](mailto:wrap@warwick.ac.uk)



**The Imaging and Discovery of M-Dwarf Debris Discs with  
ALMA**

by

**Patrick Francis Cronin-Coltsmann**

**Thesis**

Submitted to the University of Warwick

for the degree of

**Doctor of Philosophy in Physics**

**Department of Physics**

October 2022

# Contents

|  |             |
|--|-------------|
| <b>List of Tables</b>  | <b>iv</b>   |
| <b>List of Figures</b>   | <b>v</b>    |
| <b>Acknowledgments</b>   | <b>viii</b> |
| <b>Declarations</b>  | <b>ix</b>   |
| <b>Abstract</b>  | <b>x</b>    |
| <b>Abbreviations</b>   | <b>xi</b>   |
| <b>Chapter 1 Introduction</b>                                  | <b>1</b>    |
| 1.1 The Stellar Life Cycle and Its Discs . . . . .             | 1           |
| 1.1.1 Young Stellar Objects . . . . .                          | 1           |
| 1.1.2 Main-sequence stars – debris discs in brief . . . . .    | 4           |
| 1.1.3 Giant branch stars . . . . .                             | 8           |
| 1.1.4 White dwarfs . . . . .                                   | 8           |
| 1.2 Main-Sequence Debris Discs in Depth . . . . .              | 10          |
| 1.2.1 What is a debris disc? . . . . .                         | 10          |
| 1.2.2 The spatial features of debris discs . . . . .           | 24          |
| 1.2.3 Observed occurrence and trends . . . . .                 | 31          |
| 1.2.4 M-dwarfs . . . . .                                       | 35          |
| <b>Chapter 2 Methods</b>                                       | <b>39</b>   |
| 2.1 Thermal Emission and SEDs . . . . .                        | 39          |
| 2.1.1 Historic instruments . . . . .                           | 44          |
| 2.1.2 The need for ALMA . . . . .                              | 53          |
| 2.2 The Atacama Large Millimetre/submillimetre Array . . . . . | 53          |
| 2.2.1 The basis of interferometry . . . . .                    | 54          |

|                  |  |            |
|------------------|--|------------|
| 2.2.2            | Fourier transforms . . . . .   | 65         |
| <b>Chapter 3</b> | <b>ALMA imaging of the M-dwarf Fomalhaut C's debris disc</b>             | <b>82</b>  |
| 3.1              | Introduction . . . . .   | 83         |
| 3.2              | Dynamical Hypotheses and Other Motivating Factors . . . . .              | 85         |
| 3.3              | ALMA Observations . . . . .  | 88         |
| 3.4              | Results and Analysis . . . . .   | 89         |
| 3.4.1            | Initial continuum analysis . . . . .                                     | 89         |
| 3.4.2            | Continuum Modelling . . . . .  | 92         |
| 3.4.3            | Gaussian Torus . . . . .   | 93         |
| 3.4.4            | Gaussian Torus with Asymmetry . . . . .                                  | 96         |
| 3.4.5            | Gaussian Torus with Point Source . . . . .                               | 98         |
| 3.4.6            | Continuum Modelling summary . . . . .                                    | 99         |
| 3.4.7            | CO Non-Detection . . . . .   | 99         |
| 3.4.8            | Herschel/PACS Modelling and Revised SED Model . . . . .                  | 101        |
| 3.4.9            | Blackbody vs Resolved Radii . . . . .                                    | 105        |
| 3.4.10           | Scattered Light Non-Detections . . . . .                                 | 106        |
| 3.5              | Discussion . . . . .   | 112        |
| 3.6              | Conclusions . . . . .  | 114        |
| <b>Chapter 4</b> | <b>ALMA's view of the M-dwarf GSC 07396-00759's edge-on debris disc:</b> |            |
|                  | <b>AU Mic's coeval twin</b>  | <b>116</b> |
| 4.1              | Introduction . . . . .   | 117        |
| 4.2              | ALMA Observations . . . . .  | 121        |
| 4.2.1            | Continuum Analysis . . . . .   | 121        |
| 4.3              | Modelling . . . . .  | 123        |
| 4.4              | Results and analysis . . . . .   | 127        |
| 4.4.1            | Gaussian torus model . . . . .   | 127        |
| 4.4.2            | Double power law model . . . . .   | 128        |
| 4.4.3            | Flux density distribution and fractional luminosity modelling . . . . .  | 129        |
| 4.5              | Discussion . . . . .   | 133        |
| 4.5.1            | Comparison with near-IR scattered-light observations . . . . .           | 133        |
| 4.5.2            | Comparison with other M-dwarf discs . . . . .                            | 138        |
| 4.5.3            | CO non-detection . . . . .   | 138        |
| 4.6              | Conclusions . . . . .  | 139        |
| 4.7              | Appendix . . . . .   | 142        |
| 4.7.1            | Modelling posteriors . . . . .   | 142        |



|                  |  |            |
|------------------|--|------------|
| <b>Chapter 5</b> | <b>An ALMA survey of Beta Pictoris Moving Group M-dwarfs</b> | <b>145</b> |
| 5.1              | Introduction . . . . .                                       | 146        |
| 5.2              | Observations . . . . .                                       | 147        |
| 5.2.1            | Observation Sample . . . . .                                 | 147        |
| 5.2.2            | Observation Details . . . . .                                | 150        |
| 5.2.3            | Initial image analysis . . . . .                             | 152        |
| 5.3              | Results . . . . .  | 156        |
| 5.3.1            | Gaia DR3 parallaxes and binary implications . . . . .        | 156        |
| 5.3.2            | Non-significant excesses . . . . .                           | 163        |
| 5.3.3            | Significant excesses . . . . .                               | 165        |
| 5.4              | Discussion . . . . .   | 171        |
| 5.4.1            | Survey sensitivity and detection fraction . . . . .          | 171        |
| 5.4.2            | Detection fraction in context . . . . .                      | 172        |
| 5.4.3            | Radii in context . . . . .                                   | 175        |
| 5.5              | Conclusion . . . . .   | 175        |
| <b>Chapter 6</b> | <b>Conclusions</b>   | <b>179</b> |
| 6.1              | New resolved ALMA imaging of M-dwarf discs . . . . .         | 180        |
| 6.2              | An ALMA survey of M-dwarfs . . . . .                         | 183        |
| 6.3              | Summary . . . . .  | 184        |
| 6.4              | Future work . . . . .  | 185        |
| 6.5              | Future prospects . . . . .                                   | 186        |

# List of Tables

|     |   |     |
|-----|---|-----|
| 2.1 | The significant differentiating factors between ALMA Bands. . . . .     | 77  |
| 3.1 | Median model disc parameters for Fomalhaut C. . . . .                   | 94  |
| 3.2 | Median parameters for the Herschel model of Fomalhaut C's disc. . . . . | 104 |
| 4.1 | Median disc parameters for GSC 07396-00759. . . . .                     | 126 |
| 5.1 | Stars observed in the BPMG sample. . . . .                              | 149 |
| 5.2 | ALMA observation details for the BPMG sample. . . . .                   | 151 |
| 5.3 | BPMG sample observational results. . . . .                              | 154 |
| 5.4 | BPMG background sources. . . . .  | 155 |

# List of Figures

|      |   |    |
|------|---|----|
| 1.1  | The evolution of young stellar objects (YSOs) and their discs. . . . .                              | 2  |
| 1.2  | The debris disc of Fomalhaut as seen by ALMA and Hubble. . . . .                                    | 11 |
| 1.3  | Example dust size distributions. . . . .  | 15 |
| 1.4  | $\beta$ as function of grain size for GSC 07396-00759. . . . .                                      | 22 |
| 1.5  | The ways interior planets can affect debris discs. . . . .  | 26 |
| 1.6  | The different structures within debris discs. . . . .   | 29 |
| 1.7  | The stellar flare detected from Proxima Centauri in the mm. . . . .                                 | 36 |
| 2.1  | SED for the disc of Fomalhaut C. . . . .  | 40 |
| 2.2  | Fractional luminosity - temperature plot for the disc of GSC 07396-00759 .                          | 45 |
| 2.3  | The local electromagnetic radiation environment in the near-ultraviolet to<br>mid infrared. . . . . | 47 |
| 2.4  | Atmospheric windows at sea level. . . . .   | 48 |
| 2.5  | The disc of Fomalhaut as seen by different telescopes. . . . .                                      | 51 |
| 2.6  | Aerial view of ALMA. . . . .  | 54 |
| 2.7  | A two-receiver interferometer. . . . .  | 56 |
| 2.8  | A two-receiver interferometer measuring two different sources. . . . .                              | 57 |
| 2.9  | The fringe pattern response to a source of a two receiver interferometer. . .                       | 59 |
| 2.10 | A two-receiver interferometer with a time delay. . . . .  | 60 |
| 2.11 | The fringe pattern of a two-receiver interferometer and resolution. . . . .                         | 61 |
| 2.12 | The $l, m$ and $u, v$ planes, in relation to the sky and to a physical baseline. . .                | 64 |
| 2.13 | Fourier domains. . . . .  | 66 |
| 2.14 | Example 1D Fourier transforms. . . . .  | 67 |
| 2.15 | Example 2D Fourier transforms. . . . .  | 69 |
| 2.16 | The relationship between a visibility and its spatial wave. . . . .                                 | 70 |
| 2.17 | The difference in information carried by long and short baselines. . . . .                          | 71 |
| 2.18 | The effect of the Earth's rotation on measured visibilities. . . . .                                | 72 |
| 2.19 | The dirty beam. . . . .   | 73 |

|      |   |     |
|------|---|-----|
| 2.20 | Atmospheric transmission in the frequency range of ALMA's observations.                         | 78  |
| 3.1  | Naturally-weighted CLEAN image of the disc around Fomalhaut C. . . . .                          | 90  |
| 3.2  | Deprojected radial profile of the disc around Fomalhaut C. . . . .                              | 91  |
| 3.3  | Naturally-weighted dirty images of the Fomalhaut C residuals. . . . .                           | 95  |
| 3.4  | Distribution of offsets of Fomalhaut C's disc. . . . .  | 97  |
| 3.5  | CO J=3-2 spectra for the debris disc around Fomalhaut C. . . . .                                | 102 |
| 3.6  | Herschel 160 $\mu$ m PACS detection of the Fomalhaut C disc. . . . .                            | 103 |
| 3.7  | Fomalhaut C flux density distribution (SED). . . . .  | 107 |
| 3.8  | HST STIS observations of Fomalhaut C. . . . .   | 108 |
| 3.9  | VLT/SPHERE observations of Fomalhaut C. . . . .   | 110 |
| 3.10 | Plot of resolved planetesimal belt radii against stellar host luminosity. . . .                 | 113 |
| 4.1  | Naturally-weighted CLEAN image of the disc around GSC 07396-00759. . .                          | 122 |
| 4.2  | Profile of the GSC 07396-00759 disc along its major-axis. . . . .                               | 123 |
| 4.3  | Naturally-weighted dirty images of the GSC 07396-00759 residuals. . . .                         | 128 |
| 4.4  | Example SED for the disc of GSC 07396-00759. . . . .  | 130 |
| 4.5  | Plot of fractional luminosity against representative temperature for GSC 07396-00759. . . . .   | 131 |
| 4.6  | Comparison of scattered light and ALMA imaging of GSC 07396-00759's disc. . . . .               | 134 |
| 4.7  | Comparative brightness profiles observed for the disc of GSC 07396-00759. .                     | 136 |
| 4.8  | mm-wave resolved debris disc radii plotted against host stellar luminosity. .                   | 137 |
| 4.9  | CO J=3-2 spectra for the debris disc around GSC 07396-00759. . . . .                            | 140 |
| 4.10 | Posterior distributions of the Gaussian disc model for GSC 07396-00759. .                       | 143 |
| 4.11 | Posterior distributions of the double power law disc model for GSC 07396-00759. . . . .         | 144 |
| 5.1  | Naturally weighted ALMA images of the BPMG M-dwarf sample. . . . .                              | 153 |
| 5.2  | Naturally weighted ALMA image of TYC 7443-1102-1. . . . .                                       | 164 |
| 5.3  | Naturally weighted ALMA image of HD 155555 C. . . . .   | 165 |
| 5.4  | Naturally weighted ALMA image of AT Mic AB. . . . .   | 166 |
| 5.5  | Naturally weighted ALMA images of GSC 07396-00759, GJ 2006 A and AT Mic AB. . . . .             | 167 |
| 5.6  | Example SEDs for GSC 07396-00759, GJ 2006 A and AT Mic AB. . . . .                              | 168 |
| 5.7  | Fractional luminosity - temperature plots for GSC 07396-00759, GJ 2006 A and AT Mic AB. . . . . | 169 |
| 5.8  | Plot of detection limits for all observations. . . . .  | 173 |

|     |   |     |
|-----|---|-----|
| 5.9 | mm-wave resolved debris disc radii plotted against host stellar luminosity. | 176 |
|-----|---|-----|

# Acknowledgments

I would like to extend my deepest gratitude to my supervisor Grant Kennedy for the mountains of knowledge, guidance and patience he has extended to me over the past four years.

I'd like to thank all the great office mates I've had for providing my days with an interest excess: Elena, James, Tim, Ed, Matt, Sahl, Cat, Tom and Rebecca.

I'd also like to thank my excellent Dungeons & Dragons group for giving me something to look forward to every week: Chris, Jack, Matt, Matt and Tom.

Not to forget my final year friends for revitalising life after lockdown: Amena, Azib, Raph, Anna-Maria, Mairi and Vanessa.

Of course, the constant companionship of my oldest friends: Alex, Euan, Jason, Tim and Gareth.

The peerless music recommendations of: Abhinav.

I'd also like to thank my secondary-school science teacher Dr O'Neil for encouraging me to love science and keep on learning.

And finally, I'd like to thank my ultimate bastion of love and support: my Mum.

# Declarations

I declare that this thesis is my own work except where explicitly stated otherwise. This thesis has not been submitted to this or any other academic institution for any other degree or qualification. A large amount of the research presented in this thesis has been published in peer reviewed journals. In particular:

Chapter 3 This chapter is reproduced from Cronin-Coltsmann et al. [2021];

Chapter 4 This chapter is reproduced from Cronin-Coltsmann et al. [2022];

Chapter 5 This chapter contains an excerpt from my contribution to Tanner et al. [2020].

The exact contributions to these works by collaborators are declared at the start of each chapter.

# Abstract

Debris discs are an essential piece of planetary system architecture. These exo-asteroid belts and exo-Kuiper belts of stellar systems both comprise that which did not form into planets and are often indelibly marked by that which did. Observing and understanding them is necessary to understanding planetary systems as a whole.

M-dwarf debris discs are one of the largest current unknowns within debris disc science. Past surveys have found vanishingly small, if not empty, detection rates among field populations. Only eight discs are currently published in the literature, only four have been resolved, and only the disc of AU Mic has been resolved both thermally and in scattered light. Whether or not M-dwarf discs are significantly less common than the discs of earlier types, or are significantly different in dust properties and planetesimal belt morphology to the discs of earlier types, are unresolved questions.

In this thesis I present new resolved ALMA images of two M-dwarf debris discs never before observed at mm-wavelengths or thermally resolved. I also present the first ALMA survey searching for M-dwarf debris discs, identifying two new M-dwarf debris discs and presenting excellent opportunities for follow-up observation.

I analyse the newly mm-resolved Fomalhaut C debris disc, now the latest type star to have a resolved debris disc, and find the ring to have a  $880\ \mu\text{m}$  flux of  $0.9 \pm 0.1$  mJy, a radius of  $26.4 \pm 0.6$  AU and a narrow full width at half maximum of at most 4.2 AU. I find a  $3\sigma$  upper limit on the eccentricity of 0.14, neither confirming nor ruling out previous dynamical interactions with Fomalhaut A. Finally, I find that its radius is as expected from previous disc radius–host luminosity trends.

I also analyse the newly mm-resolved GSC 07396-00759 debris disc, now the second M-dwarf star to be resolved both thermally and in scattered light, and find the ring to have a  $880\ \mu\text{m}$  flux of  $1.84 \pm 0.22$  mJy and a radius of  $70.2 \pm 4.4$  AU. I confirm the total intensity scattered light radius found by Sissa et al. [2018], which is significantly smaller than the radius derived from the polarimetric scattered light observations of Adam et al. [2021], implying complex behaviour in the scattering phase function. I do not recover the brightness asymmetry found in scattered light observations, nor evidence of an extended halo of dust grains, implying that these features observed in scattered light must be limited to the small grain dust and are likely the result of pressure forces acting on the disc, such as stellar wind pressure and interaction with the interstellar medium.

Finally, I analyse ALMA observations of 33 M-dwarf systems in the  $\beta$  Pictoris Moving Group, the first such survey conducted with ALMA. I detect two sub-mm excesses that likely constitute new M-dwarf debris discs around GJ 2006 A and AT Mic A and model distributions of the disc fractional luminosities and temperatures. From the science sample of 36 M-dwarfs including AU Mic I find a disc detection rate of 4/36 or  $11.1^{+7.4}_{-3.3}\%$  that rises to  $23.1^{+8.3}_{-5.3}\%$  when adjusted for completeness and conclude that this detection rate is consistent with the detection rate of discs around G and K type stars and that M-dwarf discs are not less likely to host debris discs, but instead require longer wavelength and higher sensitivity observations than have previously been employed.



# Abbreviations

|              |   |
|--------------|---|
| log          | Logarithmic   |
| Jy           | Jansky, a measure of spectral flux density where $1 \text{ Jy} = 10^{-26} \text{ W} \cdot \text{m}^{-2} \cdot \text{Hz}^{-1}$   |
| $M_{\oplus}$ | Earth mass, $5.92 \times 10^{24} \text{ kg}$  |
| $M_{\odot}$  | Solar mass, $1.99 \times 10^{30} \text{ kg}$  |
| $L_{\odot}$  | Solar Luminosity, $3.83 \times 10^{26} \text{ W}$   |
| pc           | Parsec, 206,000 AU, $30.9 \times 10^{12} \text{ km}$  |
| AU           | Astronomical Unit, distance from Earth to the Sun, $150 \times 10^6 \text{ km}$   |
| M-dwarf      | Main-sequence, or pre-main-sequence, M-type star a.k.a. 'Red dwarf'   |
| BPMG         | $\beta$ Pictoris Moving Group, a young [ $\sim 20 \text{ Myr}$ , Bell et al., 2015; Miret-Roig et al., 2020] and nearby [ $\lesssim 100 \text{ pc}$ , Shkolnik et al., 2017] association of stars |
| RA           | Right Ascension, on-sky equatorial coordinate axis  |
| Dec          | Declination, on-sky equatorial coordinate axis  |
| IR           | Infrared, light of longer wavelength than the human eye can see, but shorter than microwave radiation   |
| NIR          | Near-Infrared light, with wavelength $\sim 0.7 \mu\text{m}$ - $3 \mu\text{m}$   |
| MIR          | Mid-Infrared light, with wavelength $\sim 3 \mu\text{m}$ - $30 \mu\text{m}$   |
| Far-IR       | Far-Infrared light, with wavelength $\sim 30 \mu\text{m}$ - $0.45 \text{ mm}$   |
| Sub-mm       | Sub-millimetre light, with wavelength $\sim 0.45 \text{ mm}$ - $1 \text{ mm}$   |
| mm-wave      | $\sim$ Millimetre-wavelength light, with wavelength $\sim 0.85 \text{ mm}$ - $5 \text{ mm}$   |
| SED          | Flux Density Distribution   |

HST Hubble Space Telescope

Hubble Hubble Space Telescope

Spitzer Spitzer Space Telescope

Herschel Herschel Space Observatory

VLT Very Large Telescope

ALMA Atacama Large Millimetre/submillimetre Array

FOV Field of View

PWV Precipitable Water Vapour

MRS Maximum Recoverable Scale

RMS Root Mean Square, a measure of noise

SNR Signal-to-Noise Ratio

FWHM Full Width at Half Maximum (of a distribution)

# Chapter 1

## Introduction

This thesis is concerned with discs. In general astrophysical terms, a disc is a collection of material in orbit around a central object, flattened into one plane and continuously spread throughout the entirety of the orbit. There are discs present at nearly every scale in astronomy, from circumplanetary discs like the ring system of Saturn, to galactic discs like that of the Milky Way. In particular, this thesis examines discs around stars. At every point in a star's lifetime there is a disc, from the protoplanetary disc in which a planetary system forms to the discs around stellar remnants, white dwarf or black hole accretion discs. In particular, this thesis focuses on *debris discs*, discs around main sequence stars. However, it is still useful to consider where these discs came from, and where they go.

### 1.1 The Stellar Life Cycle and Its Discs

#### 1.1.1 Young Stellar Objects

Before there is a star, there is its parent molecular cloud. The molecular cloud consists of mostly hydrogen and helium, and some metals that were formed by previous generations of stars. The cloud's self-gravity initially causes the formation of dense filaments which in turn begin to spherically collapse into gravitationally bound cores. As the core heats and contracts, hydrogen molecules are dissociated and hydrogen and helium atoms ionise, the core eventually reaches a point where its internal gas pressure is strong enough to resist further gravitational collapse and it becomes truly protostellar [Williams and Cieza, 2011]. Until this point we could use the label 'Class 0 Young Stellar Object (YSO)' for the burgeoning protostar, hallmarked by a lack of observable flux at wavelengths less than  $\sim 20\,\mu\text{m}$ , as the faint protostar is too deeply embedded for its light to escape. This stage is displayed at the top of Figure 1.1. At this point the envelope of infalling matter still has more mass than the forming core. The continuing accretion of the initial cloud is complex.

## Evolution of young stellar objects

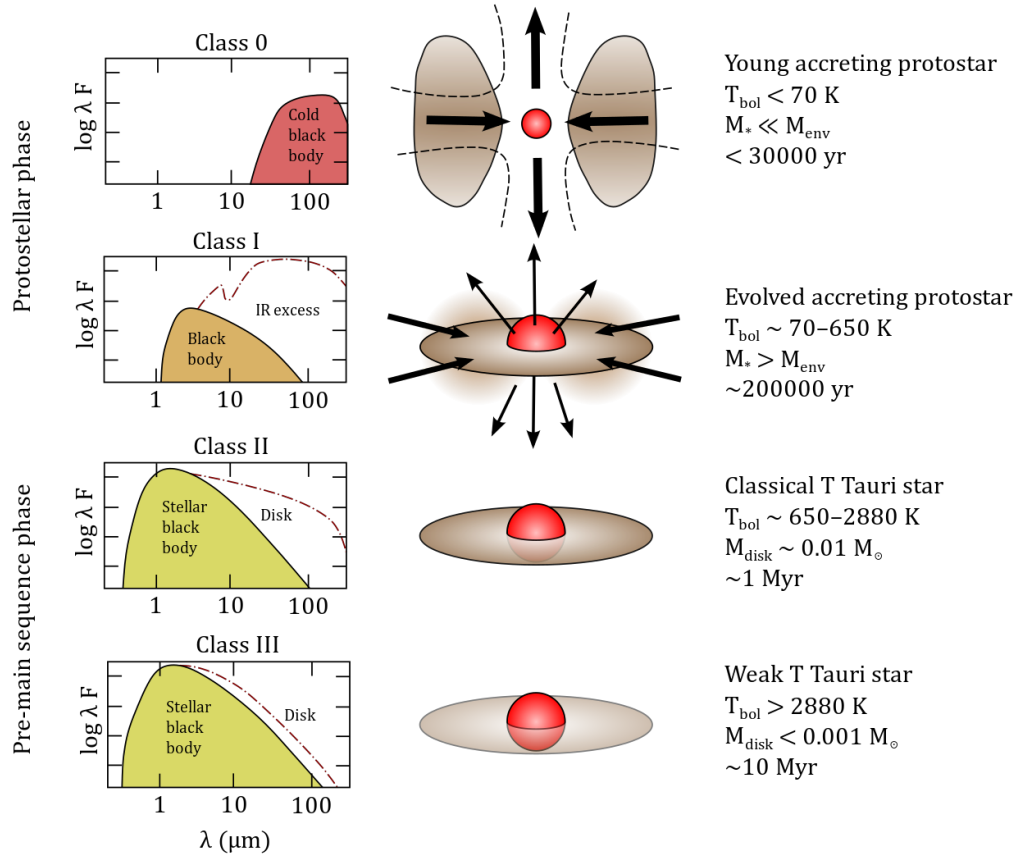


Figure 1.1: The evolution of young stellar objects (YSOs) and their discs. Left: spectral energy distributions. Centre: simplified view. Right: approximate parameters. This image was taken from Wikimedia commons [[https://commons.wikimedia.org/wiki/File:Evolution\\_of\\_young\\_stellar\\_objects.svg](https://commons.wikimedia.org/wiki/File:Evolution_of_young_stellar_objects.svg)] produced by User:Vallastro and published under Creative Commons Attribution-Share Alike 4.0 International license [<https://creativecommons.org/licenses/by-sa/4.0/deed.en>].

To begin with, the material in the cloud has some angular momentum about the core, and material that is further from the core possesses more angular momentum. During collapse as this distant material moves further in, any rotation must increase to conserve angular momentum, and through viscosity and friction the infalling material forms a circumstellar disc. The original cloud would have had a dominant angular momentum to begin with and this likely sets the final disc axis. Checking for similar inclinations of discs around stellar companions may help identify whether the stars originated from the same cloud. Not all the material can successfully accrete and large outflows of material are also forming perpendicular to the disc axis by magneto-hydrodynamic action as a consequence of the winding of magnetic field lines during accretion [Williams and Cieza, 2011].

This disc was forming even in the Class 0 phase but comes into prominence in the Class I phase that is characterised by a rising spectral slope in the near to mid-infrared and where the mass of the protostar increases beyond the mass of the remaining envelope, the envelope itself is now of similar mass to the disc. This stage is displayed second from the top of Figure 1.1.

After about 0.5 Myr all of the original envelope has either accreted onto the now-star, formed into the disc or has outflowed, leaving just the star and a *protoplanetary disc* whose mass is typically 1% of the star's. This Class II phase is characterised by a decreasing slope in the mid-IR but still a readily apparent 'infrared excess'. This stage is displayed second from the bottom of Figure 1.1.

Infrared excess is an observationally derived term that means we measure more flux from a stellar system at a specific wavelength or range of wavelengths than can be accounted for by the star's relatively hot blackbody radiation. There is additional flux observed that is in excess of the star's flux; this nearly always means that there is another cooler blackbody/blackbodies in the system that is producing the excess flux.

There is still some accretion of disc material onto the star evidenced by strong hydrogen  $\alpha$  emission; in later type stars, i.e. FGKM, this trait along with a variability in luminosity relates these stars with the star T Tauri, thus also earning these stars the label 'Classical T Tauri stars'. In earlier type stars, i.e. earlier than F0, these massive young stars may be similarly identified as 'Herbig Ae/Be stars'. The disc material is optically thick and the dust and gas in the disc may now be forming into planetesimals and protoplanets [Raymond and Morbidelli, 2022].

The star has not yet quite reached the 'main-sequence', its 'adult' life where it will spend most of its lifetime.

Young stars that are still variable in luminosity but that have lost their large gas discs and the associated infrared excess can be called Class III YSOs or sometimes 'Weak Line T Tauri stars', where 'line' refers to spectral lines that indicate accretion, such as hydrogen

$\alpha$ . This stage is displayed at the bottom of Figure 1.1.

We sometimes seem to catch young stars that may be in the process of losing their gas discs and we label these as ‘Transition Discs’. The NIR emission in these discs has dropped, as the inner dust reservoir becomes optically thin, but MIR and Far-IR emission remains. Effectively a cavity has formed between the star and a still massive outer ring. The processes that have caused this are likely a mix of: accretion of material onto the host star; dust being coagulated into larger bodies; larger bodies like planets clearing out remaining material in and near their orbits; and photoevaporation of disc material by strong stellar UV and X-ray fluxes. The disc continues to clear from the inside-out until all that remains are the main-sequence host star, orbiting planets and belts of planetesimals we call ‘Debris Discs’. About half of young stars have lost their gas-rich discs after a few Myrs and nearly all have lost them by ten Myrs. The transition phase may itself only last a few tenths of a Myr [Owen, 2016; Najita et al., 2015].

Many stars with different initial masses may also have been born at a similar time in the parent molecular cloud, forming a ‘young stellar association’. These may also be identified by astronomers as a ‘moving group’, as they typically share a common location in space and velocity through the galaxy, alternatively we can identify related stars by dynamically tracing back the movement of the stars by their age to find that a group of now more relatively disparate stars were all born in a similar place.

### **1.1.2 Main-sequence stars – debris discs in brief**

A stellar system on the main sequence may observationally comprise the following: a host star (or stars in a close binary), a companion star/s or brown dwarf/s, exo-planets, exo-zodiacal dust, an exo-asteroid belt and an exo-Kuiper belt. Exo-asteroid belts and exo-Kuiper belts we more commonly label as debris discs. All of the primordial dust and gas is removed from the system, but that does not preclude the ongoing presence of dust or gas. Here is the age of second-generation dust and gas, that originates from the debris disc.

After the era of rocky body formation in the protoplanetary disc, any material that was not either accreted/blown out or formed into a planet, instead formed ‘planetesimals’. A planetesimal is simply a rocky/icy body too small to be labelled as a planet, i.e. they do not gravitationally clear their orbits and most do not possess the self-gravity to relax into spheres, but they are larger than what can be safely considered dust or pebbles with gray space in between on the metre scale. Effectively, planetesimals are on the order of one to one thousand km in size.

Planetesimals mostly reside in rings around the host star, although some bastions survive about the Lagrange points of large planets, like the Trojan asteroids in the Solar System. Although these rings are dynamically stable, they are far from tranquil. The

planetesimals are in a constant collisional cascade.

Planetesimals collide, and in these destructive collisions they break up and produce smaller planetesimals, dust and some gas. The smaller planetesimals produced in those collisions go on to collide themselves, and so on. Over time the dust is removed from the system by the forces of stellar wind, radiation pressure and Poynting-Robinson drag (PR drag), but is replenished by the ongoing collisions. Eventually the planetesimals themselves also deplete, reducing the total mass in the disc across all sizes also reducing the disc's brightness and observability.

It is the continually replenished second generation dust that we primarily observe when looking for debris discs. The total luminosity of the dust is typically less than a thousandth the total luminosity of the host star, i.e. its 'fractional luminosity',  $L_d/L_\star$ , is constrained to:  $L_d/L_\star \lesssim 10^{-3}$ .

The evolution of the disc can be more dramatic in younger systems. The Solar System's Kuiper belt (together with the asteroid belt forming the Solar System's debris disc/s) is significantly less massive than its observed contemporaries, and indeed would not be observable with current technologies if it were around another star. We have evidence to believe that this lack of material in the Solar System's debris disc is the consequence of significant clearing in the system's past. The cratering record on the Moon and Mars, combined with the age of recovered Moon rocks, provides evidence for a past influx of impactors termed the 'Late Heavy Bombardment' (LHB), however the precise timing and duration of the LHB is widely debated [Bottke and Norman, 2017, and references therein]. One possibility is a 'Terminal Cataclysm' model, a short lived pulse of impactors 3.8-4.0 Gyr ago, when the Solar System was 0.6-0.8 Gyr old. Another possibility is a 'declining bombardment' model that starts 0.2 Gyr earlier, but with a lower impact rate that slowly tails off over hundreds of millions of years. Hybrid models that include aspects of each scenario are also possible.

The 'declining bombardment' model sources impactors from leftover planetesimals that were dynamically excited in the early Solar System by the forming protoplanets and planetary embryos but survived past the planet-formation era in addition to planetesimals from dynamically unstable regions in the young asteroid belt.

The 'Terminal Cataclysm' model is based on the disruption of planetesimal orbits by gravitational instabilities induced by planetary migration. One such planetary migration model is the 'Nice Model' [Gomes et al., 2005]: in the early Solar System the giant planets were originally in a tighter formation. Over time, planetesimals from a more massive proto-Kuiper belt occasionally crossed the outer planets' orbits, gravitationally exchanged some momentum and caused the planets' orbits to migrate. Eventually due to this migration the giant planets begin to gravitationally affect each other and their orbits were destabilised.

In the ensuing movement and eventual re-settling of the planets’ orbits, large amounts of planetesimals in both the Kuiper belt and asteroid belt had their orbits disrupted, causing the observed LHB when these disrupted orbits intersect with the inner planets. Overall, one of the end results is the thinning of the Solar System’s debris disc. However, recent research has suggested that planetary instability ought to occur much earlier within the Solar System’s history, within the first 100 Myr [de Sousa et al., 2020]. Such an early instability would be incompatible with a Terminal Cataclysm LHB.

The entirety of a LHB-like sequence is not directly observable around other stars, unless we were able to catch a system in the precise moments in which we can tell that a visible disc is likely to be unstable in the presence of a visible planet, but they may help explain why some systems do not have observable debris discs.

LHB-like events, short or long lasting, are not the only possible stochastic occurrences, and we have further evidence for another extreme event that happened in our Solar System. The ‘giant-impact hypothesis’ derived from the peculiarities of the Earth-Moon system describes a catastrophic collision between the Earth and a Mars-sized body that ended up forming the Moon. Another consequence of such an event would be a huge release of dust into solar orbit, the thermal emission of such dust and its variability across its orbit could be visible from outside of the Solar System [Kenyon and Bromley, 2005; Asphaug, 2014]. Indeed, we think we do see such traces of similar events around other stars in what we call ‘extreme debris discs’ [Su et al., 2019]. Extreme debris discs, e.g. those in the ID8 and P1121 systems, typically present in younger systems with large mid-to-near-IR excesses and accompanying fractional luminosities greater than the debris disc typical, i.e.  $L_d/L_\star \gtrsim 10^{-2}$ , that imply huge amounts of dusty material close to the star. The infrared flux has short term variation on the scale of weeks and months and can also show separate long term decay and additional variation on the scale of years. Finally, spectral observations find evidence of material that typically composes dust like olivine and forsterite [Olofsson et al., 2012]. The cohesive hypothesis for all this evidence is that one or more recent giant impacts have produced large clouds of dust and silica vapour in an orbital region close to the star where otherwise naturally collisionally evolving dust would not exist or survive long in such amounts. Short term variation in flux is due to the progression of the clouds along their orbit varying their geometry from dynamical shearing whereas the long term evolution is due to collisional evolution of the material and formation of the visible small dust grains.

Additionally, we occasionally see brightness asymmetries and dust clumps in debris discs [e.g. HD 11520, AU Mic; Crotts et al., 2022; Boccaletti et al., 2015; Chiang and Fung, 2017], for which an often posited cause is a recent large collision [Jackson et al., 2014; Kral et al., 2015].

Even closer to the star, observed in the near-IR and with interferometry, are the



hot dust ‘exo-zodis’, analogues to the Solar System’s zodiacal dust but a thousand times brighter [Defrère et al., 2015; Sezestre et al., 2019]. Sometimes the near-IR is accompanied by warm mid-IR emission, and the spectral slope observed necessitates that exo-zodi dust is dominated by small submicron grains that sit at or very close to the sublimation radius at a few stellar radii, interior to which the dust would vaporise from the energy of the incoming stellar radiation. As a traditional collisionally cascading dust belt could not survive at such a small radius due to the short collisional lifetime, alternative explanations have to be found for the presence of the dust, specifically it must be transported inwards from some external supply. It has been suggested that dust grains inwardly migrate from a distant parent planetesimal belt due to Poynting-Robertson drag, and sublimation then shrinks the grains when they reach the inner stellar system [Belton, 1966; Mukai et al., 1974; Mukai and Yamamoto, 1979], but when modelled this mechanism does not seem to produce enough flux or small enough grain sizes [Kobayashi et al., 2008, 2009, 2011; van Lieshout et al., 2014]. Alternative studies conclude that PR-drag of small grains from a parent planetesimal belts can explain exo-zodis in all but the brightest cases [Rigley and Wyatt, 2020]. An alternative scenario is that the dust is sublimated in situ off of large bodies, namely asteroids and comets that have been scattered there by planets [Bonsor et al., 2012; Raymond and Bonsor, 2014; Marboeuf et al., 2016].

This then leads us into the direct observation of comets in other stellar systems, labelled ‘exocomets’. Like comets in our own Solar System, exocomets we presume originate in distant reservoir belts - the main debris discs of the system - and are simply the local icy planetesimals that have been scattered onto inner system crossing orbits. When an exocomet nucleus comes close to its star on its orbit it will outgas and break up to create an accompanying coma and tails of gas and dust. It is the coma and tails that we can observe, through two main avenues [Strøm et al., 2020]. First, spectrally: as the cometary material passes in front of the star at distances of tens of stellar radii, ionised atoms, e.g. CaII [Ferlet et al., 1987], intercept and absorb ultraviolet starlight through the line of sight resulting in deficits in the observed stellar spectrum. These absorption features are also measurably shifted from the systemic velocity due to the comet’s own velocity relative to the star in their orbits. Over time, the changing shift of the absorption features can directly trace the motion of the exocomet. Second, photometrically: as the comet passes in front of the star the coma and tail block enough of a fraction of broadband optical starlight resulting in a time-evolving dip in measured light on the scale of tenths of a percent [Zieba et al., 2019]. The asymmetric transit signature is unique to the cometary origin: the transit begins with a traditional dip as the mostly optically dense coma passes in front of the star but this sharply turns to an exponential decay in transit depth due to the passage of the decreasingly optically deep tail, resulting in a final sawtooth shape.

An exocomet is simply an icy planetesimal from an outer reservoir that happens to have been scattered interior to its parent belt. As mentioned before the planetesimals in the parent belt are also icy as well as rocky, and in their local grinding collisions that produce the observable dust, observable gas can also be released. However production of gas is in such small quantities and with such little thermal excitement that it has only been observed in a handful of systems, e.g. Fomalhaut and TWA 7 [Matrà et al., 2017; Matrà et al., 2019a].

### 1.1.3 Giant branch stars

Debris discs can still survive into the post main sequence in a recognisable form. For example, the 2.5 Gyr old K-type subgiant star  $\kappa$  CrB retains its debris disc as resolved by Herschel [Bonsor et al., 2013]. A large planet of mass  $m$  degenerate with the unknown inclination  $i$  of the system  $m \sin i = 2.1 M_J$  is also known to be present in the system at 2.8 AU [Johnson et al., 2008]. The disc can be described by different models depending on the disc's intersection with other unknown planets or companions in the system, as either a single wide belt between from 20 to 220 AU or as two narrow belts centred on 40 and 165 AU. Bonsor et al. [2013] infer that the observability of the disc precludes an LHB-like event from having happened in the system's history, thus also constraining the migrations of any planets in the system.  $\kappa$  CrB demonstrates the potential for debris discs to both survive for several Gyrs and remain observable and for both a planetary system and a debris disc to survive as the host star moves off the main sequence. A Herschel survey found that 4 of 36 observed subgiants, including  $\kappa$  CrB, possessed infrared excesses likely indicating the presence of a debris discs [Bonsor et al., 2014], demonstrating that this is not an isolated phenomenon.

### 1.1.4 White dwarfs

Even in the stellar remnant phase do we find evidence of debris discs and planetesimals. For decades, white dwarfs have also been found to have infrared excesses [e.g. Zuckerman and Becklin, 1987; Graham et al., 1990], evidence of circumstellar dust close to the star. The generally accepted hypothesis is that the dynamical stability of planetesimals in a surviving debris disc is reduced as the host star evolves into a white dwarf, causing some planetesimals to be scattered into the inner system [Debes and Sigurdsson, 2002] where the tidal forces of the white dwarf disrupt them, forming a circumstellar dust and gas disc [Jura, 2003; Veras et al., 2014]. The dust clouds produced after a recent large planetesimal disruption have even been observed transiting the host white dwarf [Vanderburg et al., 2015; Gänsicke et al., 2016; Gary et al., 2017] and the gas in the disc can be observed from emission lines that are double-peaked due to the towards and away-from line-of-sight Keplerian rotation of the

orbit [Manser et al., 2021].

Over time the individual grains drift into the star due to Poynting-Robertson drag and other mechanisms [Rafikov, 2011; Veras et al., 2015], sublimating, accreting and ‘polluting’ the stellar atmosphere and leaving absorption lines observable via spectroscopy [e.g. Debes et al., 2012]. These elements would naturally sink into the white dwarf on a short timescale and so their observation necessitates recent and continuous replenishment, reinforcing the distant parent planetesimal belt hypothesis. Looking at these elements present tells us about the composition of the replenishing bodies. In the majority of cases it seems that the pollutants trace rocky asteroids [Ca, Mg, Fe; e.g. Hollands et al., 2018]; however, there has also been observation of volatile rich pollution [C, N, O; e.g. Harrison et al., 2018] that leads to an exocometary origin.

## 1.2 Main-Sequence Debris Discs in Depth

We return to our focus, debris discs, and examine them in more detail.

### 1.2.1 What is a debris disc?

Figure 1.2 displays two images of the Fomalhaut debris disc. The left image shows the disc as captured at a wavelength of 1.3 mm by the Atacama Large Millimetre/submillimetre Array (ALMA), at the centre of the image is the star itself. The debris disc is the clearly defined ring around the star, it is an inclined ring and the flux originates from the thermal emission of mm-sized dust grains. These dust grains share their orbits with the planetesimals whose collisions created them, and so the image also demonstrates the expected distribution of the planetesimals. The right image shows the discs as captured by the Hubble Space Telescope (Hubble/HST) over a wavelength range of 0.2-1.0 microns; at the centre of this image the star has been blocked by a coronagraph. The lines radiating from the central coronagraph are residual starlight, but in a similar position and orientation as to the left, the ring of the debris disc can be seen. Some flux from outside the clearly defined ring that does not originate from the star is also visible, particularly in the top right of the image, this light also comes from dust in the debris disc. The disc flux originates from starlight scattering off of micron sized dust grains in the ring, the scattering effect is weaker at the ansae of the disc and so these seem dimmer, but they are just as physically dense. The micron sized dust grains are more strongly affected by radiation pressure that pushes them outward from the star, and so some micron sized dust grains populate a ‘halo’ around the ring, away from the planetesimals. The inferred planetesimals, the large dust grains that share their orbit and the small dust grains that are pushed outwards are all parts of what we call a ‘debris disc’.

### Where did planetesimals come from?

How did the planetesimals that comprise the backbones of debris discs originally form? Nearly all large body formation occurred while the system was still in the protoplanetary disc phase [Williams and Cieza, 2011; Raymond and Morbidelli, 2022], and primordial dust from the original parent cloud grew into planetesimals and planets, or was removed by either accreting onto the star or being blown out from the system by stellar wind and radiation pressure.

Within the protoplanetary disc, on the simplest level, the orbiting dust grains collide. When these collisions occur at low enough relative velocities, the electrostatic forces between dust grains stick them together to produce a larger grain. With time these larger dust grains would themselves collide and stick and grow.

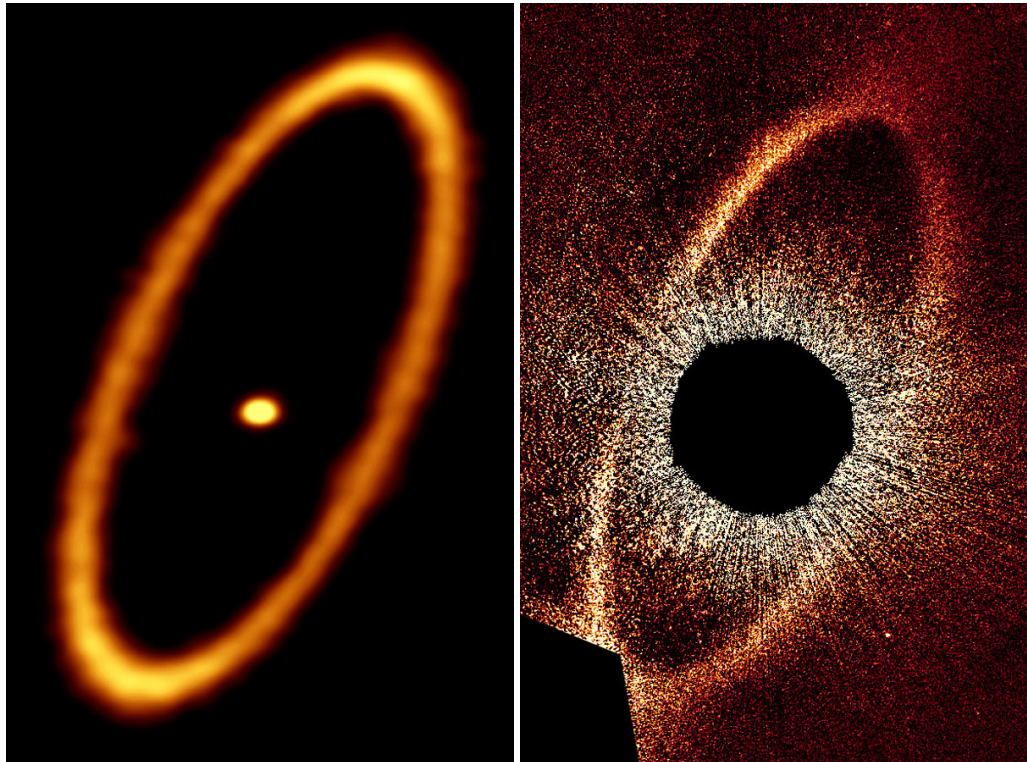


Figure 1.2: The debris disc of Fomalhaut as seen by ALMA at a wavelength of 1.3 mm (Left) and by Hubble over a wavelength range of 0.2-1.0 microns (Right). Left, the star is visible in the centre and right, the star has been blocked by a coronagraph. [Image credit: NASA, ESA and P. Kalas (University of California, Berkeley, USA), Kalas 2013; ALMA (ESO/NAOJ/NRAO); M. MacGregor, MacGregor 2017]

However, dust grains within a protoplanetary disc are constantly drifting within the disc due to the surrounding gas. The viscous fluid gas orbits at non-Keplerian velocity due to the additional radial force of gas pressure that combats or combines with the gravitational force felt, defined by the gradient of the pressure within the disc. Where the pressure gradient is negative, i.e. the pressure decreases with increasing radius, the gas orbits with sub-Keplerian velocity because the interior pressure pushing outwards reduces the effective inwards gravitational force. Where the pressure gradient is positive, i.e. pressure increases with increasing radius, the gas orbits with super-Keplerian velocity because the exterior pressure increases the effective inwards gravitational force, and so the orbiting gas must possess a greater velocity. The dust grains, which are not coupled to the gas and its pressure, instead feel the result of the gas velocity: in a sub-Keplerian zone the gas is felt as a headwind that slows down the dust and in a super-Keplerian zone the gas is felt as a tailwind that speeds the dust up. The total result is that dust grains are always having their velocity affected such that they drift in their orbits towards pressure maxima. If there is a local pressure maximum in the dust, the dust accumulates there. If there are no local pressure maxima, the location of highest pressure in the disc is closest to the star and the dust grains drift towards the star until they ultimately accrete. Because drag force is dependent on surface area, different dust grain sizes drift at different rates. Drift can cause problems for grain growth when it enforces a size-based velocity distribution that prevents agglomerative collisions for certain grain sizes and when grains drift into the star faster than they can grow to significant sizes. This problem has variably been termed the ‘radial-drift barrier’ or the ‘metre-sized barrier’ [e.g. Weidenschilling, 1977; Hayashi, 1981; Desch, 2007; Crida, 2009; Laibe et al., 2012].

So, other mechanisms are required to assist initial growth. The *streaming instability* [Youdin and Goodman, 2005] serves as one of the most significant. The streaming instability examines the result of the equal and opposite force that the dust exerts on the gas in the drag interaction. As a solid particle is buffeted and slowed by the gas headwind, it pushes back and imparts some additional momentum onto the gas, increasing the immediately local gas velocity. In the zone immediately surrounding an interacting particle or an overdense region of particles, the gas is less sub-Keplerian and so less of a headwind is felt for other particles. These other particles then do not feel as much drag and so their drift is reduced, they stay longer in the overdense region and now contribute to the overdensity, reinforcing the total effect. As the effect gets stronger and the more the overdensity grows, there is positive feedback and a large clump of material can grow and survive. An example of a pressure maximum where the streaming instability might be initiated would be the edge of a ring interior to which a forming planet is reducing the local gas density through its accretion. Eventually the clump grows large enough to constitute significantly sized planetesimals following gravitational collapse.

The favourable locations for streaming instabilities to form are where there is already enhanced densities of solid material. This can be local pressure maxima which dust has drifted into, where the pressure maxima themselves can be caused by the effects of other protoplanets in the disc. If the streaming instability requires a protoplanet to already be present to be formed, then that planet must have formed through other means, for example gravitational instability [Boss, 1997]. Enhanced particle densities and sizes can also be found at ice lines, where vapour-phase molecules freeze onto dust grains, adding to their growth.

### The collisional cascade and the size distribution

We have that our debris discs are composed of planetesimals and dust (and small amounts of gas), and that it is the dust that is observed. But how much dust and how many planetesimals relative to each other and across all sizes? What is the distribution of sizes within the disc? The *collisional cascade* describes a continuous *size distribution* of bodies, with larger bodies being broken up by collisions to form a continuous supply of smaller bodies.

The collisions of the larger bodies, sometimes called ‘parent planetesimals’, produce smaller bodies in their destruction, and these smaller bodies collide to produce even smaller bodies, and so on until the smallest dust grains are produced. This is the collisional cascade. An ideal infinite collisional cascade has a differential size distribution defined by the equation:

$$n(s) \propto s^{2-3q} \quad (1.1)$$

where  $n(s)$  is the number of grains of size between  $s$  and  $s+ds$  (interchangeably seen as  $D$  or  $a$ ) and  $q$  is the slope of the number density distribution of grains as a function of mass [Dohnanyi, 1969] and has the value  $11/6$  [Dohnanyi, 1969; Tanaka et al., 1996]. This is sometimes alternatively written in a simplified form as

$$n(s) \propto s^{-p} \quad (1.2)$$

where  $p$  (normally written also as  $q$  but changed here for clarity) represents the slope of the size distribution and is equal to  $3.5$ . Mathematically we can recognise simply that  $2 - 3 \times 11/6 = -3.5$ .

Naturally, real collisional cascades are not ideal, and they vary system to system [e.g. MacGregor et al., 2016]. There are several sources to the non-ideal behaviour:

The real distribution is naturally not infinite, but extends from an  $s_{max}$  at the top, the largest planetesimals formed in the system. In younger systems the collisional lifetimes of these largest bodies can be longer than the age of the system and so they have not necessarily

begun colliding in a given disc.

The lower limit of the size distribution is  $s_{min}$  where the amount of dust grains that are small enough to be removed from the system by pressure forces become significant, i.e.  $s_{min}$  is close to a *blowout size*  $s_{blow}$ .

$s_{max}$  will be on the order of  $\sim 100$  km and  $s_{min}$  is on the order of  $1 \mu m$ , both will vary depending on the individual system. In particular, the blowout size and thus  $s_{min}$  depend strongly on the stellar type of the host, as earlier types will have stronger radiation pressure that can blow out larger grains, and in later type stars radiation pressure can be so weak as to not blow out any grains. In these later type systems where stellar wind pressure becomes the dominant force, the age of the host also becomes important, as stellar activity varies with both type and age.

Smaller particles in the collisional cascade can also destroy particles larger than them, this is called the ‘bullet and target’ model. There is a limit to this and ‘bullets’ that are too small will not have enough kinetic energy to destroy ‘targets’ a certain degree larger than themselves. A corollary to this is that if smaller particles can destroy larger particles, and the size distribution predicts that there are vastly more smaller particles than identical particles of a certain size, then the destruction of targets of a particular size is nearly entirely due to bullets of the smallest feasible size. This idea is important when we consider grains of sizes below  $\sim 1$  mm, where pressure forces become relevant. Grains of these sizes can have ripples in their size distribution due to the disruption of equilibrium caused by the presence of the cut-off size  $s_{min}$  [Campo Bagatin et al., 1994]. As there are no grains smaller than  $s_{min}$  to contribute to the destruction of  $s_{min}$  sized grains, the density at  $s_{min}$  can be enhanced. This then results in a reduction of density above  $s_{min}$  due to enhanced destruction, and then an increased density a step beyond that in a decaying ripple pattern.

Dohnanyi [1969] also treats the differently sized bodies as having constant strength; instead a size dependent critical fragmentation energy can be applied. This is especially relevant when a distinction is made between a ‘strength’ regime, below  $\sim 100$  m where molecular forces hold bodies together, and a ‘gravity’ regime at larger sizes where gravity holds bodies together [O’Brien and Greenberg, 2003].

There is another regime present, the primordial regime where planetesimals with collisional lifetimes longer than the age of the system have not yet begun colliding, and so retain the primordial size distribution of their formation.

And so a more complicated size distribution could have larger bodies that have not yet entered the cascade that temporarily retain their shallow initial distribution, then there is a slope shallower than  $p = 3.5$  in the gravity regime down to the transition to the strength regime, which is steeper than  $p = 3.5$ . At the bottom of the size distribution towards the blowout and  $s_{min}$  there are then wiggles due to the alternating lack of bullets



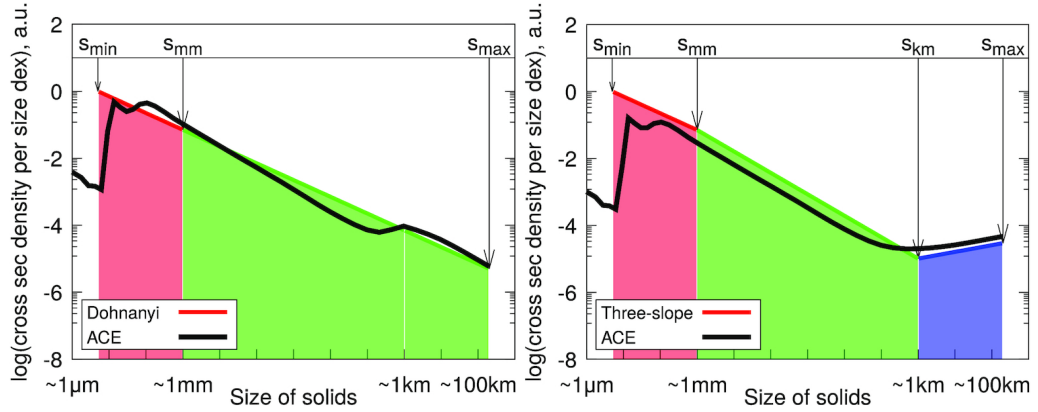


Figure 1.3: Comparison of Left: Dohnanyi [1969] size distribution model with  $p = 3.5$  and Right: the three slope model of Krivov and Wyatt [2021] with the pressure affected dust in red, the colliding planetesimals in green and non-colliding primordial planetesimals in blue. In the axes of both, a horizontal line would correspond to a power-law size distribution with  $p = 3$ . In both, the black line is the typical outcome of a collisional simulation model with the ACE code, using a size-dependent critical fragmentation energy. Both figures are taken from Krivov and Wyatt [2021].

and targets [Löhne et al., 2008; Krivov and Wyatt, 2021]. A comparison of this to the Dohnanyi [1969] theory can be seen in Figure 1.3, from Krivov and Wyatt [2021], with the more complex model labelled as the ACE code that collisionally modelled it. Beyond these, Dohnanyi [1969] also assumes a constant velocity dispersion, if instead different sizes can have different velocity dispersions,  $p$  will change as the collisional rate at each size will vary with velocity [Pan and Schlichting, 2012]. A different velocity dispersion with size is realistic for small grain sizes where pressure forces significantly effect grain dynamics.

The individual dynamics of a system can also be important. The degree of dynamical excitation of the colliding planetesimals [Thébaud and Wu, 2008], the relative orientations of colliding particles [Löhne et al., 2012] and the eccentricities of parent bodies [Pawellek et al., 2014] may all influence the overall size distribution.

The true size distribution for each individual disc is thus uncertain.

### Large bodies and stirring

For destructive collisions to occur, planetesimals must share intersecting orbits for which the relative velocities at the point of impact are large enough to achieve fragmentation. For this requirement to be met, planetesimals must be ‘stirred’. The circular primordial orbits in place during the protoplanetary disc stage resulted in net accretion that allowed for planetesimal and planet growth; without perturbation this status quo would persist into the main-sequence lifespan. A disc can either be *self-stirred* by which the largest planetesimals

within the disc perturb the other planetesimals, or *planet-stirred* by which a planet external to the disc perturbs the planetesimals.

Kenyon and Bromley [2001, 2004a,b, 2005, 2006, 2008] theorise that planetesimals embedded within the disc on the order of 1000 km size (i.e. Pluto-sized objects) are sufficiently massive to dynamically excite planetesimals into destructive orbits.

This theory has a caveat however: the time it takes to produce such a planet can be longer than the lifetime of the protoplanetary disc, particularly at large radii where growth is slower, and so the stirring can be delayed with the collisional cascade only initiating tens or even hundreds of Myrs into the main sequence life of the disc. Such a self-stirring scenario is then called *delayed stirring*. This model has difficulties explaining observations of large discs around young stars. Krivov and Booth [2018] predict that discs can instead be self-stirred by faster-forming planetesimals of 200 km size that are produced in the protoplanetary disc stage via the clumping of pebbles in turbulent vortices and streaming instabilities. If sufficiently perturbing planetesimals can be formed in the protoplanetary disc, it would remove the necessity for all self-stirred discs to be implicitly delayed and allow for observed young and bright debris discs to be explained by self-stirring.

Even in the models of Krivov and Booth [2018] there are debris discs observed to be so bright, young and at such large radii that they could not be reasonably self-stirred, namely HR 8799, HD 95086, and 49 Cet. For these discs a planet-stirred scenario must be invoked, and indeed already two of the systems are known to harbour planets already [HR 8799; HD 95086; Marois et al., 2008, 2010; Rameau et al., 2013a,b].

Mustill and Wyatt [2009] model the long-term secular interactions between a planet and planetesimals within the disc that excite and precess planetesimals orbits into intersection. They find that a planet at 1-10 AU need only have eccentricities on the orders of  $10^{-3}$ ,  $10^{-2}$ , and  $10^{-1}$  in order to effectively stir planetesimal belts at 30, 100 and 300 AU respectively.

Kenyon and Bromley [2002] investigate the possibility that stellar flybys could stir debris discs. They find that while a moderately close flyby can indeed initiate an observable collisional cascade, without a constant stirring mechanism the cascade is quickly damped on a timescale of a Myr, after which the disc will lose brightness as the rate of collisions reduces. Given the rarity of close flybys in the field and the long ages of many debris discs, they conclude that flybys are not a consistent explanation for the general debris disc observations. It may also be possible that a recent close flyby instead of/as well as stirring the disc could perturb the stability of the orbits of any planets in the system [Brown and Rein, 2022], triggering then or at a later point planetary migration and a LHB-like event. In certain systems it is possible that there can be knowledge of or at least reason to believe that there may have been a recent flyby. One example is the Fomalhaut system for which

Shannon et al. [2014] predict a dynamically chaotic evolution of the triple system. In their scenario there have been close encounters within the last 25-50 Myrs between Fomalhaut C and Fomalhaut A and B that could have affected the disc of Fomalhaut C. This hypothesis is explored in Chapter 3.

### **Dust grain removal and the blowout size**

Each dust grain in the disc feels the effects of several forces. First is the force of gravity from the host star pulling it towards the star and resulting in an orbit. The self-gravity of the disc is usually regarded as insignificant. The gravitational force of the host star is dependent on the mass of the particle, and so its volume, as well as its density as defined by its composition. Where  $G$  is the gravitational constant,  $M_\star$  is the mass of the host star,  $\rho$  is the density of the dust grain,  $a$  is the radius of the dust grain and  $r$  is the distance between the dust grain and the star, the force of gravity,  $F_G$ , on a dust grain is:

$$F_G = \frac{GM_\star \rho \frac{4}{3}\pi a^3}{r^2} \quad (1.3)$$

There are two more key forces. One of these forces originates from the dust's interaction with stellar radiation, and the other originates from the dust's interaction with stellar wind. Both of these forces can be broken down into two components. There is a radial component that directly combats gravity and reduces the effective gravity a grain feels. When a dust grain is created in a collision between larger planetesimals on an approximately circular orbit, it will feel a reduced effective gravity and so while its orbit must still cross the point it was created in, the orbit must be eccentric (or hyperbolic). This orbit will carry it further from the host star than the parent planetesimals. Then there is a tangential component that acts as a drag force reducing the orbital energy of the dust grain, thus decreasing the size of the orbit so that it spirals inwards until the dust grain is either trapped in resonance with an interior planet, accreted onto an interior planet, scattered by an interior planet or sublimated close to the star. As these drag forces are proportional to orbital velocity, they are more significant for debris discs with smaller radii, additionally, once dust has begun to drift inwards, the drag forces increase, causing the dust to more sharply spiral in. The radial component of the radiation force is commonly called 'stellar radiation pressure' and the tangential component is called 'Poynting-Robertson drag'. The radial component of the stellar wind force is called 'stellar wind ram pressure' or often just 'stellar wind pressure' and the tangential component is called 'stellar wind drag' or sometimes 'corpuscular drag'.

First we will discuss stellar radiation pressure. The photons released from the host star impart momentum upon the dust grains that thermally absorb and re-emit them. This momentum pushes dust away from the star. Unlike gravity, this force is dependent on the

surface area of the dust grain, as well as its absorption efficiency and albedo as defined by its composition [Burns et al., 1979; Krivov et al., 2006]. The force of radiation pressure,  $F_{rad}$ , on a dust grain, in the opposite direction to gravity, where  $L_\star$  is the luminosity of the host star,  $Q_{rad}$  is the radiative pressure efficiency, for which a value of 0 gives a perfect transmitter, 1 gives a perfect absorber and 2 a perfect reflector, and  $c$  is the speed of light in a vacuum, is:

$$F_{rad} = \frac{L_\star Q_{rad} \pi a^2}{c 4 \pi r^2} \quad (1.4)$$

In addition to radiation pressure acting against gravity is stellar wind ram pressure [Strubbe and Chiang, 2006]. This is the effect of stellar wind material colliding with dust grains and exchanging momentum. This will also push the dust away from the star and is dependent on the surface area of the dust. The force of stellar wind ram pressure,  $F_{SW}$ , on a dust grain, in the opposite direction to gravity, where  $\dot{M}_\star$  is the mass loss rate of the host star,  $Q_{SW}$  is the stellar wind efficiency that can alternatively be thought of as the dimensionless cross section the grain presents to stellar wind pressure and is approximately equal to 1, and  $v_{SW}$  is the speed of the stellar wind, is:

$$F_{SW} = \frac{\dot{M}_\star Q_{SW} v_{SW} \pi a^2}{4 \pi r^2} \quad (1.5)$$

There is also the stellar wind drag [Plavchan et al., 2005, 2009]. Stellar wind material can also block the orbital path of the dust and in collision there is a component of exchange along the path of motion causing a drag force on the dust. This can slow the dust down and cause it to drift closer to the star. This will be dependent on the surface area of the dust too, but also the orbital velocity of the dust. As the orbital radius of the dust grain decreases, the drag force will increase, reducing the orbit further, overall causing the dust to spiral inwards towards the star. The drift motion however is still tempered by the dust's inertia, and so larger particles with greater surface areas but also greater volumes and masses will drift more slowly. This is effectively the tangential component of stellar wind pressure.

This force is not in direct opposition to gravity, it is not balanced or reduced by anything, but does require there to be sufficient stellar mass loss for the effect to be non-negligible in comparison to the other orbit-altering effects in this system.

The force of stellar wind drag,  $F_{SWD}$ , on a dust grain, in the opposite direction to the orbital motion, where  $v_{orb}$  is the orbital velocity of the dust grain, is simply the stellar wind force multiplied by a factor  $v_{orb}/v_{SW}$ :

$$F_{SWD} = \frac{\dot{M}_\star Q_{SW} v_{SW} a^2}{4 r^2} \frac{v_{orb}}{v_{SW}} \quad (1.6)$$

we can substitute in the velocity of a circular orbit,  $v_{orb} = \sqrt{GM_\star/r}$ , as an assumption and simplify:

$$F_{SWD} = \frac{\dot{M}_\star Q_{SW} a^2 \sqrt{GM_\star}}{4r^{2.5}} \quad (1.7)$$

The final force to account for is Poynting-Robertson drag. This is the effect of the motion of the dust relative to the star as it interacts with stellar radiation. In the dust's reference frame there is a momentum exchange along the direction of travel between itself and incoming stellar photons that are not perfectly normal to the orbital direction. The grain does not see itself as travelling, and so it must be the incoming photons that have motion towards it along the orbital path [Poynting, 1904; Robertson, 1937; Burns et al., 1979]. In the star's reference frame, the dust is receiving the stellar radiation normally, but due to the dust's motion when it thermally re-emits radiation there is a blue shift of light along its velocity vector and a redshift behind. This anisotropy of emission results in a net loss of momentum along the direction of motion. The radiative equilibrium of the dust with the star means that there is no mass loss from the dust, which would otherwise keep its velocity constant despite the momentum loss, and so the loss of angular momentum results in a decrease in orbital radius and the grain will spiral in towards the star. This manifests as a drag force that reduces the velocity of the dust and drifts it closer to the star. Because the force relies on absorbing/radiating surface in the respective reference frames the force is dependent on surface area, but also the orbital velocity of the dust. The resultant drift motion however is still tempered by the dust's inertia, and so larger particles with greater surface areas but also greater volumes and masses will drift more slowly. This is effectively the tangential component of radiation pressure.

This force is not in direct opposition to gravity, it is not balanced or reduced by anything, and is in essence unavoidable. An outward pressure force might have a more significant effect than PR-drag and overall an orbit could still be made to increase in radius, but if a particle is not significantly affected by radial pressure forces, it cannot avoid PR-drag. The timescale for PR-drag is long, but not longer than the ages of main-sequence stars: for a  $2\mu\text{m}$  sized dust grain, it takes 10 Myr to drift from a belt at 50 AU into a solar mass, solar luminosity star [Wyatt et al., 1999]. Given the age of detected debris discs at tens to hundreds and even thousands of Myr, the timescale of PR-drag would be sufficient to remove the dust that is not blown out by pressure forces, making it necessary to invoke a constant replenishment of dust. This is how the collisional cascade process was first inferred to be ongoing when debris discs were originally discovered [Backman and Paresce, 1993]. There is the caveat that the slow drift of large grains can take sufficiently long that for most detectable debris discs, which by nature are the most massive discs, there is enough mass in

the cascade that the inward drift is interrupted by collisions before dust grains can leave the parent belt. After being collisionally processed into small enough grains, pressure forces can then overpower PR-drag and blow the dust from the system [Wyatt, 2005a]. This can allow us to safely ignore PR-drag as a significant dynamical factor in certain debris discs.

The force of PR-drag drag,  $F_{PR}$ , on a dust grain, in the opposite direction to the orbital motion, is simply the radiation pressure force multiplied by a factor  $v_{orb}/c$ :

$$F_{pr} = \frac{L_{\star} Q_{rad} a^2}{4r^2 c} \frac{v_{orb}}{c} \quad (1.8)$$

we can substitute in the velocity of a circular orbit,  $v_{orb} = \sqrt{GM_{\star}/r}$ , as an assumption and simplify:

$$F_{pr} = \frac{L_{\star} Q_{rad} a^2 \sqrt{GM_{\star}}}{4r^{2.5} c^2} \quad (1.9)$$

There is a mathematical measure,  $\beta$ , of the balance between the radial forces. In most cases, i.e. early type stars, it is sufficient to measure  $\beta$  as the ratio between the gravitational force a dust particle feels and the radiation pressure it feels. To be more complete, the full  $\beta$  prescription is the ratio between gravity and the pressure forces of radiation and stellar wind together. Drag forces tangential to the orbit and perpendicular of the force of gravity are left out of this prescription as they are not in balance. The drag forces are also proportional to orbital velocity, and so these effects become stronger closer to the star and become more significant for the short timescales of smaller radius warm debris discs and exo-zodi like dust populations than they are for the cold Kuiper-like belts. Without factoring in stellar wind ram pressure, we can simplify the ratio of Equations 1.3 and 1.4:

$$\beta_{rad} = \frac{3L_{\star} Q_{rad}}{16\pi GM_{\star} c a \rho} \quad (1.10)$$

Also including stellar wind ram pressure, we can simplify the ratio of Equations 1.3 and 1.4 and 1.5 together:

$$\beta_{rad+sw} = \frac{3}{16\pi GM_{\star} a \rho} \left( \frac{L_{\star}}{c} Q_{rad} + \dot{M}_{\star} v_{sw} Q_{sw} \right) \quad (1.11)$$

We can see that  $\beta$  is independent of orbital radius. We also see that because the gravitational force depends on the mass of a particle and therefore its volume, but pressure forces depend on surface area,  $\beta$  depends on grain size, and that larger grains are less susceptible to pressure forces affecting their orbits. However,  $Q_{rad}$  is also a function of grain size, as grains do not efficiently couple to light of wavelength greater than their own size [Krivov et al., 2008], this results in a turnover in  $\beta_{rad}$ , so that it does not indefinitely increase for smaller grain

sizes. We also now define the blowout size, which sets  $s_{min}$  within the collisional cascade, as the grain size for a given system at which  $\beta$  is equal to 0.5. At this point, grains of this size that are created by planetesimals on approximately circular orbits have such a velocity and see such a reduced effective gravity that they possess parabolic orbits that remove them from the system and from the collisional cascade. Grains smaller than this size possess hyperbolic orbits that also remove them from the system and the cascade. As these grains are removed from the cascade, even smaller grains beyond the  $Q_{rad}$  turnover with  $\beta_{rad}$  values once more less than 0.5 are not produced in large quantities, additionally these tiny grains, of size smaller than tenths of a micron, are subject to further effects that reduce their lifetime such as the Lorentz force and erosion from stellar wind sputtering [Krivov et al., 2008], or indeed stellar wind pressure may be sufficient to blow them out. As such, these tiny grains do not contribute significantly to either the thermal emission of the disc nor its dynamics and can usually be disregarded.

Dust  $\beta$  depends strongly on the type of the host star. Radiation pressure is directly tied to host luminosity, and so the radius and temperature of the star which are defined by its spectral type. The early type A0V star HR 4796A is theorised to have a blowout size in the range of  $\sim 5\text{-}15\mu\text{m}$ , the sun-like G8V star HD 61005 a range of  $\sim 0.5\text{-}1.5\mu\text{m}$ , and low-mass late type stars like the M1Ve AU Mic do not have a minimum grain size set by radiation pressure, as for no grain size does  $\beta_{rad}$  exceed 0.5 [Arnold et al., 2019].

Late type systems can have mass loss rates orders of magnitude higher than the mass loss rate of solar type stars due to hotter coronae and increased magnetic activity [Plavchan et al., 2005; Mullan et al., 1992; Fleming et al., 1995; Wargelin and Drake, 2001, 2002; Wood et al., 2001, 2002; Lim and White, 1996; van den Oord and Doyle, 1997]. In these systems, when radiation pressure becomes insufficient to remove dust, stellar wind becomes the dominant factor in setting a blowout size. Unfortunately, stellar mass loss and wind strength are difficult to measure on a case by case basis and there is significant spread of activity levels between similarly typed and aged stars. This makes predicting  $\beta_{rad+SW}$  for late type stars difficult. As well as type, stellar age is a significant factor for stellar activity. As stars age they tend to become more quiescent, and so over the lifetime of a late type star there is an evolution in the blowout size with older stars potentially harbouring larger reserves of smaller dust grain sizes. We do have direct evidence for stellar wind ram pressure blowout: AU Mic is not massive enough for  $\beta$  to reach 0.5 through radiation pressure alone. However, clumps of dust have been observed to be blown radially outwards from the star and this must be due to stellar wind ram pressure [Boccaletti et al., 2015; Chiang and Fung, 2017; Sezestre et al., 2017; Boccaletti et al., 2018; Grady et al., 2020].

In Figure 1.4 we can see the  $\beta$  curves for dust in the M1Ve GSC 07396-00759 system under the effect of just radiation pressure, for which  $\beta$  never exceeds 0.5, and under

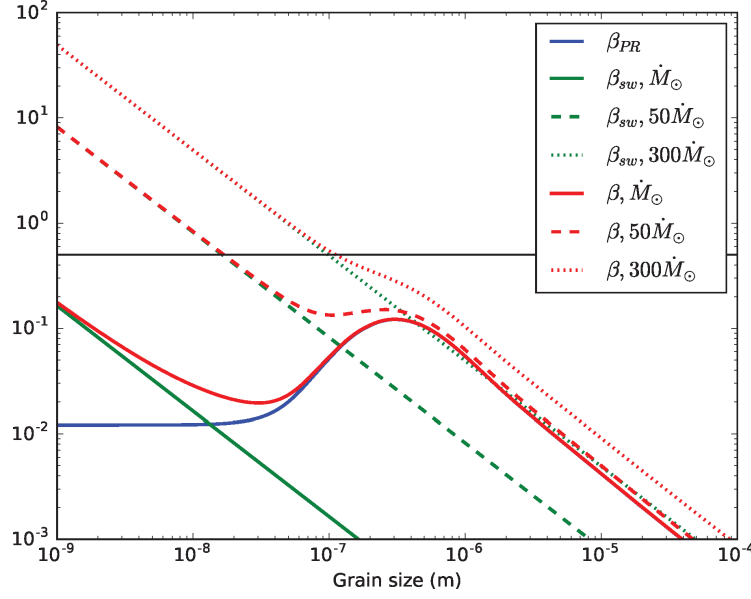


Figure 1.4:  $\beta$  as function of grain size for GSC 07396-00759, with three hypotheses for stellar mass loss rate. The horizontal black line shows  $\beta = 0.5$  where dust grains become unbound from the system. Here  $\beta_{PR}$  solely accounts for radiation pressure,  $\beta_{SW}$  solely accounts of stellar wind ram pressure and  $\beta$  is the combination of the two. This figure is taken from Sissa et al. [2018].

increasing strengths of stellar wind for which  $\beta$  does reach 0.5 at increasingly large grain sizes [Sissa et al., 2018].

### Time evolution

At the end of the era of planet formation and at the onset of the collisional cascade, a finite number of the largest bodies were produced, and over a long enough time their number will inevitably reduce as they collide. As theirs is the mass that when removed is not replenished, the lifetime of the disc is defined by the lifetime of these largest bodies.

The collisional lifetime of a large body within a disc,  $t_c$ , is determined by: the radial location of the disc, as the more distant a disc is from the star the slower the bodies within it will be moving and so the less destructive and less common their collisions will be; the width of the discs, as with more area to spread out in the less likely it is that a collision occurs; the size of the body itself, as the larger a body is the more area it has that can be collided with; the internal strength of the body, as the stronger a body is the less likely that any given collision will fragment it; the eccentricity of the body's orbit, as a more eccentric orbit is more likely to cross into other bodies' orbits and with greater relative velocity; the mass of the host star, as a more massive star will result in larger orbital velocities at a given



radius, and so more frequent and destructive collisions; and the total mass of the disc, as a more massive disc has more total bodies to collide with [Wyatt et al., 2007; Dominik and Decin, 2003].

In the simplest approximation, the rate of change of total mass in the disc,  $M_{tot}$ , with respect to time,  $t$ , is:

$$\frac{dM_{tot}(t)}{dt} = -\frac{M_{tot}}{t_c} \quad (1.12)$$

with the additional knowledge that  $t_c$  is itself proportional to  $1/M_{tot}$  the result of integrating this is:

$$M_{tot}(t) = \frac{M_{tot}(0)}{1 + t/t_c(0)} \quad (1.13)$$

If the debris disc is subject to delayed stirring, where bodies large enough to stir the disc must form in non-destructive collisions before they initiate the collisional cascade, the time-decay of Equation 1.13 will be delayed by the time it takes to form the stirring bodies,  $t_{stir}$ :

$$M_{tot}(t) = \frac{M_{tot}(0)}{1 + (t - t_{stir})/t_c} \quad (1.14)$$

The key result is that the disc mass, and therefore its fractional luminosity, is theoretically proportional to  $t^{-1}$ .

As  $t_c$  was itself inversely proportional to the total mass, an interesting result is that, all else the same, an initially more massive disc will evolve faster than a less massive disc until it ‘catches up’, and after sufficient time the total mass of an aged disc is independent of the total mass it started with [Wyatt et al., 2007].

Under more intense scrutiny and collisional modelling, the evolution of the dust mass, which is what is observed, and the total mass can be different and the decay of the disc fractional luminosity can be proportional to  $t^{-0.3 \sim -0.4}$  [Löhne et al., 2008]. This is possible as the shape of the size distribution can change over time, away from a primordial distribution that existed when the collisional cascade initiated.

### Chemical makeup and shape

What is the dust that we observe chemically made of? And do we assume spherical dust grains?

To the first approximation, we treat dust as astronomical silicates [Draine and Lee, 1984], i.e. composed of mineral compounds like olivine with chemical formulae like  $Mg_2SiO_4$ , identified on the basis of mid-IR observations of a characteristic spectral feature of the Silicon-Oxygen bond. The silicate is dubbed ‘astronomical’ as we cannot yet perfectly

replicate the precise grain composition in the laboratory, and the specific composition does not occur terrestrially. Typically we regard them as amorphous in debris discs rather than crystalline, as crystallinity requires high temperatures that require being much closer to the star [Wyatt and Dent, 2002]. For simplification we approximate the grains to be spherical, but they could be cylindrical, oblately/prolately spheroidal or more complex shapes formed from clumping. To a higher order, these grains have a silicate core but a refractory mantle of complex organic molecules [Li and Greenberg, 1997]. These grains will have a varying degree of porosity, and the vacuums of the grains can be filled with some fraction of water ice, further altering the optical properties. The degree of porosity and ice fraction will also affect the density of the grains, which can have a knock-on effect for the balance of forces and blow-out sizes, as well as for a final disc mass calculation.

When it comes to observation, each of these materials has associated optical constants [Li and Greenberg, 1997, 1998] and the optical constants for the total composite can be computed using Maxwell-Garnett Effective Medium theory [Bohren and Huffman, 1983]. The absorption efficiencies of these grains, which also determine their emission, can then be calculated with Mie theory [Bohren and Huffman, 1983], and at the extrema where Mie theory breaks down with Rayleigh-Gans theory and geometric optics [Laor and Draine, 1993].

Planetesimals in Kuiper-belt like debris discs, that formed beyond molecular ice lines, we know to contain volatiles as well as rocky and metallic material. ALMA observations of debris discs sometimes observe CO gas co-located with the dust, implying that the gas is being released in the selfsame collisions between planetesimals that release dust [Cataldi et al., 2015; Kral et al., 2016, 2019; Matrà et al., 2015; Matrà et al., 2017; Matrà et al., 2019a].

When these planetesimals are scattered into the inner stellar systems to be observed as exocomets, we can directly observe the material in their vaporised gaseous coma in transmission spectroscopy, letting us know directly part of what they are made of.

To date, we have observed the elemental species from spectroscopy of planetesimal belts and exocomet events: Carbon, Nitrogen, Oxygen, Magnesium, Aluminium, Silicon, Sulfur, Calcium, Chromium, Manganese, Iron, Nickel and Zinc [Strøm et al., 2020, and references therein].

### **1.2.2 The spatial features of debris discs**

We have covered what a debris disc is composed of internally and the ongoing physics within them. Now we will look at their large scale structure.

## Rings

We have taken it as given that debris discs exist as rings around a host star, like the Kuiper belt, as opposed to the radially complete discs of the protoplanetary era. There remains the fundamental question of why? To look at our own Solar System again, we can see that the regions where there *are not* planetesimals are the regions where there *are* planets.

Aside from the existence of trojan asteroids that survive at the Lagrange points of planetary orbits, all of the planets in the Solar System have cleared their orbits, and the space between their orbits and the next planet over, of planetesimals. The exception to this is the space between the orbit of Mars at 1.5 AU and the orbit of Jupiter at 5.2 AU, within which the asteroid belt resides. Jupiter likely began stirring this belt once it had formed, preventing any new planets from growing there [Petit et al., 2001]. The radius of the asteroid belt spans from approximately 2.1 to 3.3 AU; these are the 4:1 and 2:1 orbital mean-motion resonances with Jupiter respectively. Planetesimals close to these resonances have their orbits destabilised. Planetesimals interior to this were cleared by Mars, and exterior to this cleared by Jupiter. If there was a migration of Jupiter in the early Solar System, these resonances would have swept across the wider Mars-Jupiter gap and either collected or removed planetesimals along the way such that at the end of the migration the only asteroid belt bodies remaining were those within them [Moons, 1996]. The case is similar for the Kuiper belt: two thirds of observed Kuiper belt objects exist in the ‘classical Kuiper belt’ between the 2:3 and 1:2 mean-motion resonances with Neptune at 39 and 48 AU respectively. During an early Solar System migration Neptune would have swept the belt outwards as Neptune’s orbital radius increased. This process is thought to also be the reason why Pluto is in 2:3 resonance with Neptune [Malhotra, 2019].

These same concepts we can extrapolate to the ringed debris discs that we observe. The inner edges of rings we can predict to be truncated by the presence of a large planet immediately interior to the disc [e.g. Quillen, 2006; Chiang et al., 2009; Matrà et al., 2020; Faramaz et al., 2021; Pearce et al., 2022]. Large interior cavities in discs, and large gaps between rings can be explained by chains of smaller planets clearing material [e.g. Faber and Quillen, 2007; Su et al., 2013; Pearce et al., 2022]. Pearce et al. [2022] also find that these theoretical truncating planets can be additionally consistent with the requirements for planet based stirring models; a graphic displaying the different ways planets can interact with a debris disc in Pearce et al. [2022]’s dynamical arguments is displayed in Figure 1.5. Debris discs that are observed to be radially thin may be constrained by orbital resonances with a giant planet [Booth et al., 2017], or shepherded by two small planets in either side of the ring [Boley et al., 2012].

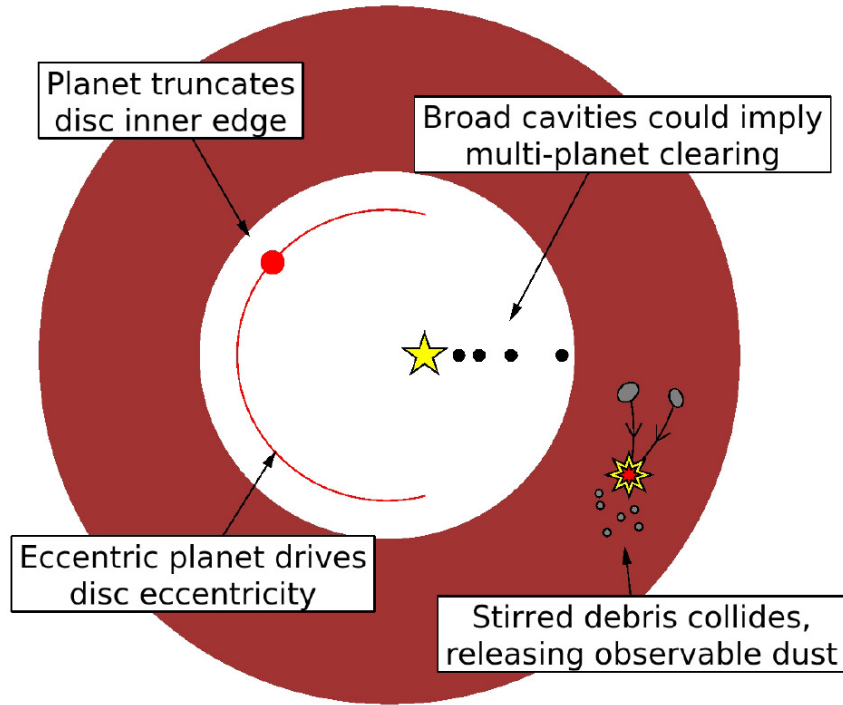


Figure 1.5: Graphic displaying the ways interior planets can affect debris discs within the system. This figure is taken from Pearce et al. [2022]

### Halo and wings

External to a well-defined far-IR bright ring, an extended ‘halo’ of dust is also sometimes seen. These haloes are sometimes visible in the mid-IR, e.g. with Spitzer [e.g. Vega; HR 8799, Su et al., 2005, 2009], around A-type stars, tracing warm tens of microns sized dust. However the halos are often much more apparent, or only seen, in optical and NIR scattered light, which trace small micron-size dust grains, as opposed to the mm sized grains traced by thermal far-IR observations [e.g. AU Mic; HD 129590, Kalas et al., 2004; Matthews et al., 2017]. The logical hypothesis is that the observations are seeing the small dust grains that are more directly affected by pressure forces and have scattered onto distant eccentric orbits. The mm dust grains, with  $\beta$  values much less than 0.5, unaffected by pressure have remained in their *birth ring* co-located with their parent planetesimals from whose collisions they were produced [Strubbe and Chiang, 2006]. In the case of the M-dwarf AU Mic, scattered light observations detect a halo stretching hundreds of AU from the star [Kalas et al., 2004], as opposed to the 40 AU radius of the birth ring [Strubbe and Chiang, 2006; Wilner et al., 2012]. Recent ALMA observations are now finding evidence of haloes observable at mm wavelengths [e.g. HD 61005, HD 32297, MacGregor et al., 2018a; Olofsson et al., 2022]. These observations could be tracing small dust grains pushed to

eccentric orbits by pressure forces in sufficient quantities to remain visible in their thermal emission. Alternatively they could be tracing a halo of large mm-grains located there through an as-of-yet unknown mechanism.

A similar but separate feature observed are the ‘swept back wings’ of discs like HD 61005, HD 15115, HD 32297 [Schneider et al., 2014]. These asymmetric features also seem to trace small dust grains externally distant to the parent planetesimal belt. The lack of axisymmetry makes stellar pressure forces unlikely as the root cause, but a pre-existing pressure-based halo of small grains could be made asymmetric by interactions with something external to the stellar system. The posited scenario is that the stellar system is moving through a region of the interstellar medium (ISM), and it is drag from the ISM that more strongly affects small grains that deforms the halo [Maness et al., 2009; Debes et al., 2009]. However, planet based scenarios have also been presented [Esposito et al., 2016; Lee and Chiang, 2016], as well as recent collisions [Mazoyer et al., 2014], as explanations. Further mm-wave observations of these systems may help break the degeneracies of these explanations, as the mm dust grains should be affected differently in dynamic, collisional and ISM based scenarios.

### **Asymmetry, clumps and transient features**

Asymmetrical features aside from the sweeping of dust halos into wing like structures are also observed in debris discs.

In the disc of AU Mic, scattered light observations find small features quickly travelling radially outwards along the surface of the disc [Boccaletti et al., 2015, 2018; Grady et al., 2020]. These seem to be unbound clouds of dust being blown out of the system by the stellar wind. Chiang and Fung [2017] theorise that these are dust ‘avalanches’ produced at the intersection of a birth ring and a second inclined ring remnant of a recently destroyed large body. Seizestre et al. [2017] posit that the origin of the dust is a single parent body close to the star on a Keplerian orbit.

The point source within the Fomalhaut A system observed with scattered light [Kalas et al., 2008; Currie et al., 2012; Kalas et al., 2013] originally hypothesised to be a planet may also be a transient dust cloud on an unbound orbit [e.g. Janson et al., 2012; Gáspár and Rieke, 2020].

‘Clumpy’ structure, i.e. anomalous unresolved signal peaks within the disc, are occasionally reported, e.g.  $\epsilon$  Eridani [Greaves et al., 2005], occasionally disputed, e.g.  $\epsilon$  Eridani [Chavez-Dagostino et al., 2016] and occasionally found to be ambiguous with a strong possibility that at least some observed clumps are background galaxies, e.g.  $\epsilon$  Eridani [Booth et al., 2017].

Ren et al. [2021] observe a large clump in the outer reaches of the face-on TWA 7

disc observed in scattered light with multiple instruments. The clump is observed at multiple epochs with sufficient time baseline that they can conclude that the clump shares the star’s proper motion and is therefore not a background galaxy. The dust seems to possess Keplerian motion around the star, but it is unclear if the clump is moving radially away from the star. If so, the clump may be unbound and being blown from the system, behaving the same way and sharing a similar origin with the moving dust features of AU Mic [Boccaletti et al., 2015]. They also identify the clump with a similar structure observed at the same location in the sub-mm [Bayo et al., 2019].

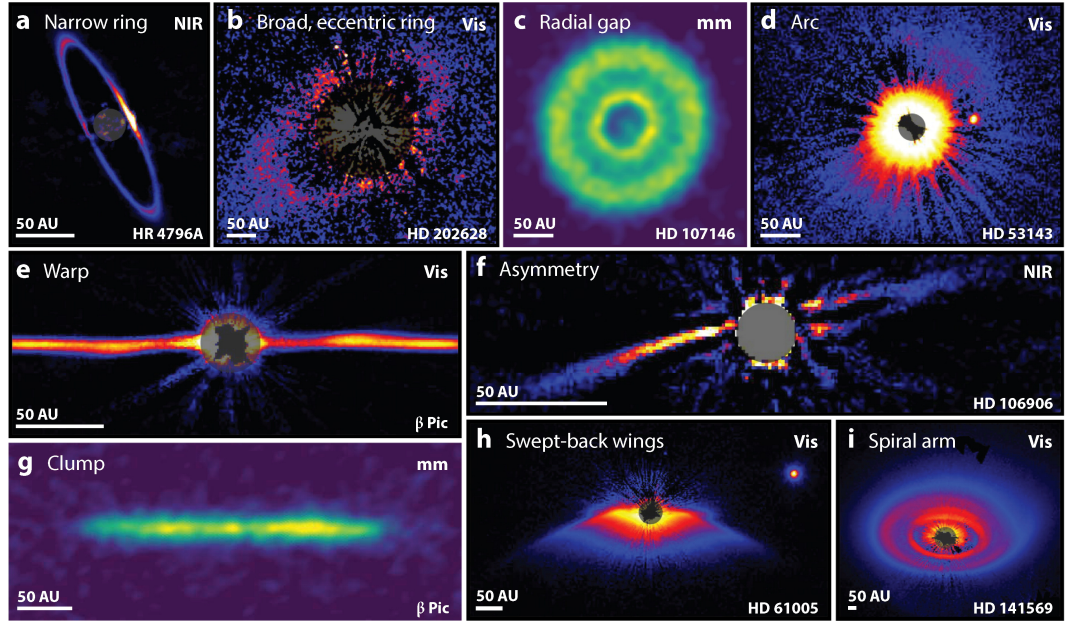
There are also brightness asymmetries observed in edge-on discs at short wavelengths. One side of the disc may appear brighter by a significant factor than on the other side of the star. For  $\beta$  Pic, the south-west side is  $\sim 1.5$ -2 times brighter than the north-west [Telesco et al., 2005]. Another example is GSC 07396-00759, which has a observed brightness asymmetry of factor  $\sim 1.5$ -2 in scattered light [Sissa et al., 2018; Adam et al., 2021]; HD 106906 is observed to be  $\sim 1.3$  times brighter in the south-east to the north-west [Kalas et al., 2015; Crotts et al., 2021]. Some observations of  $\beta$  Pictoris at mm-wavelengths have been reported to recover this asymmetry with reduced magnitude [Dent et al., 2014], with the south-west 1.15 times brighter than the north-east. However, other observations at mm-wavelengths have not recovered this asymmetry [Matrà et al., 2019a].

The  $\beta$  Pictoris belt is also warped, with not all the disc residing in one plane, as observed in small grains scattered light [Mouillet et al., 1997; Heap et al., 2000; Golimowski et al., 2006] and theorised to be due to a perturbing planet [Mouillet et al., 1997; Augereau et al., 2001]. A planet consistent with causing the warp was indeed later discovered [Lagrange et al., 2009]. The warp is not recovered in the sub-mm [Matrà et al., 2019b], suggesting the warping effect does not apply to the more massive planetesimals and large grains, although ALMA observations do detect a tilt in the carbon monoxide distribution [Matrà et al., 2017]. Tentative warps or ‘bumps’/‘tilts’ have also been suggested to be present in the discs of AU Mic [Wang et al., 2015] and HD 110058 [Kasper et al., 2015].

There is a common theme of examining structures in both scattered-light and mm-wave imaging for corroboration or lack thereof that yields insight into whether the structure is present in all bodies or just the smallest dust grains. A graphic displaying different structures and asymmetries within debris discs is displayed in Figure 1.6

## Eccentricity

Many debris discs have been observed to be eccentric, i.e. the ring appears elliptical or approximately circular but with a centre offset from the stellar location. These eccentricities can range from  $e \approx 0.21$  for HD 53143 [MacGregor et al., 2022] down to  $e \approx 0.06$  for HR 4796A and HD 15115 [Rodigas et al., 2015; Milli et al., 2017; Sai et al., 2015].



 Hughes AM, et al. 2018.  
Annu. Rev. Astron. Astrophys. 56:541–91

Figure 1.6: Graphic displaying different structures within debris discs. This figure is taken from Hughes et al. [2018] with references for each individual disc therein.

Eccentricities lower than this can be difficult to measure with current techniques without costly observation times at high resolution [e.g. Cronin-Coltsmann et al., 2021, Chapter 3].

Aside from their overall geometry, eccentric discs can have their own brightness asymmetries dependent on the wavelength of observation. When viewed in scattered light, the pericentre of the disc is closer to the host star and therefore receives more incident radiation, leading to a ‘pericentre glow’ of increased flux. The incident radiation can also warm the disc at the pericentre leading to more MIR emission [Wyatt et al., 1999]. When viewed in the sub-mm, the build up of dust at the apocentre where most of the orbital period is spent can lead to an opposite ‘apocentre glow’ [Wyatt, 2005b; Pan et al., 2016]. As the location and relative magnitudes of the glows are a function of grain size, multi-wavelength observations of the same disc can be used to probe grain emissivity and the size distribution, as MacGregor et al. [2017] do this for Fomalhaut in comparison with Marsh et al. [2005] and Acke et al. [2012]. The eccentricity and semi-major axis distribution of planetesimals in these disc should also affect the observed radial profile [Kennedy, 2020].

Eccentricity in debris discs is often linked to the secular perturbations of a theoretical eccentric planet, that may also be shaping and stirring the disc. As the observed eccentric discs are also narrow, a planet can solve both problems at once.

There are alternative scenarios however. A recent giant impact could produce a short

lived narrow eccentric dust disc, although this could be differentiated from a typical debris disc through the size distribution of the dust [Jackson et al., 2014]. Previous interactions with a companion star is also feasible for certain systems, as posited by Shannon et al. [2014] for the Fomalhaut system. Eccentricity can also be primordial from the protoplanetary disc with or without the need for a perturbing planet [Kennedy, 2020; Lyra and Kuchner, 2013]. The over-narrowness of Fomalhaut and HD 202628’s discs may require a protoplanetary origin [Kennedy, 2020]. This can be investigated through high resolution observations of the radial profile.

### Vertical structure

The vertical structure of discs is usually codified into a ‘scale height’ that may be the standard deviation of a vertical Gaussian thickness of the disc or the half width at half maximum of a different vertical density distribution. A related measure to the scale height is the ‘aspect ratio’, the ratio between the scale height of the disc and its radius. The arctangent of the aspect ratio then gives the ‘opening angle’, a measure of the angle between the midplane of the disc and a representative height of the disc at the disc location as measured from the star.

Thébault [2009] model disc collisions and find there is a natural minimum aspect ratio when observed in visible to mid-IR wavelengths of  $0.04 \pm 0.02$ . This is defined by the natural dispersion of small grain orbital inclinations as a result of mutual collisions along eccentric orbits. The necessary eccentricity of these orbits is derived from interactions with radial pressure forces. As scale height can be a function of grain size due to the influence of pressure forces, observations in scattered light, which are sensitive to small grains and their halos, may not be optimal for measuring the interior dynamics of discs that would otherwise affect the scale height of dust grains parent planetesimals.

The scale height of an optically thin debris disc can only be measured when the disc is not face-on, and an edge-on disc provides the clearest viewing geometry for measurement. Even in this case disc scale heights are often too small to be resolved in the sub-mm. When they are resolved however, we can observe the mm dust grains which more closely trace dynamical excitation within the disc.

Daley et al. [2019] measure the aspect ratio of AU Mic and infer from dynamical modelling of the underlying velocity and inclination dispersions the size of the stirring bodies within the disc. They put a lower limit on the size of the largest bodies of 400 km and an upper limit on the mass of the largest body of  $1.8 M_{\oplus}$ . These measurements also preclude the presence of a gas giant or Neptune sized planet residing just exterior to the 40 AU disc outer edge, suggesting the disc is self-stirred or stirred by an Earth sized planet.

Matrà et al. [2019b] similarly studied  $\beta$  Pictoris and find that the scale height is instead better described by the sum of two separate Gaussian distributions.  $\beta$  Pictoris would



thus mirror the Kuiper belt in possessing separate dynamically ‘hot’ and dynamically ‘cold’ populations. They find that the orbit of the detected exoplanet in the system  $\beta$  Pictoris b is unlikely to be able to excite the hot population to its inclination throughout the radial extent of the disc through secular perturbation. They also conclude that self-stirring planetesimals within the disc would only be able to produce one of the two populations. The observations could only be explained if the planetesimals were somehow born with high inclinations, or if there existed another planet that could have previously migrated to the disc’s inner edge, similar to the putative migration of Neptune towards the Kuiper belt edge.

### 1.2.3 Observed occurrence and trends

We have covered what debris discs are and the features that we find in them, but how often do we actually observe them? We cannot directly answer the question ‘what percentage of stellar systems have debris discs’ because there is a limit to what our technology and knowledge enable us to detect. A debris disc that is not massive enough, too far away or too poorly illuminated by its host star will not be detectable. Indeed, the Solar System’s Kuiper belt is itself not massive enough to be observable by our technological standards if it were placed around a neighbouring star. Even if we had ultra-sensitive instruments, we would come across a different problem - the ‘calibration limit’. If we are trying to detect debris discs via their infrared excess, we need to know exactly what they are in excess of. The infrared flux of a very dim debris disc may present an infrared excess that resides within the error bounds of our model for the stellar photosphere itself. If we do not have sufficiently accurate stellar photosphere models, or sufficient photometry to fit one, we might not be able to distinguish the flux of a debris disc even if it had been detected. There is also the ‘confusion limit’, there comes a point where an instrument is sensitive enough that there becomes a statistically significant chance that it will detect a background galaxy in any given observation which would muddy if not mimic a circumstellar infrared excess.

The limits of calibration and confusion would not be an issue if the disc were resolved, but that comes into conflict with the diffraction limit and our ability/resources to construct large enough telescopes.

Care must also be taken when comparing observations taken at different wavelengths, as the luminosity of a disc at a given wavelength will be a direct function of its temperature. Hotter discs’ blackbody spectra peaking at shorter wavelengths, and the modified blackbody tail of the disc’s spectra due to the non-ideal thermal emission of small particles, exacerbates the difficulty of observing a disc at a wavelength beyond its emission peak. Different instruments will inherently be sensitive to different discs and equally sensitive instruments may detect or not detect the same disc at different wavelengths.

Even if we cannot tell whether debris discs are objectively present, we can at least

measure how common the most massive discs are, and see if there are trends in the occurrence of massive discs across stellar characteristics like type, age, multiplicity, and presence of known planets.

### Across Type

The incidence of observable debris discs can be split roughly into three bins: A-type stars, F, G and K (FGK) type sun-like stars and M-type stars.

Su et al. [2006] searched  $\sim 160$  nearby A-type stars with known ages with Spitzer/MIPS at wavelengths of 24 and/or  $70\ \mu\text{m}$  for infrared excesses. They found to a  $3\sigma$  confidence level a detection rate of  $33\pm 5\%$ . The Herschel DEBRIS survey observed 83 A-type stars from an unbiased nearby volume limited sample at 100 and  $160\ \mu\text{m}$  with Herschel/PACS and found to a  $3\sigma$  confidence level a detection rate of  $24\pm 5\%$  [Thureau et al., 2014]. The difference between these two rates may be due to the younger average age of Su et al. [2006]’s sample.

Trilling et al. [2008] study a sample of  $\sim 184$  nearby FGK stars with Spitzer at 24 and  $70\ \mu\text{m}$ . They detected an infrared excess rate of  $3.8\pm 1.5\%$  at  $24\ \mu\text{m}$  and  $16.3\pm 3\%$  at  $70\ \mu\text{m}$ . The Herschel DUNES [Eiroa et al., 2013] survey observed a biased sample of 124 FGK-type stars within 20 pc at 100 and  $160\ \mu\text{m}$  with Herschel/PACS and found an incidence rate of  $20.2\pm 2\%$ . Montesinos et al. [2016] present the DUNES sample in combination with another 56 stars that were observed under the DEBRIS survey, but that align with the DUNES’ sampling method. Upon combination, the sample of 105 stars within 15 pc is complete for F-types (23/23), nearly complete for G-types (33/42) and contains a statistically sufficient number of K-types (49/89). This 15 pc sample was found to have a total detection rate of  $22\pm 8\%$ , and when broken down to the individual types, rates of :  $26\pm 17\%$  for F stars,  $21\pm 14\%$  for G stars and  $20\pm 12\%$  for K stars. The Herschel DEBRIS survey [Sibthorpe et al., 2018] observed an unbiased sample of 275 nearby FGK-type stars at 100 and  $160\ \mu\text{m}$  with Herschel/PACS and found a total detection rate of  $17.1\pm 2.4\%$  and when broken down to the individual types, rates of :  $23.9\pm 5\%$  for F stars,  $14.3\pm 4.3\%$  for G stars and  $13.0\pm 4.0\%$  for K stars.

Matching the Hipparcos astrometry catalogue with IRAS’ catalogue of infrared sources at  $60\ \mu\text{m}$  Rhee et al. [2007] found only a single disc around an M-type host, AU Mic, from  $\sim 900$  in the Hipparcos catalogue. Gautier et al. [2007] used Spitzer to examine 62 M-type stars at  $24\ \mu\text{m}$ , 41 of which were also observed at  $70\ \mu\text{m}$  and 20 stars at  $160\ \mu\text{m}$ , but observed no infrared excesses. The Herschel DEBRIS survey found only two discs from 89 observed M-dwarfs [GJ 581; Fomalhaut C, Lestrade et al., 2012; Kennedy et al., 2013] giving a detection rate of  $2.2^{+3.4}_{-2.0}\%$  [Sibthorpe et al., 2018]. Another Herschel survey of twice the sensitivity detected three discs from 18 M-types and 3 late K-type planet hosts [Kennedy et al., 2018a].

The rates across studies are in general agreement but individual studies come to their individual conclusions for A and FGK stars. Trilling et al. [2008] find their sample statistically indistinguishable across AFGK, but with a slight trend at  $70\ \mu\text{m}$  of decreasing excess rate with later type with possible bias from age effects. The separation between A and GK is more significant for DEBRIS [Thureau et al., 2014; Sibthorpe et al., 2018], but A and F incidence rates seem similar. In all, it is valid to say that the fraction of stellar systems with observable debris discs generally decreases with type across AFGK stars. M types are then a different case. There is a distinct possibility that there is a significantly lower rate of observed discs, but also the chance that a similar rate (at a given fractional luminosity) as for early type stars could be there and is simply hiding below a sensitivity limit.

### Across Age

Su et al. [2006]’s observations of  $\sim 160$  nearby A-type stars with Spitzer/MIPS found that the fractional luminosity of infrared excesses followed a general trend of falling off with a relationship  $t_0/t$  with a  $t_0 \sim 150$  Myr at  $24\ \mu\text{m}$  and  $t_0 \gtrsim 400$  Myr at  $70\ \mu\text{m}$ , with a wide scatter at any individual age. This finding that the warmer discs, closer to their host star, decayed faster and the  $1/t$  trend are consistent with collisional evolution theory. Rieke et al. [2005] studying A-type discs with Spitzer/MIPS at  $24\ \mu\text{m}$  combined with ISO and IRAS data find the same  $t_0/t$  with a  $t_0 \sim 150$  Myr relationship. The trend of decreasing fractional luminosity and/or detection rate is consistently recovered across such surveys [e.g. Trilling et al., 2008; Montesinos et al., 2016], but there is a large spread in the population at any given age [Decin et al., 2003] and old discs of several Gyrs can still be very bright [Sibthorpe et al., 2018].

As well as through sampling a large number of variously aged stars, age effects can be investigated by studying moving groups and clusters, collections of stars all at a similar known age and birthed with similar initial conditions.

Pawellek et al. [2021] examine the 12 F-type stars of the  $\sim 20$  Myr old [Bell et al., 2015; Miret-Roig et al., 2020]  $\beta$  Pictoris Moving Group (BPMG). If debris discs are brightest when they are young, then such a survey should find more and/or brighter discs than a sample spread across all ages. They detected nine discs from the twelve stars giving a 75% detection rate. This is significantly higher than the rate detected by Sibthorpe et al. [2018] for field F stars of which 90/92 of their sample were known to be older than 160 Myrs. They also compare their result to a collection of moving groups of age 45 Myrs and find the two samples consistent. They field three different scenarios to explain their results: i) the BPMG is representative of the population of field stars and something causes a drastic drop in disc observability over the first 100 Myr of a star’s life; ii) the BPMG is representative of field stars but the discs observed at different ages are different discs within the population;

iii) the BPMG is not representative of field stars and the young moving group formation environment was significantly different and affected disc formation and evolution. Scenario i) requires a time evolution proportional to  $t^{-2}$ , much too fast for collisional evolution and inconsistent with measured aging post-100 Myrs as observed in other studies. If LHB-like dynamical instabilities and migrating planets in the first 100 Myrs were common, they could explain the result. Scenario ii) would require that the secondary belts that go on to be visible at later times have not yet initiated their collisional cascades and that the early time visible belt be formed through a different mechanism, e.g. primordial dust swept up by depleting gas forming planetesimals through streaming instabilities in place of the remnants from the planet formation process. Scenario iii) might entail increased rate of stellar flybys truncating field star discs during their formation in denser cluster environments.

Sullivan et al. [2022] look at 76 solar type stars in the 115 Myr old Pleiades open cluster with ALMA at 1.3 mm. 71 of these were previously observed at  $24\ \mu\text{m}$  with Spitzer finding 23/71 warm excesses. They observed no discs with ALMA, a 0% detection rate. They however find that this result, simultaneous with the Spitzer detections, is consistent with collisionally evolving a randomly sampled synthetic disc population with a  $t^{-1}$  decay.

### **Planet Hosts and stellar multiplicity**

Yelverton et al. [2019] study 341 stellar systems for the effect of the presence of binary companions on the presence of an observable debris disc. They find, in accordance with previous studies [Rodriguez et al., 2015], that the population of binaries with discs is different to the population of binaries without them. They conclude that the separation of the binaries has a significant effect on the presence of a detectable debris disc. When the separation is greater than 135 AU, the detection rate,  $19\pm 4\%$ , is similar to that of single stars. That is, wide stellar multiplicity does not observably effect the likelihood there is a detectable disc present. When the separation is less than 25 AU, the detection rate,  $8\pm 1\%$ , is more than halved. The close binary may be either interfering with planetesimal formation or driving faster collisional evolution of planetesimals that do form. They found no detectable discs when the binary separation was between 25 and 135 AU. They conclude that binary separation on the scale of typical disc radii likely disrupts planetesimal formation in the protoplanetary disc phase via the clearing of material.

Yelverton et al. [2020] compare a sample of 201 systems with known radial-velocity planets and far-IR excesses with a control sample of 294 stars with far-IR excesses without known planets. They found that the disc fractional luminosities were different between the two samples, as has been reported before [e.g. Bryden et al., 2009; Kóspál et al., 2009; Matthews et al., 2014], but that this result may be due to bias. The radial velocity planet hosts were less likely to be binaries or late type stars than the control sample, these also

affect the likelihood of the presence of a detectable disc. When the samples were restricted to sun-like stars without close companions the significance of the result drastically dropped and they ultimately rule that there is no significant correlation between radial velocity planet presence and debris disc properties.

#### 1.2.4 M-dwarfs

There is plenty of room for future investigation, observation and theorising within the debris disc field, e.g. connecting them to the features we see in protoplanetary discs, examining their scale heights in the sub-mm, exploring the relationship between hot, warm and cold discs within the same system, but one of the largest holes is the question: where are all the M-star discs?

To recount and expand on what is relevant about M-dwarfs for debris disc science:

The stellar mass ranges from  $0.57 M_{\odot}$  for M0V to  $0.079 M_{\odot}$  for M9.5V [Pecaut and Mamajek, 2013]. The comparative host mass to Sun-like stars for early M-types means that the protoplanetary disc is not short on planet/planetesimal forming solids. In fact, we frequently observe M-stars to be planet hosts, even more frequently hosting observable terrestrial planets than earlier type stars [e.g. Bonfils et al., 2013; Dressing and Charbonneau, 2015; Mulders et al., 2015]. The gravitational environment is also not significantly different, and as orbital velocity scales with the square root of the stellar mass the collisional dynamics and lifetimes of similarly sized discs are also not significantly different for these late type stars.

The host stellar luminosity however, drops much more drastically, ranging from  $0.07 L_{\odot}$  for M0V to  $0.00027 L_{\odot}$  for M9.5V. This has larger consequences. A debris disc with the same mass or fractional luminosity around a late type star will be much less bright than around an early type star. That the host star cannot illuminate its disc as well will affect both thermal emission observations and scattered light observations of the disc. With less illumination also comes lower temperature: a disc at the same radius, or a scaled down radius (as luminosity drops more quickly than mass), will be colder around a M-dwarf, requiring far-IR instruments to detect thermal emission.

Another effect of the low host luminosity is that for M type stars  $\beta_{rad}$  never reaches 0.5, i.e. small grain dust cannot be blown out of the system by radiation pressure as the radiation pressure is too weak. On the other hand, as late type stars are more active, especially young ones, stellar wind takes the place of radiation pressure and removes small grain dust. This strong stellar wind can cause other phenomena as well, for example the fast moving small dust features seen in AU Mic scattered light observations.

Background galaxies are known to be frequent sources of confusion in debris disc studies, but with late type stars with more stellar activity, there is another source to be wary

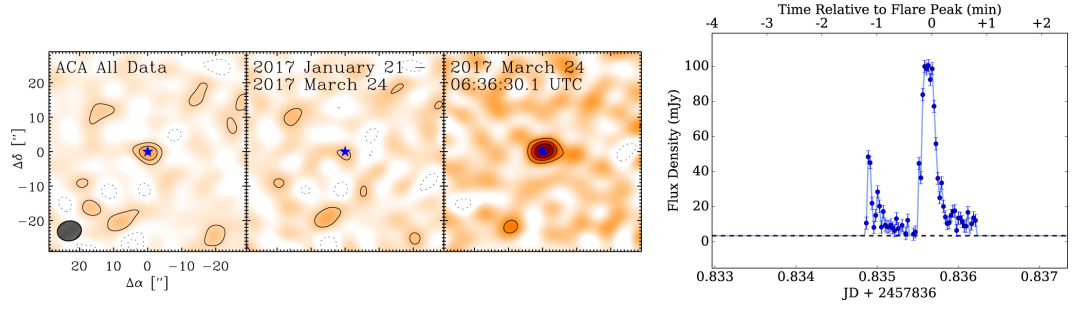


Figure 1.7: The stellar flare detected from Proxima Centauri in the mm. Left: ACA images, the left panel shows the naturally weighted image from combining all of the 13 observations, the middle panel shows just the first 12 observations with low flux at the stellar location, the right panel shows just the final 13th observation with the very high flux from the flare. Right: an ACA light curve of the point source detected in the final 13th observation showing a transient flare-like event. This figure is taken from MacGregor et al. [2018b].

off: stellar flares. In 2017 an unresolved debris disc detection around Proxima Centauri was reported [Anglada et al., 2017], however it came to pass upon further examination that the mm excess had originated from a stellar flare [MacGregor et al., 2018b]. Anglada et al. [2017] observed Proxima 13 times at 1.3 mm with the Atacama Compact Array (ACA) with each observation lasting  $\sim 1.6$  hours and combined the observations for greater signal to noise. They detected a mm flux of  $340 \pm 60 \mu\text{Jy}$  with an expected stellar flux of  $74 \pm 4 \mu\text{Jy}$ , interpreting the excess emission as deriving from a debris disc with a radius of 1-4 AU. However, when the observations were looked at individually, MacGregor et al. [2018b] found that the first 12 observations showed no excess, and only the 13th did. When this observation was split further into the individual 6.58 minute scans, only one of the seven scans showed the excess. Splitting further into 2 second intervals showed a clear flare-like light curve, as seen in Figure 1.7. A  $\sim 1$  minute flaring event with a peak flux of 100 mJy when time averaged over the all the observations had looked instead like a constant  $270 \mu\text{Jy}$  debris disc. Further research found mm-flaring to be a relatively common phenomenon. Flares have been detected around the M5.5Ve Proxima Centauri and the M1Ve AU Mic [MacGregor et al., 2020]. The flares last typically on the order of seconds to a minute, with fluxes on the order of half a dozen to dozens and up to a hundred mJy. MacGregor et al. [2020] estimate a flaring rate of 20 events per day for AU Mic and 4 events per day for Proxima. This highlights the importance of checking all unresolved late-type star ALMA observations' individual time chunks to check for transients.

The detection rate for debris discs around M-dwarfs is extremely low. Only a handful of discs are known and of these many are very young and/or close by. The eight published M-star discs are:

- the archetypal and well observed M1V AU Mic, in the BPMG at  $\sim 20$  Myr old and only 9.7 pc distant [e.g. Moshir et al., 1990; Kalas et al., 2004; Augereau and Beust, 2006; Graham et al., 2007; MacGregor et al., 2013; Schneider et al., 2014; Matthews et al., 2015; Wang et al., 2015; Wisniewski et al., 2019];
- the M4V Fomalhaut C at 440 Myr and only 7.7 pc away, part of the Fomalhaut triple system and previously detected with Herschel [Kennedy et al., 2013];
- the M3.2V TWA 7 34 pc away in the 6.4 Myr old TW Hya association resolved in scattered light and marginally resolved with ALMA [Olofsson et al., 2018; Ren et al., 2021; Bayo et al., 2019; Matr  et al., 2019a];
- the M0.5 TWA 25 in the same association but 54 pc distant resolved in scattered light [Choquet et al., 2016];
- the planet-hosting M3V GJ 581 only 6.3 pc away but 2-8 Gyr old and marginally resolved with Herschel [Lestrade et al., 2012];
- the planet hosting M2V GJ 433 at 9.1 pc and M2V GJ 649 at 10.4 pc with ages uncertain but likely to not be young and with only unresolved excesses from Herschel [Kennedy et al., 2018a];
- and the M1V GSC 07396-00759 in the BPMG at  $\sim 20$  Myr old but 71.4 pc away and previously only imaged in scattered light [Sissa et al., 2018; Adam et al., 2021].

There are several possible explanations to explain the lack of detections. There are two scenarios to consider: first that debris discs less commonly form around M-dwarfs. The increased planet detections could be the key: perhaps planet formation is extra efficient around M-dwarfs and not many planetesimals are left over or instead planetesimal and planet formation is fundamentally different around M-dwarfs due to the more compact and cooler protoplanetary disc. In cluster environments M-dwarf discs could be more easily stripped by stellar encounters [Lestrade et al., 2011] or photoevaporation [Adams et al., 2004]. Or instead the strong stellar wind drag could remove grains quickly enough to significantly affect the dynamics of the disc [Plavchan et al., 2009].

The other scenario is that they are indeed there, but they were just unable to be detected in historic surveys due to their dimness and coldness. Luppe et al. [2020] investigate whether a population of discs similar, e.g. in radius/mass etc., to those found by the DEBRIS survey but scaled by the host luminosity could exist around M-dwarfs and remain undetected due to the low host luminosity and low disc temperature. They produce synthetic disc populations for M-dwarfs observed by previous programs under several different scaling hypotheses. Namely, their hypotheses are that M-dwarf discs are as prevalent as discs about

other types while: their radii could be the same or dependent on host luminosity, their mass could be the same or dependent on host mass, the fractional luminosity could be the same, lesser or greater and the temperature of the dust is colder. They find that the lack of M-dwarf detections is consistent with nearly all of their hypotheses, and the discs were simply too dim and cold to be detected by the sensitivities of past surveys. They then predict whether future surveys would be able to detect their M-dwarf disc populations, in particular for 15 minute integration time ALMA Band 7 observations of the Herschel DEBRIS M-star sample they predict a detection rate of 4.3%-15.8%. However this has caveats, if the discs were resolved then their SNR per beam would decrease and ALMA's interferometry may not recover all of the disc flux if the angular scale is larger than the maximum recoverable size, making detection more difficult. In Band 7 over half their discs could be resolved, lowering the detection rate to 1.0%-6.3% for 15 minute observations.

If there are discs to be found, the best place to look would be nearby young moving groups, as we know younger stars are more likely to have brighter discs and the nearer a disc is the more flux we can recover from it. Given also the known existence of two M-dwarf discs there already (AU Mic and GSC 07396-00759) and the observed high incidence of discs for early type stars [Pawellek et al., 2021], the  $\beta$  Pictoris Moving Group is an ideal place to search. The instrument of observation must be far-IR and highly sensitive to detect the dim and cold discs, currently the Atacama Large Millimetre/submillimetre Array best suits this purpose. Using ALMA's high resolution to investigate the known discs, such as that of the latest type debris disc host Fomalhaut C, will also be invaluable in exploring the M-dwarf debris disc mystery.



## Chapter 2

# Methods

We have a lot of knowledge concerning the features of debris discs and we have detected hundreds of individual discs. But what are the scientific techniques we used to achieve this? We have detections, but what are our detectors, and what observational biases do they come with? How did our knowledge evolve as our telescopes evolved? What telescopes do we require to observe discs around M-dwarf stars?

To begin with, in the simplest case a detection of a debris disc comes from the infrared excess. Infrared excess is the unresolved infrared flux from the stellar location that is more than, i.e. in excess of, the expected stellar photospheric flux. The excess must come from something else that is colder than the star, circumstellar dust. If you have multiple photometry points in the infrared, you can begin to characterise the thermal spectrum of the excess through an SED.

### 2.1 Thermal Emission and SEDs

The letters of the acronym SED are derived from Spectral Energy Distribution. A ‘spectral energy distribution’ is a plot showing the distribution of energy emitted by an object across the electromagnetic spectrum. By definition an SED ought to have *energy* [J] along its y-axis and either wavelength or frequency along the x-axis, but typically *flux density* (or *irradiance*;  $[W \cdot m^{-2}]$ ) is placed along the y-axis. Thus the plot becomes instead a ‘flux density distribution’, but the acronym SED is retained by convention. This flux is often scribed as  $\nu F_\nu$ , where  $F_\nu$  is the *spectral flux density* (or *spectral irradiance*;  $[W \cdot m^{-2} \cdot Hz^{-1}]$ ). The favoured unit in radio astronomy for spectral flux density is the Jansky, Jy [ $1 Jy = 10^{-26} W \cdot m^{-2} \cdot Hz^{-1}$ ], and radio telescopes often deliver their flux measurements in some multiple of Janskys or Janskys per unit area, where the area can be steradian, beam or pixel. Not only are Janskys the more practical unit, but using the *spectral flux density*,  $F_\nu$ , in place of the *flux density* on

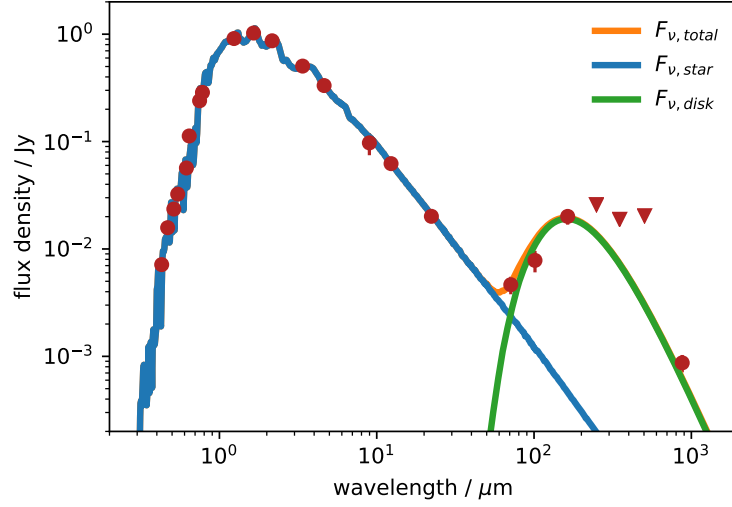


Figure 2.1: Flux density distribution (SED) for the disc of Fomalhaut C. Dots are measured fluxes and triangles are  $3\sigma$  upper limits. The stellar photosphere model is in blue, the disc model in green and the combined SED in orange. This figure is taken from Cronin-Coltsmann et al. [2021] (Chapter 3).

the y-axis of an SED has the effect of making the infrared/radio emission more visible on the plot, and so this form is often used in debris disc science. The plot is now technically a ‘spectral flux density distribution’, but Janskys are still said to measure ‘flux density’ and the acronym SED is still retained by convention.

SEDs can be applied to a variety of astronomical objects, from galaxies to stars. Circumstellar material scientists produce SEDs from the combined emission of the host star and any surrounding discs, an example SED of the Fomalhaut C system is displayed in Figure 2.1.

The goal is to describe the total emission as originating from the sum of a stellar photosphere and the thermal emission of the surrounding circumstellar matter. As the temperature of the star and the material are normally very different, thousands of Kelvin for the star and less than a few hundred Kelvin for the disc, it normally is not complex to fit a stellar photosphere and identify what remains as an excess. The stellar photosphere model is fit around optical and near-infrared photometry where their emission peaks. These measurements often originate from large sky surveys like SDSS [York et al., 2000], Gaia [Gaia Collaboration et al., 2016, 2018, 2021, 2022], 2MASS [Skrutskie et al., 2006] and WISE [Wright et al., 2010]. Depending on the temperature of the disc, the disc’s flux is generally informed by mid to far-IR and sub-mm data, with data from telescopes like WISE, Spitzer [Werner et al., 2004], Herschel [Pilbratt et al., 2010] and ALMA [Wootten and Thompson,

2009].

An infrared excess can point towards the presence of a disc, but fitting a model to the disc and characterising it is not straightforward. Essentially this is because dust grains do not emit as perfect blackbodies and so their spectral flux density is not described by the Planck function, where the Planck function is:

$$B_\nu(\nu, T) = \frac{2h\nu^3}{c^2} \frac{1}{e^{\frac{h\nu}{k_B T}} - 1} \quad (2.1)$$

for frequency  $\nu$  at temperature  $T$  where  $h$  is the Planck constant,  $c$  is the speed of light,  $k_B$  is the Boltzmann constant.

To begin with, a dust grain will emit inefficiently at wavelengths larger than its own size, more precisely at wavelengths  $> \lambda$  for a size of between  $\lambda/2\pi$  and  $2\pi\lambda$  depending on the grain's other properties [Backman and Paresce, 1993]. As grains with a temperature between  $\sim 30$ -200 K will have emission peaks at wavelengths of  $\sim 100$ -15 microns, inefficient emission is a significant factor. This would not be an issue if only one grain size was present in a disc, but the collisional cascade that perpetuates debris discs necessarily produces a distribution of grain sizes. The chemical composition and morphology of the dust grains is also significant for their emission properties.

Different approaches can be taken to address these issues when attempting to fit a model to the dust emission. The simplest is to use a so-called ‘modified blackbody’. Here, the flux is taken as the flux of a perfect blackbody multiplied by a wavelength dependent parameter, applied only at wavelengths longer than a given cut-off wavelength  $\lambda_0$ . Such a modified blackbody equation could have the form of spectral flux density:

$$F_\nu \propto B_\nu(\nu, T) X_\lambda^{-1} \quad (2.2)$$

where  $X_\lambda$  is an attenuation factor itself parameterised by slope  $\beta$  (not to be confused with the  $\beta$  of §1.2.1 that describes the balance of forces on a dust grain) [e.g. Kennedy and Wyatt, 2014]:

$$X_\lambda = \begin{cases} 1 & \text{for } \lambda \leq \lambda_0 \\ (\frac{\lambda}{\lambda_0})^\beta & \text{for } \lambda > \lambda_0 \end{cases} \quad (2.3)$$

This  $X_\lambda$  factor can be observationally determined at specific wavelengths [Wyatt et al., 2007; Wyatt, 2008]. Note this is sometimes seen as:

$$F_\nu \propto B_\nu(\nu, T) \lambda^{-\beta} \quad (2.4)$$

which may be applied at all wavelengths. An alternative, but similar (and converging to identical at long wavelengths), formulation is [Williams et al., 2004]:

$$F_\nu \propto B_\nu(\nu, T) Q_\lambda \quad (2.5)$$

where  $Q_\lambda$  is an emission efficiency factor described at all wavelengths by:

$$Q_\lambda = 1 - e^{-(\frac{\lambda_0}{\lambda})^\beta} \quad (2.6)$$

In these equations  $\lambda_0$  corresponds to where inefficient emission becomes important and can be linked to a ‘characteristic’ grain size of the disc  $\lambda_0/2\pi$ , roughly an average by weight and emissivity over the grain size distribution [Hughes et al., 2018]. Grains of all sizes contribute to the flux and information pertaining to the particular size distribution of the disc is encoded in  $\beta$ .

As  $\lambda_0$  and  $\beta$  are individual to each disc and its particular size distribution, these parameters are typically left free when fitting, although if there is not strong photometric coverage it is not uncommon for them to be poorly constrained. In cases where the simple modified blackbody does not give strong constraints or when a surplus of photometry/spectroscopy allows for a deeper dive, a more complex and physical model can be used. Conversely, if there is a lack of photometry that does not allow for strong constraints, using a more realistic model can give more useful physical limits. Examples of what a more complex model could include are:

- Multiple discs at different radial locations; this can still be through the modified blackbody method but simply with multiple dust components simultaneously fitted.
- The spatial distribution of the dust grains; dust grains at different distances to the star will have different incident stellar fluxes and thus different temperatures, this distribution can be informed by modelling of a resolved image of the disc.
- Allowing different grain sizes to possess different temperatures; smaller grains that emit inefficiently at more wavelengths will retain more of their heat and will reside at higher equilibrium temperatures than larger grains.
- Modelling the size distribution of the grains; different grains sizes have different properties as above and by including the slope parameter  $q$  as a free parameter one can shift the balance between different grain sizes.
- Setting maximum and minimum grain sizes; the minimum grain size will typically be defined by the blow-out size of the system but can be a free parameter, in particular

for low mass systems where a blow-out size is not well defined, and the maximum size will be a cut off above which little significant flux is contributed.

- Using realistic optical properties based on grain composition and chemistry.

There can be many complications, some of which are simple:

- The disc could have multiple spatial components; i.e. there are multiple discs at different radii and therefore with different temperatures in the system.
- There could not be enough IR photometry points; now that Spitzer and Herschel are defunct many new detections have a critical lack of wavelength coverage.
- There is another star very nearby along the line of sight; this may be a binary companion or a coincidental alignment. This can result in a blending of the two stars' emissions resulting in inaccurate photometry measurements and therefore an uncertain stellar photosphere. This problem is more pronounced for colder stars whose thermal emission peaks at longer wavelengths where telescope resolution is decreased due to diffraction limit effects.
- There could be not enough high-quality optical photometry; when paired with a lack of parallax measurement in particular and/or if no spectrometry is available, this can leave the type and evolutionary stage of the host star uncertain; asymptotic giant branch stars can heave off their outer layers forming a surrounding shell of dust that causes an infrared excess [e.g. Habing, 1996].
- Extinction can also affect photometry; interstellar space is not a perfect void and interstellar dust clouds can attenuate stellar fluxes, leading to inaccurate photometry measurements.

There are other dangers in relying solely on SED fitting, for example background confusion. Debris discs are not the only repositories of cold dust emitting in the infrared in the universe. A chance alignment between a galactic star and a distant dusty galaxy can appear identical to a debris disc when presented as just an SED gathered from local sky photometry. For this reason imaging is often required to confirm the presence of a disc, or at least rule out the presence of a background object.

Despite striving to produce an informed imperfect-blackbody distribution for the emission of dust grains in a debris disc, there is a useful measure that can be derived from pretending that dust grains are ideal emitters. This measure is the 'blackbody radius' of a debris disc. If in a given model only one dust temperature is fit, the corresponding blackbody

radius is the location of the dust ring if the dust indeed behaved as a perfect blackbody. If the disc radius has been resolved in imaging, we can then compare the blackbody radius to the resolved radius as a measure of how imperfectly the dust grains are behaving. The measure commonly used is called  $\Gamma$ , defined as  $R_{\text{dust}}/R_{\text{BB}}$ , the ratio of the resolved disc to the blackbody radius [Booth et al., 2012], or equivalently defined as  $(T_{\text{dust}}/T_{\text{BB}})^2$ , the square of the ratio of the dust temperature to the temperature of an ideal blackbody at the radius of the disc [Pawellek et al., 2014].  $\Gamma$  can be used as an indirect measure for probing grain size, as smaller dust grains behave more imperfectly and so are hotter than perfect blackbodies;  $\Gamma$  is observed to increase with decreasing host luminosity, which correlates to the decreased radiation pressure blowout size of less luminous hosts. Investigating this measure and identifying trends in it can also then assist in characterising unresolved discs. If there is an estimate for the typical  $\Gamma$  of a disc around a certain type host, one can model the blackbody radius of an unresolved disc from its SED, and then use the expected  $\Gamma$  factor to estimate a physical dust radius.

The information derived from modelling that creates an SED can also be used to produce an alternative plot, a plot of temperature/blackbody radius (or representative temperature/radius in a more complex model, where representative may mean something like the properties of the dust grains observed by a particular instrument) vs fractional luminosity. Such a plot can be used compare these parameters to those of other debris discs, or to compare possible models to the detection limits of individual instruments, an example of this for the disc around GSC 07396-00759 is displayed in Figure 2.2 [Cronin-Coltsmann et al., 2022, Chapter 4].

### 2.1.1 Historic instruments

To understand the history of infrared and sub-mm astronomical observations, a few key concepts must be addressed.

First is the idea of an ‘atmospheric window’, or lack thereof. The Earth’s atmosphere is not a perfect transmitter of electromagnetic energy, in fact vast swathes of the electromagnetic spectrum are mostly or entirely absorbed or scattered. Water vapour is the most significant molecule when it comes to absorption in the infra-red, with large contributions from carbon dioxide and smaller contributions from oxygen and ozone, methane and nitrogen oxides. The end result, as seen in Figures 2.3 and 2.4, is that at sea level much of the spectrum between 1 micron and 1 mm is blocked by the atmosphere, making telescopic observations very difficult from Earth’s surface. It is still technically feasible, but the telescope must be built somewhere high up and dry, with less atmosphere and water to look through. A different solution for infrared observation however is to remove the issue

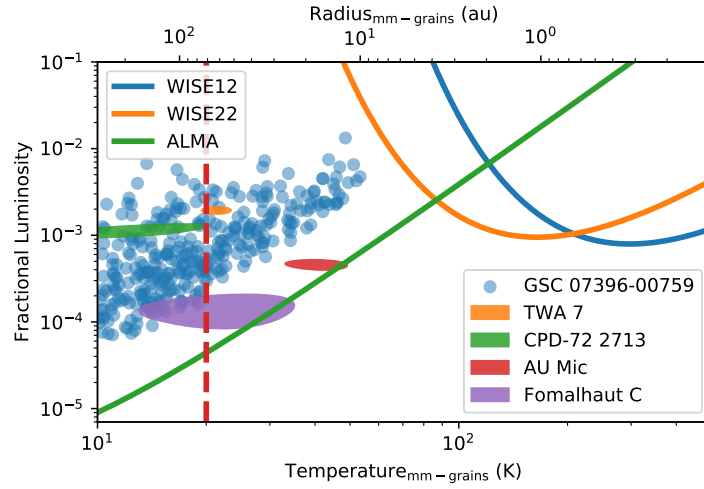


Figure 2.2: Plot of disc fractional luminosity against representative temperature/blackbody radius, i.e. the temperature and stellocentric radius of mm grains. Blackbody radius depends on host stellar temperature and is thus only accurate for GSC 07396-00759. A selection of allowed models for the disc of GSC 07396-00759 are plotted as blue circles. The distributions up to  $3\sigma$  following the same SED fitting procedure are shown for a selection of low mass host debris discs as coloured ellipses. The detection limits for the WISE 12 micron band, WISE 22 micron band and ALMA Band 7 are plotted as blue, orange and green curves respectively. The vertical red dashed line is placed at 70.2 AU, the best-fitting model radius for GSC 07396-00759's resolved disc. This figure is taken from Cronin-Coltsmann et al. [2022] (Chapter 4).

of the atmosphere entirely, by placing your telescope in space. Naturally this comes with its own expense and engineering challenges, but the results are worthwhile.

The other issue, which becomes a dominant concern when it comes to space telescopes, is the need for cooling. Mid to far infrared telescopes are looking to trace the thermal emission of distant objects, but thermal emission can originate from much closer to home. An infrared telescope needs to not be overwhelmed by the thermal emission of its immediate surroundings. Placing a telescope in the vacuum of space also assists in this manner, removing all the heat of the Earth's atmosphere from the equation, although a sun-shield is still warranted. But there is still the thermal emission of the telescope itself to contend with. To counter this, infrared space telescopes come equipped with supplies of cryogen, normally liquid helium, that is slowly expended to keep the telescope cool. Once the supply of cryogen depletes, the telescope can no longer cool itself enough that its own heat does not wash out that of the objects it observes and it can no longer continue in operation, at least for observing the longer wavelengths. A telescope's equilibrium temperature may still be cool enough to observe at the shortest wavelengths it is equipped to [e.g. SPITZER/IRAC; WISE 3.4 and 4.6  $\mu\text{m}$ ; Werner et al., 2004; Fazio et al., 2004; Wright et al., 2010; Mainzer et al., 2014].

The final consideration for observing at longer wavelengths is the diffraction limit. By the physical laws of diffraction there is a natural limit to how well resolved an image can be, the resolving angle  $\theta$ , for a telescope with a set aperture/mirror/lens size, diameter  $D$ , observing at a particular wavelength,  $\lambda$ . The diffraction limit is defined by the equation  $\theta = 1.22\lambda/D$ . Even if an optical system is not refined to reach its diffraction limit, when the wavelength of observation is increased, so too will the resolution decrease. So when telescopes observe at longer wavelengths in the far-IR, their resolution will always be naturally worse than telescopes observing at smaller wavelengths with similar mirror sizes. Larger mirrors are always more desirable, both for increasing resolution and increasing light gathering area, across all wavelengths of observation, but the construction of increasingly large mirrors is an increasingly larger technical challenge, especially if the mirror must be raised into space intact.

It is for these reasons that so many far-infrared telescopes are space telescopes, with lifespans limited by cooling supplies and with resolutions that always drag behind the optical. It would be outside of the scope of this thesis to detail every single instrument that was or is capable of observing debris discs, but some of the key contributors can be described to highlight the importance of ALMA in contemporary debris disc science.



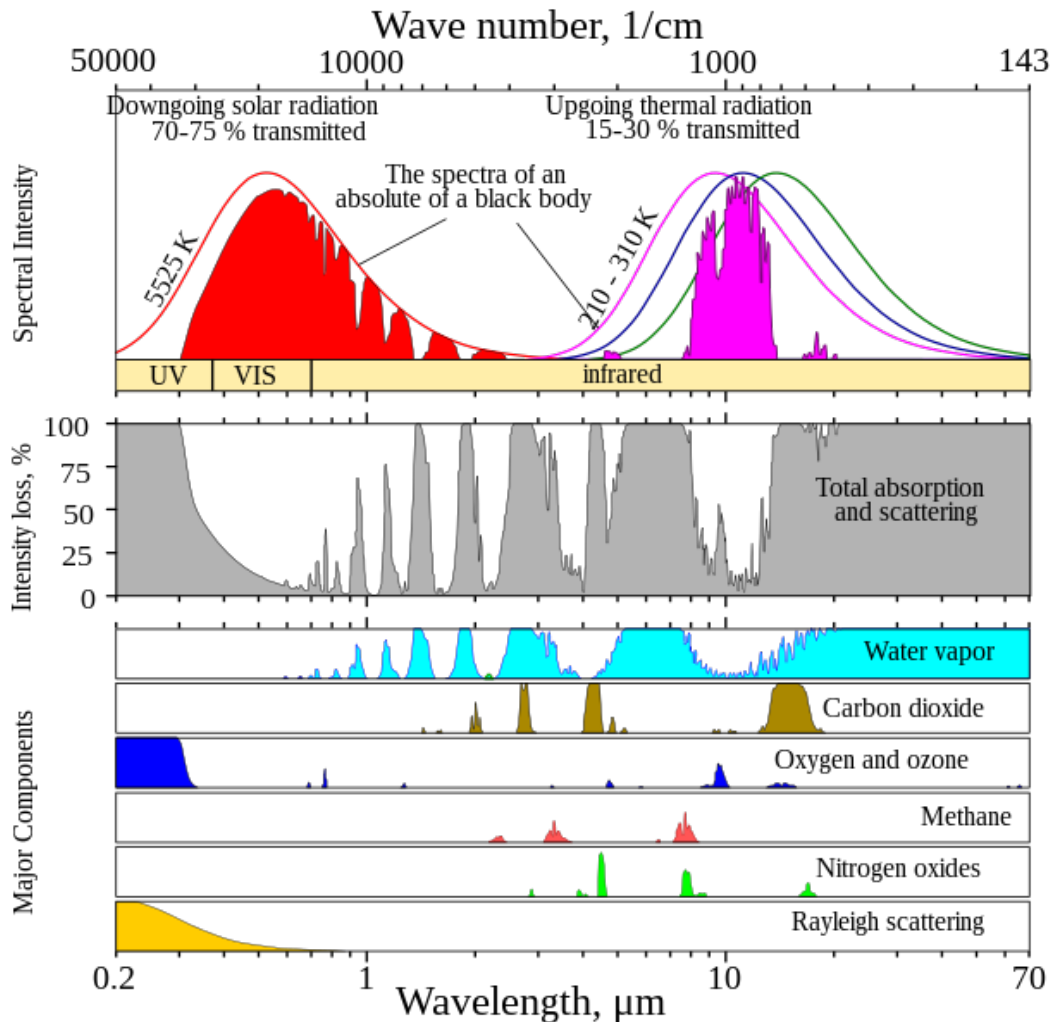


Figure 2.3: Plots describing the local electromagnetic radiation environment in the near-ultraviolet to mid infrared-regime. The top plot shows incoming radiation from the Sun as well as the Earth's own outgoing thermal emission. The middle plot shows total absorption and scattering reducing the intensity of incoming light; atmospheric windows are present where intensity loss is minimal. The bottom collection of plots show the impact of individual species in absorption and the effect of Rayleigh scattering; water vapour is noticeably the largest absorber. This image was taken from Wikimedia commons having been released into the public domain.

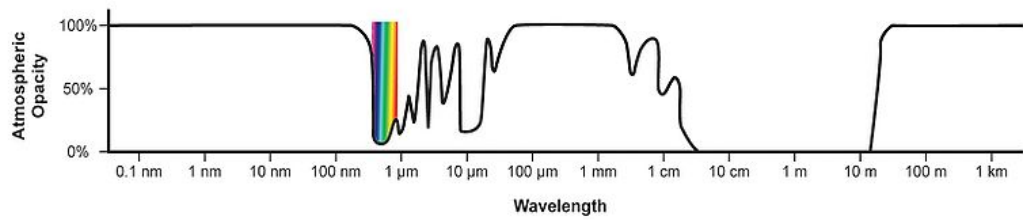


Figure 2.4: Plot showing how opaque the atmosphere at sea level is to light of a wide range of wavelengths. The rainbow denotes visible light. Multiple atmospheric windows are visible, in particular a large window is present at wavelengths between approximately 2 cm and 10 m. This image was modified from an image taken from NASA and is in the public domain.

## IRAS

The Infrared Astronomical Satellite [Neugebauer et al., 1984] was a far-IR space telescope launched in January 1983 that observed the entire sky over ten months and then ceased operations when it ran out of coolant. It observed at four wavelengths:  $12\ \mu\text{m}$ ,  $25\ \mu\text{m}$ ,  $60\ \mu\text{m}$  and  $100\ \mu\text{m}$  with  $5\sigma$  sensitivities of  $\sim 500\ \text{mJy}$  for the first three bands and  $\sim 1500\ \text{mJy}$  for the  $100\ \mu\text{m}$  band, and resolutions of  $\sim 25\ \text{arcsec}$ ,  $\sim 25\ \text{arcsec}$ ,  $\sim 50\ \text{arcsec}$  and  $\sim 100\ \text{arcsec}$  respectively.

As the first space telescope to observe the entire sky in the infrared, it was the telescope that first discovered debris discs. The first excess was detected around Vega [Aumann et al., 1984], followed by  $\beta$  Pictoris,  $\epsilon$  Eridani and Fomalhaut. Soon hundreds of stars had infrared excesses identified [Oudmaijer et al., 1992], although not all were main sequence debris discs. Note that these detections came before the Kuiper belt itself was detected [Jewitt and Luu, 1993].

IRAS was extremely important for discovering the first debris discs, but its technology has long been superseded. However, as a rare far-infrared all-sky survey, its photometry can still prove useful for particularly bright stars and discs. In terms of imaging, IRAS's resolution was too poor to fully resolve any of its detections, but could distinguish the discs from point sources [Backman and Paresce, 1993].

## WISE

The Wide-field Infrared Survey Explorer [Wright et al., 2010] is a space telescope in polar orbit around the Earth. The telescope has four different observation bands: W1:  $3.4\ \mu\text{m}$ , W2:  $4.6\ \mu\text{m}$ , W3:  $12\ \mu\text{m}$  and W4:  $22\ \mu\text{m}$ , in the All-Sky Data Release [Cutri et al., 2012; Cutri et al., 2012] it observed with respective  $5\sigma$  sensitivities of 68, 98, 860 and  $5400\ \mu\text{Jy}$ , several orders of magnitude greater than that of IRAS, with resolutions of  $\sim 6.1\ \text{arcsec}$ ,

$\sim 6.4$  arcsec,  $\sim 6.5$  arcsec and  $\sim 12.0$  arcsec respectively. WISE surveyed the entire sky and released several large data releases across its mission. To begin with the 2012 All-Sky Data release covered the entire sky with all four bands. Once the spacecraft's cryogenic supplies ran out it could only observe the  $3.4\ \mu\text{m}$  and  $4.6\ \mu\text{m}$  bands, but it continued observing, now looking for Near-Earth Objects for the NEOWISE mission [Mainzer et al., 2011, 2014]. In 2013 NEOWISE's data was released and later that year a combined catalogue dubbed ALLWISE was released [Cutri et al., 2021]. The NEOWISE mission was extended and is ongoing, continuing to release data annually [Schlafly et al., 2019; Cutri et al., 2021].

WISE's wavelength and sensitivity is highly photometrically valuable for characterising the photospheres of host stars, and sometimes the emission of particularly warm debris discs. Nearly every modern debris disc SED will use WISE data in the photosphere fitting.

Having viewed the entire sky, WISE data is also capable of discovering new warm debris discs as well as characterising known ones. For example Moór et al. [2021] use the ALLWISE catalogue to identify new six new extreme debris discs. The long time baseline of the WISE data also allowed them to probe the time-variability of their sample.

With a maximum wavelength of  $22\ \mu\text{m}$ , WISE could only observe debris discs with dust warmer than  $\sim 100$  K, and with the post-cryogenic maximum wavelength of just  $4.6\ \mu\text{m}$  the dust must be several hundreds of Kelvin to be observable, only achievable in extreme debris discs. The resolution of WISE's images is generally too poor to resolve the debris discs it is capable of observing.

## Spitzer

The Spitzer Space Telescope began operation in 2003. Its Infrared Array Camera [IRAC; Fazio et al., 2004] observed at  $3.6\ \mu\text{m}$ ,  $4.5\ \mu\text{m}$ ,  $5.8\ \mu\text{m}$  and  $8\ \mu\text{m}$  all with a resolution of  $\sim 1.2$  arcsec and respective sensitivities of 6, 7, 36 and  $54\ \mu\text{Jy}$  ( $5\sigma$  for 200 seconds of observation). The Infrared Spectrograph [IRS; Houck et al., 2004] could operate at several spectral resolutions in a range of  $5.3$  to  $40\ \mu\text{m}$ . The Multiband Imaging Photometer for Spitzer [MIPS; Rieke et al., 2004] observed at  $24\ \mu\text{m}$ ,  $70\ \mu\text{m}$  and  $160\ \mu\text{m}$  at spatial resolutions of 6 arcsec, 18 arcsec and 40 arcsec respectively. To give a perspective of its sensitivity range,  $5\sigma$  sensitivity after 200 seconds of observation was  $\sim 250\ \mu\text{Jy}$  and in its SED mode for point sources was 51, 127 and 283 mJy respectively at wavelengths of 60, 75 and  $90\ \mu\text{m}$ .

Its primary operation lasted five and a half years before its cryogenic supply ran out. However, as active cooling was not required for the  $3.6$  and  $4.5\ \mu\text{m}$  IRAC bands and in these modes the telescope continued operation until final shutdown in 2020.

Finally, a sensitive telescope observing in the far-infrared allowed for hundreds of papers published in science related to debris discs, discovering and characterising hundreds

of disc candidates [e.g. Rieke et al., 2005; Su et al., 2006; Trilling et al., 2008; Koerner et al., 2010; Chen et al., 2014].

Certain discs could be resolved for the first time, such as the four nearby and bright Vega [Su et al., 2005],  $\beta$  Pictoris [Rebull et al., 2008],  $\epsilon$  Eridani [Backman et al., 2009] and Fomalhaut systems [Stapelfeldt et al., 2004]. The disc of Fomalhaut resolved by Spitzer at 70 microns is displayed in the top left of Figure 2.5.

Spitzer was an excellent addition to the debris disc observer’s arsenal, but its main mission lifetime was finite and there was more room to go deeper into the far-IR to find cooler discs and to image at higher resolution.

## **Herschel**

The Herschel Space Observatory was designed to peer into even longer wavelengths. From 2009 until its cryogenic supply fully depleted in 2014, Herschel observed in the far-IR. Of particular relevance to debris discs science, the Photodetecting Array Camera and Spectrometer [PACS; Poglitsch et al., 2010] was capable of imaging at wavelengths of 70, 100 and 160  $\mu\text{m}$ , the FWHM of the beams were 5.6, 6.8 and 10.7 arcsec respectively. The Spectral and Photometric Imaging REceiver [SPIRE; Griffin et al., 2010] was capable of imaging at 250, 350 and 500  $\mu\text{m}$ , the FWHM of the beams were 18.1, 25.2 and 36.6 arcsec respectively. With an hour of integration time the  $5\sigma$  sensitivity of the PACS bands were 5-10 mJy and sensitivity would be confusion limited to  $\sim 6$  mJy for SPIRE. ‘Confusion limited’ means that the beam size is large enough that with a certain sensitivity it becomes statistically impossible to distinguish between emission from a given object and faint emission from unwanted extra-galactic sources also caught up in the beam.

Herschel provided much needed photometry in the far-infrared needed to fill in the SEDs of colder discs, finally allowing them to be characterised. No other telescope currently provides sensitive photometry in this wavelength range, the Earth’s atmosphere blocks light of these wavelengths and such space missions are expensive and so few and far between. Its photometry, where available, remains invaluable while SED modelling and every disc SED modelled without Herschel photometry suffers from the lack of it.

Herschel was able to well resolve debris discs, some to a new degree of clarity and some for the first time. The disc of Fomalhaut resolved by Herschel at 70 microns is displayed in the top right of Figure 2.5.

Its sensitivity also allowed it to detect many new discs for the first time, providing the best statistical disc occurrence rates yet that are still highly referenced today, such as the DEBRIS and DUNES surveys [e.g. Eiroa et al., 2013; Thureau et al., 2014; Montesinos et al., 2016; Sibthorpe et al., 2018]. With its far-IR reach it could also begin to detect new M-dwarf discs beyond the nearby AU Mic. Particularly, it discovered the disc around

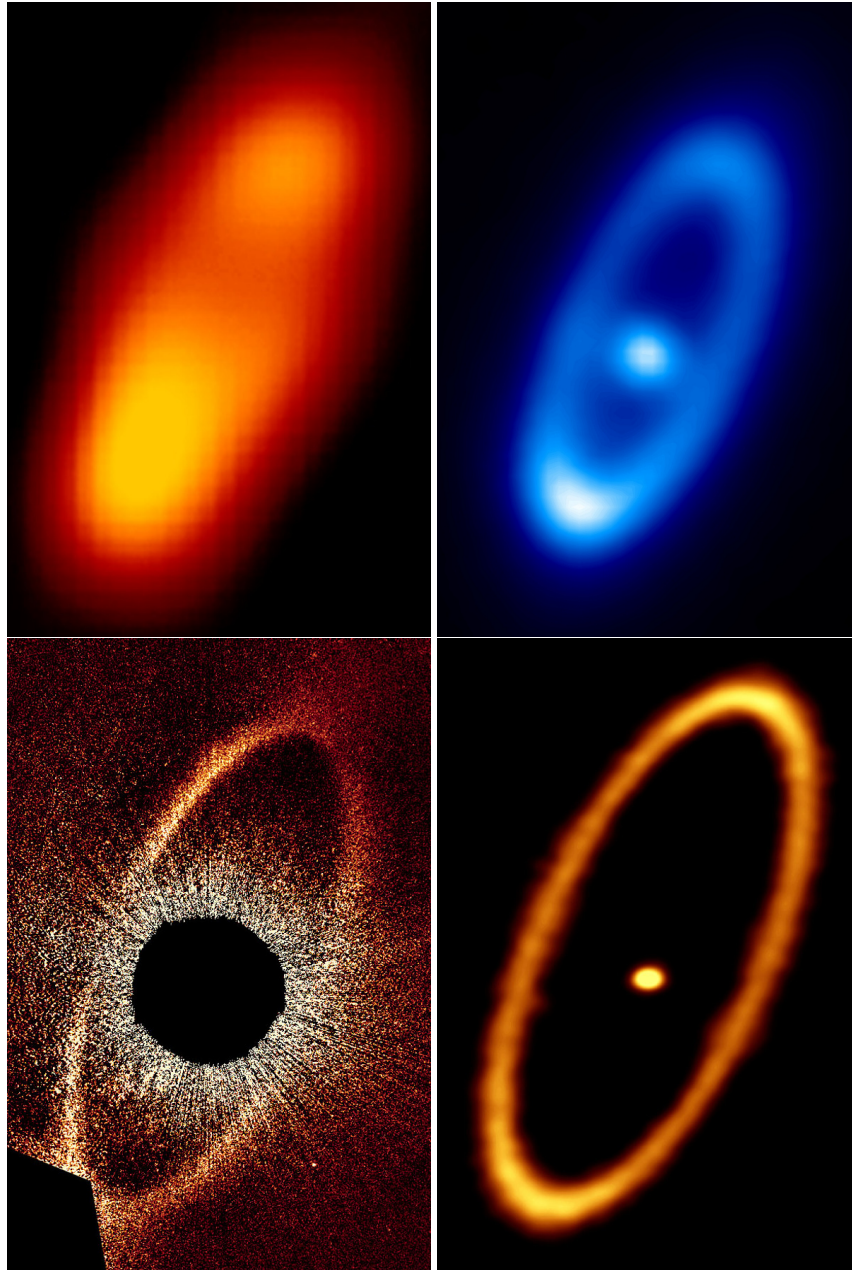


Figure 2.5: Top left: the disc of Fomalhaut as seen by Spitzer at 70 microns. [Image credit: NASA/JPL-Caltech/K. Stapelfeldt (JPL), Stapelfeldt et al. [2004]]. Top right: the disc of Fomalhaut as seen by Herschel at 70 microns. [Image credit: ESA/Herschel/PACS/Bram Acke, KU Leuven, Belgium, Acke et al. [2012]]. Bottom left: the disc of Fomalhaut as seen by Hubble over a wavelength range of 0.2-1.03 microns. [Image credit: NASA, ESA and P. Kalas (University of California, Berkeley, USA), Kalas et al. [2013]]. Bottom right: the disc of Fomalhaut as seen by ALMA at a wavelength of 1.3 mm. [Image credit: ALMA (ESO/NAOJ/NRAO); M. MacGregor, MacGregor et al. [2017]].

Fomalhaut C [Kennedy et al., 2013].

The end of the Herschel mission leaves a noticeable hole in debris disc photometric capabilities, but there is a possibility that its work could be continued in the future by the next generation Far-IR telescopes like the *Origins Space Telescope* [OST Leisawitz et al., 2018, 2021].

### Scattered Light Observations

Scattered light observations supply a good complement to infrared observations. Rather than observing the thermal emission of dust grains, they observe the starlight that is scattered off of dust in the disc. Relying on the scattering mechanism means that these observations can only take place at sub-micron to several micron wavelengths and are limited to viewing the smallest dust grains in the system as these dominate the scattering surface area. These observations thus do not trace the parent planetesimal belt but do instead trace the dynamical consequences of pressure forces in the system that primarily act on small dust grains. That is, halos of blown out dust and ‘swept-back wings’ likely from ISM interaction are often seen. Scattered light observations cannot be used to construct SEDs or probe the grain size distribution, but can inform us about the structure of a system and the forces at play. As the light is not directly emitted by the dust but originates from the star, there are a couple of consequences that must be kept in mind.

First, the star’s own direct emission would also be picked up by the telescope, and so a coronagraph must be used to mask out the stellar emission. This can prevent the inner reaches of a disc from being imaged, and/or the back/front of a disc if the system is being edge-on. Secondly, as incident flux decreases with distance from the star as  $1/r^2$ , dust that is further away is significantly less illuminated and will be less bright to our sensors, decreasing signal to noise very rapidly as one observes further from the host star. Thirdly, the observation of scattered light depends on the ‘scattering phase function’ (SPF). The scattering phase function is the likelihood of a scattered photon being directed towards the observer as a function of angle to the star, in other words a measure of how likely it is for a photon to change direction after scattering. When looking at all the unpolarised light received, a ‘total-intensity’ observation, the scattering phase function is heavily weighted towards forward-scattering. This is where the scattering angle is low and the light does not have to change its overall direction much after scattering. Due to this forward scattering propensity debris discs are much more likely to be observed in scattered light when they are edge-on, as a face-on disc would require a large scattering angle. When looking at the light of a single polarisation received, a ‘polarised light’ observation, the SPF is different, as whether or not the light will pick up a polarisation is also a function of scattering-angle. The polarised SPF is less forward-scattering than the total-intensity SPF and peaks at  $90^\circ$

scattering angles and so these observations view different sections of the disc. The host star's light is not polarised and so polarised light observations do not suffer from significant stellar contamination.

Instruments like Gemini/GPI [Macintosh et al., 2008], VLT/SPHERE [Beuzit et al., 2008, 2019a] and HST/STIS [Woodgate et al., 1998] that observe scattered light have resolved numerous discs [e.g. Esposito et al., 2020; Wahhaj et al., 2016; Sissa et al., 2018; Kalas et al., 2013], including discs that have not been fully resolved in the submillimetre such as TWA 7 [Olofsson et al., 2018; Ren et al., 2021]. The disc of Fomalhaut resolved by Hubble over a wavelength range of 0.2-1.03 microns is displayed in the bottom left of Figure 2.5.

### **2.1.2 The need for ALMA**

It seems like there is a good suite of past observations across a large wavelength range, both directly observing and mapping sky, without even mentioning many other instruments like Akari [Murakami et al., 2007], JCMT/SCUBA2 [Holland et al., 2013] and the VLA [Thompson et al., 1980]. So what is missing? Many of these instruments are either defunct, outdated, operate at inconvenient wavelengths or simply are not powerful enough. Our tools for far-infrared observations are severely limited; we would like to probe the largest dust grain sizes requiring far-IR/submm observations, allowing investigation of the deep structure of planetesimal belts by observing the large dust grains that trace the parent planetesimals; we would like to resolve a wider population of discs, requiring high resolution and sensitivity; we would like to discover the coldest discs out there, detectable only at sub-mm wavelengths at high sensitivity; and we would like to investigate the presence of cold gas in these discs, observable only with spectrally sensitive far-IR/mm instruments. ALMA is the only observatory that fits this bill, by the joint forces of a large collecting area from dozens of individual dishes and subverting the diffraction limit by measuring the Fourier transform of the sky rather than directly imaging. For comparison, the disc of Fomalhaut as resolved by ALMA at a wavelength of 1.3 mm is displayed in the bottom right of Figure 2.5.

## **2.2 The Atacama Large Millimetre/submillimetre Array**

So what is ALMA, actually? The Atacama Large Millimetre/submillimetre Array [ALMA; Wootten and Thompson, 2009] is an interferometric array comprised of 66 individual radio telescopes situated at an elevation of 5000 m atop the Chajnantor plateau in the Chilean Atacama Desert. Nominal ALMA observations use up to 50 12 m dishes; additionally the Atacama Compact Array [ACA; Iguchi et al., 2009] observes in an especially compact configuration using an additional 12 7 m dishes and 4 12 m dishes. The observatory is run





Figure 2.6: Aerial view of ALMA antennae, the cluster of smaller antennae is the Atacama Compact Array. [Image credit: Clem & Adri Bacri-Normier (wingsforscience.com)/ESO]

by a partnership of countries from Europe, the USA, Canada, Japan, South Korea, Taiwan and Chile and cost over a billion US dollars to construct. It began observing in 2011 and reached full operational status in 2013. An aerial view of some of ALMA's antennae is presented in Figure 2.6

### 2.2.1 The basis of interferometry

As an interferometer, ALMA relies on the physics of interference, the construction and destruction of the amplitude of coincident photons on the basis of their phase.

To begin with we will define a couple of coordinate systems. First, we will define a 2-dimensional spatial distribution of the intensity of an astronomical object on the sky, we will call this  $T(l, m)$ , where  $l$  and  $m$  are our orthogonal spatial axes whose units are radians, these are angular coordinates. The  $l, m$  plane is the 'plane of the sky' as commonly understood by astronomers, i.e. it is perpendicular to the line of sight. To clarify, at a position of  $l$  along one spatial axis and  $m$  along another, a point will have a given intensity, i.e. a brightness. Our second system we define as  $V(u, v)$  and we call 'visibility space'. The values at  $V(u, v)$ , we call *visibilities*. The orthogonal visibility axes  $u$  and  $v$  have units of  $\text{radians}^{-1}$ , although we commonly measure 'baseline' vectors  $\mathbf{b}$  within them in units of



wavelengths for convenience/by convention. Technically, these units of wavelengths must at some point be converted back into units of radians<sup>-1</sup>, through multiplication of a factor  $1/\lambda \text{ rad}^{-1}$ , where  $\lambda$  is the wavelength of the light being observed. A visibility point at a given  $u$  and  $v$ ,  $V(u, v)$ , is a complex number with an amplitude and phase/real and imaginary part. We will develop our understanding of  $V(u, v)$  as we go along.

If we imagine an astronomical point source in the sky, at some  $l, m$ , emitting light of angular frequency  $\omega$  and wavelength  $\lambda$  that eventually reaches Earth, that light takes a certain amount of time to reach a radio receiver here on Earth. The source is sufficiently far away that we can treat the light it emits as parallel wavefronts. If we have a second nearby receiver, that wavefront takes slightly longer to arrive due to a slight difference in path length. The wavefront travels for an extra time  $\tau_g$ . A receiver will measure the electromagnetic signal from this light, varying with time  $t$  as the light wave naturally oscillates. In ALMA's dishes, this signal is digitised into a voltage. We'll call the signal to the first receiver  $V_1$  and  $V_1 = V \cos(\omega t)$ , the signal to the second slightly more distant receiver is  $V_2 = V \cos(\omega(t - \tau_g))$ . The important measurement we want to make is the combination of the signals from the two receivers to see how they interfere. ALMA does this through multiplication in a supercomputer called the 'correlator'. After this multiplication we have a combined interfered signal  $V_1 V_2 = V^2 \cos(\omega t) \cos(\omega(t - \tau_g))$ . Using the trigonometric theorem  $\cos(a) \cos(b) = \frac{\cos(a+b) + \cos(a-b)}{2}$  we can split this into  $V_1 V_2 = \frac{V^2}{2} (\cos(\omega(2t - \tau_g)) + \cos(\omega(\tau_g)))$ . The signals are also averaged over a short time period so the  $\cos(\omega(2t - \tau_g))$  averages to zero, and we have an output signal, which we will call  $R_c$ ,  $R_c = \frac{V^2}{2} \cos(\omega \tau_g)$ . This setup is displayed in Figure 2.7.

The vector separation between two receivers we call a *baseline*,  $\mathbf{b}$ , which we measure in units of wavelengths of the light observed. If  $\hat{\mathbf{s}}$  is the unit vector describing the direction of the object in the sky and  $\mathbf{b}$  is our baseline vector, the extra distance travelled by the light to reach the second receiver is  $\mathbf{b} \cdot \hat{\mathbf{s}}$ . This means  $\tau_g = \frac{\mathbf{b} \cdot \hat{\mathbf{s}}}{c}$ , where  $c$  is the speed of light. It then follows that  $\omega \tau_g = 2\pi \frac{\mathbf{b} \cdot \hat{\mathbf{s}}}{\lambda}$  and we get the equation for the 'cosine correlation'  $R_c$ :

$$R_c = \frac{V^2}{2} \cos\left(2\pi \frac{\mathbf{b} \cdot \hat{\mathbf{s}}}{\lambda}\right) \quad (2.7)$$

So we can see that this measurement varies with baseline and the wavelength observed, and also the position of the object in the sky. The value of  $R_c$  varying with position is demonstrated in the top of Figure 2.8, and the value varying with baseline is demonstrated in the bottom of Figure 2.8.

The field of view (FOV) on the sky of an interferometer is set by the diameter of the individual dishes and the wavelength of observation, this is connected to the idea of the diffraction limit. The profile of the field of view, called the 'Primary Beam', is approximately Gaussian in shape and is normally defined by its Full Width at Half Maximum (FWHM).

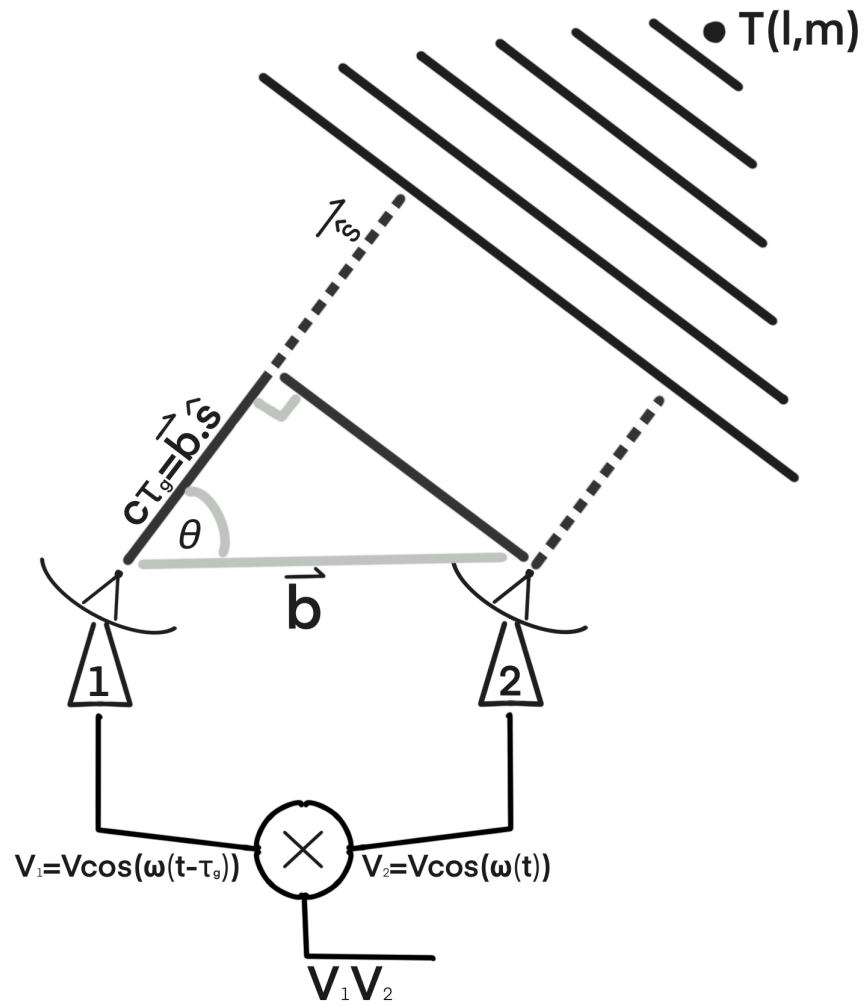


Figure 2.7: Schematic of a two-receiver interferometer measuring a path difference in light received from a distant point source.

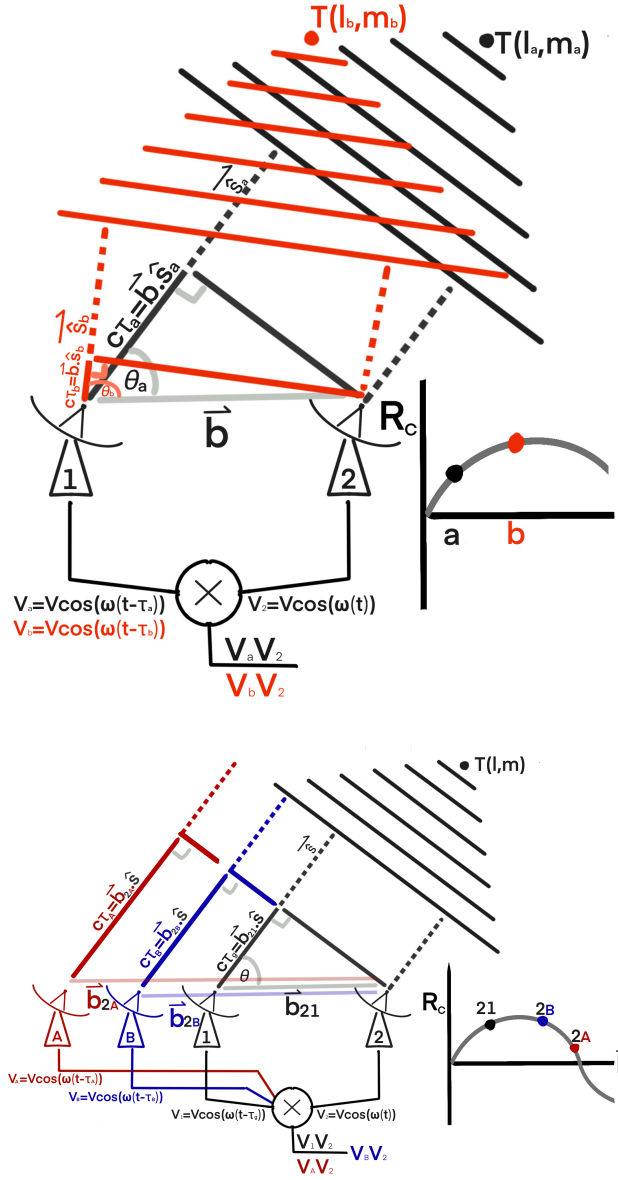


Figure 2.8: Top: Due to the change in extra path length changing the time delay  $\tau_g$ , the value of  $R_c$  varies between an observation of a source at  $T(l_a, m_a)$  in black and a source at  $T(l_b, m_b)$  in red. Bottom: Due to the change in baseline changing the time delay  $\tau_g$ , the value of  $R_c$  varies between an observation of a source using the short baseline  $\vec{b}_{21}$  in black, the medium baseline  $\vec{b}_{2B}$  in blue and the long baseline  $\vec{b}_{2A}$  in red.

For ALMA's 12 m dishes the FWHM of the primary beam is 21 arcseconds when observing at a wavelength of 1 mm, this is displayed in Figure 2.9 centre.

For a single baseline we can imagine a response to a source within the field of view as a set of fringes projected onto the sky, the fringes being described by the cosine in Equation 2.7. These fringes before the application of the primary beam are displayed in Figure 2.9 top and these fringes after the effect of the primary beam is applied is displayed in Figure 2.9 bottom.

The total signal received by a single baseline observing an extended source on the sky is proportional to the integral of this response multiplied by the entire sky brightness distribution, where we have substituted  $T(l, m)$  for a form as a function of  $\hat{s}$ ,  $T(\hat{s})$ , and where  $\Omega$  is the solid angle on the sky to be integrated over :

$$R_c = \int T(\hat{s}) \cos \left( 2\pi \frac{\mathbf{b} \cdot \hat{s}}{\lambda} \right) d\Omega \quad (2.8)$$

There are additional factors that account for instrumental response (e.g. the effective area of the receivers) and bandwidth that we will omit for brevity. Typically we want to centre the 'phase' of the fringes so that we have a maximum response at the centre of the FOV where the primary beam response is also strongest. We can introduce an artificial time delay  $\tau_0$  into the signal to shift the fringe pattern on the sky in order to centre it. ALMA simultaneously observes at multiple wavelengths over a bandpass that each have different fringe patterns. There is a singular 'phase centre' where all wavelengths of observation have a peak response that we can 'point' towards the centre of the FOV by setting  $\tau_0 \approx \tau_g$ . This idea is displayed in Figure 2.10.

From this point we can also define what makes something 'resolved'. For multiple point sources or an extended source, the light emitted from different locations is incoherent with the rest of the emission, i.e. the signals received originating from spatially separated emission do not interfere coherently and the total signal measured is the sum of the signals from all sources after they have interfered with only themselves.

If we have two equally bright point sources very close to each other, they could both reside within the same first peak of the fringes and would thus be indistinguishable from a single point source of greater brightness. This is shown in the top left of Figure 2.11.

If we can also vary our baseline to make it longer, with correspondingly higher frequency fringes, as soon as one source resides in a peak and the next in a trough of the fringes the signals would cancel to zero in the integration and we would be able to tell that there must be two separate sources. The sources are now resolved. This is shown in the top right of Figure 2.11. Mathematically, something is resolved when its angular scale  $\Delta\theta = \lambda/2b$ ; compare this to the Rayleigh criterion for resolution  $\Delta\theta = 1.22\lambda/D$  and we can see the increased performance of interferometry.

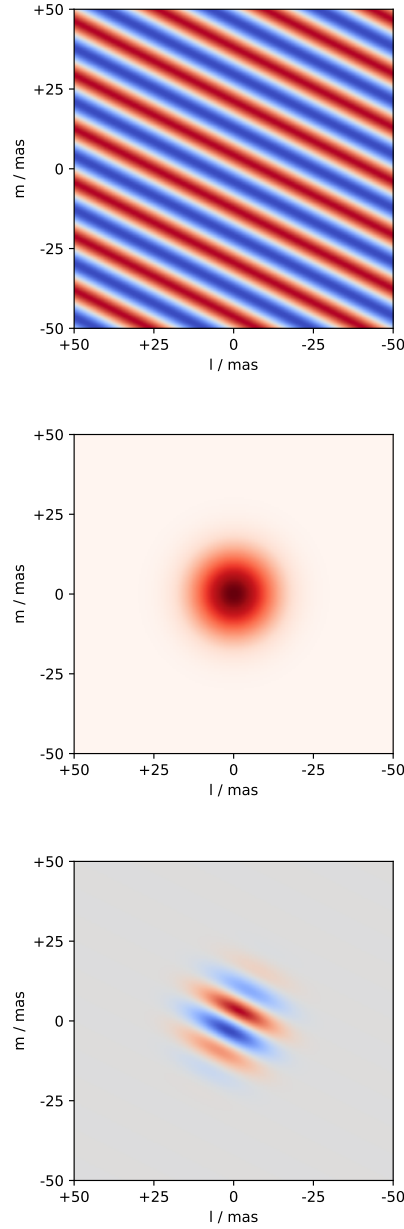


Figure 2.9: Top: The response to a source of a single baseline interferometer shown as a fringe pattern projected onto the sky. Centre: the primary beam response on the sky for ALMA's 12 m dishes. The FWHM is 21 arcseconds and response quickly drops beyond this, effectively limiting the 'useful' FOV to the primary beam FWHM. Bottom: the fringe pattern projected onto the sky after the application of a primary beam response. The value at the fringe peak in red is +1 and the value at the fringe trough in blue is  $-1$ .

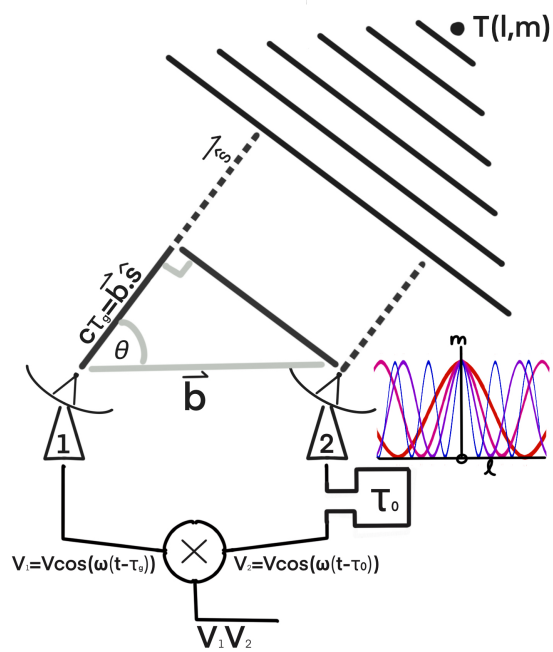


Figure 2.10: Schematic of a two-receiver interferometer measuring a path difference in light received from a distant point source with the inclusion of a time delay  $\tau_0$  to one of the signals. Also shown is the alignment of the fringes of multiple wavelengths of light on a single phase centre in one dimension.

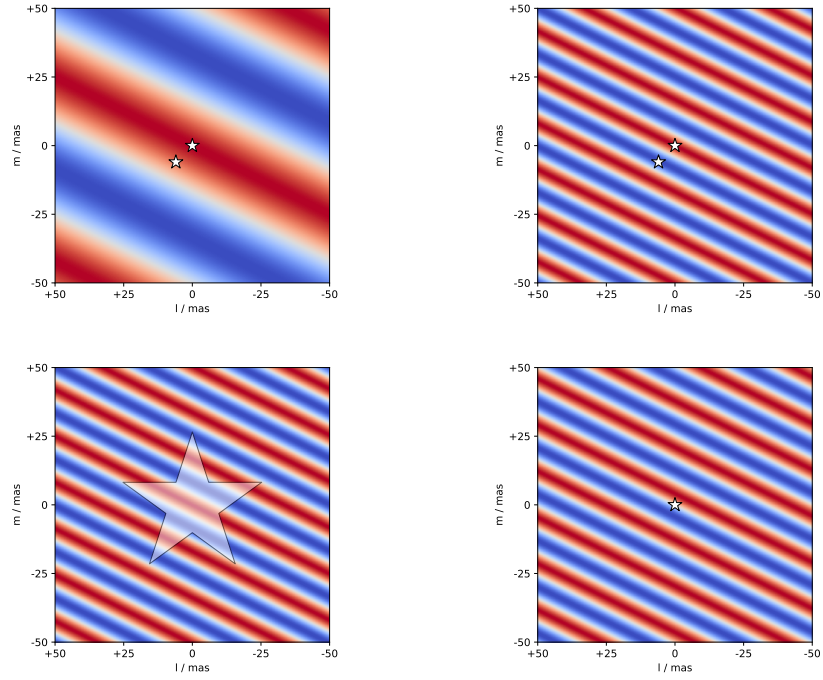


Figure 2.11: Top left: two point sources on the sky both reside within the same peak. Over the integration the total signal is positive and indistinguishable from a single bright point source. Top right: if we also have access to longer baselines, and so higher spatial frequency fringes on the sky, we can reach a point where one source resides in a peak and the other a trough. Over integration the total signal is zero and we have resolved the sources. Bottom left: as the signal of a large source is spread over several peaks and troughs, over integration the signal self-cancels and most of the flux of the source is lost. Bottom right: If a single point source resides in at a zero in the fringe, the integration returns zero signal. Shifting the fringes by a quarter wavelength would bring the source onto a peak and return a signal, and so both a sinusoidal and cosinusoidal fringe pattern are used together to ensure detection.

With an extended source, we can see the issue of ‘resolving out’ in the bottom left of Figure 2.11. Here the flux is spread across multiple peaks and troughs of the fringes, and much of the signal is lost upon integration.

If we look at the bottom right of Figure 2.11 we see that if the receivers and phase centre are not precisely pointed with a target point source at a central peak, the measurement this baseline makes could be zero. If we shift the phase of the fringes by  $90^\circ$ , we recover it. Such that we do not miss these ‘odd components’ of sources, we extend our measurement to also always include a second  $90^\circ$  shifted component. Mathematically we have an equation for the ‘sine correlation’,  $R_s$ :

$$R_s = \int T(\hat{\mathbf{s}}) \sin\left(2\pi \frac{\mathbf{b} \cdot \hat{\mathbf{s}}}{\lambda}\right) d\Omega \quad (2.9)$$

with which we will define an equation for the ‘complex correlation’  $\underline{C}$  for baseline  $\mathbf{b}$ :

$$\underline{C} = R_c - iR_s \quad (2.10)$$

or more fully:

$$\underline{C} = \int T(\hat{\mathbf{s}}) \left( \cos\left(2\pi \frac{\mathbf{b} \cdot \hat{\mathbf{s}}}{\lambda}\right) - i \sin\left(2\pi \frac{\mathbf{b} \cdot \hat{\mathbf{s}}}{\lambda}\right) \right) d\Omega \quad (2.11)$$

We should recognise an opportunity to use Euler’s formula ( $e^{ix} = \cos x + i \sin x$ ), to get:

$$\underline{C} = \int T(\hat{\mathbf{s}}) e^{-i2\pi \left(\frac{\mathbf{b}}{\lambda} \cdot \hat{\mathbf{s}}\right)} d\Omega \quad (2.12)$$

We remember that  $\hat{\mathbf{s}}$  is a unit vector whose direction is defined by the position of the source on the sky  $l, m$ , with an angle to the plane of  $\theta$ . Our coordinates  $T(l, m)$  are technically called ‘direction cosine coordinates’. The origin of the coordinate system  $T(l, m)$  is at the phase centre of the observation, which is usually also the centre of the field of view. This origin could be described by an origin vector  $\hat{\mathbf{s}}_0$  with an angle to the plane of the physical baseline of  $\theta_0$ . We can separate  $\hat{\mathbf{s}}$  into a component perpendicular to the  $l, m$  plane,  $\hat{\mathbf{s}}_0$ , and a component in the  $l, m$  plane that we will call  $\boldsymbol{\sigma}$  such that  $\hat{\mathbf{s}} = \hat{\mathbf{s}}_0 + \boldsymbol{\sigma}$ . As  $\hat{\mathbf{s}}$  and  $\hat{\mathbf{s}}_0$  are both unit vectors defined by angles from the ground,  $\boldsymbol{\sigma}$  is technically a projected angular distance on the sky. In the direction cosine coordinate system we are using,  $T(l, m)$ ,  $\boldsymbol{\sigma}$  is simply by definition the location of a source  $\begin{bmatrix} l \\ m \end{bmatrix}$ .

For a given observation phase centre,  $\hat{\mathbf{s}}_0$  is constant, and so we rewrite Equation 2.12:

$$\underline{C} = e^{-i2\pi \left(\frac{\mathbf{b}}{\lambda} \cdot \hat{\mathbf{s}}_0\right)} \int T(\boldsymbol{\sigma}) e^{-i2\pi \left(\frac{\mathbf{b}}{\lambda} \cdot \boldsymbol{\sigma}\right)} d\Omega \quad (2.13)$$

where  $e^{-i2\pi \left(\frac{\mathbf{b}}{\lambda} \cdot \hat{\mathbf{s}}_0\right)}$  is now a constant factor dependent on the chosen phase centre defined by



$\hat{\mathbf{s}}_0$ . We can now introduce the equation for a measured visibility,  $V(u, v)$ :

$$V(u, v) = e^{i2\pi(\frac{\mathbf{b}}{\lambda} \cdot \hat{\mathbf{s}}_0)} \underline{C} \quad (2.14)$$

such that:

$$V(u, v) = \int T(\boldsymbol{\sigma}) e^{-i2\pi(\frac{\mathbf{b}}{\lambda} \cdot \boldsymbol{\sigma})} d\Omega \quad (2.15)$$

A baseline is directly related to our visibility coordinates  $u$  and  $v$ . The  $u, v$  plane is parallel to the  $l, m$  plane and the projection of a physical baseline vector  $\mathbf{b}$  onto this plane corresponds to the vector  $\begin{bmatrix} u \\ v \end{bmatrix}$ . These planes and their relation to a physical baseline are shown in Figure 2.12. If the receivers were observing a source directly above them, the plane of the physical telescope baselines would also be parallel to the  $u, v$  and  $l, m$  planes, and no projection is needed. In this case if we place one receiver 500,000 wavelengths (500 kilolambda, 500 k $\lambda$ ), north and 100 k $\lambda$  east of a second receiver, the measurement those two make when they combine their signals corresponds to the point at  $V(500\text{k}\lambda, 100\text{k}\lambda)$  in visibility space. Important to note is that to place a telescope north and east of another is equally to place a telescope south and west of another, and so in this case we have also measured the visibility at  $V(-500\text{k}\lambda, -100\text{k}\lambda)$ .

The dot product of  $\mathbf{b}$  and  $\boldsymbol{\sigma}$  will naturally project  $\mathbf{b}$  onto the  $u, v$  plane, as  $\boldsymbol{\sigma}$  resides in the  $l, m$  plane that is parallel to the  $u, v$  plane. We also earlier stated that we chose  $u, v$  to be measured in units of  $\text{rad}^{-1}$ , so our baseline in terms of distance  $\mathbf{b}$  must be converted by dividing through by  $\lambda$ . And so we can now resolve the dot product from the exponent of Equation 2.15:

$$\frac{\mathbf{b}}{\lambda} \cdot \boldsymbol{\sigma} = \begin{bmatrix} u \\ v \end{bmatrix} \cdot \begin{bmatrix} l \\ m \end{bmatrix} = ul + vm \quad (2.16)$$

After converting back from functions of  $\boldsymbol{\sigma}$  to functions of  $l, m$  and going back from integrating with respect to  $\Omega$  to integrating with respect to  $l$  and  $m$ , and inserting Equation 2.16 into Equation 2.15, we finally have:

$$V(u, v) = \int \int T(l, m) e^{-i2\pi(ul+vm)} dl dm \quad (2.17)$$

The equation might look familiar at this point. We make the startling realisation that our visibilities  $V$  measured by the interferometer are simply the *Fourier transform* of the sky intensity distribution  $T$ :

$$V(u, v) \xleftrightarrow{\mathcal{F}} T(l, m) \quad (2.18)$$

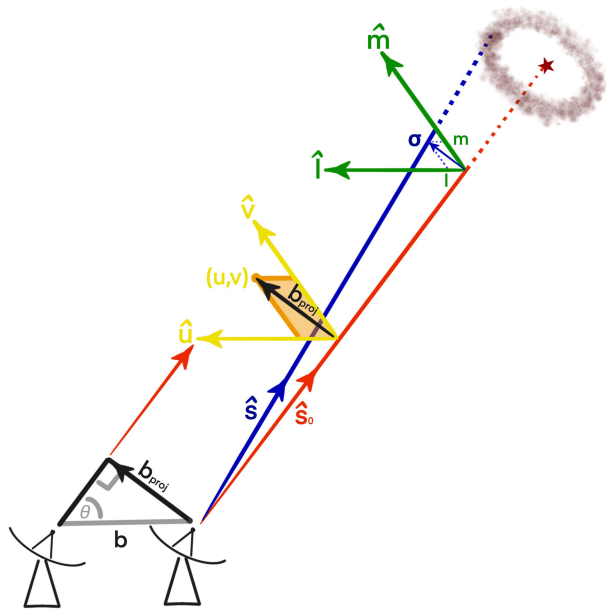


Figure 2.12: Schematic of the  $l, m$  and  $u, v$  planes in relation to the sky and a physical baseline. A point on the sky is located at  $l, m$  and is described by the vector  $\boldsymbol{\sigma}$ , the projection of the vector  $\hat{\mathbf{s}}$  onto the  $l, m$  plane. A physical baseline between two receivers has baseline vector  $\mathbf{b}$  that is projected onto the  $u, v$  plane to point  $u, v$ . The  $l, m$  and  $u, v$  planes are parallel.

explicitly:

$$\begin{aligned} V(u, v) &= \int \int T(l, m) e^{-i2\pi(ul+vm)} dl dm \\ T(l, m) &= \int \int V(u, v) e^{+i2\pi(ul+vm)} du dv \end{aligned} \quad (2.19)$$

The above mathematics are not entirely rigorous, but the derivation can be found in more detail at [https://ratt-ru.github.io/fundamentals\\_of\\_interferometry](https://ratt-ru.github.io/fundamentals_of_interferometry) and the general relationship that the intensity distribution of a distant incoherent source is a Fourier transform of its interferometric visibility is proven by the van Cittert-Zernike theorem [van Cittert, 1934; Zernike, 1938].

We can look at all of this in another way.  $V(u, v)$  is the Fourier transform of  $T(l, m)$ , and so  $T(l, m)$  is the sum of the contributions of all the spatial frequencies described by  $V(u, v)$ . A single baseline acts as a mask in the Fourier plane, or a spatial filter. What is then measured from a single baseline is how much that single spatial frequency the baseline represents contributes to the overall structure of  $T(l, m)$ .

The entire process seems convoluted, and it is important to regain sight of the fundamental use case. What we can achieve through the use of interferometry and two-receiver baselines is sensitivity to resolution scales smaller than the individual dishes are capable of alone. By using a baseline **b** comprised from two small aperture receivers we can resolve the sky on the scale that would have otherwise required a single, unfeasibly large aperture diffraction-limited receiver of diameter **b**. With two small receivers we have *synthesised* a larger receiver and circumvented the diffraction limit. This idea is called *aperture synthesis*.

To continue we must now discuss the general properties of Fourier transforms.

## 2.2.2 Fourier transforms

### One-dimensional Fourier transforms

A Fourier transform generally decomposes a signal into the frequencies of the underlying cosinusoidal/sinusoidal waves that comprise it. For example, a sound signal can be transformed into the amplitudes of its constituent notes. In such a case, the *amplitude* of the signal over *time* have been transformed into the *amplitude* of its *frequencies*. Analogously, a distribution of *intensity* across a *space* can be Fourier transformed into the *amplitude* of the *spatial frequencies* of the waves that sum to create it. This concept is displayed simply in Figure 2.13.

A Fourier transform produces a complex result: the frequencies have a real and

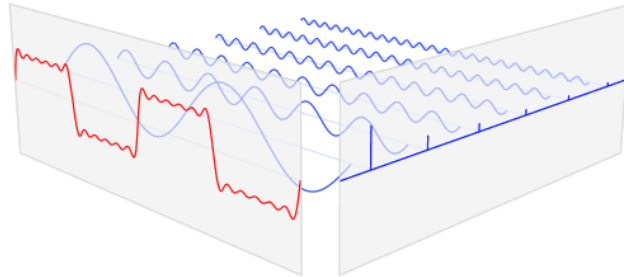


Figure 2.13: Graphic displaying two complementary Fourier domains that could be e.g. *time & frequency* or *space & spatial frequency* plotted on the left and right x-axes respectively with amplitude on the y-axes. On the left in red a one-dimensional waveform is plotted, and on the right in blue are the frequencies that constitute it. In the centre in blue are the individual waves represented by each frequency that when summed produce the red waveform. [This image was taken from Wikimedia commons having been released into the public domain].

imaginary component. In frequency space, point  $f$  has value  $(a + bi)$ . The real part describes the shape of the signal and the imaginary part describes the location. For a single frequency  $f$ , the imaginary component describes whether or not the sinusoidal wave is peaked, troughed or in between at the origin. Or alternatively, the real part describes how cosinusoidal the wave is and the imaginary part describes how sinusoidal it is. If we extend the frequency axes into negative numbers, a ‘positive’ frequency  $f$  and a hypothetical ‘negative’ frequency  $-f$  describe the same wavelength wave, and so the Fourier transform of a signal is also mirrored about the origin, however the mirror ‘negative’ frequency’s value will be the complex conjugate of the positive’s, to account for the opposite phase. This is called Hermitian symmetry and is always true if the original signal is purely real.

Some basic transform relationships are: a constant transforms to a delta function, a top-hat distribution transforms into a sinc function, a thin Gaussian transforms to a wide Gaussian, as seen in Figure 2.14.

Additionally, if we have two functions  $g(x)$  and  $h(x)$  with respective Fourier transforms  $G(t)$  and  $H(t)$ , the convolution theorem states that the Fourier transform of  $G(t) \times H(t)$

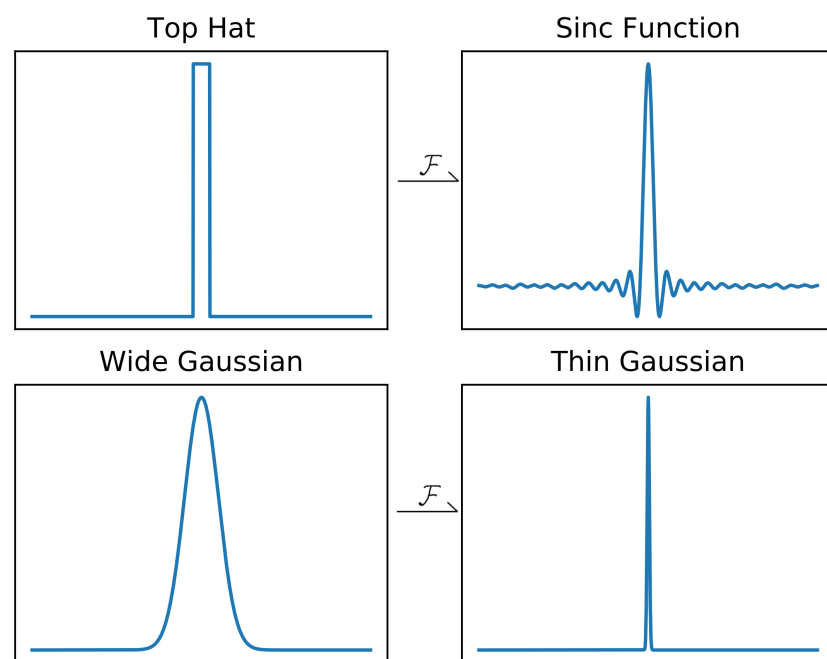


Figure 2.14: A top hat is Fourier transformed to a sinc function and a wide Gaussian is Fourier transformed into a thin Gaussian.

is equal to the *convolution* of  $g(x)$  and  $h(x)$ .

$$\begin{aligned}
g(x) &\xrightarrow{\mathcal{F}} G(t) \\
h(x) &\xrightarrow{\mathcal{F}} H(t) \\
G(t) \times H(t) &\xrightarrow{\mathcal{F}} g(x) * h(x)
\end{aligned} \tag{2.20}$$

## Two-dimensional Fourier transforms and ALMA

These basic properties all extend into two dimensions, and in our space-time it is much easier to imagine a two-dimensional spatial intensity distribution than it is to imagine a two-dimensional temporal amplitude distribution. The spatial frequencies are our visibilities - a single baseline is a single point  $u, v$  in visibility space, measuring a single visibility  $V(u, v)$ - and they describe the amplitude of composite spatial frequencies, their phase (i.e. their value at the origin or cosinusoidal/sinusoidal quality) and now their *direction*. The distance from the origin, i.e. the length of the baseline, describes the frequency of the spatial wave; the absolute value at the specific point in  $u, v$  space, i.e. the combined signal measured by the receivers of a baseline, describes the intensity or the wave; the imaginary component relative to the real component of the value describes the wave's phase; the orientation of the baseline, its angle from a given axis/its argument, describes the direction of the wave in real space. A constant still transforms to a delta function, a 2-d Gaussian transforms to a 2-d Gaussian, and a uniform disc (a 2-d top hat) transforms to a Bessel function (a 2-d sinc function) as shown in Figure 2.15.

Any image, as images are essentially 2-d intensity distributions, can be Fourier transformed into its component spatial frequencies. The sum of all the spatial waves the spatial frequencies describe recreates the image.

A  $u, v$  point, a visibility  $V(u, v)$ , which has the value  $(a + bi)$ , in any given quadrant describes the same spatial frequency as a  $u, v$  point in the opposite quadrant, at  $-u, -v$ . A wave pointed in a certain direction is indistinguishable from a wave pointed in the exact opposite direction. If the first wave is not symmetrical about the origin, i.e.  $b$  is non-zero, then for the wave described by  $V(u, v)$  to have a totally identical spatial distribution to the wave described by  $V(-u, -v)$ , the wave described by  $V(-u, -v)$  must have an oppositely valued phase. These relationships are shown in Figure 2.16. In other words, if visibility  $V(u, v)$  has value  $(a + bi)$ , visibility  $V(-u, -v)$  must have value  $(a - bi)$ , the two are complex conjugates - this is the Hermitian symmetry again and holds as the sky distribution of intensity is purely real. This also harkens back to when we stated "*that to place a telescope north and east of another is equally to place a telescope south and west of another*". When we measure the signal from a single physical telescope baseline, we actually get out a pair

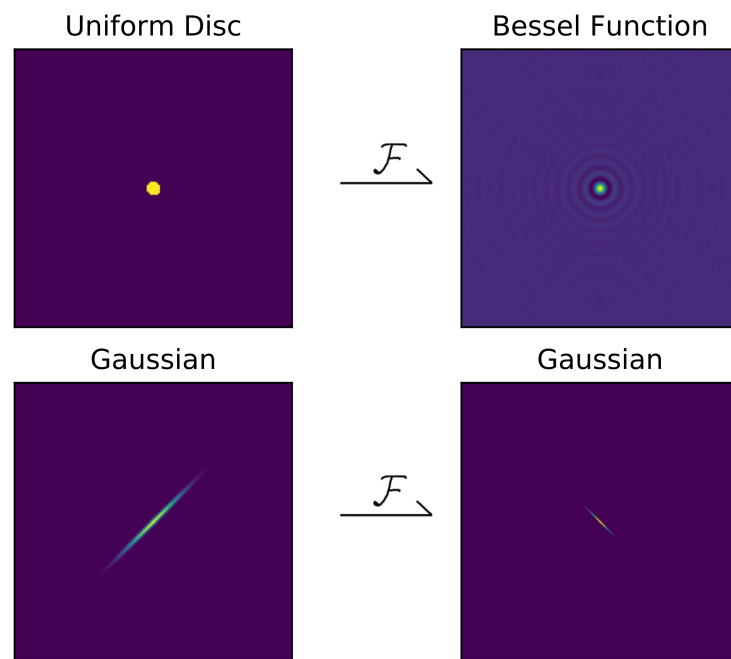


Figure 2.15: A uniform disc is Fourier transformed to a Bessel function and a Gaussian is Fourier transformed into a Gaussian. When an elliptical Gaussian is transformed, an axis that was thin becomes wide and an axis that was wide becomes thin.

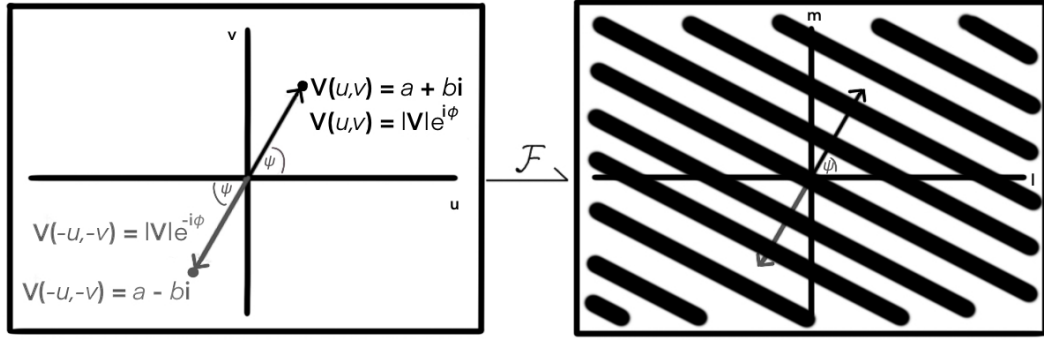


Figure 2.16: A graphic showing the relationship between Left: a visibility  $V(u, v)$  with value  $(a + bi)$ , or with value in alternative notation as  $|V|e^{i\phi}$  and Right: the spatial wave it describes. Also shown in grey is the Hermitian conjugate  $V(-u, -v)$  with oppositely phased value  $(a - bi)$  that describes the same wave. The magnitude of the visibility  $|V|$  describes the amplitude of the spatial wave; the phase of the visibility  $\phi$  describes the phase of the spatial wave at the origin; the magnitude of the visibility coordinates  $|u, v|$  describes the wavelength of the spatial wave and the angle from the origin to the visibility coordinates  $\psi$  describes the wave's direction.

of visibilities, although they are entirely dependent and so redundant.

Long baselines, at distant  $u, v$  coordinates in visibility space, describe high frequency waves, and short baselines describes low frequency waves. High frequency waves/long baseline measurements describe the fine structure of an image/intensity distribution and allow us to resolve detail, whereas low frequency waves/short baseline measurements describe the large scale flux of the distribution. This is readily seen when the frequencies are filtered as per Figure 2.17. If we do not have *coverage* of the whole visibility plane, the full image is not recovered, but still retains valuable and recognisable information.

What is less intuitive, is that large swathes of the visibilities can be lost while still transforming back to a recognisably meaningful image. The visibility space can be relatively sparsely sampled and still provide a useful output, detail and flux will always be lost but meaningful science can be still extracted. When physically constructing an interferometer, it is naturally impossible to construct every possible baseline and sample the full visibility space,  $N$  individual dishes only result in  $N(N - 1)/2$  baselines. ALMA's main array comprises 50 dishes, and so at any one time there is a theoretically a maximum of 1225 baselines, although not every receiver is active at once in practice. These baselines also measure the Hermitian conjugate visibilities and so we have double the measurements, but our coverage of  $u, v$  space is still lacking. Fortunately there is a secret weapon. We stated that the  $u, v$  plane that the vector baselines reside on is parallel to the sky  $l, m$  plane. Another key feature is that these two planes must share a common frame of reference, they cannot be independently rotated. So what happens when the Earth naturally rotates during



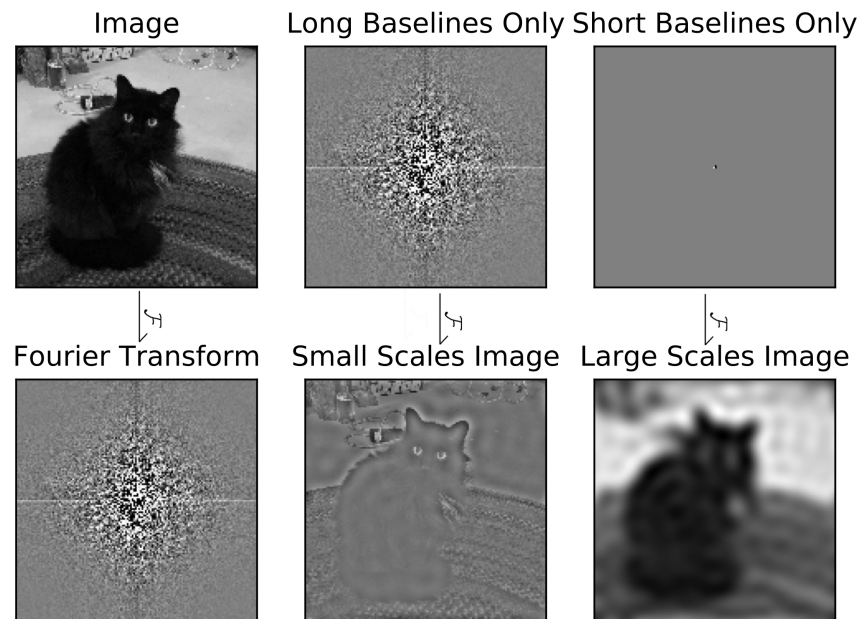


Figure 2.17: Demonstration of the difference in information carried by long and short baselines. Top left: the complete image before transformation. Bottom left: the complete Fourier transform of the complete image. Top middle: Fourier data after removal of short baseline data, the 400 central zeroed pixels are not readily discernible. Bottom middle: the inverse Fourier transform of the long baseline data, only the shortest spatial scales are preserved; edges are well defined but large scale flux information is lost. Top right: Fourier data after removal of long baseline data, the central non-zero pixels are barely discernible, comprising the central 400 of 5 million total pixels. Bottom right: the inverse Fourier transform of the short baseline data, only the large spatial scales are preserved; edges and small scale features are blurred but large scale flux is readily apparent.

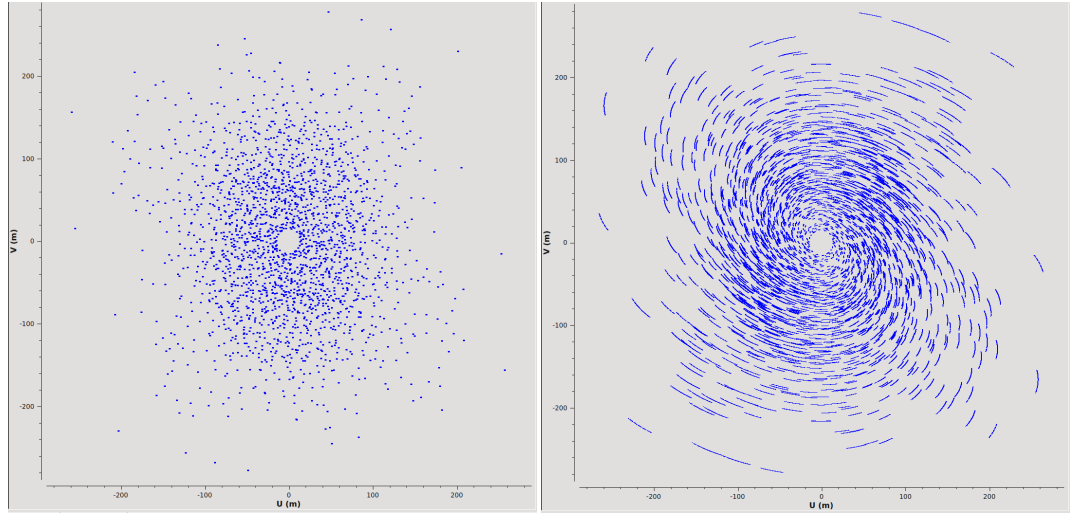


Figure 2.18: On the left are the measured visibilities after half a minute of ALMA observation. On the right are the measured visibilities after one hundred minutes of observation with significant rotation of the Earth, allowing more visibilities to be sampled.

its day/night cycle along with all the radio receivers? The receivers measure new baselines, baselines that are rotations of the previously measured ones. With increasing observation time, not only does individual photon count go up thus improving signal to noise as per a normal telescopes, but as the Earth rotates the  $u, v$  coverage increases as the physical baselines rotate in reference to the sky. This effect is sufficient to sample enough of the  $u, v$  space to be meaningful and is displayed in Figure 2.18.

Notably ALMA also has the capability of customising its baselines. Using two large transporter trucks ALMA can pick up and move its receivers to different locations to customise the baselines of its observations. As of the 2022-2023 Cycle 9 ALMA will have 10 defined configurations with maximum baselines ranging from 0.16-16.2 km.

No matter the configuration or observing time, the final sky image is always incomplete, it is called ‘*dirty*’, and its incompleteness is a function of the visibilities sampled. The measured visibilities are the multiplication of the full visibility space and the sampling function, all the measured baselines - effectively a spatial filter. Remembering the convolution theorem, Equation 2.20, we have that the *dirty* sky image is the convolution of the true sky distribution and *something*. This something is the *dirty beam* (also called the ‘synthesised beam’), the Fourier transform of the sampling function. The dirty beam is a point spread function applied to the image. These relationships are shown in Figure 2.19. If we know both the dirty image and the dirty beam, does that mean we can deconvolve back to retrieve the true sky image? No, as there are infinite solutions to a deconvolution. Just the same way that we cannot divide the measured visibilities by the sampling function to retrieve the full

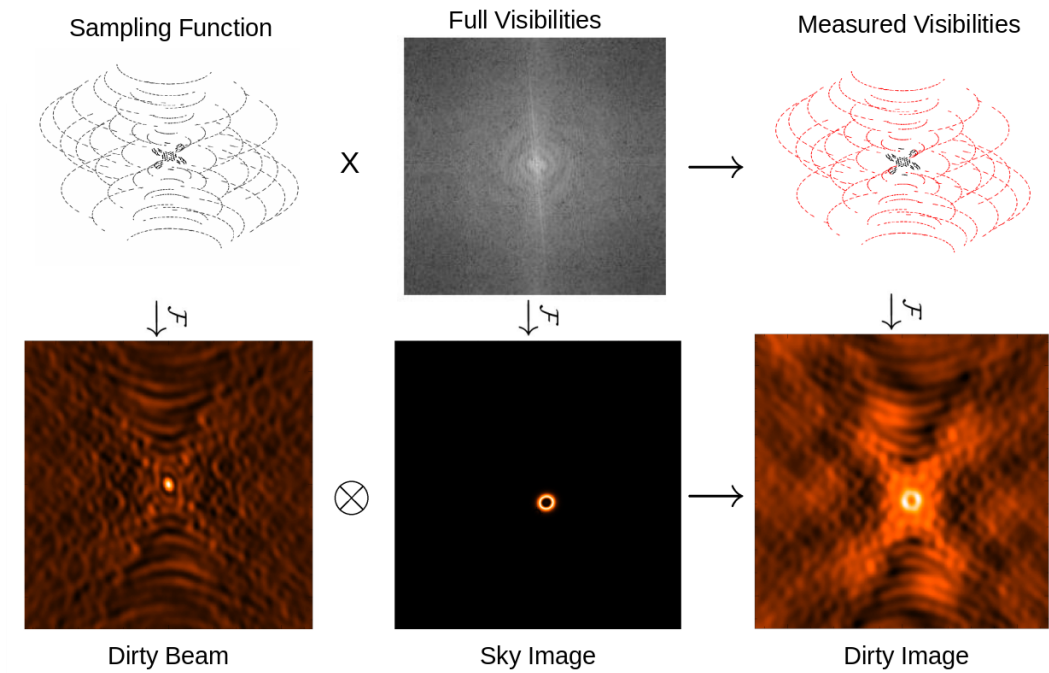


Figure 2.19: The relationships involved in creating a dirty image from measured visibilities. Top Left: The sampling function. This is defined by the telescope baselines and the length of the observation given the Earth’s rotation; these are the visibilities we will be able to sample. Top Middle: The perfect Fourier transform of the sky intensity distribution. This will be sampled by our sampling function; mathematically that operation is a multiplication. Top Right: The measured visibilities that constitute our Fourier space data. Bottom Left: The dirty beam. This is Fourier transform of the sampling function that effectively serves as a PSF for the sky intensity when producing an image. Bottom Middle: The perfect sky intensity distribution. When the dirty beam is applied as a PSF our measured result is the dirty image; mathematically this application is a convolution. Bottom Right: The dirty image. The Fourier transform of our measured visibility data and a ‘raw’ visualisation of our measurement of the sky intensity distribution. [Image credit: David Wilner].

visibilities, as this would involve dividing by an infinite number of zeroes.

That does not mean that we are totally helpless though.

## CLEAN

The CLEAN algorithm, originally published in Högbom [1974], is designed to extract a more accurate science image from the dirty image without requiring any additional information by assuming the brightest features in an image are physical and constructing a model from them. It comprises the following steps:

1. Identify the brightest pixel in the dirty image

2. Remove this pixel and place it in a separate model image
3. Convolve the model image with the dirty beam and subtract this from the original image, creating a *residual* image
4. Repeat upon the residual image until you think all physical emission has been modelled

We are effectively deconvolving through assumption. The PSF is strongest at its centre, and so the most intense parts of the dirty image are still most likely to be where physical emission is located. Subtracting the successive dirty model images removes the non-local effects the dirty beam, which is not a pure Gaussian, has on those most-likely-physical parts of the image, to allow us to have a clearer view of what remains in the residual for us to identify the next most likely physical emission. But when physical emission reaches levels similar to the noise, how can physical emission that we still wish to account for be distinguished from large noise peaks? Human input is still required, before employing the CLEAN algorithm, and between selected numbers of steps, the user selects regions of the dirty image for the algorithm to select model sources from. The user begins by themselves distinguishing what they think is physical emission. This is simple for resolved sources and/or when the user knows what they are looking for, but if in doubt the user can always not select a region and let the algorithm operate on the whole image as a check.

The cycle stops when the flux of brightest features of the image reaches some user predefined multiple of the image RMS or some fraction of the level of the brightest feature in the known noise region. At this point we have decided that we cannot distinguish between physical emission and noise.

The final model image is then reconvolved with a restoring ‘CLEAN’ beam, usually an elliptical Gaussian that has been fitted to the central response lobe of the dirty beam, to account for our fundamental resolution limits and to suppress high spatial frequency artifacts that the CLEAN algorithm can introduce. The FWHM of this final ‘CLEAN’ beam can be approximated as

$$\text{FWHM [arcsec]} = \frac{76}{\text{maximum baseline [km]} \times \text{frequency [GHz]}} \quad (2.21)$$

although as we will see we have further control over this.

The ultimate output of the CLEAN process is the final cleanly-convolved model added to the final residual, meaning we have accounted for as much of the ‘dirtiness’ due to our incomplete  $u, v$  coverage as reasonably possible.

This is not the end of the user input into producing science however. Again depending on what the user expects from the data, and typically experimented with just-in-case, the individual  $u, v$  visibilities can be weighted to enhance different spatial scales. Weighting

takes the form of multiplicative factors to the amplitudes of the individual visibility. These weighting factors  $R_i D_i T_i$  apply to the individual  $i^{th}$  visibilities  $V_i(u_i, v_i)$  to produce a new set of weighted visibilities  $V^W(u, v)$  after summing over all  $N$  visibilities:

$$V^W(u, v) = \sum_{i=1}^N R_i D_i T_i \delta(u - u_i, v - v_i) V_i(u_i, v_i) \quad (2.22)$$

where  $\delta(\dots)$  is the Dirac delta function. To begin with, all points have the ‘noise variance’ weighting factor  $R_i$  applied. The amplitudes of all visibilities  $u_i, v_i$  are divided by their variance  $\omega_i$ , explicitly: multiplied by a weight factor  $R_i = \omega_i = 1/\sigma_i^2$  and where  $\sigma_i$  is the RMS noise on the visibility  $u_i, v_i$ .

The next factor that can be optionally applied is a ‘density’ weight  $D_i$ . This is a factor proportional to the inverse of the local  $u, v$  point density. This factor accounts for the incomplete coverage of the  $u, v$  space and the tendency for there to be much fewer long baselines observed than shorter baselines. If no density weighting factor is applied, i.e.  $D_i = 1$ , the scheme is called *natural weighting* and provides the highest SNR images, as it downweights noisier baselines. ALMA’s configurations invariably have more short baselines than large baselines and so *natural weighting* also results in the largest beam/lowest resolution; in the sum of all weighted baselines the many shorter baselines (large scales in the final image) outweigh the few long baselines (fine details in the final image). Within the CASA software [McMullin et al., 2007] that is often used to process ALMA data, the  $u, v$  plane is gridded into cells with the  $u, v$  cell size equal to 2 over the FOV of the observation. More properly, the cell size is the size of the spatial frequency with a wavelength equal to  $2/\text{FOV}$ . The density weighting factor then normalises the individual visibilities by the total noise variance weight of visibilities in their given grid cell. *Uniform weighting* is the name for the direct application of this factor after the noise variance factor, explicitly here  $D_i = \frac{1}{W_i}$  where  $W_i$  is the total weight in the  $i^{th}$  cell over the total weight of all  $N$  visibilities:  $W_i = \frac{\sum_{cell=i} \omega_i}{\sum_n \omega_n}$ . This gives a total weight factor  $w_i$  for *uniform weighting* of  $w_i = \frac{\omega_i}{W_i}$ . *Uniform weighting* gives equal weight to short and long baselines as a whole, thus increasing the resolution and reduces the beam. However, as fewer long baselines are together given equal weight to more short baselines, this increase in resolution also necessarily comes with decreased SNR.

There is also the option to define a weighting scheme somewhere between these two extremes of *natural weighting* and *uniform weighting*, using a different  $D_i$  called *Briggs weighting* [Briggs, 1995; Briggs et al., 1999]. This has a slightly more complicated formalism but essentially involves a so-called ‘robust’ parameter  $R$  that controls how strongly weighted by  $u, v$  density the visibilities are. A robust parameter of  $R = -2.0$  will give weighting very similar to *uniform* and a robust parameter of  $R = 2.0$  will give weighting that is very close to *natural*. Using *Briggs weighting* and adjusting  $R$  allows one to find the

trade off between resolution and sensitivity that best suits one's observation and science.

The final possible weighting factor  $T_i$  is called the *uv taper* and is also optional. The *uv taper* is a Gaussian centred on the origin of the  $u, v$  space applied to all visibilities, thus downweighting longer baselines. A multiplicative Gaussian factor in  $u, v$  space is transformed to a convolution with a Gaussian in image space, and so this can also be seen as convolving the final image with a Gaussian, effectively smoothing the PSF. This will always reduce the resolution of the observation but increases sensitivity to extended emission and reduces artefacts caused by lack of coverage at long baselines.

There is one final-final step to producing a science image from which measurements can be taken. This is the 'primary beam correction'. Our primary beam, the response function of the receiver antennae themselves, defines our field of view but affects also our sensitivity in different parts of that field of view. Towards the centre, the response is stronger and our SNR is higher, near the edge of the field of view the response is weak and the noise grows. If flux or RMS measurements are being taken from an image, the primary beam must be taken into account. Applying this response function to the image is called 'primary beam correction' and takes the effect of decreasing the SNR at the edges of the field.

### **The data cube and CO**

As briefly mentioned already, ALMA simultaneously observes at a range of wavelengths. An ALMA observation has a general bandpass that is further split into four 'Spectral Windows' comprised of 'Channels' of optional width. On the general scale, ALMA has ten different receiver Bands of observation, from Band 3 capable of observing wavelengths between 2.6 – 3.6 mm (84 – 116 GHz) up to Band 10 capable of observing between 0.32 – 0.38 mm (787 – 960 GHz), with Bands 1 and 2 in construction and planning respectively. The Band chosen will affect the size of the beam and the receivers for the different Bands have differing sensitivities. Once a Band is chosen, the spectral windows must be selected. These windows typically have bandwidths of  $\sim 2$  GHz and must be centred somewhere in the bandwidth of the Band, thus not the entire bandwidth of a Band is actually observed at once. The windows are then split into channels, which define the spectral resolution of the observation. A spectral window that is not observing any particular spectral line, i.e. observing 'continuum' emission, will typically have 128 channels and a spectral window that is centred on a particular spectral line of interest may have up to 3840 channels.

When not observing specific spectral lines all the channels and windows can be summed to give a single two-dimensional continuum image of greater signal to noise. If this is not done, the output would instead be a three-dimensional data cube. However the process behind examining a spectral line in ALMA data is not so straightforward. First the average continuum flux per channel must be identified from the continuum data after

Table 2.1: The significant differentiating factors between ALMA Bands. All beam measurements are the FWHM of the resolution element using the same configuration: C3 with a maximum baseline of 0.5 km. Sensitivity measurements are taken from representative wavelengths within the bands that have maximum transmission as per Figure 2.20, with 30 minutes of on source integration time and with a precipitable water vapour (PWV) in the third Octile with a value of 0.913 mm. Disc flux represents the total flux at a wavelength in the centre of each Band for the archetypal M dwarf debris disc around AU Mic estimated from a modified blackbody model.

| Band | Frequency [GHz] | Wavelength [mm] | Beam ["] | Sensitivity [ $\mu$ Jy] | Disc Flux [mJy] |
|------|-----------------|-----------------|----------|-------------------------|-----------------|
| 3    | 84–116          | 2.6–3.6         | 1.52     | 13                      | 0.55            |
| 4    | 125–163         | 1.8–2.4         | 1.06     | 14                      | 2.2             |
| 5    | 163–211         | 1.4–1.8         | 0.81     | 18                      | 3.9             |
| 6    | 211–275         | 1.1–1.4         | 0.63     | 19                      | 6.5             |
| 7    | 275–373         | 0.8–1.1         | 0.47     | 28                      | 12              |
| 8    | 385–500         | 0.6–0.8         | 0.34     | 77                      | 21              |
| 9    | 602–702         | 0.4–0.5         | 0.23     | 245                     | 49              |
| 10   | 787–950         | 0.3–0.4         | 0.18     | 400                     | 78              |

masking out the region containing the spectral line. Then this ‘continuum background’ must be subtracted from the data, leaving only the spectral line flux. The channels that lie distant from the spectral line ought to be cut to save processing time, finally leaving a smaller cube centred on the spectral line containing only spectral line emission and noise, that is wide enough to safely contain any red-shifted and blue-shifted emission and some zero emission regions beyond for comparison.

ALMA observations of debris discs typically occur in Band 7, 0.8 – 1.1 mm (275 – 373 GHz), or Band 6, 1.1 – 1.4 mm (211 – 275 GHz), for several reasons. Firstly, these wavelengths provide a good middle ground between good resolution and good sensitivity to the disc sizes and fluxes expected from debris discs. These wavelengths sample the Rayleigh-Jeans tail of the blackbody emission of bodies of temperatures of around 10 – 100 K, the temperatures expected in debris discs. Of importance is the transmission of the atmosphere at ALMA’s wavelengths; even at such an elevation ALMA contends with atmospheric windows. Band 7 has generally high transmission, and so more signal is recovered, but individual spectral windows much be chosen to avoid the large drop in transmission at the centre of the band as seen in Figure 2.20. Secondly, these wavelengths sample wavelengths much longer than previous telescopes were capable of, providing a complement to previous data where it exists. Finally, these Bands contain the most significant debris disc spectral lines: the CO J=3-2 and CO J=2-1 transitions. On a less scientific note, these Bands can be less competitive for telescope proposals than Bands 8 and 9 and so using them can result in

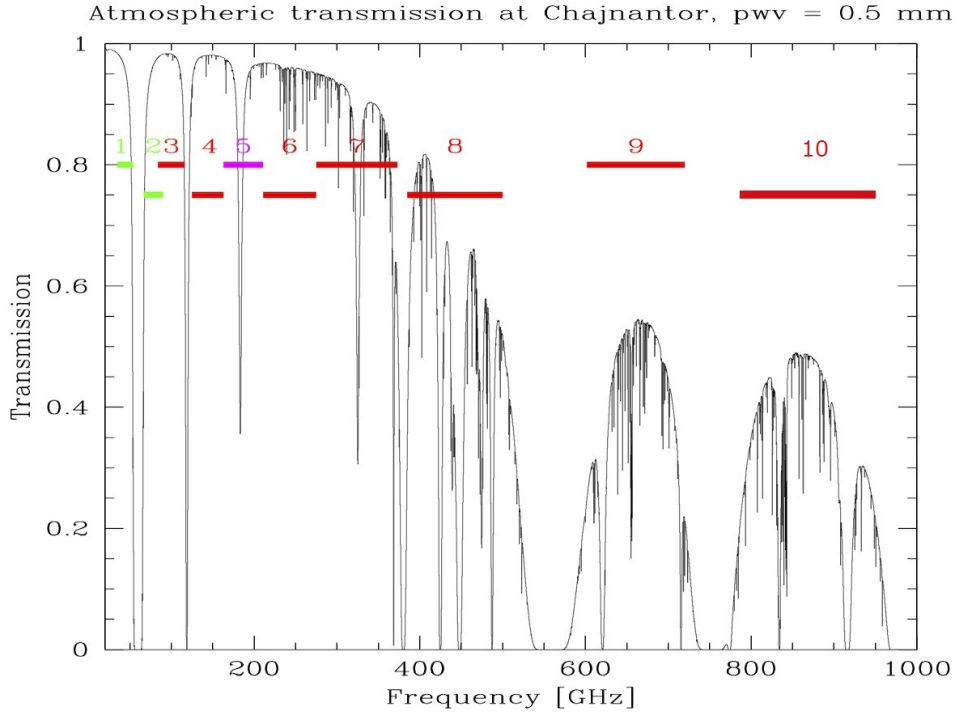


Figure 2.20: Atmospheric transmission in the frequency range of ALMA's observations. The transmission can be significantly different for different Bands as well as within a band due to specific atmospheric absorption features. Taken from ALMA cycle 5 technical handbook, <https://almascience.nrao.edu/documents-and-tools/cycle-5-docs>.

more observation time.

Even if CO is present, the observation might not be directly sensitive enough to detect it, but there is a nifty workaround that can increase the SNR of any present CO emission: spectro-spatial filtering [Matrà et al., 2015]. In a resolved debris disc that is not face-on it is expected that in either ansa of the disc any CO emission will be red or blue shifted, this shifting moves the associated emission into the channels either side of the central spectral line channel depending on the location in the disc and expected velocity of the gas relative to the line of sight. If we have an accurate approximation for the host star's mass and the disc's inclination, then we can directly predict the velocity of the gas in the disc and so we can also predict how shifted the gas emission ought to be at each part of the disc/pixel of the image, aside from the degeneracy in which side is rotating towards us. With this prediction in hand we can then identify across the cube each pixel in which we expect there to be emission and then manually move each such pixel into a single channel. If no emission is still apparent, the pixels in this new channel that we know reside within the discs' bounds from the resolved continuum image can be summed to maximise signal.



This treatment enhances the SNR more than a simple sum over all the expected channels (called the ‘moment 0’ map) as empty pixels and their noise are discarded in spectro-spatial filtering. This produces two final spectra, one for each rotation direction of the disc, that can be compared to each other and an unshifted spectrum to identify whether a signal has been recovered.

### Disc modelling and Markov chain Monte Carlo

When we have a final CLEAN science image of a resolved or partially resolved disc we could take geometric measurements of the disc’s radius, flux, inclination, position angle etc. These measurements can be helpful guides and sanity checks but depending on the image these properties may be difficult to judge, they will not provide probability distributions for the range of possible parameters given the signal, and ultimately do not exploit ALMA’s true capabilities. The more rigorous methodology would be to create a range of models and fit them directly to the visibilities such that all the data is used and without any of the potentially muddying steps of the CLEAN algorithm.

To begin with we want to choose a disc model: how many rings are there, do the rings have Gaussian/top-hat/power-law profiles, do we want to give them a height or just a width, can the ring be offset from the star, etc. With a particular disc model selected that is defined by a certain set of parameters, we can generate a model after giving values to those parameters. We can then predict how this model would appear two-dimensionally on the sky. Next we can Fourier transfer this model sky intensity distribution to produce a set of model visibilities, then we can sample these model visibilities at the baselines that ALMA observed to directly compare model visibilities with observed visibilities and calculate a  $\chi^2$ . A  $\chi^2$  is a statistical measure of how well a model fits a data usually calculated as a variation on summing the squares of the differences between each individual observed data point and model point. In my work this is performed by the GALARIO package [Tazzari et al., 2018]. In GALARIO the  $\chi^2$  is calculated as:

$$\chi^2 = \sum_{i=1}^{N_{vis}} w_i \times [(ReV_{obs\ i} - ReV_{mod\ i})^2 + (ImV_{obs\ i} - ImV_{mod\ i})^2] \quad (2.23)$$

With a way to generate a  $\chi^2$ , and therefore a goodness of fit for a model to the data, we can produce many models and compare them to find a best fit. With the right method we could also produce a probability distribution for our model parameters. To generate model parameters and explore these target parameter distributions in parameter space, often we use some variation of the Markov chain Monte Carlo (MCMC) method. To be explicit, these are

separate processes, MCMCs should not be used to optimise models, only to investigate the probability distribution of the parameter space. The basic steps of an MCMC are relatively straightforward. There exists a ‘walker’ which starts with a chosen selection of parameters. This walker then explores the parameter space according to the algorithm:

1. Propose a step to a new position in the parameter space (the function that proposes the new step is usually some sort of Gaussian probability distribution centred on the current walker location)
2. Calculate a probability of accepting the step (by evaluating the likelihood of the new position relative to the likelihood of the current position, where likelihood can be described by e.g. the  $\chi^2$ )
3. Decide to take the step or remain stationary (with probability according to the acceptance probability)
4. Repeat (until a predetermined number of steps have been taken)

After a certain number of steps, the walker ought to have sufficiently explored the target parameter probability distribution, known as the posterior distribution. The entire path a single walker has taken is called a ‘chain’ and from the chain we can extract that distribution and its metrics - quantiles and medians, etc.

To speed up the exploration it is typical to use many walkers at once, as many as computation limits can spare - preferably hundreds but at least more than twice the number of parameters. When initiating, the starting locations of all the walkers are usually taken as Gaussian blob around a central set of parameters. These central starting parameters ought to be the best fitting values of an optimisation or the median parameters of a previous MCMC run.

The total number of steps that ought to be taken depends on the walkers’ convergence, quantified in their ‘autocorrelation time’. This value is essentially a measurement of how many steps it takes the walkers to reach the target distribution to begin useful exploration. Even when starting at the median parameters of a previous run or from an optimised result this is not zero as the initialisation function that sets the values of the initial walkers is not expected to be equal to the target probability distribution, since for example parameters may be correlated (a.k.a. degenerate). After approximately ten autocorrelation lengths it is expected that the locations of all the walkers at their final step is an accurate representation of the target probability distribution. The autocorrelation length for a certain parameter, for it will be unique to each parameter, can be computed directly from the chains and can also be checked by eye by plotting the parameter values for the chains at each step and visually

identifying whether or not the chains have converged and stabilised in their evolution. Only several dozens of samples are needed to define the target distribution, but if you do not have that many walkers or you desire a greater sample of the distribution you can take a selection of steps after a defined ‘burn-in’ number which ought to be at least ten autocorrelation lengths. When sampling more than just the final step, immediately successive steps ought not to be sampled as to ensure independence of the samples.

It is often very valuable to create a ‘corner plot’ to visualise the target distribution. A corner plot displays a two-dimensional plot of each parameter plotted against each other parameter, thus for  $N$  parameters  $N(N - 1)/2$  plots are produced. This allows for easy visual identification of parameters that are not independent of each other, for independent parameters the corresponding plot ought to be close to a 2D Gaussian. Any other shape implies dependence, other departures from well behaved distributions such as bimodal distributions and alternative solutions can also be readily identified.

I used in my work the `emcee` package [Foreman-Mackey et al., 2013] which codifies a more complex version of MCMC method in Python.

With an understanding for the likely properties of the disc we are ready to investigate what these parameters could imply about the system and to compare the system with the population of debris discs as a whole.

## Chapter 3

# ALMA imaging of the M-dwarf Fomalhaut C's debris disc

### Declaration

This chapter is reproduced from the paper "*ALMA imaging of the M-dwarf Fomalhaut C's debris disc*" published in Monthly Notices of the Royal Astronomical Society, Volume 504, Issue 3, pp.4497-4510 in July 2021. All analysis and write up for this paper was performed by me except for section 3.4.10 written by Paul Kalas, bar the latter half of paragraph four starting 'The  $7\sigma$  ALMA compact source...', and section 3.4.10 written by Julien Milli, Figure 3.9 was also created by Julien Milli. The code base for the SED and fractional-luminosity fitting used in Figure 3.7 was created by Grant Kennedy.

### Abstract

Fomalhaut C (LP 876-10) is a low mass M4V star in the intriguing Fomalhaut triple system and, like Fomalhaut A, possesses a debris disc. It is one of very few nearby M-dwarfs known to host a debris disc and of these has by far the lowest stellar mass. We present new resolved observations of the debris disc around Fomalhaut C with the Atacama Large Millimetre Array which allow us to model its properties and investigate the system's unique history. The ring has a radius of 26 au and a narrow full width at half maximum of at most 4.2 au. We find a  $3\sigma$  upper limit on the eccentricity of 0.14, neither confirming nor ruling out previous dynamic interactions with Fomalhaut A that could have affected Fomalhaut C's disc. We detect no  $^{12}\text{CO}$  J=3-2 emission in the system and do not detect the disc in scattered light with HST/STIS or VLT/SPHERE. We find the original Herschel detection to be consistent with our ALMA model's radial size. We place the disc in the context of the wider debris disc

population and find that its radius is as expected from previous disc radius–host luminosity trends. Higher signal-to-noise observations of the system would be required to further constrain the disc properties and provide further insight to the history of the Fomalhaut triple system as a whole.

### 3.1 Introduction

The Fomalhaut system, one of the brightest in the night sky, has been subject to much observation, simulation and theoretical hypothesising over the past 35 years. A wide triple system, it comprises A4V star Fomalhaut A as well as K4V TW PsA (Fomalhaut B) at a 57,400 au separation, and M4V LP 876-10 (Fomalhaut C) at a 158,000 au separation [Mamajek et al., 2013]. Fomalhaut A is just 7.7 pc distant and 440 Myr old. The historic interest in the system can be attributed to two factors that are not necessarily unrelated.

Firstly, both Fomalhaut A and C possess detectable debris discs. That is, we detect the presence of gas poor dust rings around the host stars. This dust is inferred to be continually produced by a collisionally evolving parent planetesimal population and not leftover from the protoplanetary disc [e.g. Hughes et al., 2018; Wyatt, 2008]. The disc around Fomalhaut C was initially detected with Herschel PACS [Kennedy et al., 2013]; it was not spatially resolved but a temperature of 24K and radius of  $\sim 20\text{--}40$  au were estimated. Not much more about the disc could be discerned until it was recently observed with ALMA, as this paper will discuss. However, the Fomalhaut A debris disc has been clearly resolved in scattered light with HST [Kalas et al., 2005] as well as in the far-infrared with Herschel [Acke et al., 2012] and in the millimetre with ALMA [MacGregor et al., 2017; Boley et al., 2012; White et al., 2017]. These observations identify the belt as a sharply defined ring at a radius of  $\sim 135$  au, the centre of which is offset from the location of Fomalhaut A. The sharp definition of the edges and offset together imply a highly apsidally aligned population of planetesimals with a coherent eccentricity of  $0.12 \pm 0.01$ . Such disc morphologies are typically interpreted as the result of the action of a perturbing planet [Wyatt et al., 1999]. At first this perturbing planet seemed to be the directly imaged exoplanet candidate Fomalhaut Ab, a point-like object identified in HST observations [Kalas et al., 2008]. However, the point source could not be detected in the infrared and possessed a stellar-like colour, suggesting the flux originates from scattered stellar light and casting doubt on the hypothetical planet’s nature [Currie et al., 2012]. Further HST observations proved that the object was on a highly eccentric orbit that is incapable of sculpting the disc into its present morphology [Kalas et al., 2013]. Kalas et al. [2008] propose the point source is a low mass planet with a large circumplanetary ring system. A planet with a collisional swarm of irregular satellites has also been proposed and discussed [Kennedy and Wyatt, 2011; Tamayo, 2014; Kenyon et al., 2014]. But it has

also been hypothesised that the point source is just a transient dust cloud [Janson et al., 2012; Kenyon et al., 2014; Tamayo, 2014; Lawler et al., 2015; Gáspár and Rieke, 2020].

Thus a separate planet must be invoked to drive the eccentricity of Fomalhaut A’s debris ring for a planet driven scenario, however to date a second planet has not been identified in the system despite several searches [Kenworthy et al., 2013; Currie et al., 2013]. Quillen [2006] predict this belt-shaping planet to have a mass of  $0.04 - 0.14 M_{\text{Jup}}$  and Chiang et al. [2009] predict a planet mass of  $0.5 M_{\text{Jup}}$ . On the additional assumption that Fomalhaut Ab was scattered into its current orbit by this putative planet, Faramaz et al. [2015] constrain a belt-shaping Fomalhaut Ac mass to  $0.25 - 0.5 M_{\text{Jup}}$ .

Alternatively, simulations [Lyra and Kuchner, 2013] have shown gas-dust interaction could also organise dust into tight, eccentric rings. This can occur through instabilities within the disc [Klahr and Lin, 2005; Besla and Wu, 2007] but requires a significant gas presence. Herschel PACS observations failed to detect C II and O I emission lines that would have been detected had the necessary quantities of gas been present in Fomalhaut A’s disc [Cataldi et al., 2015]. Matrà et al. [2017] do detect the presence of CO in Fomalhaut A’s disc using ALMA, but not in sufficient amounts to generate the necessary instabilities.

Past stellar interactions provide another mechanism for the generation of disc eccentricities, be this a flyby from an external star or the action of companion stars within the system. The action of flybys has long been investigated both in general theory [e.g. Kenyon and Bromley, 2002; Jílková et al., 2016] and in application to specific interesting systems, such as HD 141569 [e.g. Ardila et al., 2005; Reche et al., 2009] and HD 106906 [e.g. Rodet et al., 2017; De Rosa and Kalas, 2019; Rodet et al., 2019].

In addition to the eccentric belt around Fomalhaut A, the system’s unique orbital configuration provides a second point of interest. The wide orbits of Fomalhaut’s stellar companions constitute sufficient angular momentum to preclude a common protostellar core fragmentation scenario. The system cannot have unfolded as per the model of Reipurth and Mikkola [2012], as an angular momentum exchange resulting in a third star moving to a distant orbit requires the tightening of an inner binary. Stellar capture during the original cluster dispersal resulting in two wide companions is a viable history, but relies on two independently low probability events both occurring. The current wide separations also call into question the degree to which the system is bound and how it has evolved over its 440 Myr lifetime. The magnitude of the orbital period and the relatively meagre orbital velocities have prevented any definitive knowledge of the precise orbital configuration and trajectories from being surmised, yet several dynamical models for the system have been posited.

This paper considers whether new observations of the debris disc around Fomalhaut C with ALMA can provide evidence that Fomalhaut A’s own eccentric planetesimal belt

and the triple system’s large stellar separations are connected through the system’s dynamical history. Namely, our hypothesis is that if Fomalhaut A’s eccentricity is due to previous interactions with Fomalhaut C, then Fomalhaut C’s belt may be similarly affected and also show an eccentricity. This paper presents and discusses previous works on the dynamics of the Fomalhaut system and further motivations for ALMA observations of Fomalhaut C in §3.2, followed by a description of those observations in §3.3. We then present an analysis of the observations in §3.4 and discuss implications for our understanding of the system as a whole as well as the wider context of M star debris discs in §3.5.

## 3.2 Dynamical Hypotheses and Other Motivating Factors

Kaib et al. [2017, hereafter K17] propose that the Fomalhaut triple star system has been in a meta-stable bound state since its formation, devoid of catastrophic scattering events between Fomalhaut B and C such that we are not observing the system in a transient disruption state. The effect of the Galactic tide and passing field stars lead to a complex evolution of the eccentricity of Fomalhaut B’s orbit around Fomalhaut A, such that periastron values low enough to excite the eccentricity of Fomalhaut A’s belt may have been previously attained. K17 simulate the dynamics of the Fomalhaut system, starting with the stars at their present separations and with statistically generated orbital parameters. They evolve the system over 500 Myrs under the influence of the Galactic tide and passing field stars and classify a final state as a match to the real Fomalhaut system if the stellar separations are within 50% of their current values. They find  $\sim 7\%$  of their 2000 simulations end in a matching state, but that  $\sim 51\%$  of systems passed through a matching state in the last 100 Myrs as systems oscillate between matching and unmatching. The systems that ended in a matching state are reintegrated from the initial conditions with an initially circular belt of 500 massless test particles between 127 and 143 au around A. They find 25% of these systems end with an eccentricity between 0.04 and 1 for A’s belt, due to close periastron passages of B. However, the standard deviations in longitude of pericentre and eccentricity of the test particles in these eccentric belts are significantly larger in the simulations than those derived by MacGregor et al. [2017] from ALMA observations of the belt. MacGregor et al. [2017] give their model particles a forced eccentricity and forced argument of periastron, as well as a proper eccentricity with a randomly distributed proper argument of periastron. These ranges of free eccentricities and periastron angles about the forced eccentricity result in a scatter of true eccentricities and pericenter angles for disc particles. The scatter in K17’s model values for longitude of pericentre and eccentricity are both larger than in MacGregor et al. [2017]’s best fit model as well as being out of the range extrapolated from MacGregor et al. [2017]’s uncertainties. Only 2 of the 135 simulated belts are matches to Fomalhaut’s

in all the above regards, namely median eccentricity, standard deviation in eccentricity and standard deviation in longitude of pericentre, and therefore apsidal alignment. In all, this model is viable to explain the orbital configuration of the Fomalhaut system with  $\sim 7\%$  of simulations resembling the current system after 500 Myrs;  $\sim 25\%$  of these matching systems have close periastron passages of B that can excite the eccentricity of A's planetesimal belt, however only  $\sim 1.5\%$  of the matching systems' belts ( $0.1\%$  of all simulations) are able to match A's in every regard.

Feng and Jones [2017, hereafter F17] also modelled the Fomalhaut system under perturbations from the Galactic tide and stellar encounters. They initiate their models with the current relative stellar locations and integrate 500 Myrs backwards in time. C's orbit is classified as unstable if its orbital energy is larger than 0, i.e. it is unbound. They find that in all simulations C at least passes through an unbound state. In most models the separation between A and C only ever increases as the simulation progresses, but in a few percent of models C moves in and out of bound states and ends within 1 pc of A after the 500 Myrs. These are systems on meta-stable orbits, like those proposed by K17. These systems are termed 'gravitational pairs' by F17 and likened to Cooper pairs in a superconductor, as the orbital binding energy of the system is comparable to the energy fluctuations from the Galactic tide and stellar encounters. As stable orbits are too rare and unstable orbits are too short lived, F17 conclude that A and C are likely one of these 'gravitational pairs'. They also find that in 20% of models B comes within 400 au of A, thus likely being able to excite eccentricity in A's disc as shown by K17.

An alternative scenario is proposed by Shannon et al. [2014, hereafter S14]: A and C formed together as a binary from a single molecular cloud core which was then disrupted by the capture of B. To test this hypothesis S14 conduct N-body simulations with randomly sampled initial separations and eccentricities of the AC binary; B is generated at a random location within the Hill sphere of the system with a random velocity and eccentricity. The simulation is run for 500 Myr and stars are removed if they venture more than 2 pc from A. One thousand simulations were conducted and a match is defined by simultaneous separation of AB and AC within 0.5 – 1.5 times their existing values. Over the 500 Myr run of the simulation 46% have at least one period of matching; after 500 Myr 21% of systems retain all three stars, of which 19% were never matches. As these 19% of systems remain to become unstable and may possibly match in the future, S14 estimate that in total 55% to 60% of systems will eventually pass through a Fomalhaut-like state. The matching state is temporary, on the scale of tens of Myrs, and often followed by an ejection, more often of C than B. To investigate the effects of such interactions on the discs around A and C, 50 further simulations were conducted with discs of 100 test particles placed around A and C randomly distributed within the then-known bounds of the two discs (127–143 au and



10–40 au, respectively). Of these, 38% become a match over 500 Myrs. The discs are found to rise in eccentricity, with a high level of apsidal alignment, driven by secular interaction. Five of A’s discs reach eccentricities of 0.02–0.5, reminiscent of the current Fomalhaut A system. Further close encounters can become disruptive and raise eccentricities to even higher values, but repeated close interactions are not guaranteed, allowing eccentricity to be preserved over the timescale of the matching state. For apsidal alignment to also be preserved, the timescale of differential precession would need to be longer than the timescale of the matching state. The mean eccentricities of A and C’s discs are correlated but show a strong scatter, Fomalhaut C disc eccentricities vary between  $\sim 0.025 - 0.75$ .

On the one hand, the hypothesis of S14 relies on a particular set of initial conditions, on the other, F17 and K17 make no statements on how the system would have formed. S14’s models do have a  $\sim 15\%$  success rate at describing both the current orbital configuration of the system and the morphology of A’s eccentric belt. F17 find  $\sim 1\%$  of their systems have a matching configuration and passages of B that could excite the eccentricity of A’s belt and K17 find  $\sim 2\%$  have a matching configuration and close passages of B; however K17 find these close passages only produce A-like disc morphologies in 6% of cases. Naïvely operating on these percentages alone it seems the S14 hypothesis is most likely, however the likelihood of the initial conditions arising in each of the three cases is not quantified. The S14 hypothesis may also require observing the system in a transient state just before a star is ejected, which is less likely than observing a system in a long-lived meta-stable state.

These scenarios can be distinguished in several observational ways. An extremely precise measurement could be made of the individual stellar velocities to pin down the present orbital parameters. However, given the extremely large separations and the large timescale of the orbits and small orbital velocities involved this a very difficult task. Alternatively, K17, and by extension F17, predict A’s belt to be significantly less apsidally aligned than S14 does, S14’s apsidal prediction being more consistent with current observations. Another prediction of S14 is that the eccentricity of the belt of C should be correlated with that of A; if the eccentricity of C’s belt were to be measured it could support or weaken S14’s case. Such observations and measurements are presented and discussed in §3.4 in this paper. The interaction proposed by S14 could also have driven planetary instabilities around C that later stir the disc or the collisional cascade directly, leading to its increased brightness and ease of detection, uncharacteristic of M-dwarf discs.

Disc detection rates are presently low around M-dwarfs: the Herschel DEBRIS survey detected just 2 debris discs from 94 M-dwarfs [GJ 581, Fomalhaut C; Lestrade et al., 2012; Kennedy et al., 2013, respectively] and a separate Herschel survey of M-dwarf planet hosts with greater sensitivity found 3 discs among 21 late-type stars [18 M-dwarfs and 3 K-dwarfs; Kennedy et al., 2018a]. The key question remains whether true incidence rates

for M-dwarf discs are similar to earlier type stars and it is the low luminosity of the host stars that limits their temperature and luminosity. Luppe et al. [2020] find that this may be the case, thus requiring highly sensitive observations made at far-infrared/sub-millimetre wavelengths for detection. The alternative is that discs are indeed less common around these late type stars, perhaps due to effects that more significantly affect discs around low mass hosts such as stripping from stellar encounters [Lestrade et al., 2011] or photoevaporation of the primordial disc in cluster environments [Adams et al., 2004]. It is also possible that efficient planet formation around low mass stars could use up all the disc material, consistent with the increased planet occurrence rate measured for lower mass stars [e.g. Bonfils et al., 2013; Dressing and Charbonneau, 2015; Mulders et al., 2015].

Aside from increased stirring in S14’s scenario, why else could Fomalhaut C have a detectable disc? Relative to a random selection of field M-dwarf ages, which span up to  $\sim 10$  Gyrs, Fomalhaut C is still young at 440 Myrs. Debris discs are typically found to be brightest when youngest, when their planetesimal belts have been depleted little by collisional evolution [Decin et al., 2003; Rieke et al., 2005], possibly explaining the presence of its bright disc. Fomalhaut C exists as one of the lowest mass nearby stars with a confirmed debris disc, and as one of just a handful of ALMA-detected M-dwarf debris discs, it will play an important role in our understanding of M-dwarf discs and the M-dwarf planet formation process.

### 3.3 ALMA Observations

We observed Fomalhaut C three times with ALMA in Band 7 (0.87 mm, 345 GHz) from May 21st to June 6th 2018 under project 2017.1.00561.S. All observations used baselines ranging from 15 to 314 m and 48, 45 and 47 antennae respectively with an average precipitable water vapour of  $\sim 0.7$  mm. The total on source observing duration was 102 minutes. J2148+0657 and J0006-0623 were used for pointing, bandpass and flux calibration. J2258-2758 was observed between individual target scans for time-varying atmospheric calibrations. Each pointing was updated for the proper motion of Fomalhaut C, however the proper motion over the two weeks ( $\sim 0.017''$ ) between the first and last observation is negligible in comparison to the beam size ( $\sim 1''$ ) and thus pointing differences are ignored when the observations are combined.

The spectral setup comprised four windows centered on 347.833, 335.791, 333.833 and 345.833 GHz with bandwidth 2 GHz and 128 channels for all but the last, with width 1.875 GHz and 3840 channels of width 0.424 km/s. The last window was used to search for CO gas via the J=3-2 emission line, which can be produced in planetesimal collisions and has been identified in the disc of Fomalhaut A [Matrà et al., 2017].

The raw data were calibrated with the provided ALMA pipeline script in `CASA` version 5.1.2-4 [McMullin et al., 2007]. To reduce the data volume the visibilities were averaged in 30s intervals and down to two channels per spectral window for the continuum imaging. All images were generated with the `CLEAN` algorithm in `CASA`.

### 3.4 Results and Analysis

Given the relatively low signal to noise ratio (S/N) of the emission we carried out continuum imaging using natural weighting (equivalent to Briggs weighting with a robust parameter of 2) to preserve as much signal as possible and did not attempt self-calibration. We do not use a u-v taper as the disc is not well resolved radially, and one or more point sources within the primary beam begin to dominate the emission before disc structure is strengthened. This weighting gives a synthesised beam with a position angle (PA) of  $83.16^\circ$  and major and minor FWHM of  $1.14''$  and  $0.90''$  respectively, corresponding to 8.7 and 6.9 au at a distance of 7.67 pc. The standard deviation in the area around the disc is  $\sigma = 17.5 \mu\text{Jy beam}^{-1}$  as identified by measurement from an annulus of sky exterior to the disc. This noise is for the most part uniform throughout the  $4''$  radius centre of the image where the disc is detected, where the primary beam correction is  $< 10\%$ .

#### 3.4.1 Initial continuum analysis

We will present detailed modelling of the visibilities below, but we will discuss the `CLEAN` continuum image first for a qualitative introduction and outline.

Figure 3.1 shows that Fomalhaut C's ring is not continuously detected at all azimuths, even to a  $1\sigma$  level. Approximately half of the disc area is detected at a  $2\sigma$  level with some peaks at  $3$  or  $4\sigma$ . Although the overall flux level is low, it is apparent that the flux constitutes an inclined ring. This interpretation is shown to be consistent through the modelling. The disc width appears similar to the beam size, limiting the ring's radial and vertical extents to within  $\sim 10$  au.

Figure 3.2 shows the disc's deprojected radial profile, assuming the disc PA and inclination found from the Gaussian Torus visibility modelling. Comparing the profile with a Gaussian with the same FWHM as the beam shows that the ring is strongly detected, but not radially resolved.

The disc appears brighter in the south-east quadrant with greater continuous  $>2\sigma$  detection and larger amounts of  $>3\sigma$  detection as well as the only  $4\sigma$  peak within the disc at a PA of approximately  $145^\circ$  east from north. This variation is within expected noise fluctuations given a smooth disc but it is still investigated during modelling to explore whether or not this peak is a feature of the disc and whether or not its presence affects the

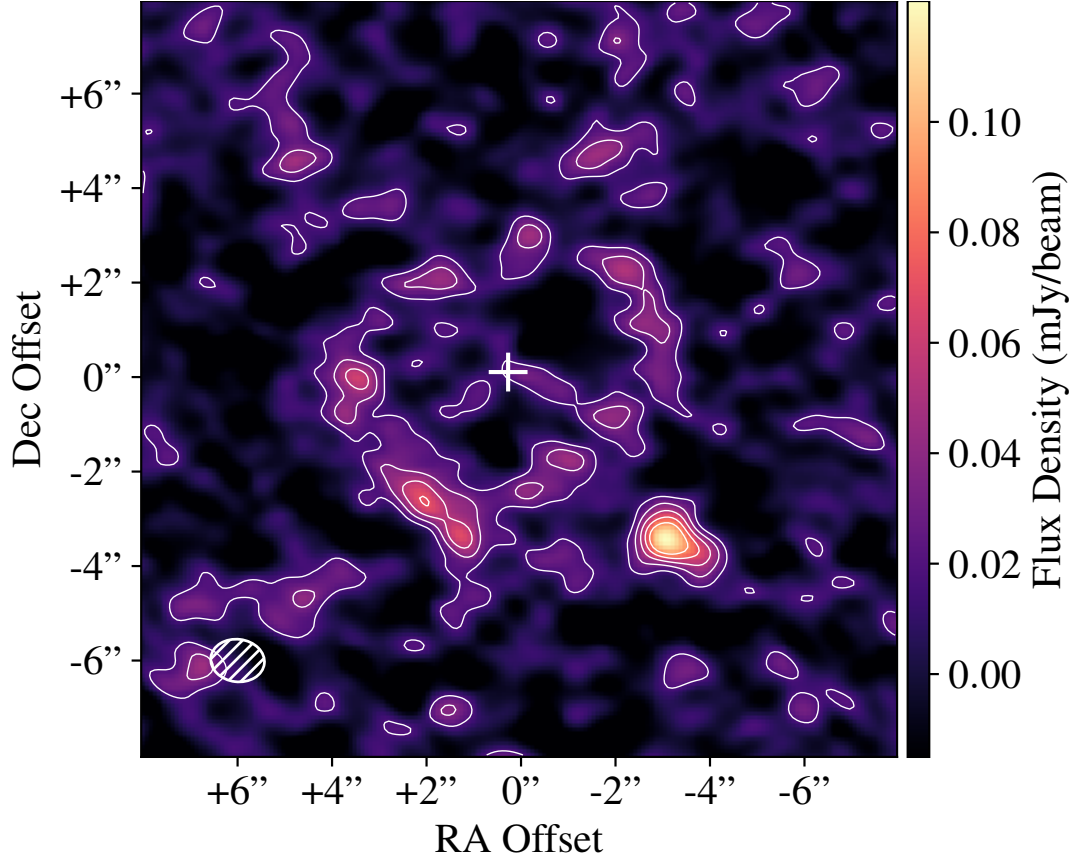


Figure 3.1: Naturally-weighted `CLEAN` image of the disc around Fomalhaut C. The ellipse in the lower left corner shows the beam size of  $1.14 \times 0.90''$ . The star is not detected. At a distance of 7.67 pc the disc radius is 26.4 au. Contours are drawn at 1, 2, 3, 4, 5 $\sigma$  with  $1\sigma = 17.5 \mu\text{Jy beam}^{-1}$ . The location of the star is marked with a + at  $342^\circ 01' 14.1'' - 24^\circ 22' 11.1''$ . Zero offset is the ALMA image phase centre at  $342^\circ 01' 13.8'' - 24^\circ 22' 11.2''$  (J2000).

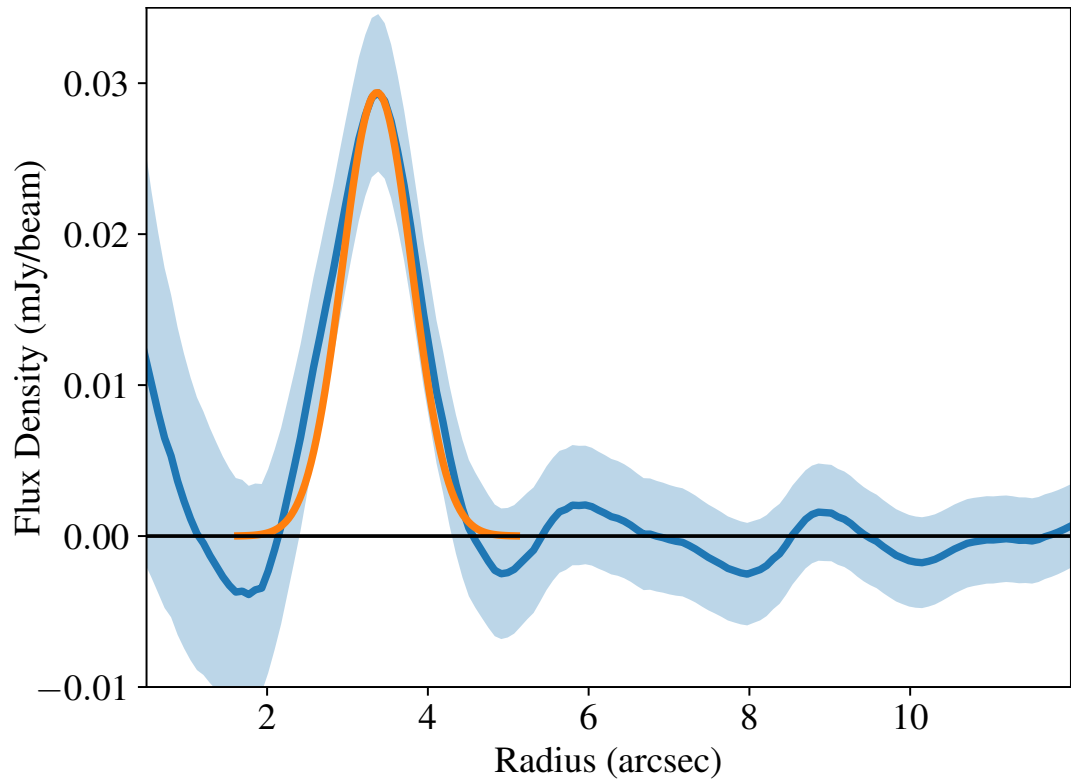


Figure 3.2: Deprojected radial profile of the disc around Fomalhaut C, computed from the CLEAN image within azimuthally averaged annuli. The shaded region denotes  $1\sigma$  uncertainties. A Gaussian with the same FWHM as the beam is plotted in orange at the peak radial flux.

fitted disc parameters. The peak S/N of the image is 7, located at a compact source in the south-west of the image 5" from the star. This external compact source we interpret as a background feature unassociated with the disc, but it is nevertheless included within the modelling. The predicted stellar photospheric flux is 15  $\mu$ Jy, consistent with there being no significant detection of the star and we find no evidence of stellar variability or flaring across the three observations. Preliminary fluxes can be taken from this image;  $\sim 0.7$  mJy is measured from the image within an elliptical annulus containing the disc. A flux of  $\sim 0.2$  mJy is measured for the compact source in the south-west. Together these sum to  $\sim 0.9$  mJy, which is consistent with the estimated disc flux of 1 mJy initially extrapolated from Herschel measurements [Kennedy et al., 2013§3.4.8].

### 3.4.2 Continuum Modelling

For a given set of parameters a rotation from sky coordinates to model coordinates (where the disc is in the x-y plane) is calculated. A 3-dimensional model disc is then generated in the sky coordinates (RA, Dec, line of sight). Using the aforementioned rotation, the corresponding model coordinate is found for each pixel and the model is consulted to identify the model flux at each location. This disc model is then collapsed into a plane, creating a 2-dimensional image in the sky plane. This image then has any compact sources added as a symmetrical 2D Gaussian with a given centre, standard deviation and flux. The image is then Fourier transformed using the GALARIO package [Tazzari et al., 2018] and the u-v locations of the ALMA data are sampled to calculate the  $\chi^2$  of the model given the data. We use the EMCEE package [Foreman-Mackey et al., 2013], a Python implementation of the Markov Chain Monte Carlo method, to explore the posterior probability distributions of our model parameters in order to derive the best-fitting model. The models are initiated near the optimal solutions indicated by previous test model iterations. We use 5000 steps, with the first 3500 being discarded based on the estimated auto-correlation lengths. For the runs we use 200 walkers and we verify upon completion that all chains have converged.

Three distinct models were implemented in order to investigate the nature of the over-brightness in the south-east of the disc and its effect on model fitting. The external south-west compact source is marginally resolved and so treated as an azimuthally symmetric two dimensional Gaussian source and is included in all models.

The **Torus** model serves to model the disc alone as a comparison for the later models. Here the south-east over-brightness constitutes simply a noise peak. The **Torus + Asymmetry** model treats the over-brightness as a feature of the disc which is thus contained within it, representing a local over-density of dust within the disc: perhaps a dust trap, pressure maximum, or recent collisional event. The **Torus + Point Source** model treats the over-brightness as unrelated to the disc but as a real feature of the image, possibly

representing a background galaxy, to be accounted for so as to not affect the parameters of the disc when fitting.

Thus all disc models share these common parameters: the disc’s total flux  $F$ , the disc average radius  $r_0$ , the disc’s Gaussian scale height  $\sigma_h$  (defined by angular elevation from the disc midplane), and scale width  $\sigma_r$  (defined by radial distance from centre of disc), the disc position angle  $PA$  (defined as east from north), the disc inclination  $I$ , the sky offset of the disc centre from the phase centre  $x_0, y_0$ ; and the radial distance from the centre of the image of the external compact source in the south-west, the compact source’s azimuthal angle in the image (measured east from north), the compact source’s Gaussian scale width and the compact source’s brightness. We find the phase-centre of the ALMA observations, and thus the image centre, to be slightly offset from the Gaia DR2 [Gaia Collaboration et al., 2016, 2018] location of the star at the time of observation and have corrected all further mention of disc offsets for this such that disc offset is always measured from the stellar location.

These Gaia corrected  $x_0, y_0$  offsets are on the plane of the sky, but any physical offset will also have some extent into (or out of) the plane of the sky. By assuming the offset is in the plane of the disc, this can be calculated using the sky offsets, position angle and inclination of the disc.

This offset is calculated for every walker at every step to also produce a  $z$  offset that is combined with the sky  $x$  (RA) and  $y$  (Dec) offsets to derive the total offset of a given model. This total offset is then divided by that individual model’s disc radius to calculate an eccentricity. The eccentricity upper limit presented in Table 3.1 is derived from the one sided  $3\sigma$  value of the final distribution of model eccentricities. This eccentricity upper limit also factors in the ALMA pointing uncertainty. The level of eccentricity derived in our models is small enough to still be well approximated by an offset circular disc, so a physically eccentric disc model is never explicitly used or needed to fit the disc.

### 3.4.3 Gaussian Torus

This model is the simplest and serves as our reference point. The best-fitting parameters are shown together with the other models in Table 3.1 and a dirty image of the residuals after subtracting the visibilities of the best-fitting model is shown in Figure 3.3 left. No discernible structure remains in the image showing that a azimuthally symmetric ring is a good representation of the data. The compact source in the south-west, outside of the disc, is also very well accounted for by the model. Using the medians of the posterior parameter distributions we calculate a  $\chi^2$  value of 3278000.7 for this model; this can be compared to the values of the other models to quantify their relative goodness of fit. We also include the relative Bayesian Information Criterion [BIC; Schwarz, 1978], which tests

Table 3.1: Median disc parameters,  $\Delta\chi^2$  and  $\Delta\text{BIC}$  values for Torus, Torus with Asymmetry and Torus with Point Source models. Uncertainties are the 16th and 84th percentiles. We find no significant degeneracies between model parameters. Offsets are measured from disc model centre to Gaia DR2 location of the star. Upper limits are one sided at  $3\sigma$ , i.e. the 0.996 quantile. The eccentricity upper limit includes the ALMA pointing uncertainty and the  $z$  offset.  $\Delta\chi^2$  and  $\Delta\text{BIC}$  values relative to Gaussian Torus model with values 3278000.7 and 3278180.7 respectively, calculated from a model produced using the median parameters.

| Parameter                                | Torus                   | Torus + Asymmetry       | Torus + Point Source    |
|--|-------------------------|-------------------------|-------------------------|
| RA Offset (")                            | $0.04^{+0.08}_{-0.08}$  | $0.05^{+0.08}_{-0.09}$  | $0.07^{+0.08}_{-0.08}$  |
| Dec Offset (")                           | $-0.07^{+0.08}_{-0.09}$ | $-0.07^{+0.09}_{-0.09}$ | $-0.02^{+0.07}_{-0.07}$ |
| Eccentricity                             | $0.04^{+0.03}_{-0.02}$  | $0.04^{+0.03}_{-0.02}$  | $0.04^{+0.02}_{-0.02}$  |
| Eccentricity $3\sigma$ Upper Limit       | 0.14                    | 0.14                    | 0.12                    |
| Inclination ( $^\circ$ )                 | $43^{+3}_{-4}$          | $42^{+4}_{-4}$          | $44^{+3}_{-3}$          |
| PA ( $^\circ$ )                          | $-59^{+7}_{-6}$         | $-58^{+7}_{-6}$         | $-63^{+6}_{-5}$         |
| Disc Flux (mJy)                          | $0.9^{+0.1}_{-0.1}$     | $0.9^{+0.1}_{-0.1}$     | $0.8^{+0.1}_{-0.1}$     |
| Radius (au)                              | $26.5^{+0.5}_{-0.5}$    | $26.4^{+0.6}_{-0.7}$    | $26.4^{+0.6}_{-0.6}$    |
| Scale Width $3\sigma$ Upper Limit (")    | 0.6                     | 0.6                     | 0.6                     |
| Scale Height $3\sigma$ Upper Limit (Rad) | 0.5                     | 0.7                     | 0.4                     |
| $N_{\text{Parameters}}$                  | 12                      | 15                      | 16                      |
| $\Delta\chi^2$                           | 0                       | -2                      | -20                     |
| $\Delta\text{BIC}$                       | 0                       | +42                     | +40                     |



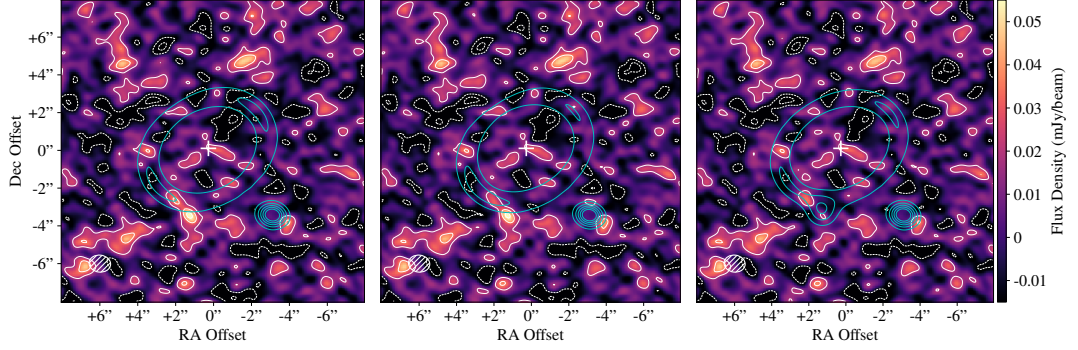


Figure 3.3: Naturally-weighted dirty images of the residuals after subtracting the individual models. Left: Gaussian torus model; Middle: asymmetric torus model; Right: torus with point source model. Cyan contours show the models and white contours show the residuals at  $-1, -2, 1, 2, 3, 4, 5\sigma$ . The location of the star is marked with a +. Zero offset is the ALMA image phase centre at  $342^{\circ}01'04.9'' -24^{\circ}22'11.2''$  (J2000).

whether the difference in  $\chi^2$  values between models is significant by penalising models with extra fitted parameters, as can be seen in its definition:  $BIC = \chi^2 + N_{\text{Parameters}} \times \ln N_{\text{dof}}$ . As the number of visibilities ( $N_{\text{dof}} = 2 \times N_{\text{vis}} = 2 \times 1639088$ ) being fitted is very large, there is a large penalty on the less simple models. A difference in BIC greater than six is considered ‘strong’ evidence that the lower valued model is preferred and a difference greater than ten is considered ‘decisive’ [Kass and Raftery, 1995].

In Figure 3.3 left we can see that after the subtraction of the disc model the peak in the south-east remains at a significance of  $3\sigma$  with a larger  $2\sigma$  extent and a total flux of about  $60 \mu\text{Jy}$ . The  $3\sigma$  peak is located just outside of the disc’s main emitting region, and the  $1\sigma$  extent reaches significantly into the disc, culminating in a  $2\sigma$  peak. There do exist multiple other  $2\sigma$  peaks within the image, but only one other  $3\sigma$  peak within the FWHM of the primary beam. This region is also the only one co-located with the known disc emission and could thus affect the fitting or be physically associated. Residuals do remain in roughly this location across the 3 separate nights of observations; however, given the even lower signal to noise of the individual nights they do not offer much information when not combined.

We can draw some preliminary conclusions from this basic model. A disc does fit the data well, with a moderate inclination of about  $40^\circ$  and a PA of about  $-60^\circ$ . The radius is well defined at 26.5 au and the disc flux is around 0.9 mJy. The south-west external compact source has a flux of around 0.2 mJy. As their posterior distributions are consistent with zero, we take the scale width and height to be unresolved and conclude only upper limits are obtainable. The model does find that the disc centre is offset from the stellar location, by  $0.15 \pm 0.09''$ . This value is the median of the total three dimensional offset distribution found by the modelling, and so is not equal to a quadrature combined two dimensional sky offset

calculated from the median RA and Dec offsets presented in Table 3.1. The uncertainty in this offset value is large, much larger than uncertainty of the Gaia DR2 location (0.00034") and the pointing uncertainty of ALMA (0.0405", here taken as 5% of the beam FWHM) as shown in Figure 3.4. Figure 3.4 shows the two dimensional distribution of offsets as well as the ALMA pointing uncertainty. The offset distribution overlaps with zero between 1 and  $2\sigma$ , and overlaps with the ALMA pointing offset uncertainty at  $1\sigma$ . The elliptical distribution of the offsets is to be expected, as there is less spread along the major axis of the disc where the S/N is highest, allowing for more precise fitting.

The median offset is  $1.2 \pm 0.7$  au, corresponding to an eccentricity of  $0.04 \pm 0.02$ . Due to the large uncertainty we do not take this result to be significant evidence of an offset, and we instead place a  $3\sigma$  upper limit on the eccentricity of 0.14. Our constraint on the eccentricity is limited by both the low S/N of the data and the ALMA pointing precision at 1" spatial resolution.

With a model flux value for the point source in the south-west we can make an estimate for the likelihood of such a background galaxy being present within the image. We will compare with the 1.2 mm galaxy number counts of Aravena et al. [2016] by converting our ALMA Band 7 870  $\mu$ m flux to a 1.2 mm equivalent. Aravena et al. [2016] provide a conversion for flux  $S$  between different bands:  $S_{1.2mm} = 0.4S_{870\mu m}$ . Our 870  $\mu$ m flux of 0.2 mJy is then equivalent to a 1.2 mm flux of 0.08 mJy. From Table 2 of Aravena et al. [2016] we estimate that there are 23,700 sources per square degree with a flux greater than 0.077 mJy. The probability of finding at least one galaxy brighter than this within a central 8 arcsecond radius, approximately the area of interest around the disk as shown in Figure 3.1, is then around 30 per cent. And so, the simplest explanation is that the south-west point source is background galaxy.

#### 3.4.4 Gaussian Torus with Asymmetry

This model treats the south-east over-brightness as a component of the disc in the form of a 3-dimensional Gaussian blob embedded within it, representing a substructure. This adds three extra parameters to the model: the blob's azimuth, the blob's azimuthal extent, and the blob's brightness. The minimum azimuthal extent is taken as the beam size (i.e.  $17^\circ$ ), and the maximum azimuthal extent is taken as a quarter of the disc (i.e.  $90^\circ$ ). The blob is centred within the disc and shares the disc's width. The disc flux value is the sum of the flux from the main disc and the blob contained within.

From examination of the residuals for this model, shown in Figure 3.3 middle, we can see that the in-disc residual in the south-east is reduced in size compared to Figure 3.3 left and no longer reaches  $2\sigma$ . Compared to the torus model, we can also see that the north-west ansa has decreased in flux, showing that the disc's general flux has decreased, with

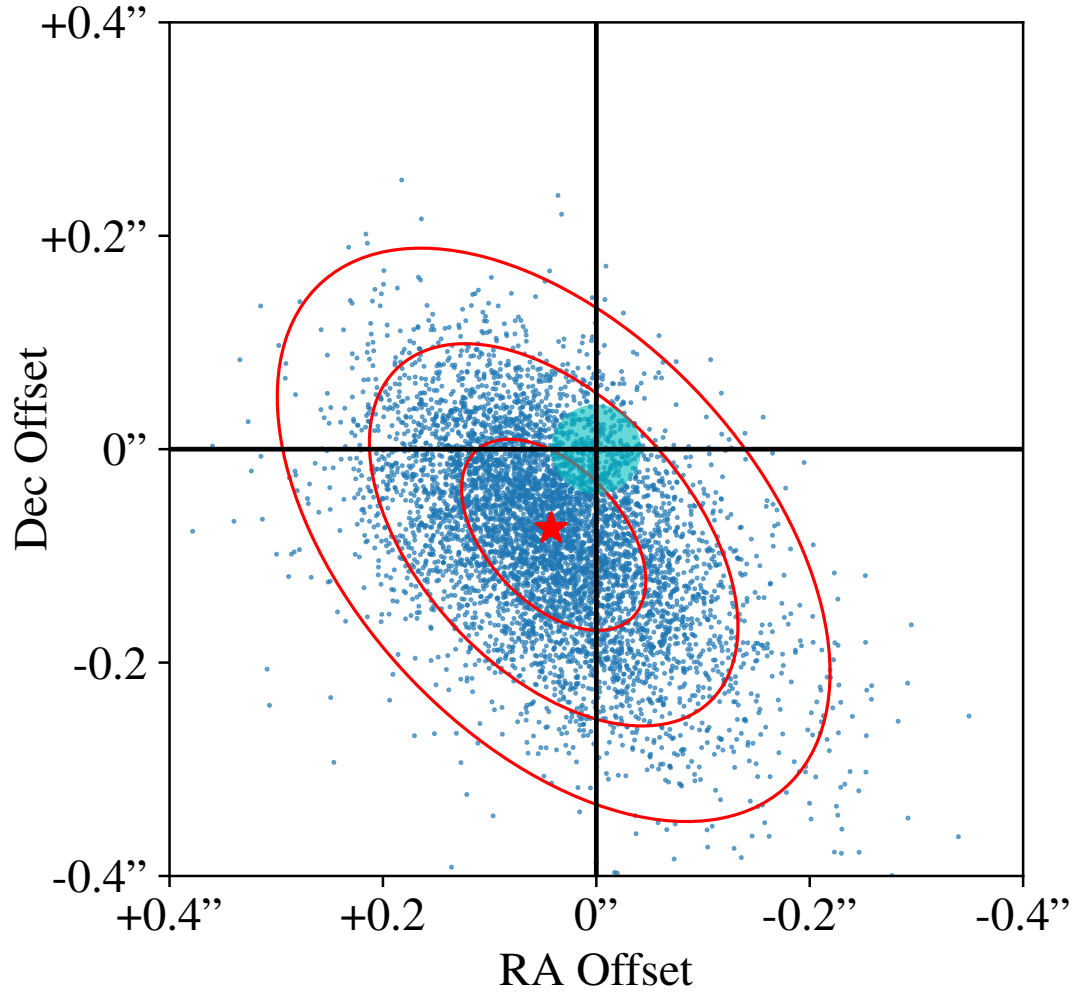


Figure 3.4: Distribution of offsets from *EMCEE* for the torus model. The stellar location is at the origin. Blue points are individual model disc centre offsets from each walker at every 50th step after initial discarding. The red star denotes the median offset and the successive red ellipses contain 68, 95 and 99.7 % of the offsets respectively. The blue shaded region is the  $1\sigma$  ALMA absolute pointing precision. The Gaia stellar location uncertainty would be too small to be seen.

the asymmetry taking up the extra flux needed at the south-east ansa. The asymmetry itself makes up  $10^{+16}_{-7}$  per cent of the flux of the disc, for a disc flux of 0.9 mJy this corresponds to  $0.09^{+0.14}_{-0.06}$  mJy. The distribution is consistent with zero flux showing that the asymmetry is not required to replicate the data. The asymmetry is centred  $3 \pm 25^\circ$  counter-clockwise from the south-east ansa of the disc and has a Gaussian scale azimuth of  $34 \pm 16^\circ$ .

This fit slightly decreases the  $\chi^2$  value, but has a large increase in BIC. This increase in the BIC shows that the model does not justify the inclusion of extra parameters, consistent with the flux of the blob being consistent with zero. Most of the disc parameters remain very similar to the torus model with the only notable change in parameter value being a slight increase in the  $3\sigma$  upper limit in scale height.

### 3.4.5 Gaussian Torus with Point Source

This model treats the south-east over-brightness as a background compact source, similar to the external compact source in the south-west. It also adds four extra parameters to the basic model, the radial distance from the centre of the image of the point source, its azimuthal angle in the image (measured east from north), its Gaussian scale width and its brightness. The fitting is also restricted such that the point source can only reside within the vicinity of the disc in the south-east quadrant.

Upon inspecting the residuals for this model in Figure 3.3 right it can be seen that not even a  $2\sigma$  contour remains in the south-east region of the disc. The  $\chi^2$  of this fit is also significantly less than the other two models, being 20 less than the basic Gaussian torus model showing that it fits the data best. However, the flux of the compact source is consistent with zero and the BIC is still significantly larger than for the basic torus model, meaning that the inclusion of extra parameters is not justified by the decrease in  $\chi^2$ . Whether or not the over-brightness truly is the result of a background source is less important; what this model allows us to consider is how the disc is fit without its influence. In this model the over-brightness point source accounts for 0.1 mJy of flux, and the rest of the disc possesses just 0.8 mJy. The disc flux is consistent with the flux of the previous models but these values show that the model disc fluxes could be inflated if the south-east point source is real and not associated with the disc. Again, while within uncertainty, the PA of the disc has relaxed to  $63^\circ \pm 6$  as opposed to the previous two models'  $58^\circ \pm 7$ . This is not a significant effect but may be a sign that the fitting was attempting to align the south-eastern ansa of the disc with the over-brightness to account for it. The reduction in Dec offset and slight increase in RA offset could also be attributed to a similar effect. With the addition of the point source, the disc has shifted to the north-east, moving the ansa away from the over-brightness. But, although the direction of the offset has shifted, the magnitude has not been significantly reduced as can be seen from the derived eccentricity and eccentricity upper limit. We also

see a return to a more moderate scale width than the previous model and a slight reduction in scale height. The flux density distribution of the two compact sources is unknown, but their contributions at shorter wavelengths could contaminate the disc flux from the Herschel data, this possibility is explored in §3.4.8.

### 3.4.6 Continuum Modelling summary

In summary, the debris disc around Fomalhaut C is detected and resolved with ALMA, and the radius and orientation are well constrained. A Gaussian torus represents the dust ring well, but the radial and vertical scale heights are unresolved, with only upper limits available. Disc parameters are consistent with each other between the different models, but only the torus with point source model does not leave  $2\sigma$  residuals in or near the south-east sector of the disc. The basic torus model has the lowest BIC and thus is the preferred model. As the basic torus model's residuals leave the over-brightness mostly outside of the disc's bound and as the asymmetric disc model failed to find a significantly better fit, it can be concluded that the south-east over-brightness is not likely associated with the system. That the torus with point source model did not find a significantly better fit than the other models implies that the over-brightness is most likely just a noise peak. It could be a background object, but our BIC values show that there is not enough significance to conclude such. The similarity across modelling results finds that this feature does not significantly affect the fitted disc parameters. If real, observations at a later epoch would be able to confirm the nature of the point source if it does not share the proper motion of the star.

A small offset of the disc centre from the star is consistent across all models, but is not significant. In all our models, the distribution of offsets retrieved from EMCEE overlaps with zero between 1 and  $2\sigma$ , and overlaps with the ALMA pointing offset uncertainty.

### 3.4.7 CO Non-Detection

The spectral setup of the ALMA observations was designed to allow a search for CO gas produced in collisions of planetesimals that are rich in volatiles via the J=3-2 emission line. After subtracting the continuum emission, visual inspection revealed no clear signal in both the dirty cube and a moment-0 map produced by summing pixels across the channels in the velocity range where gas is expected.

To enhance the signal of potential CO in the system we also employed the spectro-spatial filtering approach as described in Matrà et al. [2015] under the assumption that any CO present would be co-located with the dust. In this method pixels are spectrally shifted within the data cube to account for the expected radial velocities from the Keplerian motion within the disc, here we assume a stellar mass for Fomalhaut C of  $0.18 M_{\odot}$  [Pecaut and

Mamajek, 2013]. We use the torus model from §3.4.3 as a spatial filter, masking all pixels that are not co-located with model continuum emission that reaches at least 10% of the peak model flux. Figure 3.5 shows the corresponding spectra for the spatial filter alone and the spectro-spatial filter assuming either the north-west or the south-east ansa is rotating towards us. No signal is discernible in any of the produced spectra and so we calculate a  $3\sigma$  detection limit. With the application of the spectro-spatial filtering and with channel widths of 0.424 km/s we calculate a  $3\sigma$  upper limit on the CO flux of 16 mJy km s<sup>-1</sup>. This limit accounts for both the 10% flux calibration uncertainty from ALMA and the correlation of adjacent channels.

A direct flux comparison of the CO non-detection for Fomalhaut C to the CO detection for Fomalhaut A is not straightforward, as the latter observations were not of the CO J=3-2 transmission line, but of the CO J=2-1 transmission line with ALMA Band 6 [Matrà et al., 2017], and the CO excitation environment in the Fomalhaut C disc is uncertain. We might compare to the initial ALMA Band 7 observation of Fomalhaut A [Matrà et al., 2015] in which a flux limit of 160 mJy km s<sup>-1</sup> was calculated, however this was an ALMA Cycle 0 observation and the continuum sensitivity was also 3.5 times lower than in our observation. An appropriate example against which to compare Fomalhaut C is provided through the M-dwarf TWA 7 [Matrà et al., 2019a] for which CO J=3-2 was detected with a integrated flux of  $91 \pm 20$  mJy km s<sup>-1</sup> at a distance of 34 pc.

To set an approximate constraint on the CO+CO<sub>2</sub> mass fraction of the planetesimals, we make a simple comparison of the collisional mass loss rate and flux limit with those of TWA 7. Following the prescription set out in the appendix of Matrà et al. [2017], we compute the mass loss rate for Fomalhaut C's smallest grains of  $\dot{M}_{D_{\min}}$ . The minimum grain size,  $D_{\min}$ , is an unknown here in the regime of stellar wind dominated grain removal and we do not have enough short wavelength data to retrieve an estimate from the flux density distribution as in Matrà et al. [2019a]. The minimum grain size for TWA 7 was found to be 0.1 μm and using this number as a fiducial value for Fomalhaut C we get  $\dot{M}_{D_{\min}} = 6 \times 10^{-5} M_{\oplus} \text{ Myr}^{-1}$ . For comparison the value is  $3 \times 10^{-3} M_{\oplus} \text{ Myr}^{-1}$  for TWA 7. The CO+CO<sub>2</sub> mass (which photodissociates in time  $t_{\text{phd}}$ ) is estimated as

$$M_{\text{CO+CO}_2} = t_{\text{phd}} \frac{f_{\text{CO+CO}_2}}{1 - f_{\text{CO+CO}_2}} \dot{M}_{D_{\min}}, \quad (3.1)$$

where  $f_{\text{CO+CO}_2}$  is the fraction of planetesimal mass in CO and CO<sub>2</sub> ice [Matrà et al., 2017]. Thus, if we assume the same CO excitation and lifetime for Fomalhaut C as for TWA 7, and that the observed CO flux is proportional to the CO mass, then it is only the difference in mass loss rates and planetesimal CO+CO<sub>2</sub> fraction that changes the observed CO flux. TWA 7 has a 50× higher mass loss rate and CO flux 5× higher than our upper limit, but

Fomalhaut C is  $4.4\times$  closer, so with Fomalhaut C we could have detected CO at half of TWA 7's observed level for the same CO+CO<sub>2</sub> fraction. Thus,  $f_{\text{CO+CO}_2}$  is constrained to be at least  $\sim 2\times$  lower than for TWA 7. The ice fraction for the planetesimals of TWA 7 was found to be  $\geq 70\%$ , so for our assumptions the non-detection does not appear to be particularly constraining compared to the  $\lesssim 10\%$  fractions observed in the Solar system [Le Roy et al., 2015]. We can now also compare our ice fraction constraint with Fomalhaut A's ice fraction of  $4.6\%–76\%$  [Matrà et al., 2017] to find that the two are consistent.

### 3.4.8 Herschel/PACS Modelling and Revised SED Model

With the additional knowledge of the Fomalhaut C disc's geometry, and of the presence of a nearby background compact source, it is worth re-analysing the Herschel data [Kennedy et al., 2013] to see if new information can be gleaned, or to see if the background source partially contaminated the original detection. Total contamination of the original detection is highly improbable as the chance of detecting a debris disc around a randomly chosen M star is already very low. We use the level 2.5 data product  $160\ \mu\text{m}$  PACS image from November 2011 (Observation IDs 1342231937, 1342231938; Observing Day 906) as our data for model comparison. For reference, we show our best fit ALMA torus model in contours over the Herschel detection in Figure 3.6.

A similar approach was taken to modelling the Herschel data as was taken for the ALMA data as described in §3.4.2. A model is generated using the median disc parameters of the Gaussian torus model from §3.4.3. The disc model's stellar location is centred on the Gaia DR2 location of Fomalhaut C at the time of the Herschel observation, however the compact source is assumed to be in the background and thus its position is not corrected for proper motion between the dates of the Herschel and ALMA observations. The entire model is then allowed to be offset from the centre to account for the imprecise Herschel pointing, with a Gaussian prior set on the offset using the absolute pointing performance of  $1.12''$  at  $1\sigma$  provided by ESA within the observing date range of the observation<sup>1</sup>. The model is then convolved with a Herschel  $160\ \mu\text{m}$  point-spread-function (PSF) and re-binned to the  $3.2''$  pixel scale of the Herschel image. A flat background offset is added to the model image before subtraction from the observational data for calculation of the  $\chi^2$ . Two PSFs are tested, an empirical PSF is adapted from a  $160\ \mu\text{m}$  calibration observation of the point source  $\gamma$  Dra from the same Observing Day (Observation IDs 1342231899/1342231900) and a high resolution synthesised PSF from observations of Vesta and Mars provided by Bocchio et al. [2016]. Aside from the  $x$  (RA) and  $y$  (Dec) image offsets the only other parameters allowed to vary are the radius of the disc, the flux of the disc, the flux of the compact source and the flat background flux of the model. The implementation of a flat

<sup>1</sup><https://www.cosmos.esa.int/web/herschel/pointing-performance>

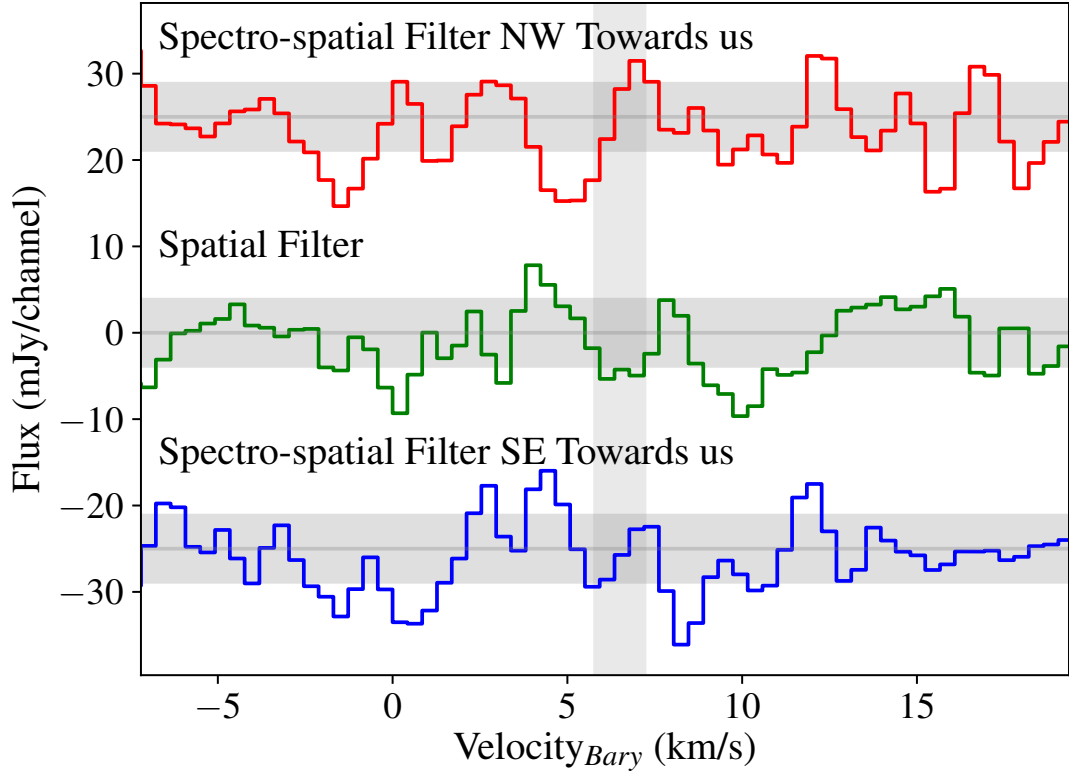


Figure 3.5: CO J=3-2 spectra for the debris disc around Fomalhaut C using spatial and spectro-spatial filtering techniques. The centre spectrum (green) is filtered only by the bounds of the disc as per our Gaussian Torus model. The top and bottom spectra have had disc pixels shifted within the data cube by their expected Keplerian velocities, and are vertically displaced for graphical clarity. As there are two possible rotations of the disc with either ansa rotating towards us there are two possible shifts. There is no significant signal in any spectrum. Horizontal shaded regions denote the  $1\sigma$  uncertainty of the spectrum taken over a larger range of velocities after subtraction of a second order polynomial background. The vertical shaded region denotes the expected centre of the signal at the  $6.5 \pm 0.5 \text{ km s}^{-1}$  stellar radial velocity.



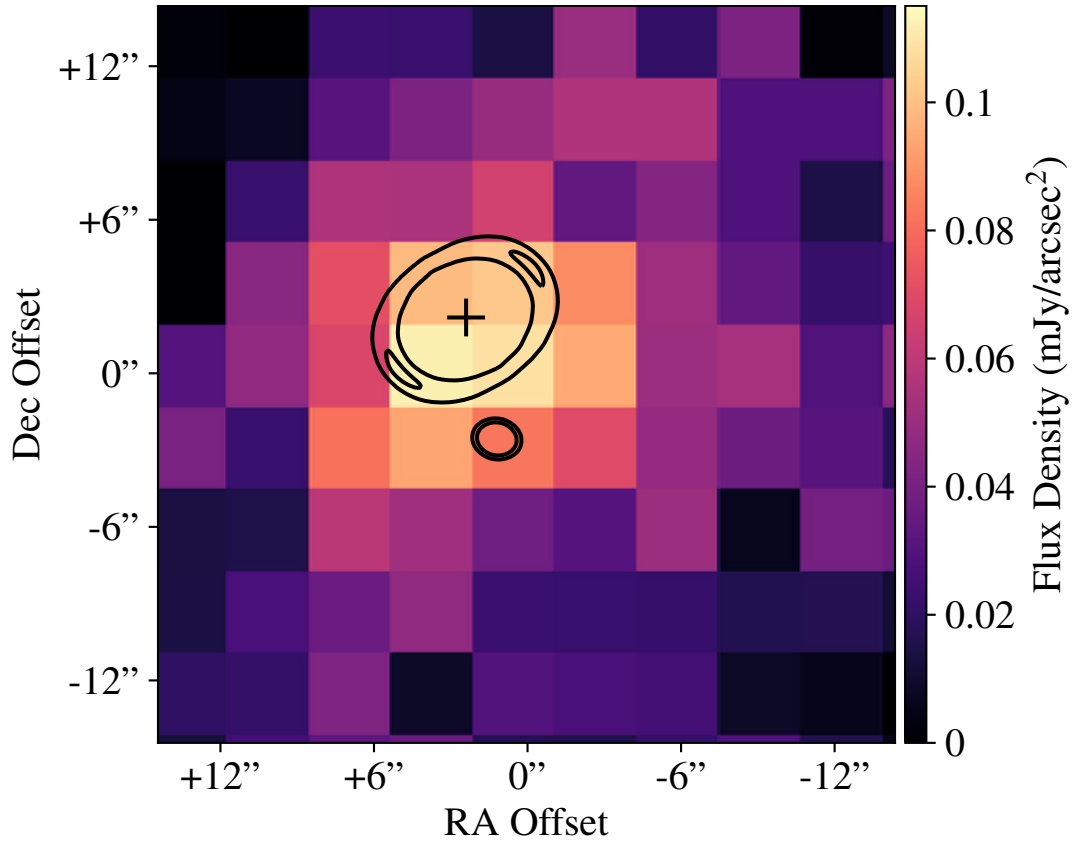


Figure 3.6: Herschel 160  $\mu\text{m}$  PACS detection of the Fomalhaut C disc. In black are contours of 1, 2 $\sigma$  from the ALMA best fit torus model, assuming zero proper motion of the external compact source appropriate for a background galaxy. The Gaia DR2 location of the star is marked with a +. Zero offset is at  $342^{\circ}01'09.6'' - 24^{\circ}22'12.1''$  (J2000). Our best fit pointing correction of +0.54" RA, +0.33" Dec has been applied to the Herschel image.

Table 3.2: Median parameters for the Herschel model with Empirical and Synthesised PSFs. Telescope offsets are measured between the Herschel image coordinate Gaia DR2 stellar location and the model stellar location.

| Parameter                             | Empirical PSF             | Synthesised PSF           |
|---------------------------------------|---------------------------|---------------------------|
| Telescope RA Offset (")               | $0.5^{+0.6}_{-0.6}$       | $0.6^{+0.6}_{-0.6}$       |
| Telescope Dec Offset (")              | $0.3^{+1.1}_{-1.1}$       | $0.3^{+1.1}_{-1.1}$       |
| Disc Radius (")                       | $3.7^{+2.0}_{-2.2}$       | $3.5^{+2.3}_{-2.2}$       |
| Disc Flux (mJy)                       | $18^{+7}_{-7}$            | $15^{+6}_{-7}$            |
| Compact Source Flux (mJy)             | $0.9^{+0.6}_{-0.5}$       | $0.9^{+0.5}_{-0.5}$       |
| Background (mJy/arcsec <sup>2</sup> ) | $0.050^{+0.006}_{-0.006}$ | $0.053^{+0.006}_{-0.006}$ |

background is justified as the annulus of width  $\sim 10''$  (3 pixels) around the detection of Fomalhaut C’s disc has a median pixel value of  $\sim 0.2$  mJy, which the model will need to be able to account for. The disc and compact sources fluxes are allowed to vary as their relative proportions are unknown at the wavelength of observation due to their unknown spectral slopes. The radius of the disc is allowed to vary in order to investigate whether radiation forces and stellar winds from the host star are significant enough to blow out the smaller grains probed by Herschel to larger radii, to probe the potential presence of a small grain halo as Matthews et al. [2015] found for AU Mic. We use EMCEE to fit model discs and compact sources to the Herschel data. We use 100 walkers and as we find the largest auto-correlation time across all parameters to be 160 steps, we use 2000 steps and discard the first 1600 steps.

The results are summarised in Table 3.2 and are highly consistent between the two PSFs. We find that a small pointing offset is favoured, but within the  $1\sigma$  absolute pointing uncertainty of  $1.12''$ . The radius of the disc is not found to be well constrained, but are consistent with the resolved ALMA value. Smaller radii still fit the data well, implying the disc is either unresolved or not substantially resolved with Herschel; radii larger than  $\sim 5 - 6''$  do not fit the data well. Thus we conclude that there is not sufficient evidence to suggest that the grains probed by Herschel lie at significantly larger radii than the grains probed by ALMA. A flat background flux of  $\sim 0.05$  mJy/arcsec<sup>2</sup> is fit by the model, but is not interpreted as significant evidence of a halo of small grains as large amounts of the Herschel map not associated with Fomalhaut C share this non-zero flux. The flux fitted to the disc is  $\sim 16$  mJy, consistent with the original reported detection of  $15.5 \pm 2.8$  mJy. The compact source is found to only contribute  $\sim 0.86$  mJy. We therefore conclude that the Herschel detection of the Fomalhaut C disc is not significantly contaminated by the compact source

identified by ALMA.

The model flux found for the south-west compact source has a wide uncertainty, and is subject to further systematic uncertainties. But with rough flux estimates at both 160  $\mu\text{m}$  and 870  $\mu\text{m}$  we can estimate a flux ratio of these two wavelengths of 1.5 – 7.5. This ratio range would be inconsistent with a sub-millimetre galaxy in the rest frame, but would be consistent with a galaxy at a redshift  $z = 2 - 4$  [Casey et al., 2014]. We note that this redshift range is outside of the sample of  $z = 1.6 \pm 0.4$  used by Aravena et al. [2016], thus causing a potential conflict with the probability estimate that the source is a galaxy. However, we again highlight the systematic uncertainties in the flux derived from the Herschel modelling; if the background source contributed significantly less to the Herschel flux, such a large redshift would not be needed.

As we have found that the original Herschel flux measurements are consistent with the ALMA findings and that the compact source did not significantly contaminate the detection, those values are kept the same for the fitting of a new blackbody dust model with inclusion of the ALMA flux measurement (see Yelverton et al. [2019, 2020] for details of the SED fitting method). The dust model is a modified blackbody spectrum: beyond the fitted parameter  $\lambda_0$  there is an additional multiplication factor of  $(\lambda/\lambda_0)^{-\beta}$  as small grains do not efficiently radiate at wavelengths larger than their own size. The flux density distribution (SED), Figure 3.7, has not been significantly adjusted from Kennedy et al. [2013] and the parameters remain consistent. A dust temperature of  $20 \pm 4$  K is found, corresponding to a blackbody radius (the distance between the dust and the star if the dust grains were perfect blackbodies) of  $13 \pm 5$  au, with a fractional luminosity of  $L_{\text{dust}}/L_{\star} = 1.5 \pm 0.2 \times 10^{-4}$ . While  $\lambda_0$  is not well constrained, we find  $\beta = 1.5 \pm 0.4$ .

### 3.4.9 Blackbody vs Resolved Radii

With the newly resolved radius of the disc of 26 au the blackbody radius of 13 au can be seen to be a significant underestimate. This is a common finding for debris discs around all host stellar types [Rodriguez and Zuckerman, 2012; Booth et al., 2012; Pawellek et al., 2014] implying the presence of small dust grains that are hotter than black bodies due to their inefficient long wavelength emission. We can use a measure of this called  $\Gamma$ , defined as  $R_{\text{dust}}/R_{\text{BB}}$ , the ratio of the resolved disc radius to the blackbody radius [Booth et al., 2012], or equivalently defined as  $(T_{\text{dust}}/T_{\text{BB}})^2$ , the square of the ratio of the dust temperature to the temperature of an ideal blackbody at the resolved radius  $R_{\text{dust}}$  of the disc [Pawellek et al., 2014]. The  $\Gamma$  factor for Fomalhaut C’s disc is  $1.9 \pm 0.7$ .

The loose trend [Pawellek et al., 2014] is that  $\Gamma$  increases with decreasing stellar luminosity, albeit with strong scatter. This trend is linked to typical grain sizes decreasing towards stars with lower luminosities exhibiting weaker radiation pressure on the dust, i.e.

the blowout size and with it the minimum grain size  $D_{\min}$  decreases with decreasing stellar luminosity. Smaller grains are typically hotter than larger grains due to decreased emission efficiency and thus the blackbody discrepancy grows. Working from Pawellek et al. [2014]’s relations Fomalhaut C’s ( $L_{\text{FomC}} \approx 0.005 L_{\odot}$ )  $\Gamma$  should be larger at  $\sim 5 - 12$ , more similar to that measured for GJ 581 ( $L_{\text{GJ581}} \approx 0.01 L_{\odot}$ ). As it stands Fomalhaut C’s  $\Gamma$  is even smaller than the  $\sim 3 - 4$  of AU Mic ( $L_{\text{AUMic}} \approx 0.1 L_{\odot}$ ). However there are a couple of key caveats aside from the large observed scatter.

Firstly, visible light absorption efficiency significantly decreases for smaller astrosilicate particles [ $\lesssim$  microns; Krivov et al., 2008] serving to plateau the trend of increasing dust temperature with decreasing grain size as decreasing absorption efficiency begins to counter the decreasing emission efficiency. Around lower temperature stars this turnover would be reached at comparatively larger minimum grain sizes as the peak stellar emission is moved to longer wavelengths. Secondly, as radiation pressure from low mass stars begins to become too weak to remove grains altogether, Poynting-Robertson drag (P-R drag) and stellar wind [e.g. Wyatt et al., 2011; Reidemeister et al., 2011; Plavchan et al., 2005] become the dominant grain-removal mechanisms. The radiation pressure dominated trend of decreasing  $D_{\min}$  with decreasing stellar luminosity is now disrupted and it is unclear how the relationship proceeds to lower luminosities. As a very low luminosity star these effects would be particularly prominent for Fomalhaut C and could explain why Pawellek et al. [2014]’s  $\Gamma$  trend has appeared to have flattened or possibly even turned over in the low mass regime in which Fomalhaut C belongs. Aside from Fomalhaut C, AU Mic is the only other M star currently thermally resolved in high resolution [TWA 7 is only marginally resolved with ALMA and GJ 581 is only marginally resolved with Herschel; Bayo et al., 2019; Lestrade et al., 2012, respectively]; as more M-star debris discs are resolved with ALMA it will be valuable to investigate  $\Gamma$  and grain sizes in this low mass regime of low temperature hosts, stellar wind and small grains.

### 3.4.10 Scattered Light Non-Detections

#### HST/STIS Observations

We attempted to detect dust-scattered light around Fomalhaut C using HST/STIS coronagraphy. STIS comprises a  $1024 \times 1024$  pixel CCD with various occulting elements in the focal plane and a scale of  $0.05077''/\text{pixel}$ . However, STIS does not have a pupil-plane mask to suppress the four diffraction spikes from HST’s secondary support structure, nor does it have filters, effectively operating at the wide optical throughput of the system ( $\lambda_c = 0.5858 \mu\text{m}$ ,  $\Delta\lambda = 0.4410 \mu\text{m}$ ).

Fomalhaut C was observed at two epochs: UT 2014-11-12 (HST-GO-13725) and

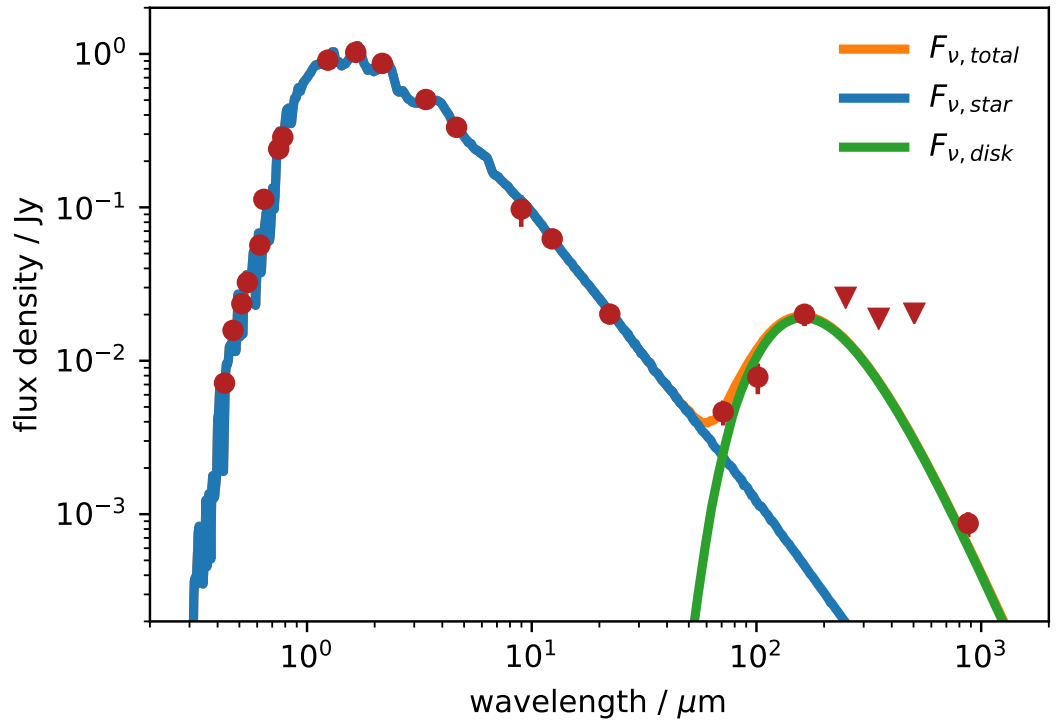


Figure 3.7: Fomalhaut C flux density distribution (SED). Dots are measured fluxes and triangles are  $3\sigma$  upper limits [Kennedy et al., 2013]. The stellar photosphere model is in blue, the disc model in green and the combined SED in orange.

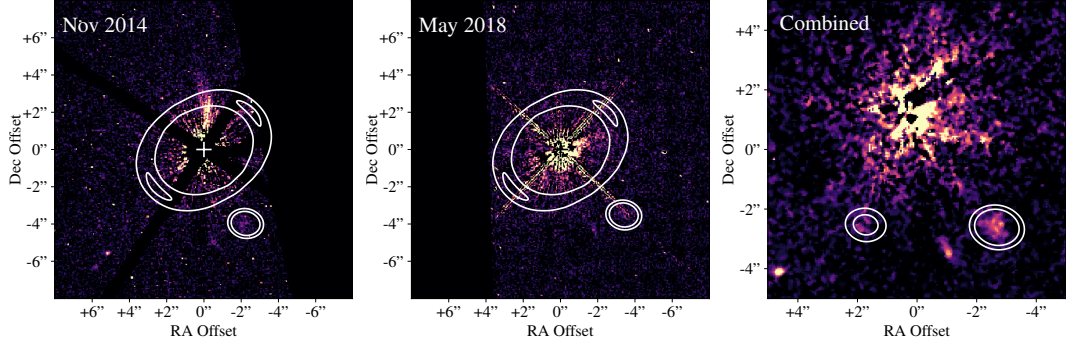


Figure 3.8: HST STIS observations of Fomalhaut C. Left: Initial November 2014 observation with diffuse linear structure apparent north of the star. The disc is not detected but the background source found by ALMA external to the disc in the south-west is also detected by STIS. In white are contours of  $1, 2\sigma$  from the ALMA best fit torus model, assuming no proper motion of the external compact source. The Gaia DR2 location of the star at the epoch of observation is marked with a  $+$ . Zero offset is at  $342^{\circ}01'12.8'' - 24^{\circ}22'10.5''$  (J2000). Middle: May 2018 observation with diffuse linear structure north of the star not detected. The disc is not detected and the background source external to the disc is potentially obscured by the telescope's diffraction spikes. Overlays as before. Zero offset is at  $342^{\circ}01'14.1'' - 24^{\circ}22'11.1''$  (J2000). Right: Combined observations of all HST epochs to increase background object SNR, Fomalhaut C is blurred due to high proper motion and thus we do not plot the disc model contours. The exterior compact source is detected in the south-west, but a potential in-disc point source in the south-east is not detected. In white are contours of  $1, 2\sigma$  of the two compact sources, within the disc and exterior to the disc, from the ALMA best fit torus with point source model assuming no proper motion. Zero offset is at  $342^{\circ}01'13.0'' - 24^{\circ}22'11.6''$  (J2000).

2018-05-28 (HST-GO-15172) as shown in Figure 3.8 left and middle respectively. At each epoch Fomalhaut C was occulted behind BAR5 with width  $\sim 0.4''$ , and observed at two telescope roll angles separated by  $\sim 30^\circ$  in two consecutive orbits. Each orbit in the 2014 epoch comprised six exposures of 397 seconds whereas the 2018 epoch had six 379 second exposures. Cosmic rays were removed in each \*.flt.fits exposure by interpolation over the bad pixels identified in the \*.pl files and then the six exposures per orbit were median combined. The sky background was sampled in a region on the detector farthest away from the occulted star and subtracted. Finally the images were divided by the integration time. To subtract the point-spread function, the final image from the first orbit was iteratively shifted and subtracted from the second orbit.

The 2014 data revealed a diffuse, nearly-linear structure extending northward from Fomalhaut C between  $1.2''$  (the edge of the occulted region) and  $3''$  radius. The morphology and surface brightness resembled a background galaxy also seen  $18.4''$  to the east of Fomalhaut C, highlighting the possibility that the Fomalhaut C extended feature was also a background galaxy. This finding motivated the 2018 observations in order to check for common proper motion of the feature with the star. However, the feature was not detected anywhere in the 2018 field, showing it to be a spurious artifact in the 2014 data.

No circumstellar nebulosity is detected in the STIS data with a  $3\sigma$  limited surface brightness of  $3.39 \mu\text{Jy arcseconds}^{-2}$  at  $3''$  radius from the star (using a zero point of  $1 \text{ DN/s/pixel} = 4.55 \times 10^{-7} \text{ Jy}$ ). The  $7\sigma$  ALMA compact source south-west of Fomalhaut C is detected in the 2014 observation (Figure 3.8 left). It may also be detected in the 2018 observation (Figure 3.8 middle), but its location is obscured by the telescope's diffraction spikes. The ALMA source is significantly detected in a combined image of all HST observations (Figure 3.8 right), showing that it is indeed real. These detections together demonstrate that the source does not share Fomalhaut C's proper motion and is a background object. In neither epoch nor in the combined image is there a significant detection of a potential south-east point source within the disc per the ALMA torus with point source model.

### VLT/SPHERE Observations

Fomalhaut C was observed with the high-contrast imager VLT/SPHERE [Beuzit et al., 2019b] as part of the SPHERE High-Angular Resolution Debris Disks Survey<sup>2</sup> [SHARDDS, Wahhaj et al., 2016; Choquet et al., 2017; Marshall et al., 2018]. This survey is an imaging search for discs around stars within 100 pc having an infrared excess greater than  $10^{-4}$ . It uses the IRDIS subsystem [Dohlen et al., 2008] in broad band H ( $\lambda = 1.625 \mu\text{m}$ ,  $\Delta\lambda = 0.290 \mu\text{m}$ ) and the apodised Lyot coronagraph of diameter 185 mas. Fomalhaut C was observed at 2

<sup>2</sup>ESO programs 096.C-0388 and 097.C-0394

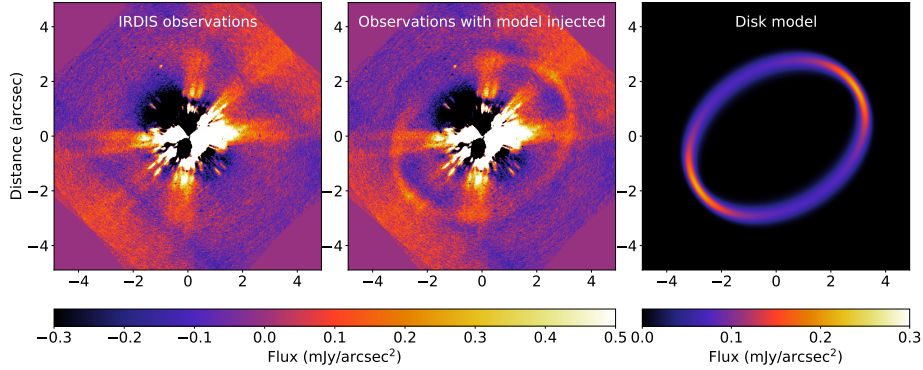


Figure 3.9: Left: final reduced image after combinations of two epochs of observation with SPHERE/IRDIS. The radially extended signal seen at four different position angles originates from the diffraction pattern of the telescope spiders, which are not entirely suppressed by the pupil stop of the Lyot coronagraph. Middle: final reduced image after injection of a disc model into the data before post-processing. Right: scattered light model injected in the data.

epochs on the nights of 11 October 2015 and 3 June 2016, with an exposure time of 40 minutes on-source for each visit. The observations were carried out in pupil-stabilised mode, however very little sky rotation was obtained (only  $1.5^\circ$ ) because the target was observed outside the meridian crossing. Angular Differential Imaging [ADI, Marois et al., 2006] is therefore not practical due to severe self-subtraction of any astrophysical signal [e.g. Milli et al., 2012]. At the expected separation of the disc of  $\sim 3.4''$ , the background noise is the main contributor to the noise. We therefore derotated the frames to align North vertically on the detector, subtracted the median azimuthal profile for each frame at each separation, and median-combined all frames to obtain the final reduced images at each epoch. We averaged the reduced images of the two epochs to produce the final image shown in Figure 3.9 (left). The disc is not detected in scattered light in the IRDIS image and we calculate a  $3\sigma$  surface brightness detection limit of  $173 \mu\text{Jy arcsecond}^{-2}$  at  $3.4''$  from the star, assuming a stellar brightness in the H band of 7.527 mag [1.01 Jy; 2MASS Cutri et al., 2003]. Post processing could change this value, so to derive meaningful constraints based on the ALMA detection, we used the median parameter Gaussian torus model of the disc to generate an image (Figure 3.9 right) that we injected into the SPHERE data. We then scaled up the image until it was clearly detected in the final reduced image (Figure 3.9 middle). We find that the integrated brightness of the model is 1.0 mJy, which represents an upper limit on the total disc scattered light brightness. The maximum surface brightness reached at the ansae of the disc is  $\sim 200 \mu\text{Jy arcsec}^{-2}$ , showing that our  $3\sigma$  surface brightness detection limit is reasonable.



### Limits on dust albedo

That the disc was not detected with either HST/STIS or VLT/SPHERE could be owing to its unfavourable viewing geometry. At an inclination of  $\sim 43^\circ$  low scattering angles are unavailable to observation, which leaves the strong forward scattering peak that can enhance disc surface brightness inaccessible. However, an upper limit on the dust albedo can still be calculated from the surface brightness upper limit averaged over all scattering angles. While this would not be an estimate of a proper Bond or geometric albedo, and while the precise effect of the scattering phase function is still unknown, this rough albedo estimate can still inform us as to whether our non-detection implies significantly nonreflective dust grains. Following the process outlined in section 3.3.3 of Marshall et al. [2018], we use the equation for reflection for optically thin dust from Weinberger et al. [1999]:

$$\tau\omega = 4\pi\phi^2 \frac{S}{F} \quad (3.2)$$

where  $\tau$  is the optical depth,  $\omega$  is the albedo,  $\phi$  is the angular separation of the scatterers from the host star (i.e. the disc semi-major axis in arcseconds),  $S$  is the surface brightness of the disc in  $\text{mJy arcsecond}^{-2}$  and  $F$  the stellar flux in mJy. We also use the approximation for optical depth:

$$\tau = \frac{2f\phi \cos(i)}{d\phi(1-\omega)} \quad (3.3)$$

where  $f$  is the fractional luminosity of the disc,  $i$  the inclination and  $d\phi$  the disc width in arcseconds. We combine the two to eliminate  $\tau$  and have:

$$S = \frac{fF\omega}{(2\pi\phi d\phi \cos(i))(1-\omega)} \quad (3.4)$$

into which we can insert our Gaussian torus model values from §3.4.3 and surface brightness upper limits to extract our albedo upper limit. From the SPHERE observations we retrieve an albedo upper limit of 0.67 at  $1.625 \mu\text{m}$  and from the STIS observations we retrieve an upper limit of 0.54 at  $0.5858 \mu\text{m}$ . Typical debris disc dust albedos range between 0.05–0.15 [e.g. Marshall et al., 2018; Choquet et al., 2018; Golimowski et al., 2011; Krist et al., 2010; Kalas et al., 2005] and typical Kuiper belt objects have average albedos of 0.11 – 0.17 [Vilenius, E. et al., 2012]; precision on this level is needed to begin distinguishing between compositional models [Marshall et al., 2018; Choquet et al., 2018]. Thus these upper limits are too high to comment on dust composition.

### 3.5 Discussion

In our ALMA observations we do not find evidence for a significant eccentricity in Fomalhaut C’s disc, and it is most likely that Fomalhaut C has a less eccentric disc than Fomalhaut A. In the context of S14’s models, the system’s history thus remains inconclusive. Figure 6 in S14 shows that in their scenario the eccentricity of Fomalhaut A’s disc should be correlated with the eccentricity of C’s disc, but with a large scatter. No definite prediction could be made for an eccentricity in C’s disc; in S14’s Figure 6 it can be seen that for A discs reminiscent of the real A with eccentricities between 0.025 and 0.5, the corresponding C disc eccentricities vary between  $\sim 0.025 - 0.75$ . Thus, our  $3\sigma$  upper limit of 0.14 cannot rule out the S14 history. However, if an eccentricity did exist below this limit, at such a magnitude the origin of the eccentricity could just as much be attributed to other factors, such as an eccentric planet within the system. A larger eccentricity would have been more unusual, thus implying an unusual cause, e.g. the S14 scenario. Further observation increasing the S/N and the precision of the offset modelling would not therefore necessarily help break the degeneracy of the Fomalhaut system’s potential histories; however, deeper observations can also reveal other observable quantities such as the dust density distribution that can also trace system dynamics.

The still indefinite history of the Fomalhaut system precludes a ruling on the ‘typicality’ of the Fomalhaut C debris disc’s brightness amongst the M star disc population, as the disc could have been additionally stirred by gravitational interactions with Fomalhaut A per S14’s scenario. With a fractional luminosity of  $1.5 \times 10^{-4}$  the disc is certainly very bright, on par with the disc around AU Mic, an earlier type M0 star that is  $\sim 1/40$  times the age. AU Mic will not retain its current brightness for the next 400 Myr, as disc mass tends to decrease over time due to collisional grinding of planetesimals and removal of dust from the system through radiation pressure, solar winds and P-R drag [Wyatt, 2008]. This does not mean that Fomalhaut C’s disc was necessarily significantly brighter in the past as the time of onset of its collisional cascade is unknown. It is still within the realm of possibility that the Fomalhaut C debris disc originated from a protoplanetary disc that formed a greater mass in planetesimals than AU Mic’s and evolved to its current state via natural collisional grinding. While Fomalhaut C is significantly older than AU Mic, in comparison to field M stars as a whole Fomalhaut C is still young at only 440 Myr old compared to ages ranging up to 10 Gyrs. A proper study of disc occurrence and comparison for M stars could select a sample of stars of similar ages, preferably young while the discs are statistically likely to be brightest.

It is however possible and useful to compare the Fomalhaut C disc’s radius with that of other resolved debris discs. Matrà et al. [2018] find a correlation between disc radius

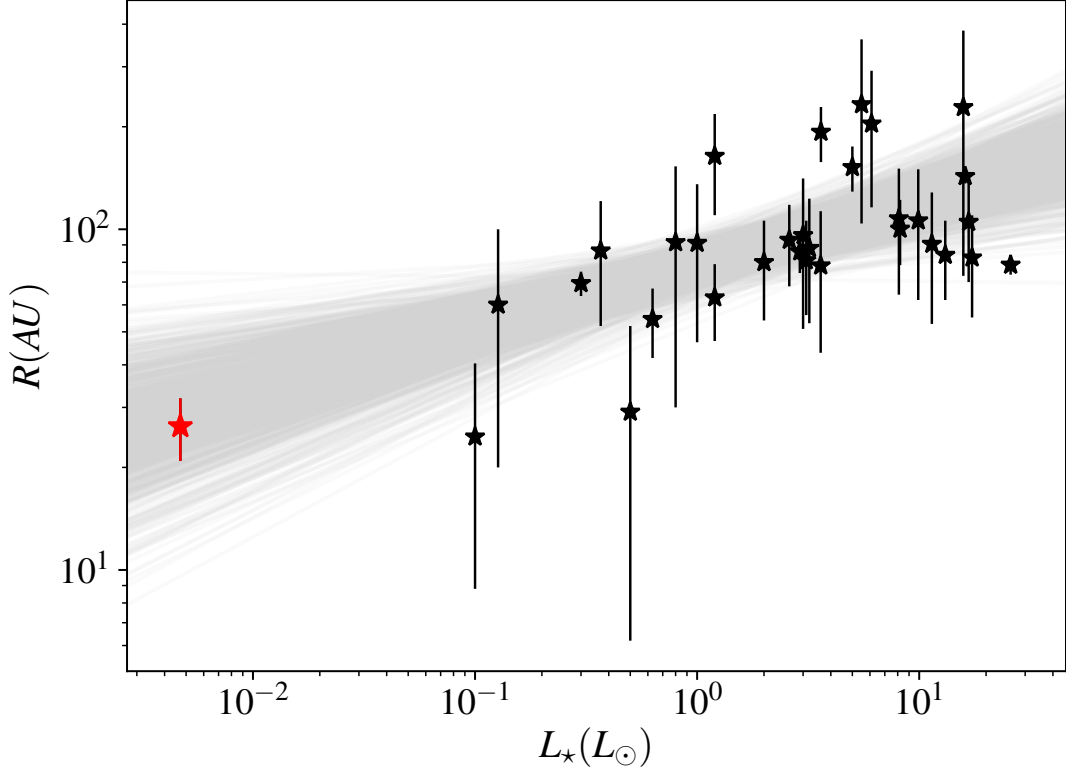


Figure 3.10: Resolved planetesimal belt radii against stellar host luminosity. The error bars represent disc widths or the upper limits thereof. Fomalhaut C is highlighted in red and the error bar represents the  $3\sigma$  limit on the disc’s FWHM. Grey lines show 1000 power laws sampled from the parameter distributions of Matrà et al. [2018].

and host star luminosity, but their sample is truncated at the low luminosity end, having no discs with hosts of lower luminosity than AU Mic, at  $0.1 L_{\odot}$ . Fomalhaut C has a luminosity of  $0.005 L_{\odot}$  and thus significantly extends the range of the parameter space. In Figure 3.10 we plot Matrà et al. [2018]’s sample, with the updates from Sepulveda et al. [2019] and references therein, and with the addition of Fomalhaut C. We also plot a representative sample of power law fits from the parameter distributions calculated by Matrà et al. [2018]. The radius of the disc around Fomalhaut C is found to be wholly consistent with the rest of the sample, lying close to the centre of the bundle of representative power laws. At least in relation to radius, the Fomalhaut C disc appears typical, but more discs around low luminosity host stars are required to fill out this region of the parameter space in order to be able to conclude that the relationship holds.

Regarding Figure 3.10 we are reminded of the context of the width of the Fomalhaut C disc; the disc is relatively narrow, similar to the likes of  $\epsilon$  Eri [Booth et al., 2017], HR 4796A [Kennedy et al., 2018b] and indeed Fomalhaut A [Kalas et al., 2005; Acke et al., 2012;

MacGregor et al., 2017]. Narrow rings are very often also offset from the stellar location [Hughes et al., 2018]. The typical eccentricities of these narrow discs are  $\sim 0.1$  and so the non-detection of an eccentricity in Fomalhaut C’s disc does not mark it as unusual for its narrowness. Postulated reasons for narrow rings can be similar to those for eccentric discs: shepherding planets for the inner and outer radii [Boley et al., 2012], which would predict sharp edges that our current resolution is unable to constrain; confinement by the orbital resonances of a single planet, like the bounds of the Kuiper belt, another narrow disc, at the 3:2 and 2:1 resonances with Neptune [Hahn and Malhotra, 2005]; or dust-gas interaction mechanisms [Lyra and Kuchner, 2013]. If the bounds of Fomalhaut C’s disc correspond to 3:2 and 2:1 resonances of an unseen planet, our model would suggest a planet at an orbital distance of  $\sim 17\text{--}20$  au.

### 3.6 Conclusions

In this work we have presented the first resolved sub-millimetre observations of the planetesimal debris disc around Fomalhaut C (§3.4.1), now the lowest mass star to have its disc resolved in thermal emission. Our modelling has revealed the geometry of the ring as well as its radius and submillimetre flux. We try three distinct models to investigate the nature of the over-brightness in the south-east quadrant of the disc and conclude that the symmetric Gaussian torus model is the best fitting (§3.4.6). We search for an offset of the centre of the disc from the stellar location but do not find any significant eccentricity, instead placing a  $3\sigma$  upper limit. Higher signal-to-noise and/or resolution observations will be necessary to improve the precision of an offset measurement and to measure the disc’s scale width and height. We also do not detect any CO gas in the system but place a  $3\sigma$  upper limit of  $17 \text{ mJy km s}^{-1}$ .

We revisit the original Herschel observations with our best-fitting ALMA model to consider a scenario where the smaller grains visible at shorter wavelengths lay at larger radii due to radiation pressure and stellar wind forces blowing them out, but do not find evidence for a small grain halo. We can conclude however that the original Herschel observations were not significantly contaminated by the compact source apparent outside of the ring in the ALMA observations (§3.4.8).

With the ring’s radius resolved we compare the disc’s blackbody radius to its resolved radius to calculate  $\Gamma = R_{\text{dust}}/R_{\text{BB}}$  and compare it to discs around stars of other spectral types. We find that Fomalhaut C’s  $\Gamma$  factor is smaller than might be expected from the trends of earlier type stars but also outline several caveats that could disrupt the trends for very low mass stars (§3.4.9).

The Fomalhaut C disc has not been detected in scattered light with either HST/STIS

in the optical or VLT/SPHERE in the near-infrared, but we use our ALMA model’s geometry to find upper limits on surface brightness and dust albedo. These limits are not constraining enough to investigate different dust composition models (§3.4.10).

The lack of a significant offset measurement precludes a judgement on the likelihood on any particular dynamical history model for the Fomalhaut triple system. In combination with the paucity of thermally resolved M star debris discs this uncertainty in history makes it difficult to rule on the disc’s typicality or to place it within the context of low mass star discs. We do place it in the context of debris discs across all types by adding it to Matrà et al. [2018]’s radius–luminosity sample and find that the Fomalhaut C’s disc radius is entirely consistent with the greater trend (§3.5).

## Chapter 4

# ALMA's view of the M-dwarf GSC 07396-00759's edge-on debris disc: AU Mic's coeval twin

### Declaration

This chapter is reproduced from the paper "*ALMA's view of the M-dwarf GSC 07396-00759's edge-on debris disc: AU Mic's coeval twin*" published in Monthly Notices of the Royal Astronomical Society, Volume 512, Issue 4, pp.4752-4764 in June 2022. All analysis and write up for this paper was performed by me except for section 4.4.3 written by Grant Kennedy, bar the final two paragraphs starting 'Overall, Figure 5 shows that the dust temperature...'. The code base for the SED and fractional-luminosity fitting used in Figure 4.4 and Figure 4.5 was created by Grant Kennedy.

### Abstract

We present new ALMA Band 7 observations of the edge-on debris disc around the M1V star GSC 07396-00759. At  $\sim 20$  Myr old and in the  $\beta$  Pictoris Moving Group along with AU Mic, GSC 07396-00759 joins it in the handful of low mass M-dwarf discs to be resolved in the sub-mm. With previous VLT/SPHERE scattered light observations we present a multi-wavelength view of the dust distribution within the system under the effects of stellar wind forces. We find the mm dust grains to be well described by a Gaussian torus at 70 au with a FWHM of 48 au and we do not detect the presence of CO in the system. Our ALMA model radius is significantly smaller than the radius derived from polarimetric scattered light observations, implying complex behaviour in the scattering phase function. The

brightness asymmetry in the disc observed in scattered light is not recovered in the ALMA observations, implying that the physical mechanism only affects smaller grain sizes. High resolution follow-up observations of the system would allow investigation into its unique dust features as well as provide a true coeval comparison for its smaller sibling AU Mic, singularly well observed amongst M-dwarf systems.

## 4.1 Introduction

Many stars are host to discs of circumstellar matter. While the host star is still very young ( $\lesssim 10$  Myrs), these discs are composed of primordial dust and gas from the initial molecular cloud, and emit light in the near-infrared to millimetre ranges. As the discs age they lose their gaseous material to leave behind some dust and any planetesimals that have formed. The collisional grinding of these planetesimals produces cold secondary dust that is observed in the far-infrared to millimetre and is classified as a debris disc [e.g. Wyatt, 2008; Hughes et al., 2018]. The dust produced by planetesimal collisions in a debris disc is constantly removed by radiation pressure as well as Poynting-Robertson drag and stellar wind forces, stellar wind forces being dominant over radiation pressure for grain removal around low-luminosity M-dwarfs [e.g. Wyatt et al., 1999; Thébault and Wu, 2008; Plavchan et al., 2005; Augereau and Beust, 2006; Reidemeister et al., 2011]. The defining observable features of a debris disc are typically a fractional luminosity  $L_{\text{disc}}/L_{\star}$  of  $\leq 10^{-2}$ , a lack of large amounts of warm dust emitting in the near-IR, and a lack of large quantities of  $\text{H}_2$  gas. If any gas is present, e.g. CO, it is usually considered to be secondary, having also been released by planetesimal collisions [e.g. Marino et al., 2016; Matrà et al., 2017; Kral et al., 2019; Matrà et al., 2019a].

The Herschel DEBRIS survey detected debris discs around 17 percent of nearby main sequence FGK-type stars [Sibthorpe et al., 2018], but found only 2 discs from 89 M-dwarfs [Lestrade et al., 2012; Kennedy et al., 2013]. However, a later Herschel survey of 21 planet-hosting late-type stars, of which 18 were M-dwarfs, with approximately twice the sensitivity to fractional luminosity as the DEBRIS survey detected 3 discs [Kennedy et al., 2018b]. There is thus an open question [e.g. Plavchan et al., 2005, 2009; Gautier et al., 2007; Heng and Malik, 2013; Binks and Jeffries, 2017; Luppe et al., 2020] as to whether so few M-dwarf discs have been detected because they represent a fundamentally rarer and/or lower mass population to those of earlier type hosts, or whether the low luminosity of the host M-dwarfs, resulting in low disc fluxes and temperatures, hinders a similar population from being detectable. Later type stars have a measured increase in planet occurrence rate [e.g. Bonfils et al., 2013; Dressing and Charbonneau, 2015; Mulders et al., 2015], which hints that perhaps efficient planet formation can affect the incipient debris disc by using up

rocky material. Alternative scenarios for decreasing disc occurrence around late type stars include material stripping from stellar encounters [Lestrade et al., 2011], photoevaporation of the primordial disc while the star is still present within its early cluster environment [Adams et al., 2004] and removal of dust by stellar-wind drag [Plavchan et al., 2009]. With so few known M-dwarf discs, it is important then to understand as fully as possible the discs that we do know and that we have well imaged.

For a long period of time, the well imaged representative of M-dwarf discs has been the M1V star AU Microscopii. The excess of infrared radiation, the hallmark of circumstellar material, of AU Mic was first detected with IRAS [Moshir et al., 1990]. Only  $9.72 \pm 0.04$  pc [Gaia Collaboration et al., 2018] distant and with a fractional luminosity of  $4 \times 10^{-4}$  [Matthews et al., 2015], AU Mic has been subject to detailed study ever since at a range of wavelengths observing both thermal emission and optical/Near-IR scattered light [e.g. Kalas et al., 2004; Augereau and Beust, 2006; Graham et al., 2007; MacGregor et al., 2013; Schneider et al., 2014; Matthews et al., 2015; Wang et al., 2015; Wisniewski et al., 2019]. These high-resolution multi-wavelength views have resulted in myriad discoveries about the disc’s physics. For example, Strubbe and Chiang [2006] devise a ‘birth ring’ model for AU Mic where a parent population of planetesimals at 43 au produces micrometer size dust grains that are then transported inwards by stellar wind drag and Poynting-Robertson drag, and outwards by radiation pressure and stellar wind ram pressure. Boccaletti et al. [2015, 2018]; Grady et al. [2020] observe fast moving dust features in scattered light travelling outwards along the disc, possibly dust ‘avalanches’ originating from the point of intersection of the birth ring and a second, inclined ring leftover from the catastrophic disruption of a large planetesimal [Chiang and Fung, 2017] or material released from a parent body on a Keplerian orbit closer to the star [Sezestre et al., 2017]. Daley et al. [2019] were able to estimate the sizes and masses of bodies within the disc through resolving its vertical structure.

These works highlight the value of obtaining resolved images in both thermal emission and scattered light. Fomalhaut C is as of yet the only other M-dwarf to have a fully resolved debris disc in thermal emission [Cronin-Coltsmann et al., 2021]. However the disc was not detected with either HST/STIS nor VLT/SPHERE, the star is twenty times the age of AU Mic and the system may have a complicated disc-affecting dynamical history with its associated stars Fomalhaut A and B [Shannon et al., 2014]. The complexity of the Fomalhaut system precludes Fomalhaut C from being a good representative. With so much learned from the single system of AU Mic, it becomes increasingly valuable to have true coeval systems to compare AU Mic with and so that what we know of AU Mic’s disc can be put into context.

As debris discs age, they deplete their reservoirs of planetesimals and are able to



replenish less and less dust, meaning over time they become less bright [Decin et al., 2003; Rieke et al., 2005]. In part, AU Mic owes its large fractional luminosity to its youth. AU Mic is a member of the  $\beta$  Pictoris Moving Group (BPMG), a young [ $\sim 20$  Myr, Bell et al., 2015; Miret-Roig et al., 2020] and nearby [ $\lesssim 100$  pc, Shkolnik et al., 2017] association of stars. Pawellek et al. [2021] find a 75% occurrence rate of discs around F type stars in the BPMG, a significantly higher rate than for field stars.

An excellent place to search for AU Mic analogues is thus the BPMG, from which recently the late-type K7/M0 star CPD-72 2713 [Moór et al., 2020; Tanner et al., 2020] and the K1 star BD+45° 598 [Hinkley et al., 2021] have also recently had debris discs identified. 35 M-dwarfs in the BPMG have recently been observed in Band 7 with ALMA (Cronin-Coltsmann et al. in prep), yielding several new detections and one resolved disc. This resolved disc is GSC 07396-00759, an M1V star at a distance of 71.4 pc. No WISE mid-IR excess is detected for GSC 07396-00759, nor for AU Mic, making ALMA the best option for both detection and characterisation of such M-dwarf debris discs. The disc of this star has been previously imaged in near-IR scattered light with VLT/SPHERE IRDIS in both total intensity [Sissa et al., 2018, hereafter S18; IRDIFS H2/H3] and polarimetric [Adam et al., 2021, hereafter A21; IRDIS DPI] modes, and is now detected for the first time in thermal emission. With a host star of similar spectral type and from the same young moving group, and therefore of very similar age, in addition to the disc being edge on, resolved in the sub-mm and well imaged in scattered light, GSC 07396-00759’s disc is a near perfect twin to AU Mic’s, finally providing a coeval comparison.

S18’s total intensity scattered light observations are subject to a strongly forward-scattering phase function that accentuates the brightness of the disc at small scattering angles and dims outer reaches off the major-axis. They find that the observed disc spine can be geometrically described up to  $1.2''$  by an unflared disc of radius 96 au and an inclination of  $84.5 \pm 3.6^\circ$  as they demonstrate in the lower panel of their Figure 2. They find a large brightness asymmetry, with the disc appearing brighter in the south-east by a factor  $\sim 1.5$ -2. They also find ripples along the spine of the disc, and in the outer ranges of the disc they observe evidence of warp-like swept-back material, reminiscent of the swept-back ‘wings’ of HD 61005 [e.g. Schneider et al., 2014; Olofsson et al., 2016].

S18 then forward model the volumetric dust density distribution  $n(r, z)$ , as a double power law (see Equation 4.2) and find that the disc density peaks at  $r_0 = 70 \pm 1$  au and has a profile that is as expected from dust produced in a birth ring and pushed out by strong radial forces [Strubbe and Chiang, 2006].

A21 also observe disc emission extending to  $1.3''$  (93 au), as well as a moderate brightness asymmetry by a factor  $\sim 1.4$ -1.6, and evidence of a warp in the disc on the north-west side. In contrast to S18, A21 model the disc as dust grains originating from a

parent planetesimal belt at a radius  $r_0$  with a Gaussian scale width  $\delta_r$ , equivalent to our Equation 4.1. The dust grains then populate orbits defined by their interaction with stellar wind and radiation pressure forces before the scattering phase function is applied to derive the models to compare with the data.

Through their modelling A21 find disc properties consistent with S18 except for a disc radius of  $107 \pm 2$  au, but they find a degeneracy between their model radius and the anisotropic scattering factor  $g$ , which for higher values weights scattering efficiency to smaller scattering angles. A larger, more forward scattering  $g$  diminishes flux at the ansae and focuses it at the disc centre, allowing for a larger model radius while still accurately describing the data. A21 do rerun their modelling with the disc radius fixed to the S18 result of 70 au, and indeed a lower  $g$  is then fitted, however the model residuals are noticeably poorer in the outer reaches of the disc: the lower radius model describes their data less well.

A21 conclude that their new 107 au estimate of the reference radius, i.e. the birth ring of planetesimals, is likely a better estimate than S18’s 70 au radius. Both S18’s and A21’s best-fitting model parameters can be found in Table 4.1.

Sub-mm observations trace larger dust grains that are less affected by pressure forces and retain their orbits closer to where they were produced, thus tracing more directly the location of the planetesimal birth ring. Resolved sub-mm observations such as those presented in this paper serve a key role in breaking the degeneracy between  $g$  and  $r_0$  and solving the discrepancy between the total intensity and polarimetric scattered light model radii.

GSC 07396-00759 is itself a wide separation companion of the well-studied close-binary V4046 Sgr at a distance of 12300 au [Torres et al., 2006; Kastner et al., 2011]. V4046 Sgr possesses both a gas-rich circumbinary disc and evidence of ongoing accretion [e.g. Stempels and Gahm, 2004; Öberg et al., 2011; Rosenfeld et al., 2013; Rapson et al., 2015; Kastner et al., 2018; D’Orazi et al., 2019; Martinez-Brunner et al., 2022]. The survival of the more primordial-like disc of V4046 Sgr may be attributed to its binary nature, as Alexander [2012] find close binaries to possess longer lived discs than single stars. Nevertheless, the association of the two systems draws into question the nature of the disc around GSC 07396-00759 which the new ALMA observations presented herein can shed further light on.

This paper presents the new Band 7 ALMA observations of GSC 07396-00759 in §4.2, followed by a description of the modelling process and modelling results in §4.3 and §4.4. In §4.5 we present our analysis with respect to the previous scattered light observations and we place the disc in the context of both the growing M-dwarf disc population and the wider debris disc population across spectral types.

## 4.2 ALMA Observations

GSC 07396-00759 was observed with ALMA in Band 7 (0.87 mm, 345 GHz) on April 6th 2018 under project 2017.1.01583.S as part of a larger survey of M-dwarfs in the  $\beta$  Pictoris Moving Group (Cronin-Coltsmann et al. in prep). The observation used baselines ranging from 15 to 484 m and 43 antennae. The average precipitable water vapour was  $\sim 0.75$  mm. The total on source observing duration was 16 minutes. QSOs J1826-2924 and J1924-2914 were used for atmospheric and water vapour radiometer calibration; J1826-2924 was used for phase calibration; J1924-2914 was used for pointing, flux and bandpass calibration.

The spectral setup comprised four windows centred on 347.937, 335.937, 334.042 and 346.042 GHz with bandwidth 2 GHz and 128 channels for all but the last with width 1.875 GHz and 3840 channels. The last window was used to search for CO gas via the J=3-2 emission line, which has also been detected in another young debris disc around the M-dwarf TWA 7 [Matrà et al., 2019a].

The raw data were calibrated with the provided ALMA pipeline script in CASA version 5.1.2-4 [McMullin et al., 2007]. To reduce the data volume the visibilities were averaged in 30 second intervals and down to two channels per spectral window for the continuum imaging. All images were generated with the CLEAN algorithm in CASA.

### 4.2.1 Continuum Analysis

Figure 4.1 shows a CLEAN image of GSC 07396-00759's disc. We use natural weightings to maximise the signal to noise ratio (S/N), having found that other weighting schemes do not provide a significant enough improvement in beam size to justify their loss in S/N. This weighting gives a synthesised beam with major and minor full width at half maxima (FWHM) of  $0.68''$  (48.6 au) and  $0.55''$  (39.3 au) respectively and a position angle (PA) of  $66.4^\circ$ . We identify the standard deviation in an annulus exterior to the disc to be  $\sigma = 40 \mu\text{Jy beam}^{-1}$ . This noise is uniform throughout the central area where the disc is detected and the primary beam correction there is  $< 10\%$ .

The disc is detected along the majority of its profile with at least  $4\sigma$  and detection peaks at  $10\sigma$  at the disc ansae. It is apparent that the flux constitutes a highly inclined ring with a radius of  $\sim 1''$  and a position angle of  $\sim -30^\circ$ ; the disc is unresolved along the minor-axis and the emission perpendicular to the major-axis appears to have a scale similar to the beam size, thus limiting the disc's maximum vertical extent to within 50 au. The disc is radially resolved, as shown in Figure 4.2. The dip in the profile of the disc at  $\sim 1''$  on the north-west side is on the scale of the beam, and therefore is likely the result of noise. As the south-east side only peaks  $1\sigma$  higher than the north-west, resulting in a difference in integrated flux of  $\sim 10\%$  with integrated fluxes of  $\sim 0.88$  mJy and  $\sim 0.80$  mJy respectively,

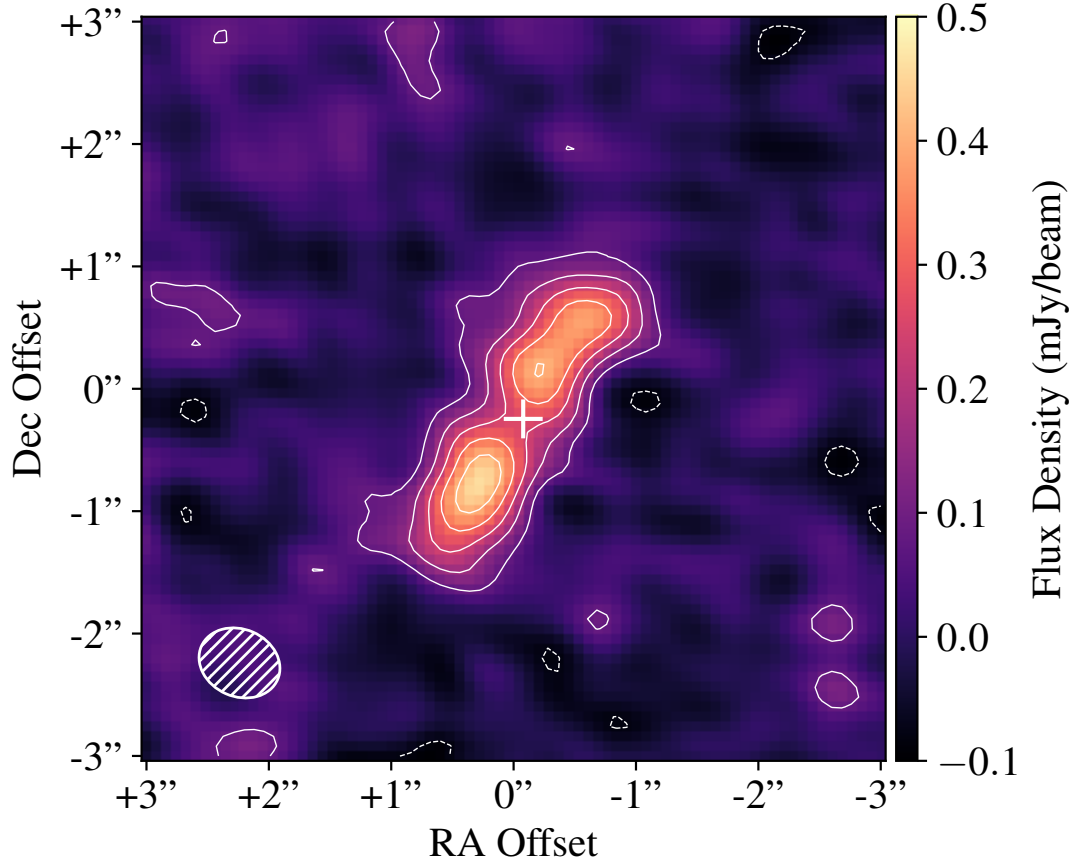


Figure 4.1: Naturally-weighted `CLEAN` image of the disc around GSC 07396-00759. The ellipse in the lower left corner shows the beam size of  $0.68 \times 0.55''$ . The star is not detected. At a distance of 71.4 pc the apparent disc radius is  $\sim 70$  au. Contours are drawn at  $\pm 2\sigma, 4\sigma, 6\sigma, 8\sigma, 10\sigma$  with  $1\sigma = 40 \mu\text{Jy beam}^{-1}$ . The Gaia location of the star is marked with a + at  $273^\circ 35' 31.2'' \pm 0.26$  mas  $-32^\circ 46' 11.09'' \pm 0.20$  mas. Zero offset is the ALMA image phase centre at  $273^\circ 35' 31.3'' -32^\circ 46' 10.9''$  (J2000).

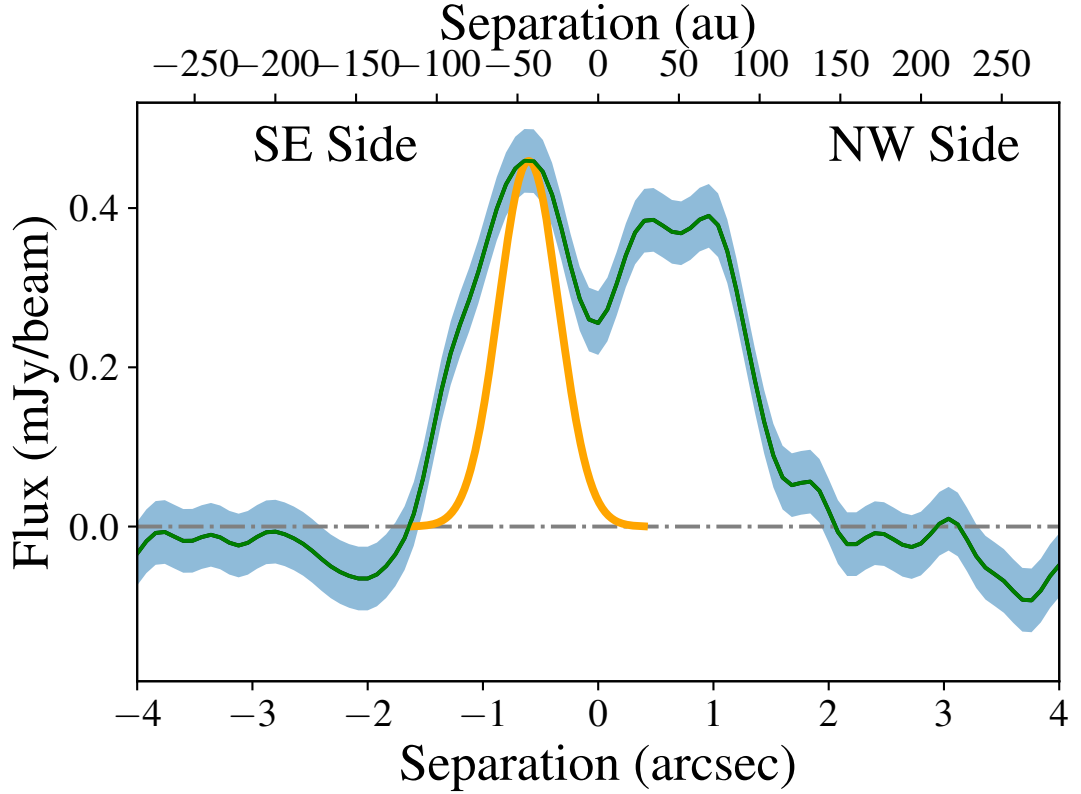


Figure 4.2: Profile of the disc along its major-axis; the flux of the centre pixel along the disc major-axis is plotted in green, blue swathes show the RMS and a Gaussian with the same FWHM as the beam is plotted in orange at the peak radial flux. Zero separation is the best fitting model centre from §4.3.

we conclude that there is not strong evidence of asymmetry, but note that it was the south-east side that was significantly brighter in the scattered light observations of S18 and A21.

### 4.3 Modelling

To extract probability distributions of the disc parameters we fit models directly to the u-v ALMA data. This is done by first creating a 3-dimensional disc model. A rotation from sky coordinates to model coordinates is calculated and used to find the corresponding model coordinate for each pixel in a volume centred on the star, and the given parameters are consulted to identify the model flux at each pixel location. This model disc is then collapsed into the sky plane in order to create a 2-dimensional image<sup>1</sup>. We use the `GALARIO` package [Tazzari et al., 2018] to Fourier transform this image and to sample the u-v locations of the data to calculate a  $\chi^2$ . Posterior probability distributions of the model parameters are

<sup>1</sup><https://github.com/drgmk/alma>

explored with the `EMCEE` package [Foreman-Mackey et al., 2013], an implementation of the Markov Chain Monte Carlo method in Python. We initiate our models near the solutions of previous test runs. We use 3000 steps and discard the first 2700 as the maximum auto-correlation length of the parameter chains is 270 steps. We use 100 walkers and verify that all the chains have converged upon completion.

We first implement a simple **Gaussian** torus model, with parameters defined by the following equation for a model dust volume density distribution  $n(r, z)$ :

$$n(r, z) \propto e^{-\frac{1}{2}\left(\frac{r-r_0}{\sigma_r}\right)^2} \times e^{-z^2/2h^2} \quad (4.1)$$

where  $r_0$  is the radius of peak flux,  $\sigma_r$  is the Gaussian scale width (where the FWHM is  $2.355 \times \sigma_r$ ) and  $h = r \times \tan(\psi)$  and where  $\psi$  is disc opening angle. In their scattered light modelling S18 use a fixed  $\psi$  of 0.04, found by Thébault [2009] to be the ‘minimum natural observed aspect ratio’ for dust grains observed at visible to mid-IR wavelengths. Dust grains observed at mm wavelengths whose orbits are not affected by radial forces are not expected to conform to this minimum aspect ratio, however trialling a similar model with  $\psi$  as a free parameter finds  $\psi$  unresolved in the ALMA data with a  $3\sigma$  upper limit of 0.18. We thus choose to fix  $\psi$  to 0.04 in our modelling for consistency with the modelling of S18.

Our second model follows the equation used in S18 for direct comparison, i.e. a **Double Power Law** with different density slopes interior and exterior to  $r_0$ :

$$n(r, z) \propto \left[ \left( \frac{r}{r_0} \right)^{-2a_{\text{in}}} + \left( \frac{r}{r_0} \right)^{-2a_{\text{out}}} \right]^{-1/2} \times e^{-z^2/2h^2} \quad (4.2)$$

where  $a_{\text{in}}$  and  $a_{\text{out}}$  are the inner and outer slopes respectively.

Both models possess a parameter for the total flux of the disc as well as an inclination, a position angle and RA and Declination (Dec) offsets of the disc model centre from the ALMA phase-centre. The ALMA phase-centre is found to be slightly offset itself from the Gaia DR2 [Gaia Collaboration et al., 2016, 2018] location of the star at the time of observation. All subsequent reported offsets have had that Gaia to phase-centre offset subtracted such that the offset measurements are relative to the Gaia location at the time of observation. We also include a parameter for scaling the weightings of the u-v data points as their absolute uncertainty can be offset as described in Matrà et al. [2019b] and Kennedy [2020].

We calculate a naïve ‘plane-of-sky’ eccentricity of the disc by simply taking the offset vector in the plane of the sky and dividing by the disc radius, and use the given offset and radius posteriors to form a posterior distribution of eccentricities with uncertainty reported that includes the uncertainty of ALMA’s astrometric precision (calculated per §10.5.2 of

the ALMA Cycle 6 Technical Handbook<sup>2</sup>, to give 0.036''); the Gaia astrometric precision is negligible in comparison at 0.33 mas. As the disc is highly inclined, we cannot accurately discern any offset perpendicular to the plane of the sky. Because the true eccentricity,  $e$ , could be larger if the pericenter were not 90° to the line of sight (i.e. if  $\omega$ , the argument of pericentre, is not equal to 0°), we do not quote an eccentricity measurement in Table 4.1, and we instead provide a  $3\sigma$  upper limit on  $e \cos(\omega)$ , i.e. the projection of the eccentricity vector along the major-axis of the disc. This upper limit is derived from the offset posterior distribution after the dot product is taken between the offset vector and the unit vector of the major-axis of the disc.

---

<sup>2</sup><https://almascience.nrao.edu/documents-and-tools/cycle6/alma-technical-handbook>

Table 4.1: Median disc parameters,  $\Delta\chi^2$  and  $\Delta\text{BIC}$  values for Gaussian and double power law models. Best fitting parameters for S18’s total intensity scattered light modelling and A21’s polarimetric scattered light modelling are also included for comparison. Uncertainties are the 16th and 84th percentiles. Offsets are measured from the disc model centre to the Gaia DR2 location of the star at the time of observation. Upper limits are at  $3\sigma$  above the mean, i.e. the 99.87th percentile. The disc flux uncertainty includes the 10% ALMA flux calibration uncertainty. The  $e \cos(\omega)$  upper limit includes the ALMA astrometric precision. The  $e \cos(\omega)$  upper limit is calculated from the projection of the offset vector along the major-axis of the disc.  $\Delta\chi^2$  and  $\Delta\text{BIC}$  values relative to Gaussian model with values 721281.0 and 721384.6 respectively, calculated from a model produced using the median parameters.

| Parameter                              | Gaussian               | Double Power Law       | Total Intensity Scattered Light | Polarimetric Scattered Light |
|--|------------------------|------------------------|---------------------------------|------------------------------|
| RA Offset (")                          | $0.06^{+0.03}_{-0.03}$ | $0.06^{+0.03}_{-0.03}$ | —                               | —                            |
| Dec Offset (")                         | $0.00^{+0.04}_{-0.04}$ | $0.00^{+0.04}_{-0.03}$ | —                               | —                            |
| $e \cos(\omega)$ $3\sigma$ Upper Limit | 0.17                   | 0.16                   | —                               | —                            |
| Inclination ( $^\circ$ )               | $85^{+3}_{-3}$         | $85^{+3}_{-3}$         | $82.7^{+0.1}_{-0.1}$            | $84.3^{0.3}_{-0.3}$          |
| PA ( $^\circ$ )                        | $-32^{+1}_{-1}$        | $-32^{+1}_{-1}$        | $-31.1^{+0.1}_{-0.1}$           | $-31.3^{+0.7}_{-0.7}$        |
| Disc Flux (mJy)                        | $1.84^{+0.22}_{-0.21}$ | $1.83^{+0.21}_{-0.21}$ | —                               | —                            |
| Radius (au)                            | $70.2^{+4.1}_{-4.7}$   | $77.7^{+8.0}_{-7.1}$   | $69.9^{+0.9}_{-0.8}$            | $107^{+2}_{-2}$              |
| Scale Width (au)                       | $20.3^{+4.3}_{-4.1}$   | —                      | —                               | $27^{+1}_{-1}$               |
| $\alpha_{in}$                          | —                      | $3.5^{+4.5}_{-1.9}$    | $2.8^{+0.2}_{-0.2}$             | —                            |
| $\alpha_{out}$                         | —                      | $-8.9^{+1.9}_{-2.0}$   | $-2.6^{+0.1}_{-0.1}$            | —                            |
| $N_{\text{Parameters}}$                | 8                      | 9                      | —                               | —                            |
| $\Delta\chi^2$                         | 0                      | +1.9                   | —                               | —                            |
| $\Delta\text{BIC}$                     | 0                      | +14.9                  | —                               | —                            |



## 4.4 Results and analysis

### 4.4.1 Gaussian torus model

This simple model serves as the default hypothesis, tracing an azimuthally symmetric parent planetesimal belt or ‘birth ring’ localised to one radius and with a radially symmetric dust distribution about that radius. Given the spatial resolution, the use of a Gaussian is not specific; equally a top-hat distribution or single-power law could have been used [e.g. Kennedy et al., 2018b]. The important factors for the radial dust distribution are radial symmetry and a measure of disc width. The best-fitting parameters are presented in Table 4.1 along with those of the double power law model and S18 and A21’s scattered light models. The corner plot derived from the modelling is presented in Figure 4.10. We show a dirty image of the residuals after subtraction of a model formed from the medians of the posterior-parameter distribution, with the model contours overplotted, in Figure 4.3 left. Figure 4.3 left also contains an inset showing the distribution of model disc centres in comparison to the stellar location and ALMA astrometric precision.

The residuals show no remaining structure, demonstrating that an azimuthally and radially symmetric model fits the data well. Only a single  $2\sigma$  residual overlaps with the bounds of the disc, a negative residual in the north-west. At  $1-2\sigma$  this feature is likely noise and accounts for the shape of the disc profile, Figure 4.2.

We use the median-parameter model to calculate a  $\chi^2$  value of 721281.0 as well as calculating the Bayesian Information Criterion [BIC; Schwarz, 1978] of 721384.5. The BIC penalises models for including extra parameters to identify whether an improvement in  $\chi^2$  is justification to conclude a model is a significantly better fit to the data. It is defined as  $BIC = \chi^2 + N_{\text{Parameters}} \times \ln N_{\text{dof}}$ , and as we fit to a large number of visibilities ( $N_{\text{dof}} = 2 \times N_{\text{vis}} = 2 \times 209496$ ) the inclusion of even a single extra parameter imposes a large penalty. A  $\Delta BIC$  of greater than 6 is considered ‘strong’ evidence and a  $\Delta BIC$  of greater than 10 is considered ‘decisive’ evidence that the lower valued model is significantly preferred to fit the data [Kass and Raftery, 1995].

The median parameters of this disc model largely align well with the parameters found from S18’s and A21’s scattered light modelling. The model inclination and position angle are within  $1\sigma$  of both. Our radius measurement is in significant agreement with the S18 model and significant disagreement with the A21 model. Our limit on the disc’s Gaussian scale width is found to be consistent with A21’s measurement.

We measure a median offset from the stellar position to the disc model centre of  $5.0^{+2.1}_{-1.7}$  au (before combination with the  $\sim 2.6$  au ALMA astrometric uncertainty), visualised in the inset of Figure 4.3 left, this results in a median eccentricity of  $0.08^{+0.05}_{-0.04}$  (after combination with the ALMA astrometric uncertainty). The distribution of offsets is more

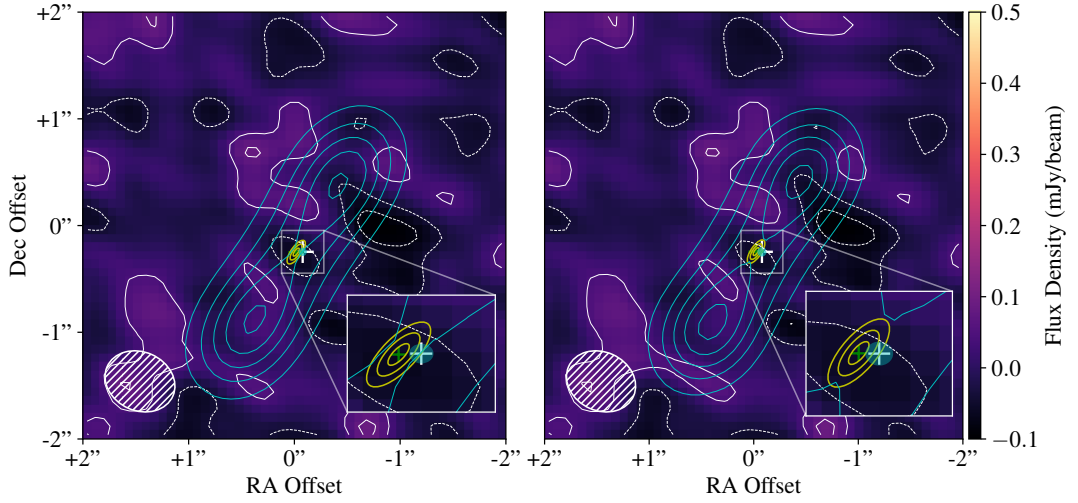


Figure 4.3: Naturally-weighted dirty images of the residuals after subtracting the individual models. Left: Gaussian model; Right: double power law model. Cyan contours show the models at  $2\sigma$ ,  $4\sigma$ ,  $6\sigma$ ,  $8\sigma$ ,  $10\sigma$  and white contours show the residuals at  $-1\sigma$ ,  $-2\sigma$ ,  $1\sigma$ ,  $2\sigma$ . The location of the star is marked with a +. Zero offset is the ALMA image phase centre at  $273^{\circ}35'31.3'' - 32^{\circ}46'10.9''$  (J2000). The inset shows a zoom near the star to illustrate that the disc model centre uncertainty (yellow contours at  $1\sigma$ ,  $2\sigma$ ,  $3\sigma$ ) and the ALMA astrometric precision (grey circle centred on the stellar location,  $1\sigma$ ) are large enough that an offset is not significantly detected.

constrained perpendicular to the major-axis of the inclined disc as smaller shifts in offset in this direction will move comparatively more flux out of the bounds of the disc. Given our modelling uncertainty and the sizeable ALMA astrometric uncertainty we conclude that this measurement is not significant evidence of underlying eccentricity. If an offset is present at this magnitude, a higher resolution observation with smaller parameter uncertainty and a smaller pointing uncertainty would be able to make a significant measurement. We can instead place a  $3\sigma$  upper limit on eccentricity along the major-axis of the disc,  $e \cos(\omega)$ , of 0.17.

At this wavelength (0.87 mm) we measure the flux of the disc to be  $1.84^{+0.22}_{-0.21}$  mJy (the uncertainties of which have been combined in quadrature with the 10% ALMA flux calibration uncertainty), which informs our SED modelling in §4.4.3.

#### 4.4.2 Double power law model

This model serves as a direct comparison to S18's scattered-light model, to investigate whether the distribution of millimetre sized dust grains, visible in sub-mm thermal emission, overlaps with, or is similar in shape to, the distribution of micrometre sized dust grains, visible in the scattered light.

Figure 4.3 right displays the dirty residual image for this model. It is immediately apparent that the two models produce nearly indistinguishable residuals, and this is attested to in the broad similarities of the parameter distributions. The only significant departure between the two models is the larger radius of the double power law model, although this comes with almost twice the uncertainty in values and remains consistent with the previous measurement. The median eccentricity of  $0.07^{+0.03}_{-0.03}$  and the  $e \cos(\omega)$  upper limit of 0.16 are both slightly smaller than the Gaussian’s model, but not significantly.

A steep outer slope of  $\alpha_{\text{out}} \sim -9$ , which is incongruous with S18’s scattered light model, is found for this model which necessitates a larger radius to still account for the flux most distant from the centre. The Gaussian distribution is comparatively wider and so can account for this flux without extending the radius, at the cost of a slightly increased concentration of flux at the centre. A shallower outer slope would increase the flux at this distant range, but would also necessarily increase the flux beyond it, which would be inconsistent with the data. This steep outer slope demonstrates a lack of evidence for millimetre dust grains beyond a confined birth ring, i.e. the radial forces of the system are too weak to transport the millimetre dust grains as they have for the micrometre dust grains.

The inner slope measurement is more similar to the scattered light model, but has a very large uncertainty and so is not significant evidence of physical similarity.

The double power law model is largely degenerate as shown in the modelling corner plot in Figure 4.11. Radius is degenerate with both  $\alpha_{\text{in}}$  and  $\alpha_{\text{out}}$ , and  $\alpha_{\text{in}}$  and  $\alpha_{\text{out}}$  are degenerate with each other: a smaller radius with steeper  $\alpha_{\text{in}}$  and shallower  $\alpha_{\text{out}}$  fits the data as well as a larger radius with shallower  $\alpha_{\text{in}}$  and steeper  $\alpha_{\text{out}}$ .

This model is found to have both a larger  $\chi^2$  and a significantly larger BIC, these measures together with the significant degeneracies of the model, the large uncertainties in the unique parameters  $\alpha_{\text{in}}$  and  $\alpha_{\text{out}}$ , and the similarity of the residual images, allow us to conclude that the model is unnecessarily complicated given the data.

#### 4.4.3 Flux density distribution and fractional luminosity modelling

In addition to the ALMA observations reported here, GSC 07396-00759 has been observed with Gaia [Gaia Collaboration et al., 2016, 2018], 2MASS [Skrutskie et al., 2006], and WISE [Wright et al., 2010], which we use to constrain the properties of the stellar photosphere and disc using the Spectral Energy Distribution (SED) fitting method described by Yelverton et al. [2019].

However, without spectral data points in the far-infrared from instruments such as Spitzer/MIPS or Herschel/PACS/SPIRE, the disc SED is poorly constrained. Figure 4.4 demonstrates this problem with an example 50K blackbody distribution plotted through the measured ALMA flux; with only a single data point for the disc’s thermal emission, in the

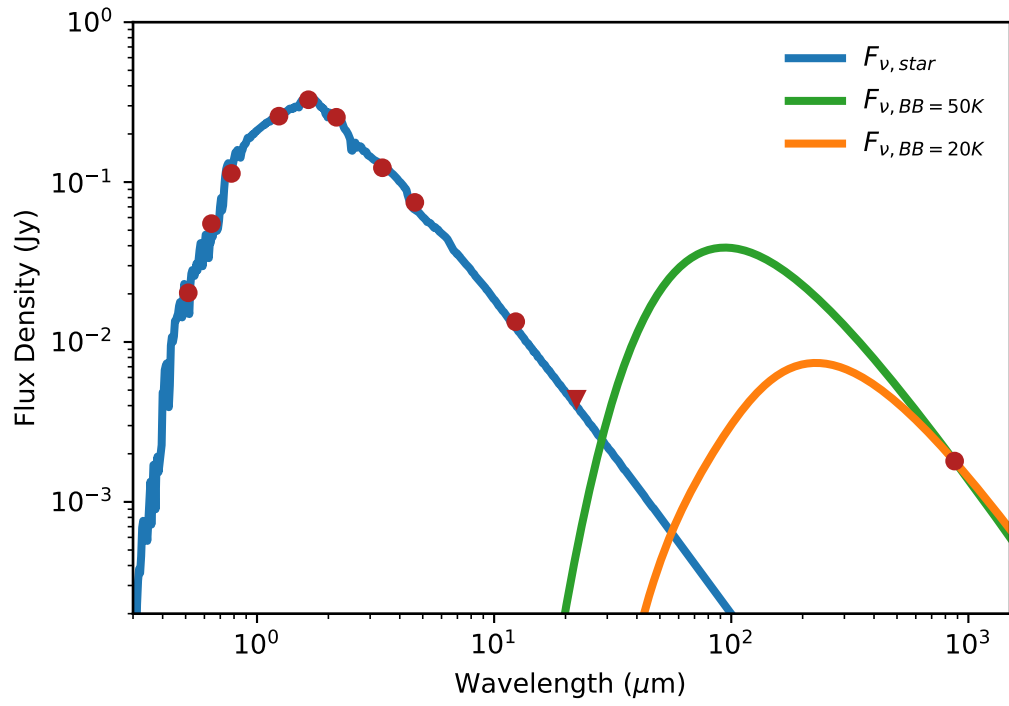


Figure 4.4: Example flux density distribution (SED) for the disc of GSC 07396-00759. Dots are measured fluxes and triangles are  $3\sigma$  upper limits. The stellar photosphere model is in blue and example blackbody distributions at 20 and 50 K are fitted through the ALMA flux in orange and green respectively. With only one flux point measuring the thermal emission of the disc, a large range of temperatures and fractional luminosities could describe the disc.

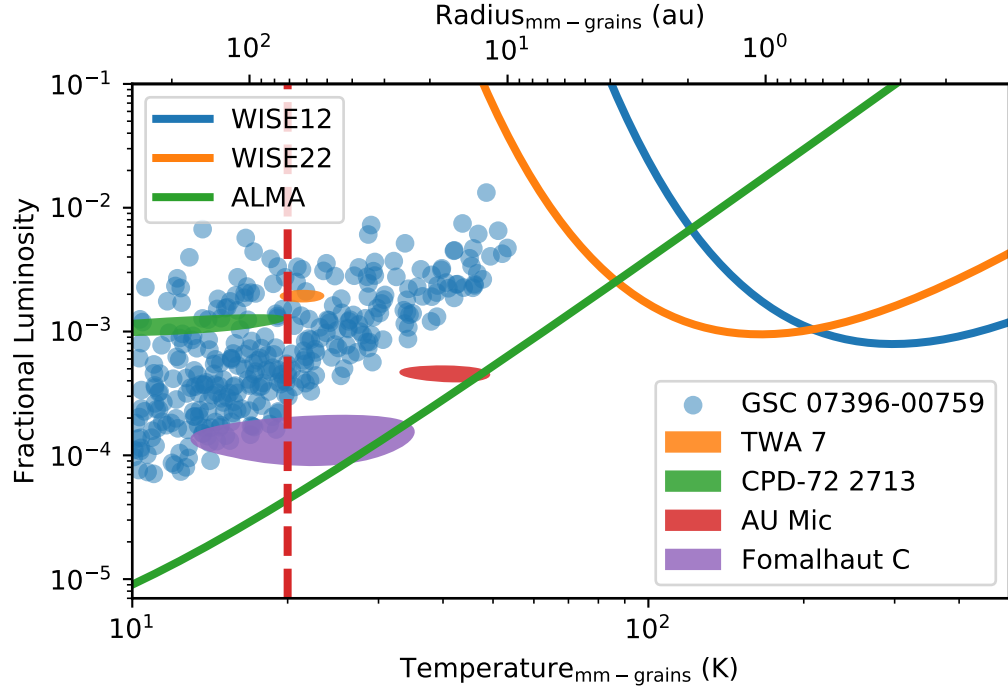


Figure 4.5: Plot of fractional luminosity against representative temperature/blackbody radius, i.e. the temperature and stellocentric radius of mm grains. Blackbody radius depends on host stellar temperature and is thus only accurate for GSC 07396-00759. A selection of allowed models for the disc of GSC 07396-00759 are plotted as blue circles. The distributions up to  $3\sigma$  following the same SED fitting procedure are shown for a selection of low mass host debris discs as coloured ellipses. The detection limits for the WISE 12 micron band, WISE 22 micron band and ALMA Band 7 are plotted as blue, orange and green curves respectively. The vertical red dashed line is placed at 70.2 au, our best-fitting radius for GSC 07396-00759’s disc.

sub-mm at the tail of the distribution, a large range of disc temperatures and luminosities can be fitted. Some constraints are still possible, as a dust temperature significantly greater than 50K would result in greater mid-infrared emission than is observed with WISE.

To provide a stronger constraint on fractional luminosity and temperature we model the disc emission with a more physical model using realistic grain optical properties and a size distribution [e.g. Augereau et al., 1999; Wyatt and Dent, 2002]. Here we assume astronomical silicates [Draine and Lee, 1984], though our results are fairly insensitive to the choice of grain properties. To compute the spectrum of a single disc model, we assume all dust resides at a single stellocentric distance, but that grains of each dust size have a temperature that depends on their size (dictated by their wavelength-dependent emission efficiency). All grain sizes between the minimum size  $D_{\min}$  and a maximum size of 10 cm are summed, with weights set by the size distribution slope  $q$  (where  $dN/dD \propto D^{2-3q}$ ). Here we restrict models to  $10/6 < q < 12/6$ ; below the lower bound  $\sigma_{\text{tot}}$  becomes dominated by large grains, and above the upper bound mass is concentrated in small grains, neither of which is thought to be the case for debris discs. The remaining parameter is the total surface area of emitting dust  $\sigma_{\text{tot}}$ . Given an individual disc model, the fractional luminosity can be computed by integrating the disc spectrum and dividing by the stellar luminosity. For our purposes here the benefit of this model compared to a simple modified blackbody is that the mm-wave spectral slope is restricted by reasonable assumptions about the size distribution.

To constrain the disc properties we model the optical/IR and ALMA photometry with a star + disc model. The stellar parameters of GSC 07396-00759 are well-constrained, but the disc properties are not, with  $D_{\min}$ ,  $q$ , and  $\sigma_{\text{tot}}$  spanning a wide range of parameter space. However, because our method uses MultiNest [Feroz et al., 2009], the resulting distribution of disc parameters can be used to illustrate the allowed disc properties in terms of fractional luminosity and temperature, as shown in Figure 4.5. While grains for any individual model have a range of temperatures, on this plot the temperature refers to the coolest grains, i.e. the grains on the scale of millimetres that have efficient emission of mm-wave radiation, which have the same temperature as a blackbody. While the fractional luminosity would follow a single locus for a pure blackbody model, the vertical spread of points occurs because a range of size distributions are allowed at a given dust temperature, with lower  $q$  models corresponding to more blackbody-like spectra that have lower fractional luminosity, and higher  $q$  models giving steeper mm-wave spectral slopes and higher fractional luminosities. Due to the differing definitions of the reported temperatures, these temperature values will be much lower than those found from a modified blackbody model and so comparisons should not be drawn between findings of the two separate modelling techniques.

Overall, Figure 4.5 shows that the dust temperature is unlikely to be higher than 60K, and that for dust temperatures above 10K the disc fractional luminosity is greater than

about  $10^{-4}$ . We can also see that our models for the disc of GSC 07396-00759 share the space occupied by other M-dwarf discs, namely TWA 7 [Bayo et al., 2019], CPD-72 2713 [Moór et al., 2020; Tanner et al., 2020; Norfolk et al., 2021], AU Mic and Fomalhaut C [Kennedy et al., 2013; Cronin-Coltsmann et al., 2021], with a temperature  $\sim 10$ -50 K and a blackbody radius  $\sim 10$ -200 au. However, assuming that all of the dust collocates precisely at the best-fitting ALMA radius we can narrow the probable range occupied by our models with our knowledge of the disc’s observed radius which sets a limit on the blackbody temperature in the disc.

Imposing this restriction with our observed radius of 70 au limits the model coolest grains to the blackbody temperature at 70 au of 20 K, i.e. on the vertical red dashed line in Figure 4.5. This now also constrains the fractional luminosity to at least above  $2 \times 10^{-4}$ , brighter than Fomalhaut C’s disc but similar to the discs in the younger systems.

## 4.5 Discussion

### 4.5.1 Comparison with near-IR scattered-light observations

We display a comparison of ALMA and SPHERE/IRDIS data, as well as the ALMA best-fitting Gaussian torus model in Figure 4.6, recalling that the scattering phase functions have a strong effect on how flux is distributed as a function of scattering angle for the SPHERE scattered light data. From the data alone, the total-intensity IRDIFS flux does not appear to be more extended than the ALMA Band 7 flux, or even the ALMA dust model. The polarimetric IRDIS DPI flux however does visibly extend past  $\sim 1.5''$ , beyond both the ALMA Band 7 flux and our underlying dust distribution model, implying that smaller micron sized dust grains are present at more distant radii than mm sized dust grains. To probe further, a comparison between the models produced for each observation is needed.

As displayed in Table 4.1 the disc’s position angle and inclination are consistent across all three observations’ models. We however find that our best fitting model radius of 70.2 au supports S18’s model radius over A21’s model radius. Even the larger radius of our double power law model with its larger error bounds is still interior to that of A21. As larger dust grains are a more direct tracer of the planetesimal birth ring, the ALMA derived radius is likely the most accurate, lending more weight to the total intensity scattered light model over the polarimetric scattered light model. This would thus imply that the polarimetric model is indeed overestimating the anisotropic scattering factor  $g$ , as suggested by A21 themselves. That A21’s fixed 70 au radius, low  $g$  model did not account for all the flux at the distant reaches of their observations indicates that the Henyey-Greenstein prescription used by A21 is probably too simple.

The ALMA double power law finds a much steeper outer slope than that of S18’s

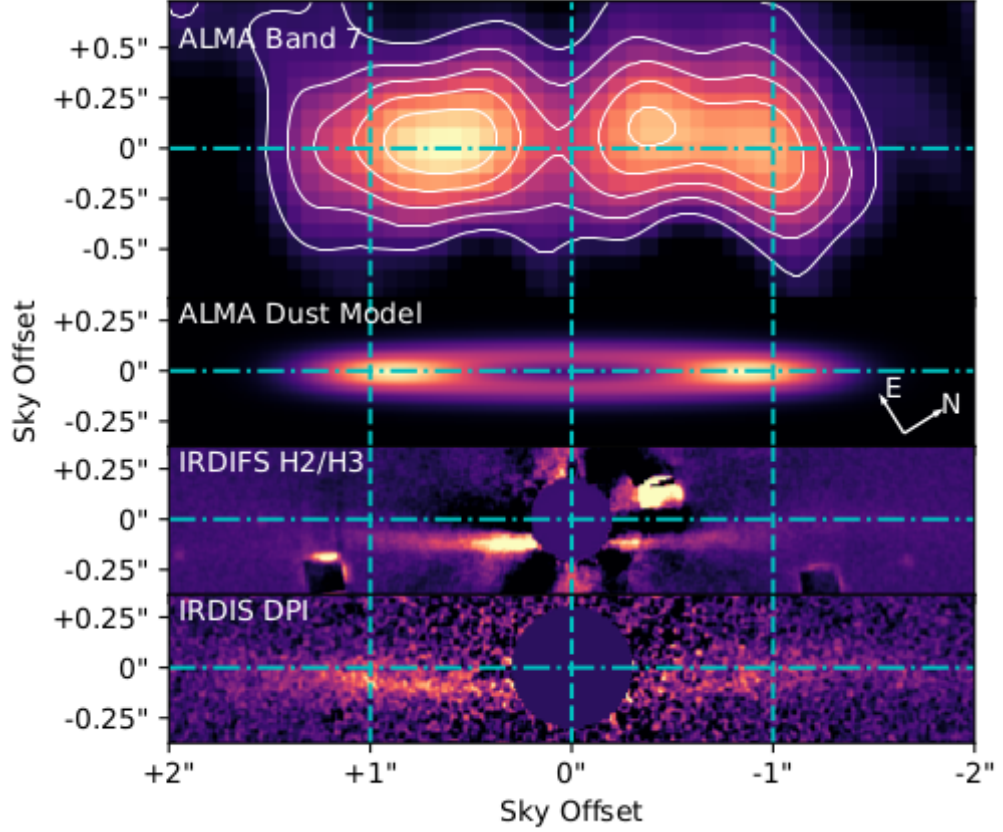


Figure 4.6: Comparison of GSC 07396-00759's disc as imaged in ALMA Band 7 with  $+2\sigma$ ,  $4\sigma$ ,  $6\sigma$ ,  $8\sigma$ ,  $10\sigma$  contours (top, aligned with model centre at zero offset), ALMA best-fitting Gaussian torus model (second from top), SPHERE/IRDIFS H2/H3 (second from bottom) and SPHERE/IRDIS DPI (bottom). The horizontal dash-dotted lines cross through the location of the model centre for the ALMA data/model and the star for the SPHERE data, parallel to the major-axis of the disc. The central regions of the SPHERE data have been removed to account for the coronagraphic masks and high noise levels surrounding the masks. The vertical dashed lines pass through the ALMA best-fitting model radius of the disc and zero offset.



model, limiting the physical dust presence inferred to less than radii of  $1.5''$ . This indicates that the shallow outer slope of S18’s model and associated dust presence at outer radii, as well as the visually extensive flux of A21’s observations, necessitate a strong radial pressure force to move small dust grains onto eccentric orbits. S18 note that their outer slope aligns well with predictions of the behaviour of small dust grains in the outer regions of debris discs under the effects of stellar radiation and wind pressures [Strubbe and Chiang, 2006; Thébault and Wu, 2008]. For this low luminosity, but young and late-type system, stellar wind ram pressure is the most likely candidate for the pressure force, as posited in A21. The steep outer slope also suggests the eccentricities of mm-sized grains and planetesimals are low, otherwise the outer slope would be smoother [Marino, 2021].

Figure 4.7 shows a comparison of the profiles of the three data sets, for the ALMA data derived from the flux of the centre pixel along the major-axis and for the SPHERE data derived from the brightest pixel in a slice of the disc perpendicular to the major-axis at each separation step, the differing approaches warranted due to the significantly higher resolution of the SPHERE data. The scattering phase functions will heavily dampen the visual radial extent of the disc in the scattered light data, thus Figure 4.7 is intended for a comparison of the potential brightness asymmetries in each dataset rather than apparent radii. However, even with the effects of the scattering phase function, the IRDIS DPI profile visibly extends beyond  $1.5''$  and both the ALMA Band 7 and IRDIFS profiles.

Both S18 and A21 observe a brightness asymmetry in the disc, with the south-east side brighter than the north-west, but by a larger factor in the June 2017 S18 total intensity data than the June 2018 A21 polarimetric data. Our April 2018 ALMA observation is consistent with there being no detected asymmetry, attributing the apparent dip on the north-west side to a noise feature. Looking at the  $1\sigma$  bounds of the ALMA profile in Figure 4.7, we can place a limit on a possible sub-mm brightness asymmetry of less than a factor  $\sim 1.5$ . It is not unfeasible that a brightness asymmetry is present in the sub-mm, but we infer that it is very unlikely to be at the same level as seen by IRDIFS and unlikely to be at the same level as seen by IRDIS DPI. The time baseline between observations is too short for dust causing an asymmetry to be removed totally from the system, which would happen on orbital timescales of  $\sim 750$  years, and so the asymmetry must be enhanced in small grain sizes. Thus whatever mechanism is causing the brightness asymmetry more strongly affects the more mobile small micron sized dust grains, and is not noticeably affecting the underlying planetesimal population nor the population of mm sized dust grains. This points towards a pressure force, such as interaction with the interstellar medium [e.g. Maness et al., 2009; Debes et al., 2009] or asymmetric small dust production and/or removal such as a coronal mass ejection [Osten et al., 2013]. A recent massive collision could also produce a dust asymmetry that evolves differently for dust grains with different  $\beta$  values, where  $\beta$  is

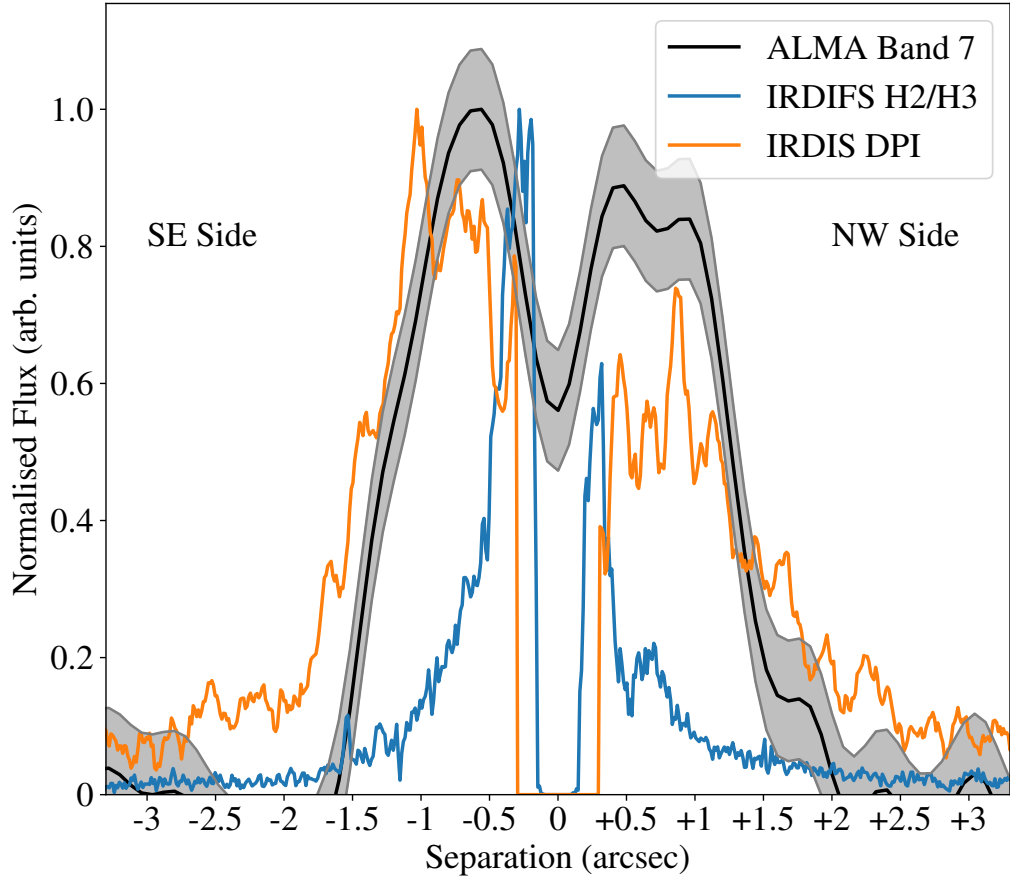


Figure 4.7: Comparative brightness profiles of the ALMA Band 7 and SPHERE/IRDIS total intensity and polarimetric data. For the ALMA data, the flux of the centre pixel along the disc major-axis is taken at each separation step. For the SPHERE data the peak brightness is taken from a slice of pixels at each separation step along a swathe parallel to the disc major-axis. Each profile is normalised to its brightest component. The gray swathe shows the ALMA RMS. The IRDIS DPI image has been smoothed by a uniform filter of width ten pixels. Zero separation is the best fitting model centre from §4.3.

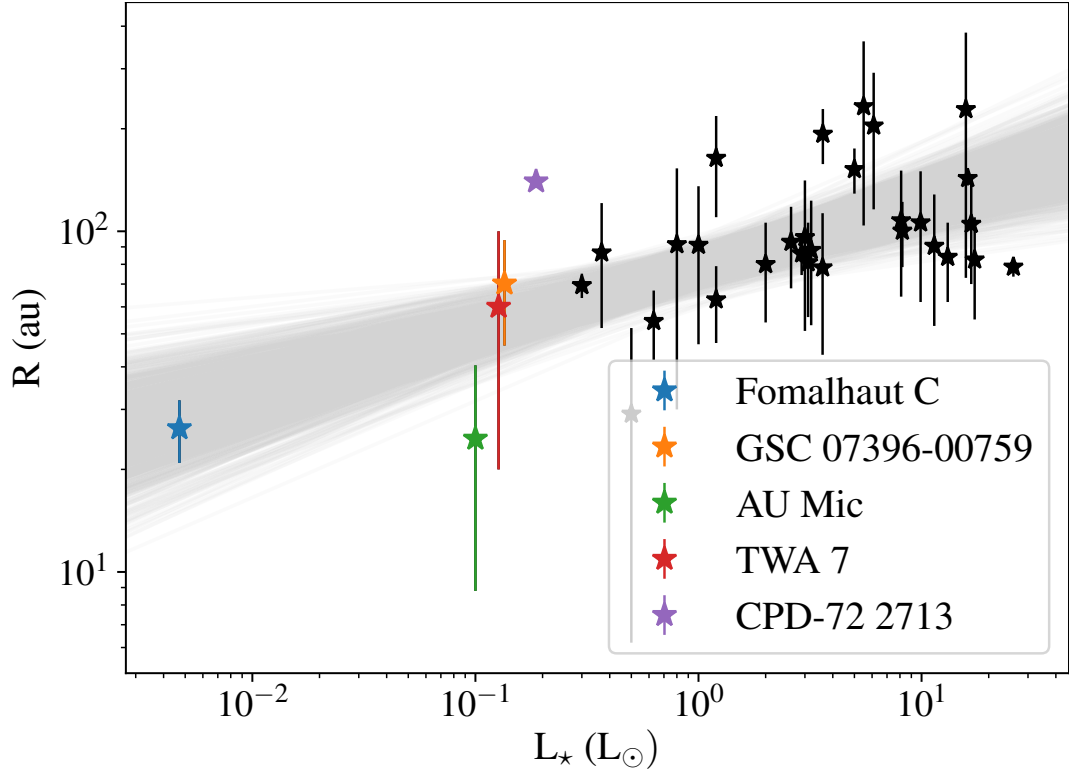


Figure 4.8: mm-wave resolved debris disc radii plotted against host stellar luminosity. Error bars represent disc FWHM or upper limits. The five latest type stellar hosts are highlighted in colour, CPD-72 2713 is plotted without a width as a fixed width of  $0.2R$  was assumed to facilitate fitting a radius [Moór et al., 2020]. Transparent grey lines show a sample of 1000 power laws from the parameter distributions of Matrà et al. [2018].

the radial force to gravitational force ratio. In M-dwarf systems  $\beta$  depends strongly on the strength of the stellar wind, which is still an unknown for GSC 07396-00759. As  $\beta$  is size dependent, this would result in differently apparent asymmetries depending on the grain size probed by the observation [Jackson et al., 2014; Kral et al., 2015].

A warp in the north-west of the disc is observed in both scattered light data sets. In Figure 4.6 slight evidence for a warp in the ALMA data may be visually identified in the north-west, but it is difficult to extricate this from the larger noise features overlapping the north-west of the disc as seen in Figure 4.3. The observation most likely does not possess the necessary resolution to uncover a warp if one exists in the sub-mm grain and parent planetesimal distributions. Higher resolution sub-mm follow up observations would allow this to be investigated.

### 4.5.2 Comparison with other M-dwarf discs

GSC 07396-00759's disc's radius of 70 au is about double that of AU Mic's disc's radius of  $\sim 24\text{--}40$  au [Daley et al., 2019], and we find GSC 07396-00759's disc to be of intermediary width when the widths are presented as ratios to their radii: a FWHM of 50 au for GSC 07396-00759 gives a ratios of 0.7 and Marino [2021] finds a ratio of 0.97 for AU Mic, in comparison to the M-dwarf host Fomalhaut C's thinner disc with radius 26.4 au, FWHM upper limit of 11 au and ratio upper limit of 0.42. GSC 07396-00759's disc's radius is comparatively similar to the  $\sim 60$  au radius of the face-on debris disc around the young  $[7.5 \pm 0.7]$  Myr old, Ducourant et al., [2014] M2Ve star TWA 7 derived from marginally resolved ALMA observations [Bayo et al., 2019; Matrà et al., 2019a]. TWA 7 has also been shown to possess considerable structure when viewed in scattered light [Ren et al., 2021; Olofsson et al., 2018]. The asymmetry of GSC 07396-00759 could be similar to that of TWA 7, if TWA 7 were viewed edge-on, which is apparent in scattered light but only marginally identified in the sub-mm [Ren et al., 2021]. CPD-72 2713's disc remains unusually large for its type with its radius of 140 au [Moór et al., 2020], twice that GSC 07396-00759's.

To visualise these comparisons we place GSC 07396-00759 on the radius–luminosity plot presented in Matrà et al. [2018], with the addition of the sample presented in Sepulveda et al. [2019], Fomalhaut C [Cronin-Coltsmann et al., 2021] and CPD-72 2713 [Moór et al., 2020]. CPD-72 2713 is presented without a disc width as a fixed FWHM of  $0.2R$  was used to reduce degeneracy while fitting for a radius in the marginally resolved observation. The sample of mm-wave resolved discs at M0–M2 is growing and is appearing to remain largely consistent both within the subset and with the greater planetary belt demographic, both in terms of the average of the radii across the sample and the breadth of the spread of their radii.

The growing sample of these discs that are resolved in both the sub-mm and scattered light will also help to elucidate the mechanisms of stellar wind forces in this regime where the low luminosity of the host star is insufficient to remove dust grains via radiation pressure and stellar wind forces become dominant, as is the case for GSC 07396-00759 [Sissa et al., 2018; Adam et al., 2021].

### 4.5.3 CO non-detection

We searched for evidence of volatiles released by planetesimal collisions via the CO gas J=3–2 emission line, as per our ALMA spectral setup. We subtracted the continuum emission and visually inspected both the dirty cube and the moment-0 map collapsed over the range of velocities where emission would be expected, finding no immediate signal.

To increase our sensitivity to a small amount of CO we use the spectro-spatial

filtering technique first described in Matrà et al. [2015], assuming that CO would be co-located with the dust. This method shifts pixels in the spectral cube based on the expected Keplerian orbital velocity at their location into a single channel to enhance signal; we have assumed a stellar mass of  $0.62 M_{\odot}$  [Adam et al., 2021]. However, the low stellar host mass, large disc radius and low spectral resolution all limit the effectiveness of the technique. Our spatial filter is taken from our Gaussian torus model from §4.4.1, masking all pixels not co-located with model continuum emission of at least 10% the maximum emission.

In Figure 4.9 we display the spectra corresponding to the spatial filter alone, and spectro-spatial filters with either assumption of the north-west section of the disc rotating towards us, or the south-east section rotating towards us. We do not detect any trace of CO gas and instead find a  $3\sigma$  upper limit on the CO flux of  $30 \text{ mJy km s}^{-1}$ , calculated from the RMS in combination with ALMA’s 10% flux calibration uncertainty and the effect of the correlation of adjacent channels.

We can compare this detection limit to the detection of CO J=3–2 emission in the disc of the similar luminosity M-dwarf TWA 7 [Matrà et al., 2019a]. At a distance of 34 pc an integrated flux of  $91 \pm 20 \text{ mJy km s}^{-1}$  was measured for TWA 7; scaling our limit for GSC 07396-00759 to this distance gives a limit at 34 pc of  $132 \text{ mJy km s}^{-1}$ . This means that our observations would not have detected a TWA 7 analogue, i.e. if GSC 07396-00759 shared the same collisional mass loss rate, photodissociation timescale, excitation environment and CO mass as TWA 7, but our limit would have been close to the underlying CO flux.

Matrà et al. [2019a] derive an already large CO ice fraction of  $\geq 70\%$  for TWA 7, thus we can conclude that our non-detection likely does not constrain the presence of CO in the system or its ice fraction in planetesimals in a meaningful way; but we can at least say that the disc is not gas-rich, solidifying its status as an evolved debris disc and not a primordial disc like that of GSC 07396-00759’s companion system V4046 Sgr.

## 4.6 Conclusions

We have resolved the debris disc around the M1V star GSC 07396-00759 in mm-wave thermal emission for the first time, making it one of only a small handful of M-dwarfs with resolved debris discs, and one of only two both fully resolved in scattered light and thermal emission along with AU Mic. We model the geometry of the underlying dust distribution, and inferred birth ring of planetesimals, as revealed by ALMA, well constraining the disc radius to  $70.2^{+4.1}_{-4.7} \text{ au}$  and sub-millimetre flux to  $1.84^{+0.22}_{-0.21} \text{ mJy}$ . We trial a simple Gaussian disc model as well as a double power law model to investigate the radial extent of the mm dust grains and find the Gaussian model to be the more appropriate fit. We do not find the

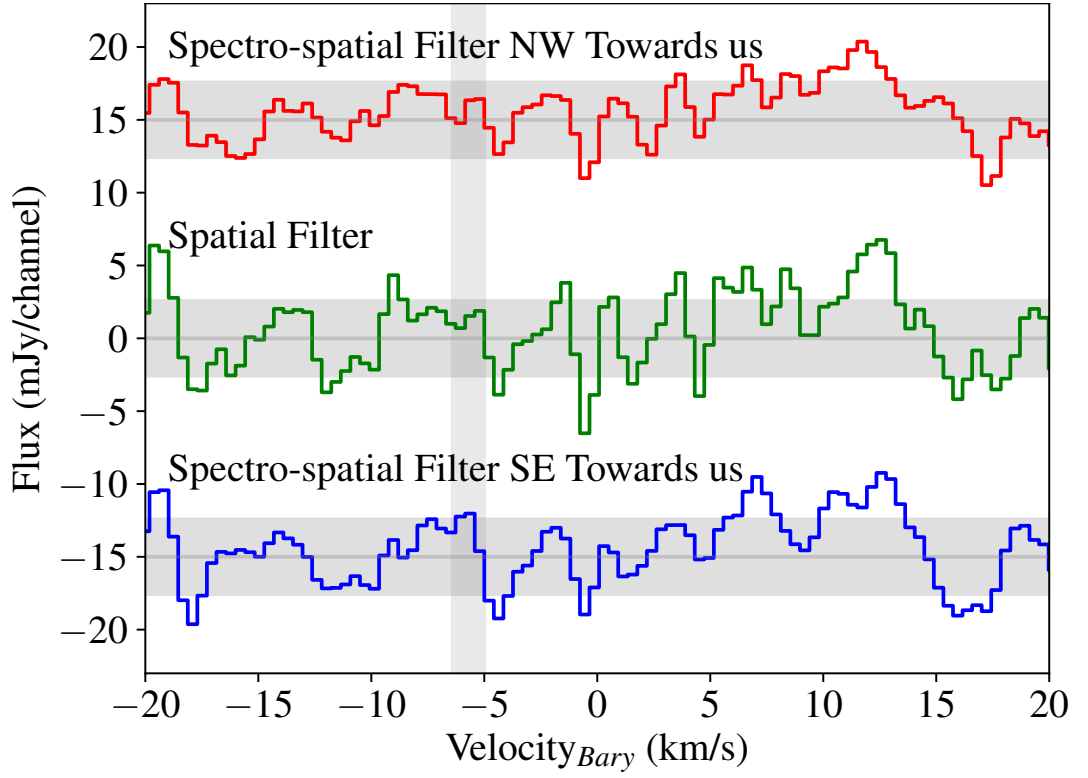


Figure 4.9: Spatially and spectro-spatially filtered CO J=3-2 spectra for the debris disc around GSC 07396-00759. The  $1\sigma$  uncertainty of the spectrum is measured over a larger range of velocities and is denoted by the horizontal shaded regions. The expected centre of the signal at the  $-5.7 \pm 0.8 \text{ km s}^{-1}$  stellar radial velocity is denoted by the vertical shaded region.

disc centre to be significantly offset from the stellar location and so place an upper limit on any underlying disc eccentricity along the major-axis. We also do not detect the presence of CO gas within the system, further distancing the evolutionary states of this debris disc and the primordial disc around the associated star V4046 Sgr.

We compare our sub-millimetre findings with previous scattered light observations, in both total intensity [Sissa et al., 2018] and polarimetry [Adam et al., 2021]. Our double power law model has a significantly steeper outer slope in the dust distribution than the total intensity model, i.e. Sissa et al. [2018] infer micron sized dust grains to be present at much larger radii than we infer mm size dust grains to be present at. Sissa et al. [2018]’s model thus requires a radial pressure force predominantly affecting smaller dust grains, most likely the action of stellar wind in this low host star luminosity system. Our sub-millimetre radius measurement is a stronger tracer of the underlying planetesimal belt and so confirms the radius measurement made by Sissa et al. [2018] over Adam et al. [2021], implying that complex behaviour of the polarised scattering phase function was responsible for the large radius measurement made by the latter.

We do not significantly detect in the sub-millimetre the brightness asymmetry apparent in both the scattered light observations. This implies that the physical mechanism behind the asymmetry is a pressure force acting on smaller dust grains or related to asymmetric production/removal of small dust. However, higher signal to noise sub-millimetre observations could still reveal an asymmetry in the mm dust grains. Our ALMA observations are also not of significantly high resolution to identify any warps in this disc, as also observed in scattered light.

We do not have enough measurements of the disc flux in the far-infrared/sub-millimetre to constrain an SED for the disc. However, we do explore the possible disc fractional luminosity/representative dust temperature parameter space to identify that the disc around GSC 07396-00759 is likely to possess a greater fractional luminosity than the disc around Fomalhaut C, and could have a similar or even greater fractional luminosity than the discs around low mass stars AU Mic, CPD-72 2713 and TWA 7. The radius of GSC 07396-00759’s disc, almost thrice that of AU Mic’s disc but similar to that of TWA 7’s, places it in good agreement with the proposed radius–luminosity relationship proposed by Matrà et al. [2018], and the disc width is moderate among the greater population of mm-wave resolved debris discs.

As an edge-on M-dwarf debris disc well resolved both in the sub-millimetre and in scattered light, and with dust features apparent in the scattered light that are not present in the sub-millimetre, GSC 07396-00759 is an excellent candidate for follow-up observations, to investigate low host luminosity stellar wind dominated discs and the source of the system’s own unique features as well as to finally provide a true coeval disc to compare the discoveries

from its twin AU Mic with.

## 4.7 Appendix

### 4.7.1 Modelling posteriors

Figure 4.10 and figure 4.11 show the posterior distributions of select parameters from the MCMC fitting of the Gaussian and double power law models respectively, where parameters are shared between our models and S18 or A21's we have plotted their median parameters for comparison. As displayed in Figure 4.10 the Gaussian model only shows a large degeneracy in the  $x$  and  $y$  offsets and a slight degeneracy between  $r_0$  and  $\sigma_r$ . As displayed in Figure 4.11 the double power law model as well as the  $x$  and  $y$  offset degeneracy there are significant degeneracies between  $r_0$ ,  $a_{\text{in}}$  and  $a_{\text{out}}$ .



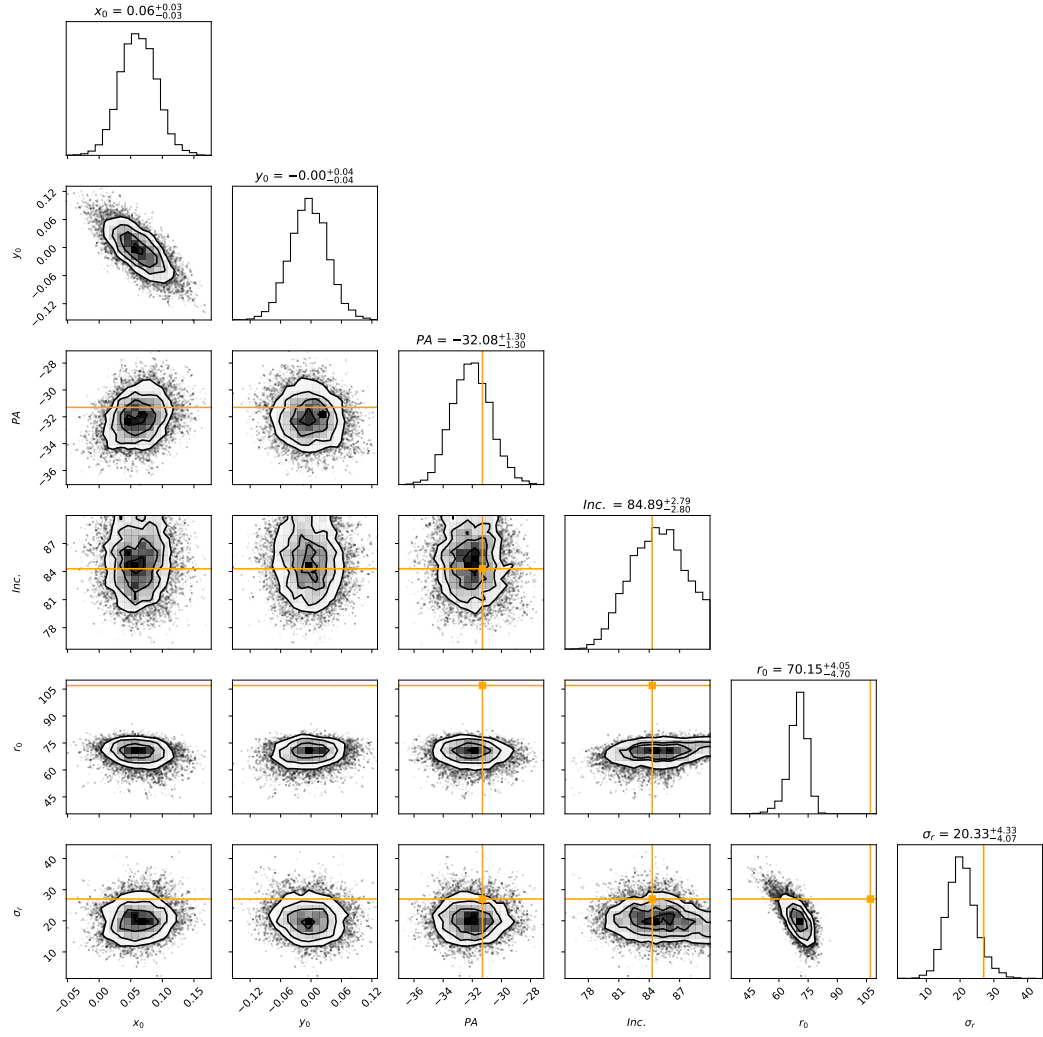


Figure 4.10: Posterior distributions of parameters from MCMC fitting of the Gaussian disc model. Where model parameters are shared, the median parameters of Adam et al. [2021] are overplotted in orange for comparison.

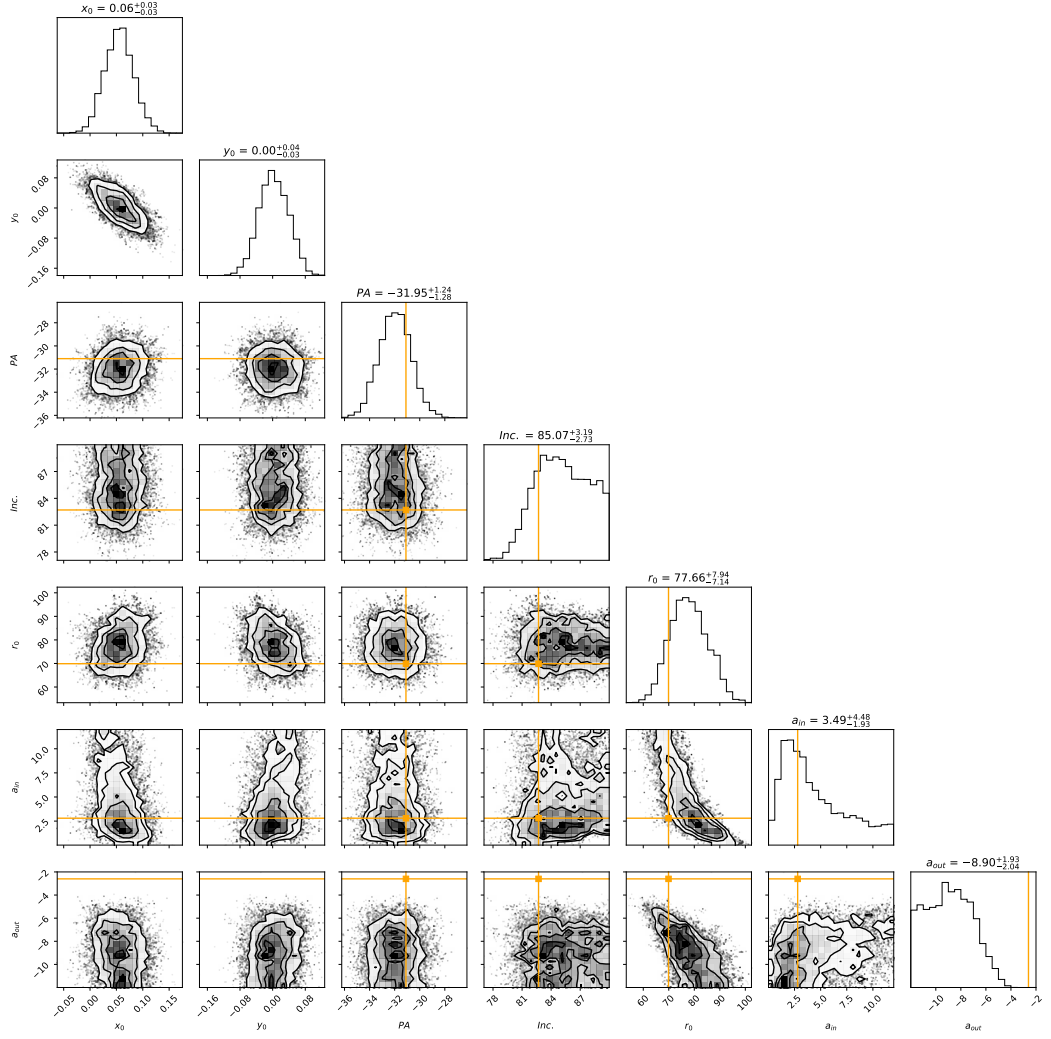


Figure 4.11: Posterior distributions of parameters from MCMC fitting of the double power law disc model. Where model parameters are shared, the median parameters of Sissa et al. [2018] are overplotted in orange for comparison.

## Chapter 5

# An ALMA survey of Beta Pictoris Moving Group M-dwarfs

### Declaration

Part of this chapter, §5.3.2, is an excerpt from the paper ‘*Herschel Observations of Disks Around Late-type Stars*’ [Tanner et al., 2020] published in Publications of the Astronomical Society of the Pacific in August 2020. All the writing and analysis in this chapter was performed by me. The code base for the SED and fractional-luminosity fitting used in Figure 5.6, Figure 5.7 and Figure 5.8 was created by Grant Kennedy.

### Abstract

Previous surveys in the far-infrared have found very few, if any, M-dwarf debris discs among their samples. It has been questioned whether M-dwarf discs are simply less common than earlier types, or whether the low detection rate derives from the wavelengths and sensitivities available to those studies. The use of the highly sensitive, long wavelength Atacama Large Millimetre/submillimetre Array can shed light on the problem. This chapter presents a survey of M-dwarf stars in the young and nearby Beta Pictoris Moving Group with ALMA at Band 7 (880  $\mu\text{m}$ ). From the observational sample I detect two new sub-mm excesses that likely constitute unresolved debris discs around GJ 2006 A and AT Mic A and model distributions of the disc fractional luminosities and temperatures. From the science sample of 36 M-dwarfs including AU Mic I find a disc detection rate of 4/36 or  $11.1^{+7.4}_{-3.3}\%$  that rises to  $23.1^{+8.3}_{-5.5}\%$  when adjusted for completeness. I conclude that this detection rate is consistent with the detection rate of discs around G and K type stars and that the disc properties are also likely consistent with earlier type stars. I additionally conclude that M-dwarf stars are not

less likely to host debris discs, but instead require longer wavelength and higher sensitivity observations than have previously been employed.

## 5.1 Introduction

M-dwarfs are the most abundant type of star in the sky [Ledrew, 2001], and these stars have a multitude of detected planets [e.g. Bonfils et al., 2013; Dressing and Charbonneau, 2015; Mulders et al., 2015]. However, when it comes to debris discs M-dwarfs are distinctly lacking. The far-IR Herschel DEBRIS survey detected infrared excesses around 17% of FGK type stars [Sibthorpe et al., 2018] and 24% of A-type stars [Thureau et al., 2014], but only detected two excesses around M-types [GJ 581; Fomalhaut C; Lestrade et al., 2012; Kennedy et al., 2013] from 89 for a detection rate of 2%. There are only eight M-dwarf discs published in the literature, and of these only 5 have been fully resolved, AU Mic [MacGregor et al., 2013; Daley et al., 2019], Fomalhaut C [Cronin-Coltsmann et al., 2021] and GSC 07396-00759 [Cronin-Coltsmann et al., 2021] with ALMA and AU Mic [Kalas et al., 2004], TWA 7 [Choquet et al., 2016], TWA 25 [Choquet et al., 2016] and GSC 07396-00759 [Sissa et al., 2018; Adam et al., 2021] in scattered light, confirming that the infrared excesses indeed originate from circumstellar discs.

The low rate of disc detections could be because the discs simply aren't there. It is possible that the high incidence of planets around M dwarfs marks a high efficiency of planet formation, limiting leftover material that would constitute a debris disc. Alternatively photoevaporation [Adams et al., 2004] and stellar encounters [Lestrade et al., 2011] could strip material from M star discs that are forming in cluster environments. If discs are present, their underlying physics is different to discs around earlier type stars. The low host luminosity is not significant enough for radiation pressure to overcome gravity and instead stellar wind becomes a significant force. It's possible that strong stellar wind drag could remove grains quickly enough that the discs dynamics are different, affecting observability [Plavchan et al., 2009].

Alternatively, a population of discs similar to that around early type stars could exist around M-dwarfs but remain difficult to detect with far-IR methods. The low host luminosity would illuminate a disc less well and heat one to a lower temperature, requiring more sensitive, longer wavelength observations than those employed by previous surveys. The Atacama Large Millimetre Array is the best suited contemporary telescope to fulfill these requirements. Luppe et al. [2020] investigate the capability of ALMA to detect a DEBRIS-like population of M-dwarf discs around the DEBRIS sample of M-stars and conclude that for 15 minutes of observation at Band 7 there would be a 4-16% detection rate if all the discs were unresolved and detection rate of 1-6% if some discs are large or

close enough to be resolved. If the discs are resolved, the signal per beam would be reduced and/or some flux would be unrecoverable if the angular scale of the disc is larger than the maximum recoverable scale of the observation’s interferometry.

Debris disc detection rate and fractional luminosity is known to decrease with age as material is lost from the system due to blow out and the reservoir of parent planetesimals collisionally depletes [Decin et al., 2003; Rieke et al., 2005; Trilling et al., 2008; Montesinos et al., 2016]. For this reason, if a survey were to be optimised to recover as many disc detections as possible a sample of young stars should be selected. The  $\beta$  Pictoris Moving Group (BPMG) is both young [ $\sim 20$  Myr, Bell et al., 2015; Miret-Roig et al., 2020] and nearby [ $\lesssim 100$  pc, Shkolnik et al., 2017], making it a valuable stellar sample. Pawellek et al. [2021] analyse the F-type population of the BPMG with far-IR photometry and ALMA and find a 75% detection rate, a significantly higher rate than for the old field stars of the DEBRIS F star sample [Sibthorpe et al., 2018], further solidifying the BPMG as a good candidate sample to search for new discs. Indeed, already two of the published M-dwarf discs, AU Mic and GSC 07396-00759, are members of the BPMG.

In this chapter I present observations of the BPMG M-dwarf sample with ALMA. The observational details are presented in §5.2. The results of the survey for individual stars of interest is presented in §5.3 and new disc detections and the context of the detection rate is discussed in §5.4.

## 5.2 Observations

### 5.2.1 Observation Sample

The observation sample was selected in 2017 for ALMA Cycle 5 based on these criteria: identified as a known member from the literature of the BPMG, identified as an M-type, and the star is within ALMA’s observable declination range - i.e. between  $\sim -65^\circ$  and  $40^\circ$ . These sources were used for the sample selection: Binks and Jeffries [2016]; Malo et al. [2013]; Shkolnik et al. [2012]; Schlieder et al. [2010]; Lépine and Simon [2009]; Zuckerman et al. [2001]. The sample is unbiased with respect to the previous detection of known infrared excesses.

AU Mic is a member of the scientific sample but was not chosen to be observed in the survey as it has already been significantly observed with ALMA. Had it been observed, it would definitely have been re-detected and the new re-observation would not significantly build upon previous observations.

The sample was observed under project 2017.1.01583.S, with further details to follow in §5.2.2. There were 33 individual ALMA observations, of which two contained both stars of a well studied binary within the field of view (HD 139084 AB and AT Mic AB)

and a further three contained two Gaia DR3 sources with parallax measurements within the field of view for a total of 38 confirmed BPMG member stars observed. Two more observations contain possible binaries with the presence of a second Gaia DR3 source without a parallax but with an appropriate G magnitude and sub-arcsecond separation from the primary. TYC 7443-1102-1 is listed alternatively as K9IVe [Pecaut and Mamajek, 2013] and M0.0V [Lépine and Simon, 2009], and so was included in this sample and treated as an M-dwarf, it was later noted to have an infrared excess in Herschel PACS [Tanner et al., 2020]. One of these extra stars, HD 139084 A is a K0V, and so is not part of the scientific sample. Adding AUMic brings the scientific sample to 38 confirmed M-dwarfs.

UCAC4 345-006842 (AKA Karmn J05084-210) was intended to be observed but the ALMA observation was mispointed, so it was not observed and must be removed from the scientific sample. GJ 3305 (AKA StKM 1-497), GJ 182 (AKA V1005 Ori) and TWA 22 (AKA ASAS J101727-5354.4) were intended to be observed with ALMA, but the scheduling blocks were timed out at the end of the observing period, so they were not observed and must be removed from the scientific sample.

Table 5.1 displays details of our sample of stars. Spectral types for this table were taken from SIMBAD [Wenger et al., 2000] unless otherwise noted with an asterisk, luminosities are taken from stellar SED models using available photometry and parallaxes unless otherwise noted with an asterisk. For asterisk noted properties we make estimates using the online ‘Modern Mean Dwarf Stellar Color and Effective Temperature Sequence’ table<sup>1</sup> of Pecaut and Mamajek [2013]. The spectral type of TYC 7443-1102-1 marked with two asterisks is derived from Lépine and Simon [2009].

---

<sup>1</sup>[http://www.pas.rochester.edu/~emamajek/EEM\\_dwarf\\_UBVIJHK\\_colors\\_Teff.txt](http://www.pas.rochester.edu/~emamajek/EEM_dwarf_UBVIJHK_colors_Teff.txt)

Table 5.1: Stars observed in our sample. Spectral types are derived from SIMBAD unless marked with asterisks, luminosities are taken from stellar SED models using available photometry and parallaxes unless otherwise noted with an asterisk. For asterisk noted properties we make estimates using the online temperature sequence table of Pecaut and Mamajek [2013]. The spectral type of TYC 7443-1102-1 marked with a two asterisks is derived from Lépine and Simon [2009]

| Name                       | Alternative name           | Type    | Luminosity [ $L_{\odot}$ ] | Distance [pc] | Notes  |
|----------------------------|----------------------------|---------|----------------------------|---------------|--|
| 2MASS J05195327+0617258    | GSC2.3 N9OB003170          | M6.5V*  | 0.0057                     | 96.1          | -  |
| 2MASS J05241914-1601153 AB | PM J05243-1601 AB          | M4.5    | 0.043                      | 31.1          | GDR3 Binary  |
| 2MASS J19102820-2319486    | 1SWASP J191028.18-231948.0 | M4      | 0.11                       | 59.0          | Possible GDR3 Binary                                 |
| 2MASS J20333759-2556521    | SCR J2033-2556             | M4.5    | 0.0305                     | 43.5          | -  |
| ASAS J164301-1754.4        | UCAC4 361-079084           | M0.5    | 0.141                      | 71.1          | -  |
| Barta 161 12               | UCAC4 414-001790           | M4.3V   | 0.05                       | 37.3          | Spectroscopic Binary                                 |
| BD+30 397 B                | V* AG Tri B                | M0      | 0.078                      | 40.9          | Companion to BD+30 397 A                             |
| CD-57 1054                 | GSC08513-00572             | M0Ve    | 0.174                      | 26.9          | -  |
| EPIC 211046195             | 2MASSW J0335020+234235     | M8.5V   | 0.00402                    | 51.2          | -  |
| GJ 2006 A                  | ** LDS 18A                 | M3.5Ve  | 0.053                      | 35.0          | Companion to GJ 2006B                                |
| GJ 2006 B                  | ** LDS 18B                 | M3.5Ve  | 0.0429                     | 35.0          | Companion to GJ 2006A                                |
| GJ 3076                    | LP 467-16                  | M5.93   | 0.008                      | 17.2          | -  |
| GSC 07396-00759            | ASAS J181422-3246.2        | M1Ve    | 0.135                      | 71.4          | Companion to V4046 Sgr                               |
| GSC 08350-01924 AB         | 1RXS J172919.1-501454 AB   | M3V     | 0.163                      | 62.6          | GDR3 Binary  |
| HD 139084                  | CD-57 6042 A               | K0V     | 0.98                       | 39.3          | Companion to HD 139084 B, Spectroscopic Binary       |
| HD 139084 B                | CD-57 6042 B               | M5Ve    | 0.0203                     | 39.3          | Companion to HD 139084                               |
| HD 155555 C                | V824 Ara C                 | M3Ve    | 0.044                      | 30.3          | Companion to HD 155555 AB                            |
| L 836-122                  | GJ 3832                    | M3.5V   | 0.015                      | 28.6          | -  |
| LP 353-51                  | HIP 11152                  | M1V     | 0.0641                     | 27.2          | -  |
| LP 476-207 AB              | GJ 3322 AB                 | M3.5V   | 0.07                       | 33.2          | GDR3 Binary/Spectroscopic Binary                     |
| MCC 124                    | HIP 50156                  | M0.7V   | 0.132                      | 23.4          | -  |
| AT Mic A                   | GJ 799 A                   | M4.5Ve  | 0.035                      | 9.9           | Companion to AT Mic B, companion to AU Mic           |
| AT Mic B                   | GJ 799 B                   | M4.5Ve  | 0.031                      | 9.8           | Companion to AT Mic A, companion to AU Mic           |
| RX J0217.9+1225            | PM J02179+1225             | M4      | 0.0593                     | 63.1          | -  |
| Smethells 20               | TYC 9073-762-1             | M1Ve    | 0.134                      | 50.6          | -  |
| TYC 2211-1309-1            | RX J2200.7+2715            | M0.0V   | 0.0841                     | 35.6          | -  |
| TYC 6872-1011-1            | 1RXS J185803.4-295318      | M0Ve    | 0.275                      | 74.2          | Spectroscopic Binary                                 |
| TYC 7443-1102-1            | PM J19560-3207             | M0.0V** | 0.154                      | 51.3          | Companion to UCAC3 116-474938                        |
| UCAC2 19527490             | 2MASS J18580464-2953320    | M3V*    | 0.12                       | -             | Likely Companion to TYC 6872-1011-1                  |
| UCAC2 20312880             | RX J0613.2-2742            | M3.5    | 0.089                      | 32.7          | Double star  |
| UCAC3 116-474938           | 2MASS J19560294-3207186    | M4      | 0.11                       | 51.3          | Companion to TYC 7443-1102-1, Double star            |
| UCAC3 124-580676           | SCR J2010-2801             | M3.0Ve  | 0.11                       | 48.0          | Possible Gaia DR3 Binary/Spectroscopic Binary        |
| UCAC3 176-23654            | RX J0534.0-0221            | M3      | 0.066                      | 34.4          | -  |
| V* TX PsA                  | ** LDS 793 B               | M5IVe   | 0.0203                     | 20.8          | Companion to V* WW PsA                               |
| V* WW PsA                  | ** LDS 793 A               | M4IVe   | 0.0462                     | 20.8          | Companion to V* TX PsA                               |
| AU Mic                     | HD 197481                  | M1Ve    | 0.0962                     | 9.7           | Not observed in this project, companion to AT Mic AB |

### 5.2.2 Observation Details

All new observations were performed by ALMA Band 7 (0.87 mm, 345 GHz) under project 2017.1.01583.S. The observations were spread across configurations C43-1, C43-2, and C42-3 depending on stellar distance to retain sensitivity to a similar physical scale and avoid resolving out disc emission. Observation details for individual sources can be found in Table 5.2.

The spectral setup for all observations comprised four windows centred on 347.937, 335.937, 334.042 and 346.042 GHz with bandwidth 2 GHz and 128 channels for all but the last with width 1.875 GHz and 3840 channels. The last window was used to search for CO gas via the J=3-2 emission line, which has also been detected in another young debris disc around the M-dwarf TWA 7 [Matrà et al., 2019a].

The raw data were calibrated with the provided ALMA pipeline script in CASA version 5.1.2-4 [McMullin et al., 2007]. To reduce the data volume the visibilities were averaged in 30 second intervals and down to two channels per spectral window for the continuum imaging. All images were generated with the CLEAN algorithm in CASA.



Table 5.2: ALMA Band 7 observation details for stars observed under project 2017.1.01583.S. Note some stars were observed in multiple configurations and are listed once for each individual observation. MRS is maximum recoverable scale and PWV is mean precipitable water vapour.

| Name                       | Integration time [minutes] | No. Antennae | Min-Max baseline [m] | MRS ["] | Date                | PWV [mm] | Calibrators                        |
|----------------------------|----------------------------|--------------|----------------------|---------|---------------------|----------|------------------------------------|
| 2MASS J05195327+0617258    | 16.13                      | 43           | 15.1 - 782.1         | 4.4     | 28.08.18            | 0.3      | J0552+0313, J0423-0120             |
| 2MASS J05241914-1601153 AB | 14.62                      | 43           | 15.1 - 313.7         | 6.6     | 07.07.18            | 0.5      | J0524-0913, J0522-3627             |
| 2MASS J19102820-2319486    | 14.11                      | 45           | 15.1 - 500.2         | 5.3     | 19.05.18            | 0.9      | J1924-2914, J1751+0939             |
| 2MASS J20333759-2556521    | 14.16                      | 44           | 15.1 - 483.9         | 5.6     | 06.04.18            | 0.7      | J2056-3208, J1924-2914             |
| 2MASS J20333759-2556521    | 14.16                      | 46           | 15.1 - 500.2         | 5.7     | 04.05.18            | 0.3      | J2056-3208, J1924-2914             |
| ASAS J164301-1754.4        | 14.67                      | 45           | 15.1 - 500.2         | 5.3     | 19.05.18            | 0.9      | J1733-1304, J1517-2422             |
| Barta 161 12               | 14.70                      | 46           | 15.0 - 313.7         | 7.0     | 31.05.18            | 0.8      | J0141-0928, J0006-0623             |
| BD+30 397 B                | 30.47                      | 44           | 15.1 - 500.2         | 5.6     | 24.08.18            | 1.0      | J0423-0120, J0238+1636             |
| CD-57 1054                 | 17.20                      | 46           | 15.1 - 313.7         | 7.0     | 04.07.18            | 1.0      | J0550-5732, J0519-4546, J0506-6109 |
| CD-57 1054                 | 17.20                      | 43           | 15.1 - 440.4         | 7.0     | 12.08.18            | 0.9      | J0550-5732, J0519-4546, J0506-6109 |
| EPIC 211046195             | 21.25                      | 49           | 15.1 - 783.5         | 4.3     | 31.08.18            | 0.8      | J0336+3218, J0510+1800             |
| GJ 2006 A                  | 14.61                      | 45           | 15.0 - 313.7         | 7.0     | 23.05.18            | 0.3      | J0040-3243, J2258-2758             |
| GJ 2006 B                  | 14.61                      | 45           | 15.0 - 313.7         | 7.0     | 23.05.18            | 0.3      | J0040-3243, J2258-2758             |
| GJ 3076                    | 18.20                      | 46           | 15.1 - 313.7         | 6.9     | 30.06.18            | 0.7      | J0117+1418, J0006-0623             |
| GSC 07396-00759            | 14.67                      | 44           | 15.1 - 483.9         | 5.6     | 06.05.18            | 0.7      | J1924-2914, J1826-2924             |
| GSC 08350-01924 AB         | 15.18                      | 47           | 15.0 - 313.7         | 7.0     | 19.05.18            | 0.3      | J1650-5044, J1717-5155, J1924-2914 |
| GSC 08350-01924 AB         | 16.19                      | 46           | 15.1 - 500.2         | 5.2     | 19.05.18            | 0.9      | J1650-5044, J1717-5155, J1924-2914 |
| HD 139084 AB               | 17.19                      | 48           | 15.0 - 313.7         | 7.4     | 18.05.18            | 1.0      | J1524-5903, J1427-4206             |
| HD 155555 C                | 21.25                      | 44           | 15.1 - 500.2         | 6.0     | 06.05.18            | 0.8      | J1703-6212, J1427-4206             |
| L 836-122                  | 14.67                      | 46           | 15.0 - 313.7         | 6.9     | 15.05.18            | 1.1      | J1408-0752, J1337-1257             |
| LP 353-51                  | 25.20                      | 44           | 15.1 - 500.2         | 5.6     | 24.08.18            | 0.9      | J0423-0120, J0238+1636, J0237+2848 |
| LP 476-207 AB              | 17.19                      | 44           | 15.1 - 500.2         | 5.4     | 23.08.18            | 0.7      | J0510+1800, J0449+1121             |
| MCC 124                    | 21.75                      | 44           | 15.1 - 500.2         | 6.0     | 06.05.18            | 0.7      | J1025+1253, J1058+0133             |
| ATMic AB                   | 14.65                      | 47           | 15.0 - 313.7         | 7.0     | 19.05.18            | 0.3      | J1924-2914, J2056-3208             |
| RX J0217.9+1225            | 17.70                      | 45           | 15.1 - 783.5         | 4.3     | 06.09.18            | 0.6      | J0211+1051, J0006-0623, J0224+0659 |
| Smethells 20               | 18.70                      | 44           | 15.1 - 782.1         | 4.7     | 26.08.18 & 27.08.18 | 0.8      | J1834-5856, J1924-2914, J1723-6500 |
| TYC 2211-1309-1            | 24.26                      | 46           | 15.1 - 783.5         | 4.2     | 05.09.18            | 0.7      | J2253+1608, J2217+2421, J0006-0623 |
| TYC 6872-1011-1            | 14.62                      | 45           | 15.1 - 500.2         | 5.3     | 19.04.18            | 0.9      | J1924-2914, J1751+0939             |
| TYC 7443-1102-1            | 12.61                      | 48           | 15.1 - 483.9         | 5.6     | 22.08.18            | 0.8      | J1924-2914, J2056-4714             |
| UCAC2 19527490             | 14.62                      | 45           | 15.1 - 500.2         | 5.3     | 19.04.18            | 0.9      | J1924-2914, J1751+0939             |
| UCAC2 20312880             | 13.33                      | 46           | 15.0 - 313.7         | 7.0     | 24.05.18            | 0.6      | J0536-3401, J0522-3627             |
| UCAC2 20312880             | 14.67                      | 47           | 15.0 - 330.6         | 6.0     | 05.06.18            | 0.7      | J0536-3401, J0522-3627             |
| UCAC3 116-474938           | 14.62                      | 48           | 15.1 - 483.9         | 5.6     | 22.08.18            | 0.8      | J1924-2914, J2056-4714             |
| UCAC3 124-580676           | 14.62                      | 48           | 15.1 - 483.9         | 5.6     | 22.08.18            | 0.8      | J1924-2914, J2056-4714             |
| UCAC3 176-23654            | 12.09                      | 43           | 15.1 - 782.1         | 4.4     | 28.08.18            | 0.3      | J0552-0313, J0423-0120             |
| V* TX PsA                  | 14.62                      | 46           | 15.0 - 455.5         | 6.9     | 11.05.18            | 0.4      | J2258-2758, J0006-0623             |
| V* WW PsA                  | 14.62                      | 46           | 15.0 - 455.5         | 6.9     | 11.05.18            | 0.4      | J2258-2758, J0006-0623             |

### 5.2.3 Initial image analysis

Figure 5.1 shows naturally weighted images of the observational sample generated with the CLEAN algorithm in CASA. The sample was also visually inspected with 1'' and 2''  $uv$  tapers to search for diffuse emission. To extract photometry point source models were fit to the visibilities using the CASA *uvmodelfit* task at each Gaia DR3 stellar location. We do not allow the offset parameters to vary in these fits to avoid fitting to nearby non-stellar point sources except in the cases of detections and near detections as discussed in §5.3. The results of these fits and the image parameters can be found in Table 5.3 and significant detections are highlighted in bold, parameters for GSC 07396-00759 are taken from Cronin-Coltsmann et al. [2022, Chapter 4] and the radius measurement for AU Mic is taken from MacGregor et al. [2013], the expected stellar emission and an  $880\mu\text{m}$  flux for AU Mic are estimated from a combined dust and stellar SED model.

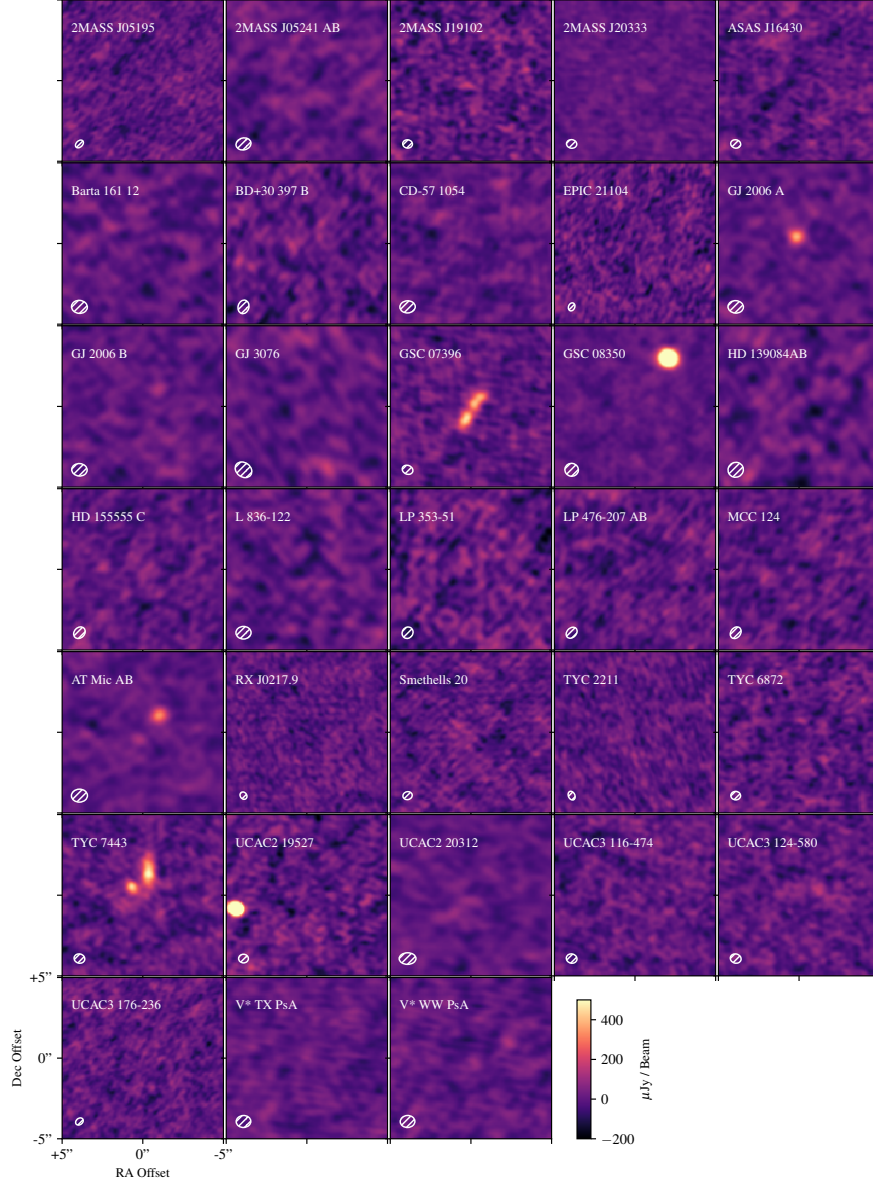


Figure 5.1: Naturally weighted ALMA 880 $\mu$ m images of our BPMG M-dwarf sample. For all observations except for BD+30 397B and HD 139084 AB, the star is within 2 arcseconds of the centre of the image. The ellipses in the lower left corners show the restoring beams.

Table 5.3: Sample observational results. Sources in bold have significant excess detections. Parameters for GSC 07396-00759 are taken from Cronin-Coltsmann et al. [2022, Chapter 4] and the radius measurement for AU Mic is taken from MacGregor et al. [2013], the expected stellar emission and an  $880\mu\text{m}$  flux for AU Mic are estimated from a combined dust and stellar SED model.

| Name                      | RMS [ $\mu\text{Jy}/\text{beam}$ ] | Stellar Flux [ $\mu\text{Jy}$ ] | Signal [ $\mu\text{Jy}/\text{beam}$ ] | Beam Size [ $''$ ] | Disc radius [AU] |
|---------------------------|------------------------------------|---------------------------------|---------------------------------------|--------------------|------------------|
| 2MASS J05195327+0617258   | 40                                 | 0.1                             | -32                                   | 0.573              | -                |
| 2MASS J05241914-1601153 A | 43                                 | 8                               | 15                                    | 0.939              | -                |
| 2MASS J05241914-1601153 B | 43                                 | -                               | 41                                    | 0.939              | -                |
| 2MASS J19102820-2319486   | 50                                 | 5                               | -9                                    | 0.607              | -                |
| 2MASS J20333759-2556521   | 23                                 | 3                               | 41                                    | 0.640              | -                |
| ASAS J164301-1754.4       | 47                                 | 3                               | 0.6                                   | 0.626              | -                |
| Barta 161 12              | 40                                 | 6                               | -0.5                                  | 0.985              | -                |
| BD+30 397 B               | 85                                 | 6                               | 10                                    | 0.853              | -                |
| CD-57 1054                | 40                                 | 2                               | 26                                    | 0.954              | -                |
| EPIC 211046195            | 46                                 | 0.5                             | -87                                   | 0.515              | -                |
| <b>GJ 2006 A</b>          | 33                                 | 6                               | 391                                   | 0.958              | <34              |
| GJ 2006 B                 | 33                                 | 6                               | 2                                     | 0.957              | -                |
| GJ 3076                   | 36                                 | 6                               | 38                                    | 1.110              | -                |
| <b>GSC 07396-00759</b>    | 40                                 | 2                               | 1840                                  | 0.683              | 70               |
| GSC 08350-01924 AB        | 25                                 | 6                               | -12                                   | 0.840              | -                |
| HD 139084                 | 60                                 | 20                              | 133                                   | 0.960              | -                |
| HD 139084 B               | 60                                 | 10                              | -22                                   | 0.960              | -                |
| HD 155555 C               | 40                                 | 9                               | 93                                    | 0.792              | -                |
| L 836-122                 | 45                                 | 3                               | -60                                   | 0.938              | -                |
| LP 353-51                 | 57                                 | 8                               | 19                                    | 0.734              | -                |
| LP 476-207 A              | 45                                 | 20                              | 28                                    | 0.772              | -                |
| LP 476-207 B              | 45                                 | -                               | 42                                    | 0.772              | -                |
| MCC 124                   | 45                                 | 20                              | 6                                     | 0.785              | -                |
| <b>AT Mic A</b>           | 27                                 | 70                              | 335                                   | 0.994              | <10              |
| AT Mic B                  | 27                                 | 60                              | 120                                   | 0.994              | -                |
| RX J0217.9+1225           | 37                                 | 2                               | -12                                   | 0.485              | -                |
| Smethells 20              | 47                                 | 5                               | 75                                    | 0.582              | -                |
| TYC 2211-1309-1           | 37                                 | 5                               | -4                                    | 0.568              | -                |
| TYC 6872-1011-1           | 47                                 | 4                               | -35                                   | 0.606              | -                |
| TYC 7443-1102-1           | 47                                 | 5                               | -                                     | 0.670              | -                |
| UCAC2 19527490            | 50                                 | 3                               | -28                                   | 0.606              | -                |
| UCAC2 20312880            | 33                                 | 10                              | 39                                    | 1.042              | -                |
| UCAC3 116-474938          | 40                                 | 6                               | 80                                    | 0.671              | -                |
| UCAC3 124-580676          | 47                                 | 7                               | 7                                     | 0.679              | -                |
| UCAC3 176-23654           | 40                                 | 7                               | 25                                    | 0.519              | -                |
| V* TX PsA                 | 30                                 | 8                               | 36                                    | 0.908              | -                |
| V* WW PsA                 | 35                                 | 20                              | 78                                    | 0.908              | -                |
| <b>AU Mic</b>             | -                                  | 110                             | 13000                                 | -                  | 40               |

Table 5.4: Background sources. RMS is local to the background source.

| Observation             | RMS [ $\mu$ Jy/beam] | Source flux [ $\mu$ Jy/beam] | Source Ra [hr:min:sec] | Source Dec [ $^{\circ}$ : $'$ : $''$ ] |
|-------------------------|----------------------|------------------------------|------------------------|--|
| 2MASS J20333759-2556521 | 40                   | 600                          | 17:29:20.474           | -50.14.51.117                          |
| GSC 08350-01924         | 25                   | 1600                         | 0:33:36.964            | 25.57.03.591                           |
| Barta 161 12            | 90                   | 1600                         | 1:35:14.759            | -7.12.52.259                           |
| LP 353-51               | 110                  | 800                          | 02:23:26.601           | 22.43.54.846                           |
| TYC 2211-1309-1         | 80                   | 650                          | 22:00:41.823           | 27.15.20.179                           |
| TYC 7443-1102-1         | 47                   | 2200                         | 19:56:04.396           | -32.07.37.640                          |
| TYC 7443-1102-1         | 47                   | 440                          | 19:56:04.474           | -32.07.38.475                          |
| UCAC2 19527490          | 65                   | 3000                         | 18:58:05.016           | -29.53.33.824                          |
| UCAC2 20312880          | 55                   | 760                          | 06:13:13.748           | -27.41.59.131                          |
| UCAC3 116-474938        | 85                   | 800                          | 9:56:03.108            | -32.07.29.08                           |
| V* TX P8A               | 60                   | 1300                         | 22:44:59.826           | -33.15.32.550                          |

Serendipitous sources within  $10''$  of the phase centre whose flux reached at least  $5\sigma$  were identified in the primary beam-corrected CLEAN images and are presented in Table 5.4. Sources are identified in ten of the fields. Two sources are present in the TYC 7443-1102-1 field, one of which is resolved to be  $2''$  along one axis. The sources are not associated with any stars and so are likely to be background galaxies. The galaxy number count model of Popping et al. [2020] can be used to estimate the expected number of galaxies with a flux of at least  $0.5$  mJy/beam to be present within a  $10''$  radius of the phase centre of 33 observations. The expected number of background sources is  $12^{+4}_{-10}$ , consistent with our detections.

Significant flux at the stellar location is measured for GJ 2006 A, GSC 07396-00759, AT Mic A and AT Mic B, and TYC 7443-1102-1. GSC 07396-00759 shows a clearly resolved edge-on disc. The flux from TYC 7443-1102-1 cannot be differentiated from the background confusion close the stellar location and so this source is considered significantly confused with no local flux measurement able to be taken. These sources are discussed in more detail in §5.3.

Where significant flux is measured at the stellar location we check the observations for signs of mm stellar flares, as these can be mistaken for debris discs [e.g. Anglada et al., 2017; MacGregor et al., 2018b]. The observations were split into their individual scans and re-imaged to check for variance of the flux along the time baseline of the observations. No evidence for flaring was found.

The  $^{12}\text{CO}$  J=3-2 transition line was also checked in these observations by producing CLEAN continuum-subtracted images with the *uvcontsub* algorithm in CASA and searching for significant emission at the stellar location and around the expected stellar radial velocity. No CO emission was found in any observation.

A stacked image was also made from the non-detections in which the star is expected to lay within  $0.5''$  of the phase centre. With this criterion 2MASS J05241914-1601153 AB, BD+30 397 B, GJ 2006 B, HD 139084 B, LP 476-207 AB, UCAC2 19527490, UCAC2 20312880 and UCAC3 124-580676 are excluded. We also exclude TYC 7443-1102-1 due to its confusion. The stacked image is thus constituted of the remaining 21

observations and has an RMS of  $1\sigma = 10 \mu\text{Jy}/\text{beam}$ . The mean expected stellar emission is  $6 \mu\text{Jy}/\text{beam}$ . No significant flux is found at the centre of the stacked image with a measurement of  $12 \mu\text{Jy}/\text{beam}$ , the  $3\sigma$  upper limit on the mean flux for these non-detections is thus  $30 \mu\text{Jy}/\text{beam}$ , and the  $3\sigma$  upper limit on mean flux *excess* above the stellar flux is  $24 \mu\text{Jy}/\text{beam}$  which at a mean distance of 44 pc corresponds to a disc 25 times less bright than AU Mic.

## 5.3 Results

### 5.3.1 Gaia DR3 parallaxes and binary implications

The third data release of the Gaia satellite [Gaia Collaboration et al., 2022] has improved our astrometric knowledge of our candidate sample since both the proposal submission and observations, some stars now have accurate parallaxes where there was none before, and other stars have been resolved as binaries with new measurements of their separation. Multiplicity can cause errors in astrometric solutions [Lindgren et al., 2018] and this is possibly the root cause for previous difficulty in finding accurate parallaxes. A measure for non-standard uncertainty in Gaia observations is the astrometric excess noise, `astrometric_excess_noise` (epsi), representing modelling errors and measuring the disagreement between observations of the source and its best fitting model expressed as an angle in units of milli-arcseconds<sup>2</sup>. The epsi in an ideal case should be zero, but for reference the median excess noise for sources with six-parameter solutions is 0.169<sup>3</sup>. A related parameter is the significance of the astrometric excess noise, `astrometric_excess_noise_sig` (sepsi), for which a value greater than two indicates that the epsi is significant, i.e. the observations of the star significantly differ from its best fitting model. The epsi, when guided by the sepsi, can be used to infer the presence of companions [e.g. Groenewegen, 2018; Kervella et al., 2019].

Multiplicity can also affect the likelihood a system contains a detectable debris disc. Yelverton et al. [2019] find that disc detection rate is more than halved in comparison to single stars when binary separation is less than 25 AU, that the disc detection rate is zero when the separation is between 25 and 135 AU, and that larger separations do not affect disc detection rates. However, the systems studied in that paper were for the majority sun-like, and while a small number of M-type systems were included, the conclusion might not extend to them. All binaries in the sample are now discussed below.

<sup>2</sup>[https://gea.esac.esa.int/archive/documentation/GDR3/Gaia\\_archive/chap\\_datamodel/sec\\_dm\\_main\\_source\\_catalogue/ssec\\_dm\\_gaia\\_source.html](https://gea.esac.esa.int/archive/documentation/GDR3/Gaia_archive/chap_datamodel/sec_dm_main_source_catalogue/ssec_dm_gaia_source.html)

<sup>3</sup>[https://gea.esac.esa.int/archive/documentation/GDR3/Data\\_processing/chap\\_cu3ast/sec\\_cu3ast\\_quality/ssec\\_cu3ast\\_quality\\_properties.html](https://gea.esac.esa.int/archive/documentation/GDR3/Data_processing/chap_cu3ast/sec_cu3ast_quality/ssec_cu3ast_quality_properties.html)

### **2MASS J05241914-1601153 AB**

2MASS J05241914-1601153 (AKA PM J05243-1601, UCAC4 370-008199) has previously been noted as a double star [Messina et al., 2017; Miret-Roig et al., 2020] and did not have an accurate parallax prior to Gaia DR3. A has Gaia G magnitude of  $12.496 \pm 0.004$  and B has a magnitude of  $12.778 \pm 0.004$ , so the stars are of a similar brightness and type. A has a parallax of  $32.06 \pm 0.80$  mas and B has a parallax of  $32.27 \pm 0.14$  mas placing the stars at 31.1 pc and consistent with co-planar in the plane of the sky, this would equate their separation of  $0.37''$  at the time of observation to 11.5 AU. This separation would reduce the likelihood of there being a detectable disc; if a disc is present there is the possibility that it would be circumbinary, which would be resolved by our detections observations.

### **2MASS J19102820-2319486**

2MASS J19102820-2319486 (AKA 1SWASP J191028.18-231948.0, EPIC 215900519) did not have a parallax measurement prior to Gaia DR3, but now has a measured parallax of  $17.0 \pm 0.2$  mas, putting it at 59 pc. Messina et al. [2017] label it as a single star, however Gaia DR3 also revealed a second source at a  $0.3''$  separation without a parallax or proper motion but with a G magnitude of  $12.882 \pm 0.006$  compared to 2MASS J19102820-2319486's magnitude of  $12.528 \pm 0.004$ . The excess astrometric noise for both sources is moderate, the excess astrometric noise is 1.394 mas and the significance of astrometric noise value is 1390 for the source with parallax and the  $\epsilon$  is 2.198 mas and the  $\sigma$  is 1900 for the source without parallax. This could explain the lack of a previous fit for 2MASS J19102820-2319486 and the lack of a fit for the second source. Multiplicity can be a cause of astrometric noise, and so it is possible the two sources indeed constitute a binary, if approximately in the plane of the sky the separation would be 18 AU. This separation would reduce the likelihood of there being a detectable debris disc around either star and any disc could be circumbinary if present.

### **Barta 161 12**

Barta 161 12 (AKA UCAC4 414-001790, ASAS J013514-0712.9, 2MASS J01351393-0712517) is listed as a double-lined spectroscopic binary by [Malo et al., 2014] and Gaia DR3 detects only one star, thus the binary separation is likely less than 25 AU, this would reduce the likelihood of there being a detectable disc and any disc present would likely be circumbinary.

### **BD+30 397 B**

BD+30 397 B (AKA 2MASS J02272924+3058246, GSC 02323-00566, AG Tri B) is a companion to BD+30 397 A. The pair's parallax is consistent with them being approximately co-planar in the plane of the sky and their separation of 22.2'' equates to 910 AU. Their separation is unlikely to affect the likelihood of there being a detectable disc around either star.

BD+30 397 B has a high noise in Table 5.3 as the observation was pointed near the centre of the binary, placing BD+30 397 B at the edge of the primary beam, raising the local noise. Despite this pointing, BD+30 397 A is outside the 12'' FWHM of the primary beam, and as such is unobserved.

### **GJ 2006 AB**

GJ 2006 AB (AKA LDS 18A, 2MASS J00275023-3233060, UCAC3 115-1206) have parallax consistent with being approximately co-planar in the plane of the sky and their separation of 17.9'' equates to 625 AU. Their separation is unlikely to affect the likelihood of there being a detectable disc around either star.

### **GSC 07396-00759**

GSC 07396-00759 (AKA ASAS J181422-3246.2, CAB 25B, UCAC4 287-163100), as noted in Cronin-Coltsmann et al. [2022, Chapter 4], is a wide separation companion of the well-studied close-binary V4046 Sgr at a distance of 12300 au [Torres et al., 2006; Kastner et al., 2011]. V4046 Sgr possesses both a gas-rich circumbinary disc and evidence of ongoing accretion [e.g. Stempels and Gahm, 2004; Öberg et al., 2011; Rosenfeld et al., 2013; Rapson et al., 2015; Kastner et al., 2018; D'Orazi et al., 2019; Martinez-Brunner et al., 2022]. Their separation is unlikely to affect the likelihood of there being a detectable disc around either star.

### **GSC 08350-01924 AB**

GSC 08350-01924 (AKA 1RXS J172919.1-501454, UCAC2 10274954) has been listed as a binary in previous works [Alonso-Floriano et al., 2015; Messina et al., 2017] and Zúñiga-Fernández et al. [2021] conclude it not to be a spectroscopic binary. Gaia DR3 has resolved the binary and identified parallaxes for each star for the first time. A has a parallax of  $16.15 \pm 0.06$  mas and B has a parallax of  $15.95 \pm 0.078$  mas putting the binary at 62.3 parsecs [Bailer-Jones et al., 2021]. The stars do not have an extremely large excess astrometric noise but it is still very significant, the epsi is 0.480 mas and the sepsi is 320 for the closer



source and the  $\epsilon$  is 0.613 mas and a significance of astrometric noise value  $\sigma_{\epsilon}$  is 480 for the distant source. Thus although only separated by 0.7'' in the plane of the sky, the two are likely widely separated into the plane of the sky by approximately  $140,000 \pm 60,000$  AU, consistent with not being a spectroscopic binary, but with this level of astrometric noise there remains the possibility that the two are separated by significantly less distance. A has a Gaia G magnitude of  $12.295 \pm 0.003$  and B has a magnitude of  $12.573 \pm 0.003$ , so the stars are of a similar brightness and type. Their separation is unlikely to affect the likelihood of there being a detectable disc around either star.

### **HD 139084 AB**

HD 139084 AB (AKA CD-57 6042 AB, 2MASS J15385757-5742273 AB) have parallax measurements of  $25.8 \pm 0.2$  mas and  $25.55 \pm 0.02$  mas respectively and are separated by 10.3'' on the sky. The stars therefore constitute a wide binary with a likely separation of at least 50,000 AU. Their separation is unlikely to affect the likelihood of there being a detectable disc around HD 139084 B, although HD 139084 A is known to be a single lined spectroscopic binary [Nielsen et al., 2016] which would reduce its likelihood of hosting a detectable disc.

HD 139084 AB have a higher noise in Table 5.3 as the observation was pointed at the centre of the binary, placing both stars at the edge of the primary beam, raising the local noise.

### **HD 155555 C**

HD 155555 C (AKA V824 Ara C, UCAC3 47-295205, 2MASS J17173128-6657055) is companion to the short period binary HD 155555 AB with a separation on the sky of 34''; at a distance of 30.3 pc this equates to a separation on the sky of 1000 AU. Additionally, HD 155555 C possesses a parallax of  $32.88 \pm 0.03$  mas and HD 155555 AB have a parallax of  $32.95 \pm 0.02$  mas, making them unlikely to be approximately co-planar in the plane of the sky. The binary separation sky would be approximately 13,000 AU perpendicular to the plane of the sky. Their separation is unlikely to affect the likelihood of there being a detectable disc around either star.

### **LP 476-207 AB**

LP 476-207 (AKA HIP 23418, GJ 3322, 2MASS J05015881+0958587) is a literature double lined spectroscopic binary [Delfosse et al., 1999] with an orbital period of 11.9 days [Messina et al., 2017]. Gaia DR3 resolves two stars, we will label LP 476-207 AB as these two separated components, making the spectroscopic binary LP 476-207 AaAb (or possibly

BaBb). A has a parallax of  $42.04 \pm 0.03$  mas and B has a parallax of  $42.10 \pm 0.09$  mas, thus the two are consistent with being approximately co-planar in the plane of the sky. A has a G magnitude of  $10.568 \pm 0.003$  and B has a magnitude of  $11.420 \pm 0.004$ , thus A is likely the primary and dominates the flux from the system. Their separation of  $1.4''$  on the sky at 33.2 pc equates to 46.5 AU. This separation would make it unlikely that the system hosts a debris disc.

### **AT Mic AB**

AT Mic (AKA GJ 799 , HD 196982, HIP 102141, CD-32 16135, 2MASS J20415111-3226073) is a literature close binary system and is highly likely to be a distant companion to AU Mic [Adams et al., 1927; Caballero, 2009; Shaya and Olling, 2011; Messina et al., 2016] with an on-sky separation of 0.23 pc which equates to 47,000 AU on the sky. The AT Mic AB binary have Gaia G magnitudes of  $9.576 \pm 0.003$  and  $9.605 \pm 0.003$  respectively, so the stars are of a similar brightness and type. The system has been observed to show significant evidence of proper motion [Messina et al., 2016, and references therein] and Malkov et al. [2012] provide an orbital period of 209 yr with a semi-major axis of  $3.18''$ , corresponding to 31 AU, and an eccentricity of  $e = 0.26$  for the binary.

Gaia DR3 measures the parallaxes for the AT Mic binary of  $100.79 \pm 0.07$  mas and  $101.97 \pm 0.08$  mas, which would be inconsistent with the two being approximately co-planar in the plane of the sky, equating to a separation of 23,300 AU. However, The Gaia DR3 observations for AT Mic A have an excess astrometric noise of 0.509 mas and a significance of astrometric noise value of 330, and AT Mic B has values of 0.502 mas and 311 respectively. For comparison, their wide separation companion AU Mic has values of 0.098 mas and 6.1 respectively. The level of astrometric noise is significant and could mean that the uncertainty of the Gaia parallaxes is underestimated.

Given the extensive historic observation of the system, observed apparent orbital motion and high excess astrometric noise on the Gaia parallaxes, it is likely that the Gaia parallaxes for this system are untrustworthy. Thus, we will continue with the understanding that the stars are co-planar and so are separated primarily by the  $2''$  on the sky. Using Malkov et al. [2012]’s orbital parameters the semi-major axis of the binary is 31 AU.

The separation with AU Mic would be unlikely to affect the likelihood of either system hosting a detectable disc, but the AT Mic binary separation would make it unlikely that the system hosts a debris disc.

### **TYC 6872-1011-1 and UCAC2 19527490**

TYC 6872-1011-1 (AKA 1RXS J185803.4-295318, UCAC4 301-253452, 2MASS J18580415-2953045) is reported as a double lined spectroscopic binary in Zúñiga-Fernández et al. [2021]. The binary separation is likely less than 25 AU; this would reduce the likelihood that the system hosts a detectable disc and any disc could be circumbinary.

UCAC2 19527490 (AKA 2MASS J18580464-2953320) does not have a reported parallax in either the literature or Gaia DR3. Gaia DR3 measures a very large excess astrometric noise, the  $\epsilon_{\text{psd}}$  is 59 mas and the  $\sigma_{\text{psd}}$  is 240,000, which could be indicative of a close binary companion. A close companion would reduce the likelihood that the system hosts a detectable disc and any disc could be circumbinary.

UCAC2 19527490 is only separated from TYC 6872-1011-1 by 28.3" on the sky, and the two share very similar proper motions and radial velocities, and so it has been posited before that the two are companions [Moór et al., 2013]. This would place UCAC2 19527490 at 74.2 pc alongside TYC 6872-1011-1 and their separation would equate to 2100 AU. This separation would not reduce the likelihood of either star hosting a detectable disc.

### **TYC 7443-1102-1 and UCAC3 116-474938**

TYC 7443-1102-1 (AKA 2MASS J19560438-3207376, PM J19560-3207, UC 4054A) and UCAC3 116-474938 (AKA 2MASS J19560294-3207186, BWL 53) are known to be companions. The two have parallaxes of  $19.49 \pm 0.02$  mas and  $19.5 \pm 0.7$  mas respectively, consistent with being approximately co-planar in the plane of the sky. At a distance of 51.3 pc their separation of 26.3" equates to 1350 AU. This separation would not reduce the likelihood of either star hosting a detectable disc.

UCAC3 116-474938 is also listed as a literature double star [Messina et al., 2017], this is not resolved by Gaia DR3 but the star has a high excess astrometric noise, the  $\epsilon_{\text{psd}}$  is 5.59 mas and the  $\sigma_{\text{psd}}$  is 4000, indicating the possible presence of a close companion. A close companion would reduce the likelihood of the system hosting a detectable disc.

### **UCAC2 20312880**

UCAC2 20312880 (AKA RX0613.2-2742, TSN 2, 2MASS J06131330-2742054) is a literature double star [Messina et al., 2017]. This is not resolved by Gaia DR3 but the star has a high excess astrometric noise, the  $\epsilon_{\text{psd}}$  is 2.5 mas and the  $\sigma_{\text{psd}}$  is 960, indicating the possible presence of a close companion. A close companion would reduce the likelihood of the system hosting a detectable disc.

### **UCAC3 124-580676**

UCAC3 124-580676 (AKA SCR J2010-2801, 2MASS J20100002-2801410) is a literature spectroscopic binary and is listed as types M2.5+M3.5 in Messina et al. [2017]. Gaia DR3 resolves two stars at a 1'' separation but without a parallax for the secondary. The two stars have Gaia magnitudes of  $12.449 \pm 0.005$  and  $12.207 \pm 0.004$  indicating that the two are of similar type. The excess astrometric noise for the sources is very high, the  $\epsilon_{\text{psf}}$  is 2.02 mas and the  $\sigma_{\text{psf}}$  is 490 for the source with parallax and the  $\epsilon_{\text{psf}}$  is 14.2 mas and the  $\sigma_{\text{psf}}$  is 7360 for the source without parallax, explaining the lack of fit for the secondary. If approximately in the plane of the sky the separation would be 48 AU. This separation would make it unlikely that the system hosts a debris disc.

### **TX PsA and WW PsA**

TX PsA (AKA GJ 871.1 B, UCAC2 17853886, 2MASS J22450004-3315258 ) and WW PsA (AKA CD-33 16206, GSC 07501-00987, HIP 112312, 2MASS J22445794-3315015) are known companions. Their Gaia DR3 parallaxes are  $48.00 \pm 0.03$  mas and  $47.92 \pm 0.03$  mas respectively. Bailer-Jones et al. [2021] measure distances of  $20.826 \pm 0.013$  pc and  $20.843 \pm 0.012$  pc respectively, so the stars could be but are not necessarily approximately co-planar in the plane of the sky. The stars are separated in the plane of the sky by 36''; at a distance of 20.8 pc this equates to 750 AU. This separation would not reduce the likelihood of either star hosting a detectable disc.

### **Binaries summary**

As it is not an M-star, HD 139084 is excluded from the below summary.

One system has a Gaia DR3 resolved binary with both parallaxes and a separation of less than 25 AU (2MASS J05241914-1601153 AB, this separation is less than the observation beam size). One system has a Gaia DR3 resolved binary with one parallax and a potential separation of less than 25 AU (2MASS J19102820-2319486, this separation is less than the observation beam size). Two stars are spectroscopic binaries with no resolved companions in Gaia DR3 (Barta 161 12, TYC 6872-1011-1). Two stars are literature double stars unresolved in Gaia DR3 but with high excess astrometric noises (UCAC2 20312880, UCAC3 116-474938). One star is not previously listed as a multiple star but has very high excess astrometric noise (UCAC2 19527490). In total there are six or seven systems with a binary separation less than 25 AU that are less than half as likely to possess detectable debris discs than single star, assuming that the results of Yelverton et al. [2019] extend to M type stars.

One star is a spectroscopic binary and has two stars resolved in Gaia DR3 with one parallax and a potential separation between 25 and 135 AU (UCAC3 124-580676). One system is a spectroscopic binary and has two stars resolved in Gaia DR3 with both parallaxes and a separation between 25 and 135 AU (LP 476-207 AB). One system is a binary and has two stars resolved in Gaia DR3 with both parallaxes (that likely have underestimated uncertainties), has literature orbital parameters and a separation between 25 and 135 AU (AT Mic AB, this separation is greater than the observation beam size).

In total there are three systems with a binary separation between 25 and 135 AU that are very unlikely to possess detectable debris discs, assuming that the results of Yelverton et al. [2019] extend to M type stars.

Four of the above stars are also companions to other stars with a separation greater than 135 AU (UCAC2 19527490, UCAC3 116-474938, AT Mic AB)

A further 11 stars are Gaia DR3 resolved companions to other stars with all parallaxes and a separation greater than 135 AU (BD+30 397 B, GJ 2006 A, GJ 2006 A, GSC 07396-00759, GSC 08350-01924 A, GSC 08350-01924 B, HD 139084 B, HD 155555 C, TYC 7443-1102-1, TX PSA, WW PSA). The on-sky separation of GSC 08350-01924 AB is less than the observation beam size. The multiplicity of these stars is unlikely to affect the likelihood of the presence of a detectable debris disc.

### 5.3.2 Non-significant excesses

#### TYC 7443-1102-1

This star has an unresolved Herschel PACS excess as reported in Tanner et al. [2020]. Two distinct sub-mm sources are clearly detected in the ALMA observation displayed in Figure 5.2, neither of which are centred at the Gaia DR2 proper-motion adjusted location of the star. The two sources are 1.4" and 0.9" distant from the stellar location and have flux densities of  $2.20 \pm 0.05$  mJy/beam and  $0.44 \pm 0.05$  mJy/beam respectively. The brighter of the two sources is resolved along one axis.

The ALMA absolute pointing accuracy for this observation is  $\sim 30$  mas and the error on the Gaia stellar location is sub-milliarcsecond. Therefore, these mm-wave sources are most likely not associated with the star and constitute background galaxies. For a putative debris disk to be detected with PACS but not with ALMA, the spectral slope of the dust emission would need to have  $\gamma \lesssim -1$ , steeper than is seen for well-characterised cases [e.g. Gáspár et al., 2012; MacGregor et al., 2016]. Larger surveys (that are less precise) find  $\gamma$  values in the range of  $-0.5$  -  $-1$  [Holland et al., 2017; Sibthorpe et al., 2018]. Thus a scenario where the PACS detection is of a circumstellar disk that is then not detected by ALMA is improbable. Therefore the Herschel excess most likely also originated from

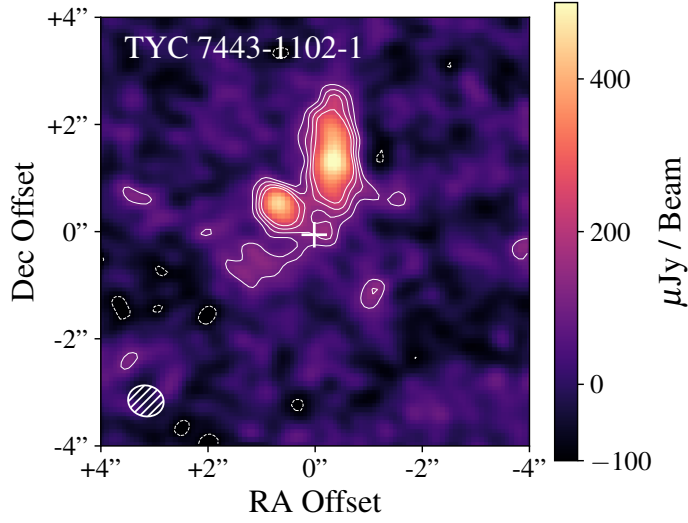


Figure 5.2: Naturally weighted ALMA 880 $\mu$ m image of TYC 7443-1102-1. The stellar location is marked with a +. The ellipse in the lower left corner shows the restoring beam. Contours are  $-3\sigma$ ,  $-2\sigma$ ,  $2\sigma$ ,  $3\sigma$ ,  $4\sigma$ ,  $5\sigma$ .

these contaminating sources and the conclusion is drawn that a circumstellar disk around TYC 7443-1102-1 is not detected.

As the observation is significantly contaminated at the stellar location we remove the observation and star from the scientific sample going forward.

### HD 155555 C

The  $93 \pm 40 \mu$ /beam flux at the stellar location of this observation, as displayed in Figure 5.3, is between the  $2\sigma$  level of  $80 \mu$ Jy/beam and the  $3\sigma$  level of  $120 \mu$ Jy/beam, and so it warranted a further analysis. We apply the *uvmodelfit* task again, now allowing the offset parameters to vary, and find a flux of  $116 \pm 40 \mu$ /beam at a separation of  $0.21 \pm 0.07''$ , that could be consistent with the stellar location.

The stellar flux is only expected to be  $9 \mu$ Jy/beam and so if the flux is real it would constitute an excess. As there are multiple  $2\sigma$  peaks within  $2''$  of the stellar location, combined with the offset of the flux, we rule the flux measurement to likely be the result of noise. Given 33 observations there is approximately a 10% chance that at least one observation will have a  $3\sigma$  peak at the stellar location, and so we do not think it unlikely that the flux in this observation could derive from noise.

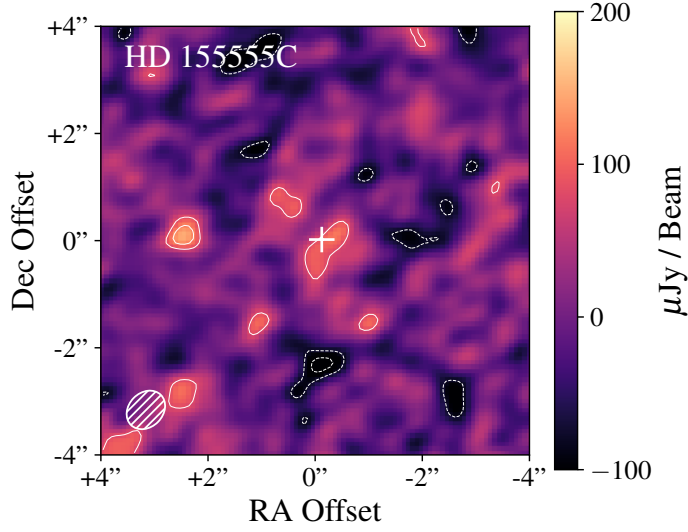


Figure 5.3: Naturally weighted ALMA 880 $\mu$ m image of HD 155555 C. The stellar location is marked with a +. The ellipse in the lower left corner shows the restoring beam. Contours are  $-3\sigma$ ,  $-2\sigma$ ,  $2\sigma$ ,  $3\sigma$ ,  $4\sigma$ ,  $5\sigma$ .

#### AT Mic B

A flux of  $120 \pm 27 \mu\text{Jy}/\text{beam}$  is measured at the stellar location of this observation, as displayed in Figure 5.4, reaching a significance of  $4\sigma$ . We apply the *uvmodel* task again, now allowing the offset parameters to vary, and find a flux of  $125 \pm 27 \mu\text{Jy}/\text{beam}$  at a separation of  $0.09 \pm 0.06''$ , consistent with the expected Gaia DR3 stellar location.

However, the expected stellar flux is  $60 \mu\text{Jy}/\text{beam}$ . We can rule that the star is significantly detected, but after subtracting the expected stellar flux the remaining mm-wave excess of  $65 \mu\text{Jy}/\text{beam}$  does not reach the  $3\sigma$  level of  $81 \mu\text{Jy}/\text{beam}$  for this observation. And so it is concluded that an excess is not significantly measured for this star.

#### 5.3.3 Significant excesses

##### GSC 07396-00759

This observation clearly resolves a bright, edge-on debris disc, as displayed in Figure 5.5 consistent with position angle, inclination and approximate radius consistent with the previous scattered light observations of this disc Sissa et al. [2018]; Adam et al. [2021]. An in-depth analysis of this disc is presented in Cronin-Coltsmann et al. [2022, Chapter 4].

The disc has an integrated mm flux of  $1.84 \pm 0.22 \text{ mJy}$  and a radius of  $70.2 \pm 4.4 \text{ AU}$ , an example SED is displayed in Figure 5.6 and a fractional luminosity-temperature plot with

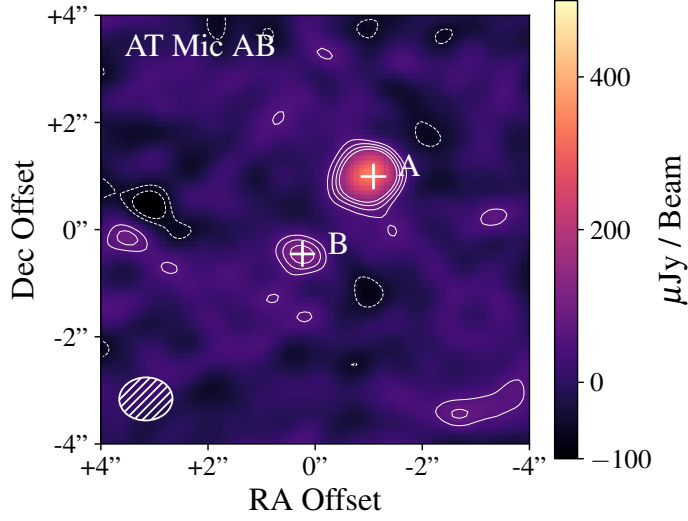


Figure 5.4: Naturally weighted ALMA 880 $\mu$ m image of AT Mic AB. The stellar locations are marked with a + and an A/B. The ellipse in the lower left corner shows the restoring beam. Contours are  $-3\sigma$ ,  $-2\sigma$ ,  $2\sigma$ ,  $3\sigma$ ,  $4\sigma$ ,  $5\sigma$ .

a distribution of dust models is displayed in Figure 5.7 (note that these models use a modified blackbody for consistency and not amorphous silicate as in Chapter 4). With a lack of far-IR photometry it is difficult to constrain an SED and model temperature, but with a resolved radius of 70.2 AU the mm dust grains would have a temperature of 20 K and so we can limit the likely models to those close to 20 K, i.e. close to the dashed red line in Figure 5.7. Limited to these models the fractional luminosity likely ranges from  $\sim 1 \times 10^{-4}$ - $5 \times 10^{-3}$ . More details on the SED fitting procedure can be found in Cronin-Coltsmann et al. [2022, Chapter 4] and Yelverton et al. [2019].

### GJ 2006 A

A flux of  $390 \pm 33 \mu\text{Jy}/\text{beam}$  is measured at the stellar location of this observation, as displayed in Figure 5.5, reaching a significance of  $11\sigma$ . We apply the *uvmodelfit* task again, now allowing the offset parameters to vary, and find a flux of  $391 \pm 27 \mu\text{Jy}/\text{beam}$  at a separation of  $0.03 \pm 0.02''$ , consistent with the expected Gaia DR3 stellar location. Subtracting the expected stellar flux of  $6 \mu\text{Jy}/\text{beam}$  from the measured flux leaves a mm excess of  $385 \pm 33 \mu\text{Jy}/\text{beam}$ , remaining at  $11\sigma$ .

Having ruled out stellar flaring this mm excess likely constitutes an unresolved debris disc. The beam size of the observation sets an upper limit on the radius of the disc, a beam semi-major axis of  $0.96''$  sets a radius upper limit of 34 AU. An example SED is presented



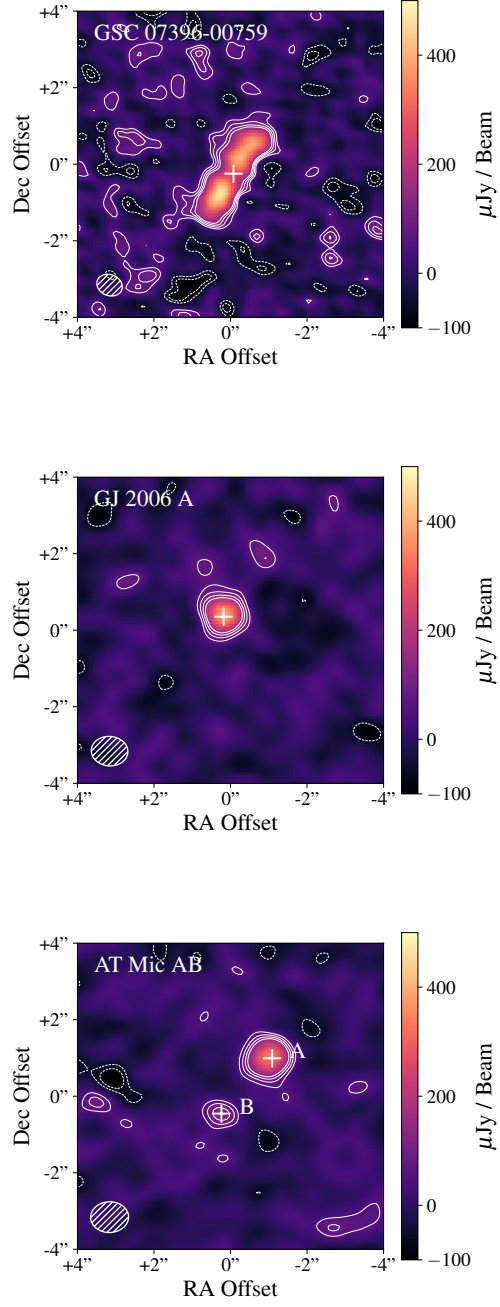


Figure 5.5: Naturally weighted ALMA 880 $\mu$ m images of GSC 07396-00759, GJ 2006 A and AT Mic AB. The stellar locations are marked with a +. The ellipses in the lower left corners show the restoring beams. Contours are  $-3\sigma$ ,  $-2\sigma$ ,  $2\sigma$ ,  $3\sigma$ ,  $4\sigma$ ,  $5\sigma$ .

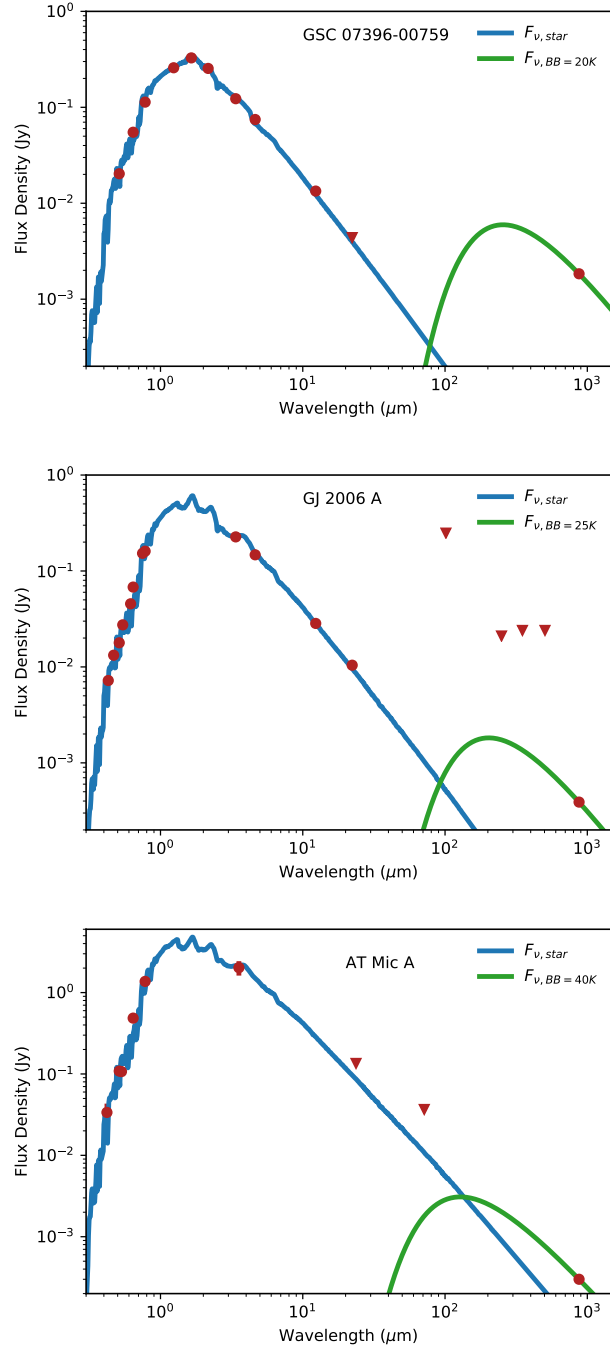


Figure 5.6: Example SEDs for GSC 07396-00759, GJ 2006 A and AT Mic A. Dots are measured fluxes and triangles are  $3\sigma$  upper limits. The stellar photosphere models are in blue and example blackbody distributions through the ALMA flux are in green. With only one flux point measuring the thermal emission of the discs, a large range of temperatures and fractional luminosities could describe the discs.

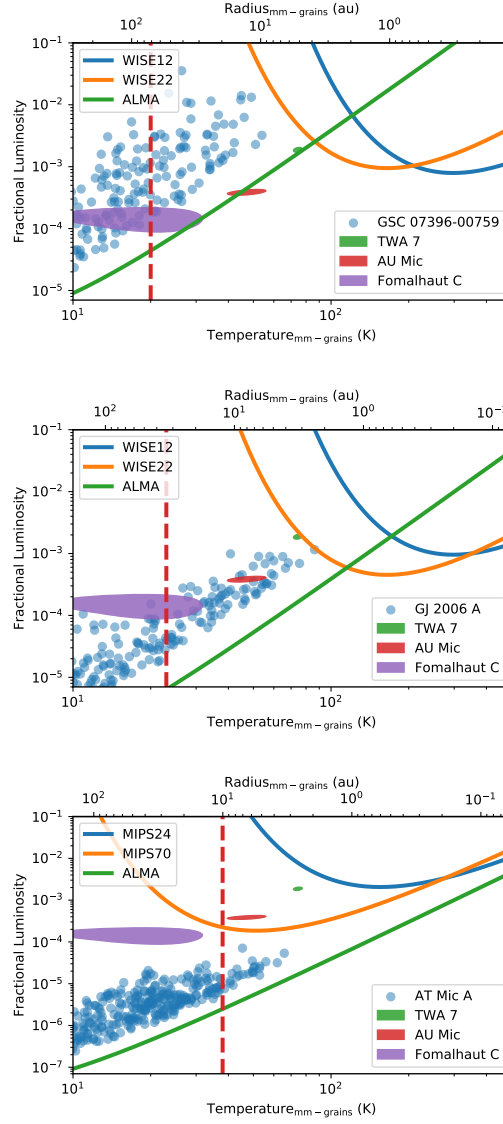


Figure 5.7: Plots of fractional luminosity against representative temperature/blackbody radius, i.e. the temperature and stellocentric radius of mm grains. Blackbody radius depends on host stellar temperature and is thus only accurate for the host of interest. A selection of allowed models for the discs of GSC 07396-00759, GJ 2006 A and AT Mic A are plotted as blue circles. The distributions up to  $3\sigma$  following the same modified blackbody SED fitting procedure are shown for a selection of low mass host debris discs as coloured ellipses. The detection limits for several instruments are plotted as blue, orange and green curves respectively. The vertical red dashed lines show the resolved radius or radius upper limits of the discs.

in Figure 5.6 and a fractional luminosity-temperature plot with a distribution of dust models is displayed in Figure 5.7. With a lack of far-IR photometry it is difficult to constrain an SED and model temperature, but with an upper limit of 34 AU on the disc radius we can place a lower limit on the mm grain temperature of 25 K, i.e. to the right of the dashed red line in Figure 5.7. Limited to these models the fractional luminosity likely ranges from  $\sim 2 \times 10^{-5}$  -  $1 \times 10^{-3}$ .

### AT Mic A

A flux of  $319 \pm 27 \mu\text{Jy}/\text{beam}$  is measured at the stellar location of this observation, as displayed in Figure 5.5, reaching a significance of  $11\sigma$ . We apply the *uvmodelfit* task again, now allowing the offset parameters to vary, and find a flux of  $335 \pm 27 \mu\text{Jy}/\text{beam}$  at a separation of  $0.13 \pm 0.03''$ . Subtracting the expected stellar flux of  $70 \mu\text{Jy}/\text{beam}$  from the measured flux leaves a mm excess of  $265 \pm 27 \mu\text{Jy}/\text{beam}$ , reaching  $8\sigma$ .

We consider the apparent  $\sim 0.13 \pm 0.03''$  separation, approximately one eighth of the beam size, between the expected stellar location of AT Mic A and the mm source. The uncertainty of the *uvmodelfit* is not consistent with the stellar location; however, while Gaia positional astrometric uncertainties are reported as sub-milliarcsecond, the ALMA astrometric precision for this observation (calculated per §10.5.2 of the ALMA Cycle 6 Technical Handbook<sup>4</sup>) is  $0.065''$ . Considering also the  $0.09 \pm 0.06''$  offset for AT Mic B's flux, which is in a similar direction, it is likely that the offset for both stars is the result of either uncertain ALMA pointing or possibly the effect of orbital motion. Having also ruled out stellar flaring, we conclude that this excess flux is evidence of an unresolved debris disc around AT Mic A.

The beam size of the observation sets an upper limit on the radius of the disc: a beam semi-major axis of  $1''$  sets a radius upper limit of 10 AU. The semi-major axis of Malkov et al. [2012] of 31 AU would make this disc the first binary system to have a detected debris disc where the binary separation is between 25 and 135 AU, however it is uncertain if Yelverton et al. [2019]'s conclusions extend to M dwarfs and if not, this may not be unusual.

An example SED is presented in Figure 5.6 and a fractional luminosity-temperature plot with a distribution of dust models is displayed in Figure 5.7. With a lack of far-IR photometry it is difficult to constrain an SED and model temperature, but with an upper limit of 10 AU on the disc radius we can place a lower limit on the mm grain temperature of 40 K, i.e. to the right of the dashed red line in Figure 5.7. Limited to these models the fractional luminosity likely ranges from  $\sim 5 \times 10^{-6}$  -  $5 \times 10^{-5}$ .

<sup>4</sup><https://almascience.nrao.edu/documents-and-tools/cycle6/alma-technical-handbook>

## 5.4 Discussion

### 5.4.1 Survey sensitivity and detection fraction

To review our BPMG M-dwarf sample, excluding TYC 7443-1102-1 and including AU Mic, we have: 33 observations containing 34 well resolved and well separated literature M dwarfs; an additional three Gaia DR3 M dwarfs with parallaxes, although one of these three stars is close enough to the primary that a disc would likely be circumbinary; two of the total sample stars are also spectroscopic binaries; and there are an additional 2 Gaia DR3 M dwarf candidates without parallaxes. We treat binaries where dust is likely circumbinary as one system for the sake of the sample, and we do not include stars without Gaia DR3 parallaxes as we cannot verify that they are local M-dwarfs and not more distant brighter stars. With these constraints our scientific sample is 36 M-dwarf hosts.

Of these systems we have four significant detections, GSC 07396-00759, GJ 2006 A, AT Mic A and AU Mic. This makes our detection fraction  $4/36$  or  $11.1\%$ . We derive an uncertainty on this using the uncertainty in small number binomial statistics method set out in the appendix of Burgasser et al. [2003], for a result with uncertainties of  $11.1^{+7.4}_{-3.3}\%$ .

We can also calculate a completeness adjusted detection rate, adjusting for the survey's differing sensitivity for different observations. This is calculated by measuring the completeness for each of our detections, i.e. if that disc flux were present for each observation, what fraction of the observations would have significantly detected it? This is exemplified in Figure 5.8, in which the shading indicates the local completeness. In the dark bottom of the plot no observation would have been able to detect a disc, and in the white top all observations would have been able to detect a disc. We have plotted our four detections with  $1\sigma$  error bars from the fractional luminosity-temperature distributions seen in Figure 5.7, after constraining them with our disc radius information. Only the GSC 07396-00759 models within  $4.3$  AU of  $70.2$  AU are considered, in accordance with the radius fitting of Cronin-Coltsmann et al. [2022, Chapter 4]; only the models with radii smaller than  $34$  AU and  $10$  AU are considered for GJ 2006 A and AT Mic A respectively. The completeness fraction for our four sources are: GSC 07396-00759:  $36/36$ , i.e. all our observations could have detected a GSC 07396-00759-like disc if one were present; GJ 2006 A:  $33/36$ ; and AU Mic:  $33/36$ ; AT Mic A:  $7/36$ , i.e. only seven of our observations were sensitive enough to have detected an AT Mic A-like disc. Dividing through by these completion fractions and summing results in our completeness adjusted detection fraction:  $8.3/36$  or  $23.1\%$ . With the same method of uncertainties applied we get:  $23.1^{+8.3}_{-5.3}\%$ .

Given that much of the weight of this completeness adjusted result derives from AT Mic A alone, an effect that is exacerbated in the small number regime, and as the uncertainties in the disc parameters are not taken into account, the uncertainties on the

completeness adjusted detection fraction are likely underestimated. To investigate these effects I generated one million sets of four synthetic debris disc detections. Within each set each disc had a radius selected randomly from between 10 and 100 AU with linearly spaced probability and a fractional luminosity selected randomly from between  $10^{-3}$  and  $10^{-7}$  with logarithmically spaced probability. The host star luminosity was then selected randomly from the luminosities of the stars in our sample without replacement. The completeness adjusted detection fraction was calculated for each set and over the one million sets a distribution of synthetic completeness adjusted fractions was formed. The median of this distribution with its distance to the 16th and 84th percentiles was  $29.9^{+12.3}_{-8.9}\%$ . While the synthetic fraction is not significantly larger than the observed fraction, its greater uncertainty does imply that the uncertainties on the observed completeness adjusted detection fraction are indeed likely underestimated. This process has made large assumptions about the underlying M-dwarf disc population, however there not yet enough well-observed M-dwarf debris discs to build a more informed model population.

The completeness adjusted detection fraction implies that there could be another three to four AT Mic A-like discs hiding amidst the rest of the sample but that the observations were not sensitive enough to detect them. This is still consistent with the  $30 \mu\text{Jy}/\text{beam}$   $3\sigma$  mean flux limit from the stacked image produced from 21 of our observations containing 21 of the remaining 32 non-detection stars. If these 21 stars have  $3.7 \times 21/32$   $265 \mu\text{Jy}/\text{beam}$  fluxes between them, the mean flux would be only  $31 \mu\text{Jy}/\text{beam}$ .

#### 5.4.2 Detection fraction in context

To begin with, we compare our  $11.1^{+7.4}_{-3.3}\%$  detection rate and  $23.1^{+8.3}_{-5.3}\%$  completeness adjusted rate to the DEBRIS M sample. The DEBRIS survey detected just 2/89 ( $2.2^{+3.4}_{-2.0}\%$ ) M-dwarf discs; immediately our detection rate is significantly higher. We cannot immediately conclude that this is due to ALMA's capability to detect M-dwarf discs over Herschel's however, as Pawellek et al. [2021] measure a 9/12 (75%) detection rate for F star discs in the BPMG, compared to the 22/92 ( $23.9^{+5.3}_{-4.7}\%$ ) rate for F stars of the DEBRIS survey presented in Sibthorpe et al. [2018]. If whatever was the root cause of Pawellek et al. [2021]'s high detection rate for BPMG F stars holds for BPMG M stars, be it a matter of youth, formation environment or some other factor, it could raise the base detection rate. In a simple calculation, if the BPMG has an approximately three times higher detection base rate, the DEBRIS M-dwarf fraction adjusted to the BPMG M-dwarf sample would only be 6%, still nearly half our non-adjusted rate, although within uncertainty due to the small number statistics. Comparing also to the 1/900 detection rate of Rhee et al. [2007]'s IRAS search for M-dwarf discs and Gautier et al. [2007]'s 0/62 Spitzer detection rate, we do conclude that ALMA has enabled us to probe M-dwarf discs in a way that previous telescopes were not able to due to

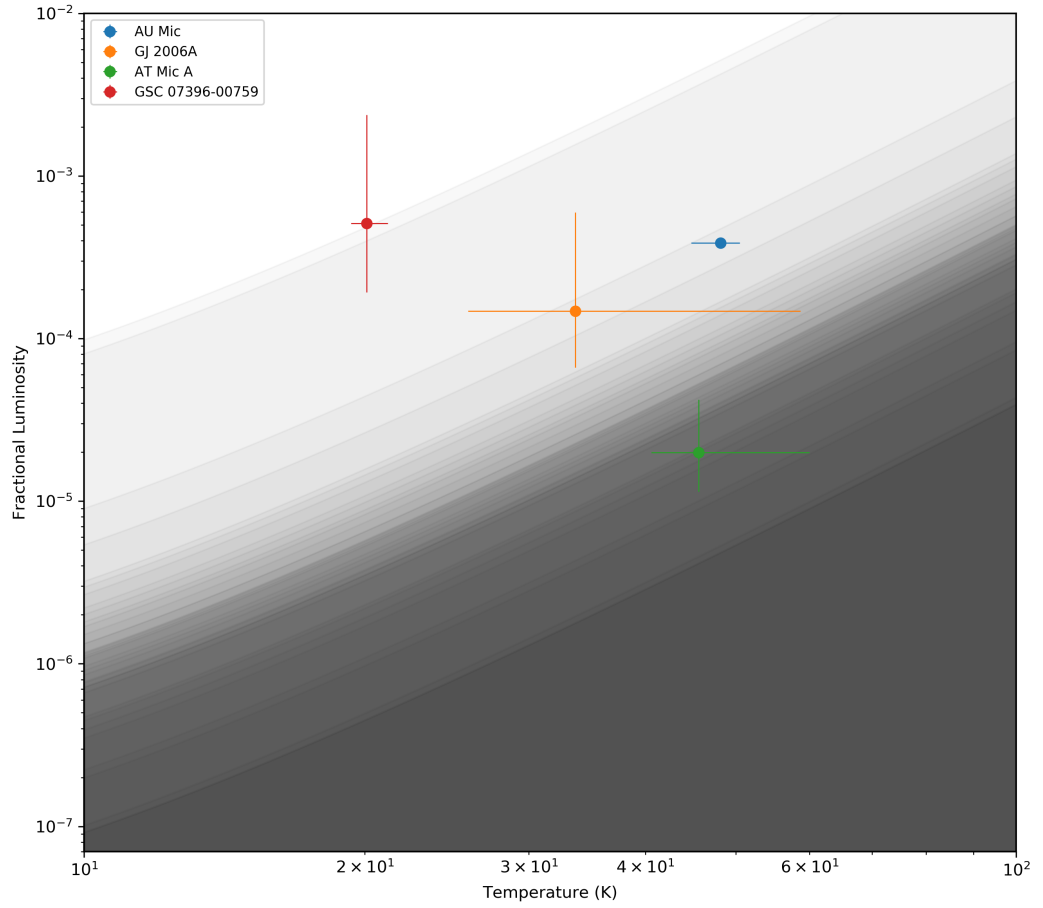


Figure 5.8: Plot of detection limits for all observations. Local shading shows completeness for that observation where the white in the top-left corner is 100% and the darkest gray in the bottom right corner is 0%. The four detections of our sample are plotted to demonstrate their completeness and the survey's general sensitivity.

their wavelength and sensitivity limitations.

Comparing our M-dwarf BPMG sample to Pawellek et al. [2021]’s F-type BPMG sample, our detection rate is seven times lower than the F-type rate. However, the F-type sample are all within 25 pc, unlike our M-type sample that ranges up to 100 pc. To account for this we should compare our completeness-corrected rate, but this is still three times lower. F-types have been previously measured to possess greater detection rates than G and K types, but only by a factor of  $\sim 1.7$  as measured by Sibthorpe et al. [2018] in the DEBRIS FGK sample. It is possible that the higher rate is otherwise because the significantly brighter host stars illuminate the discs more, perhaps allowing them to be more easily detected. Pawellek et al. [2021]’s sample ranges from F0V to F9V ( $5.71 L_{\odot}$  to  $1.69 L_{\odot}$ ) while our M-type sample ranges from M0V - M8.5V ( $0.275 L_{\odot}$  to  $0.004 L_{\odot}$ ). M-dwarf samples span a large luminosity range and their luminosities can be several orders of magnitude lower than FGK type star luminosities. It is possible that the F-type BPMG sample and the M-type BPMG sample host similar discs but the host luminosities affect observability too significantly. If this scenario were true we would need to draw caution when comparing our detection rates to older samples as the older field M-dwarf disc sample detection rate could be much lower than our BPMG rate. It is also possible that whatever mechanism boosts the detectability of BPMG F-type discs does not similarly apply to late type stars; this scenario would mean we can more directly compare our results to age-spread field star surveys like DEBRIS.

Compared to the Herschel DEBRIS G and K samples’ detection rates of  $14.3^{+4.7}_{-3.8}\%$  and  $13.0^{+4.5}_{-3.6}\%$  respectively and completeness adjusted rates of  $24.6^{+5.3}_{-4.9}\%$  and  $22.5^{+5.6}_{-4.2}\%$  respectively, our  $11.1^{+7.4}_{-3.3}\%$  detection rate and  $23.1^{+8.3}_{-5.3}\%$  completeness adjusted rate are consistent, if not following the slight trend of decreasing detection rate with type.

We now compare to the Luppe et al. [2020] predictions for an ALMA survey of DEBRIS-like M-dwarf discs. Our sample has been observed for approximately 15 minutes per star with ALMA Band 7, and the observations were designed to reduce the likelihood that discs would be resolved. It is unlikely that any discs would be larger than the maximum recoverable scales of our observations, but as evidenced by GSC 07396-00759 discs could still have been resolved, reducing the flux per beam. Without correcting for resolution Luppe et al. [2020] predict 15 minutes of observation at Band 7 of the Herschel DEBRIS sample of M-dwarfs scaled as DEBRIS-like discs to attain a detection rate of  $4.3 \pm 0.9\%$  to  $15.8 \pm 0.5\%$ , entirely consistent with our observations. If the DEBRIS sample and the BPMG stellar samples are broadly similar, this would imply that M-dwarf discs are overall similar to earlier type stars’ discs in terms of radius, total surface area, temperature and fractional luminosity, when scaled by stellar mass and luminosity.

The DEBRIS sample is selected from the closest stars, but over a range of ages. Pawellek et al. [2021] has shown based on their high detection rate for F type discs that



the BPMG sample could be significantly different to the DEBRIS sample. Ultimately, to investigate whether M-dwarf discs differ from earlier type discs one would need to use the scaling relationships of Luppe et al. [2020] and apply their process to the known FGK-type BPMG discs to produce a theoretical FGK-like M-dwarf sample to compare our sample to. However, the small number statistics would likely inhibit differentiation of Luppe et al. [2020]’s different scaling relationships.

Ultimately we conclude that our ALMA Band 7 detection rate is evidence towards the hypothesis that M-dwarf discs are not significantly less common than earlier type discs, but that the telescopes employed in previous surveys could not efficiently observe the low temperature and fluxes of M-dwarf discs due to their low host luminosities.

### 5.4.3 Radii in context

In Figure 5.9 we plot the mm-wave radii of all mm resolved debris discs against the host luminosity, as first presented in Matr  et al. [2018]; added to the original sample are the stars presented in Sepulveda et al. [2019], Fomalhaut C [Cronin-Coltsmann et al., 2021] and CPD-72 2713 [Mo r et al., 2020]. We plot the resolved radius of the GSC 07396-00759 disc and upper limits for GJ 2006 A and AT Mic A. We can see that GSC 07396-00759’s radius is consistent with the trend of the earlier type sample, if the disc of GJ 2006 A is close to the upper limit it would also be consistent. Although there is a large scatter, the upper limit on the radius of AT Mic A’s disc is very small. However, we note that this is specifically a plot of resolved radii and that many discs of radii less than ten astronomical units have been inferred from SEDs, and they could not be resolved due to instrumental constraints, as this disc is not resolved due to instrument constraints. The AT Mic A disc would still be small by mm-wave detection standards, however the sample of stars at this low luminosity is very poor and it remains unknown whether this radius limit would be unusual for its host luminosity and mass. As the AT Mic binary are only separated by 30 AU, their orbits would prevent circumstellar discs larger than approximately 10 AU from surviving.

## 5.5 Conclusion

The Beta Pictoris Moving Group provides an excellent candidate sample of M-dwarfs to observe with ALMA to uncover new M-dwarf debris discs and resolve the question as to whether M-dwarf discs are rare or just difficult to observe. In this chapter I have presented new ALMA Band 7 observations of 33 M dwarf systems comprising at least 37 M-dwarf stars.

We identify 11 background sources, likely sub-mm galaxies, of which one is resolved. The occurrence of background sources is consistent with the predictions of galaxy

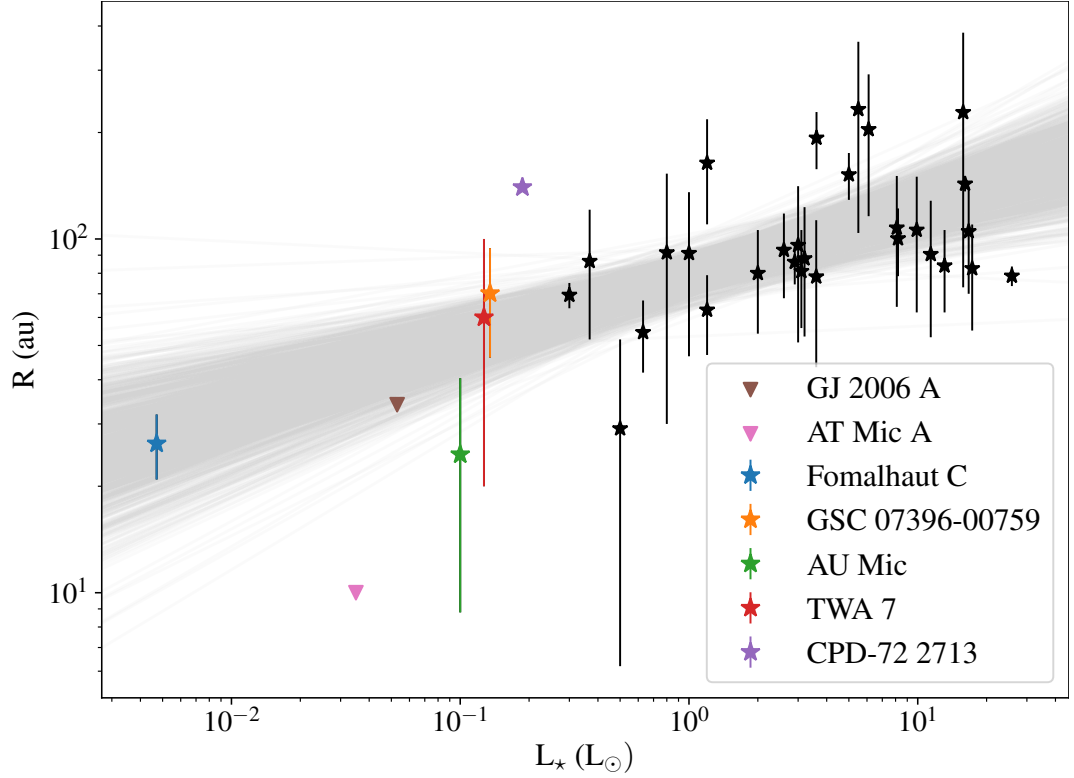


Figure 5.9: mm-wave resolved debris disc radii plotted against host stellar luminosity. Error bars represent disc FWHM or upper limits. The five latest type stellar hosts are highlighted in colour, CPD-72 2713 is plotted without a width as a fixed width of  $0.2R$  was assumed to facilitate fitting a radius [Moór et al., 2020]. Also added are upper limits for the discs of GJ 2006 A and AT Mic A. Transparent grey lines show a sample of 1000 power laws from the parameter distributions of Matrà et al. [2018].

number count models [Popping et al., 2020]. We identify the observation of TYC 7443-1102-1 as severely contaminated by two of these background galaxies.

We examine the consequences of new Gaia DR3 astrometric information for the multiplicity of our sample. Due to their binarity we estimate that three of our systems are very unlikely to possess detectable discs due to their separation and that six to seven of our systems have a reduced likelihood of possessing detectable discs assuming that the results of Yelverton et al. [2019] extend to M-dwarfs. Another 13 of our stars have binary companions that don't affect disc detection likelihood.

We note two of our observations come close to our  $3\sigma$  criterion for detection. The flux at the stellar location of HD 155555 C could be noise or a dim excess, the star may be worth considering for future re-observation. AT Mic B has a  $4\sigma$  flux at the stellar location, but only a  $2\sigma$  excess above the expected stellar flux and so cannot be confirmed as a significant excess detection, this small excess in addition to its proximity at 9.8 pc and its association with AT Mic A and AU Mic this star is worth re-observing in the future. If future observations of AT Mic A are made, AT Mic B will naturally be observed serendipitously due to the small binary separation, and so it may be likely that this star's disc hosting candidacy will be determined in the future.

We identify one resolved disc, GSC 07296-00759 with an integrated flux of 1.84 mJy, and identify two unresolved mm-wave excess detections around GJ 2006 A with a flux of  $385 \mu\text{Jy}/\text{beam}$  and AT Mic A with a flux of  $265 \mu\text{Jy}/\text{beam}$ . We confirm that none of these stars show evidence of stellar flaring and none of the discs show evidence of  $^{12}\text{CO}$  J=3-2 emission. We explore the fractional luminosity-temperature parameter space for these discs and present fractional luminosity ranges.

We stack 21 of our non-detection observations with the stars within  $0.5''$  of the observation phase centre and calculate a  $3\sigma$  upper limit on the mean mm-wave excess of  $24 \mu\text{Jy}/\text{beam}$  for those stars.

We calculate a detection rate of  $4/36$ ,  $11.1^{+7.4}_{-3.3}\%$ , for our M-dwarf sample including AU Mic. We also present a completeness fractional luminosity-temperature plot for our observations and calculate a completeness adjusted detection rate of  $23.1^{+8.3}_{-5.5}\%$ , but I note that these errors are very likely to be underestimated.

We place our detection rate in context and conclude that it is consistent with the Herschel DEBRIS GK detection rate and the ALMA survey predictions of Luppe et al. [2020], allowing us to conclude that M-dwarf debris discs are not significantly less common than earlier type discs but instead require longer wavelength and more sensitive observations to account for the low host luminosity.

Finally we examine the disc radius upper limits of our new detections and conclude that GJ 2006 A is likely consistent with the wider luminosity-radius sample and trend but

that although the upper limit on the disc of AT Mic A is particularly small it resides in too sparse a parameter space to be fully contextualised.

## Chapter 6

# Conclusions

Before the work that constitutes this thesis was conducted, only eight M-dwarfs debris discs had been published in the literature. Of these, only four had been fully resolved with at least one instrument, with only AU Mic having been resolved in thermal emission [MacGregor et al., 2013; Daley et al., 2019]. Of the four resolved discs, only two, AU Mic and TWA 7 had been imaged at mm-wavelengths, with TWA 7 being only marginally resolved with ALMA [Bayo et al., 2019]. Just AU Mic alone had been fully resolved in both scattered light [Kalas et al., 2004] and thermal observations, allowing for simultaneous investigation of the distribution of micron sized dust grains in more distant orbits under the effects of stellar wind ram pressure and mm sized dust grains co-located with the parent planetesimal belt.

Large scale surveys detected few, or no M-dwarf debris discs. Rhee et al. [2007] found just one M-dwarf disc, AU Mic, from matching IRAS data to 900 Hipparcos stars. Gautier et al. [2007] observed no M-dwarf discs with Spitzer from 62 stars. The Herschel DEBRIS survey found two discs from 89 M-dwarfs, for a detection rate of  $2.2^{+3.4}_{-2.0}\%$  [GJ 581, Fomalhaut C; Lestrade et al., 2012; Kennedy et al., 2013, respectively]. A smaller but more sensitive Herschel survey of 18 M-dwarf and 3 late K-dwarf planet hosts with Herschel found another two discs on top of GJ 581 within their sample [Kennedy et al., 2018a].

There remained the question ‘where are all the M-star discs’? Does the low detection rate of historic surveys imply that M-dwarfs are much less likely to form and/or keep debris discs? Or do more sensitive surveys like Kennedy et al. [2018a] and the scaling calculations made in Luppe et al. [2020] show that a similar population of M-dwarf discs do exist, but require more sensitive and longer wavelength observations to find them?

For the discs that do exist, the question is: ‘what are they like’? Are M-dwarf discs just like earlier type discs but scaled down in mass/radius/fraction luminosity, or does stellar wind becoming the dominant pressure force have more profound effects on disc dynamics?

Are the few discs that we have detected the rare outliers, with moving dust clumps like AU Mic [Boccaletti et al., 2015, 2018; Grady et al., 2020] and layered rings like TWA 7 [Ren et al., 2021]?

The work presented in this thesis has made strides in answering these questions.

## 6.1 New resolved ALMA imaging of M-dwarf discs

In Chapters 3 and 4 of this thesis I have presented new resolved ALMA Band 7 observations of two M-dwarf debris discs.

In Chapter 3 I presented the first ALMA observations of the debris disc around Fomalhaut C, an M4V star in the non-hierarchical Fomalhaut triple system and now the latest type star to have a resolved debris disc.

I review previous literature regarding the dynamical set-up and history of the Fomalhaut triple system and examine whether resolved observations could lend evidence to any of the suggested scenarios. I then demonstrated that the disc was clearly detected and radially resolved, as well as identifying a likely background object and a possible asymmetry in the disc.

My modelling derived strong conditions on the disc's  $880\,\mu\text{m}$  flux of  $0.9\pm0.1\,\text{mJy}$  and radius of  $26.5\pm0.5\,\text{AU}$ , but could not resolve the disc's scale width or height instead placing an upper limit of  $4.6\,\text{AU}$  on the Gaussian scale width of the disc and  $3.8\,\text{AU}$  on its Gaussian scale height. I searched for an offset from the disc centre to the expected location of the star, could not conclude that one existed with significant certainty, neither providing evidence for nor against the hypothesis of Shannon et al. [2014] regarding the Fomalhaut triple system's history. My modelling did not suggest that there was significant evidence for the presence of an asymmetry within the disc and I did not detect any carbon monoxide within the disc, concluding that the CO/CO<sub>2</sub> ice fraction of the discs' planetesimals must be at least approximately half the ice fraction of TWA 7's planetesimals, assuming a similar excitation environment, but is consistent with both Solar System's and Fomalhaut A's ice fractions.

My best-fitting ALMA model allowed us to revisit previous scattered light non-detections with HST/STIS and VLT/SPHERE. I identified the background source in the ALMA image as also present in the optical HST image and as not sharing the star's proper motion, confirming that it is not associated with the system. The HST non-detection was calculated to place a  $3\sigma$  limited surface brightness of  $3.39\,\mu\text{Jy arcseconds}^{-2}$  at  $3''$  radius from the star. The NIR SPHERE non-detection was calculated to place a  $3\sigma$  surface brightness detection limit of  $173\,\mu\text{Jy arcsecond}^{-2}$  at  $3.4''$  from the star. I used these limits

to also calculate limits on the dust albedo. From the SPHERE observations I retrieved an albedo upper limit of 0.67 at  $1.625\ \mu\text{m}$  and from the HST observations I retrieved an upper limit of 0.54 at  $0.5858\ \mu\text{m}$ . Both of these limits were too large to meaningfully comment on as typical debris disc dust albedos range between 0.05-0.15 [e.g. Marshall et al., 2018; Choquet et al., 2018; Golimowski et al., 2011; Krist et al., 2010; Kalas et al., 2005] and typical Kuiper belt objects have average albedos of 0.1-0.17 [Vilenius, E. et al., 2012].

With an accurate model of the disc geometry and with the detection of a background galaxy close to the star, I also re-analysed the Herschel observations of Fomalhaut C. I found the Herschel observations to be compatible with the ALMA model and that the background source was unlikely to have significantly contaminated the Herschel flux.

With vetted Herschel fluxes and a new sub-mm flux measurement an SED model was created for the disc finding a best fitting dust temperature of  $20\pm 4\ \text{K}$ , corresponding to a blackbody radius of  $13\pm 5\ \text{AU}$ , and a best fitting fractional luminosity of  $1.5\pm 0.2\times 10^{-4}$ .

With a blackbody radius from the SED I calculated the  $\Gamma$  factor, the ratio between a disc's resolved radius and its blackbody radius and found that it was smaller than expected for a host star of Fomalhaut C's luminosity following the trend identified in Pawellek et al. [2014]. I highlighted the potential caveats and proposed that the increasing role of stellar wind ram pressure in removing small dust from the system could serve to flatten the trend at lower host luminosities.

Finally, I placed the mm-resolved radius of Fomalhaut C on the resolved radius–luminosity plot first presented in Matrà et al. [2018], extending the parameter space by over an order of magnitude into the low-luminosity regime and found that the radius of the Fomalhaut C disc is consistent with other resolved debris discs and the general power-law trend of decreasing radius with decreasing host-luminosity. I also postulate that the disc's narrowness could be the hallmark of an unseen planet with the system.

In Chapter 4 I presented the first ALMA observations of the debris disc around GSC 07396-00759, an M1V star in the  $\sim 20\ \text{Myr}$  old  $\beta$  Pictoris Moving Group and a wide companion to the gas-rich circumbinary disc hosting V4046 Sgr binary system. This makes the disc the second M-dwarf debris disc to be clearly resolved in both thermal and scattered light imaging.

I review the previous scattered-light observations, VLT/SPHERE observations in total intensity as published by Sissa et al. [2018] and in polarimetry as published by Adam et al. [2021], and consider how resolved ALMA observations could break the degeneracy of the different disc models suggested. I then demonstrated that the disc was clearly detected and radially resolved and that there was not significant evidence of a brightness asymmetry within the disc.

My modelling derived strong conditions on the disc's  $880\ \mu\text{m}$  flux of  $1.84 \pm 0.22\ \text{mJy}$  and radius of  $70.2 \pm 4.4\ \text{AU}$ . I found a best fitting Gaussian scale width of  $20.3 \pm 4.2\ \text{AU}$  but could not resolve the disc's scale height. The mm-grains trace the parent planetesimal belt location and so my radius measurement confirms the total intensity scattered-light radius measurement made by Sissa et al. [2018] over the polarised scattered light measurement of Adam et al. [2021], implying that complex behaviour of the polarised scattering phase function was responsible for the large radius measurement made by the latter.

I searched for an offset from the disc centre to the expected location of the star, could not conclude that one existed with significant certainty, placing a  $3\sigma$  upper limit on  $e \cos(\omega)$  of 0.17. I did not detect any carbon monoxide within the disc, but calculate that we would not be able to detect a TWA 7-like amount of CO gas within the system and conclude that our non-detection is not significantly informative.

My modelling did not suggest there was significant evidence to favour a double power law disc model over a Gaussian model, suggesting that large mm-sized dust grains do not share the wider ranging orbits of small micron sized dust grains as found by the double power law model of Sissa et al. [2018]. By comparing the radial profiles of the three observations I identify that polarimetric observations measure disc flux radially beyond the total intensity and ALMA fluxes. In the case of the total intensity observations, the lack of flux is likely an effect of the forward scattering-favouring scattering phase function, but the lack of flux in the ALMA observations is another indication that the mm-dust grains, and so the parent planetesimals, are restricted to smaller radii and that the scattered light observations are measuring a halo of small dust grains. This halo necessitates a strong radial pressure force to shift small dust grains onto wider eccentric orbits, and I conclude that this pressure is likely stellar wind ram pressure in this late-type system.

Having not observed a significant brightness asymmetry in the ALMA data, I place an upper limit on a sub-mm brightness asymmetry of  $\sim 1.5$  compared to the asymmetries of  $\sim 1.5$ -2 measured in the scattered light observations. I conclude that this implies that whatever is causing the asymmetry more strongly affects smaller dust grains, and thus is likely a pressure force of some kind, for example interaction with the interstellar medium [e.g. Maness et al., 2009; Debes et al., 2009] or asymmetric small dust production and/or removal such as a coronal mass ejection [Osten et al., 2013].

Without photometry in the FIR a meaningfully constrained SED model could not be created, but a fractional luminosity - temperature plot was presented to demonstrate the distribution of disc models for GSC 07396-00759 in comparison to other more strictly constrained late-type discs. Resolving the disc also allowed me to constrain the temperature parameter space that disc models could physically inhabit. Thus I concluded that the fractional luminosity of the disc is greater than  $2 \times 10^{-4}$ , greater than the fractional luminosity



of Fomalhaut C, but in the range of the other late-type discs.

Finally I compare the disc’s radius in relation to its fractional luminosity to the wider context of mm-resolved debris discs and find the disc to be consistently sized with the M0V~M2V sample and the general power-law trend of decreasing radius with decreasing host-luminosity. I recommend that the disc be re-observed with ALMA at high resolution to perform similar scale-height analyses as performed for AU Mic [Daley et al., 2019] to compare the deeper properties of the discs.

## 6.2 An ALMA survey of M-dwarfs

In Chapter 5 I presented the first ALMA survey looking for M-dwarf debris discs. This survey studied the young, nearby  $\beta$  Pictoris Moving Group (BPMG). The chapter presents ALMA Band 7 observations of 33 M-dwarf systems comprising at least 37 M-dwarf stars.

Firstly, I present CLEAN images of the 33 observed systems and tabulate mm flux measurements taken from the expected stellar locations in each observations as well as noting the expected stellar emission and the noise level of the observations and highlighting the significant excess detections. Where excess is observed at the stellar locations I also check the observations for evidence of stellar flaring and CO gas and find evidence for neither. I also created a stacked image of the 21 non-detections for which the expected stellar location is within  $0.5''$  of the observation phase centre and from this image I place a  $3\sigma$  upper limit on the mean flux excess above the stellar flux of  $24 \mu\text{Jy}/\text{beam}$ . Additionally, I identify significant mm flux sources not associated with the stellar systems in ten of the observations, and conclude that these are likely background galaxies, having calculated using the galaxy number counts of Popping et al. [2020] that  $12^{+4}_{-10}$  background galaxies were expected to be detected.

I review the significant Gaia DR3 parallax updates for the sample, identifying where parallaxes are measured for the first time and where new binary companions are observed for the first time as well as identifying what impact the multiplicities of the sample have for the likelihood of detecting a debris disc within the system.

I examine several interesting observations that do not constitute significant stellar excess detections. Namely, I identify the observation of TYC 7443-1102-1 as significantly contaminated by a resolved background galaxy; I remark that while the observation of HD 155555 C is very close to  $3\sigma$ , there are enough similar  $2\sigma$  peaks close to the phase center that I do not think it likely that the flux at the stellar location constitutes a significant excess; finally I note that while the observation of AT Mic B does reach a  $4\sigma$  flux at the stellar location,  $2\sigma$ ’s worth of this flux can be accounted for by the stellar photosphere, and thus there is only an insufficiently significant  $2\sigma$  flux excess at the stellar location.

I then review the three new significant mm flux excess detections of the survey. I briefly summarise the results for the resolved disc of GSC 07396-00759 that was more deeply investigated in Chapter 4. For GJ 2006 A I present a  $880\ \mu\text{m}$  flux excess of  $385 \pm 33\ \mu\text{Jy}/\text{beam}$ , a radius upper limit of 34 AU and a fractional luminosity of  $\sim 2 \times 10^{-5} - 1 \times 10^{-3}$ . For AT Mic A I present a  $880\ \mu\text{m}$  flux excess of  $265 \pm 27\ \mu\text{Jy}/\text{beam}$ , a radius upper limit of 10 AU and a fractional luminosity of  $\sim 5 \times 10^{-6} - 5 \times 10^{-5}$ .

Without Far-IR photometry informative SEDs could not be produced for each star, and so I display example SEDs. I also display fractional luminosity-temperature plots for each detection that in combination with observational radius limits constrain the likely fractional luminosities of the discs.

With the detections reviewed I present a detection fraction of  $11.1^{+7.4}_{-3.3}\%$ . I present a figure exemplifying the survey completeness and calculate a completeness adjusted detection fraction of  $23.1^{+8.3}_{-5.5}\%$ , but I note that these errors are very likely to be underestimated.

With a detection fraction calculated I place the survey in the context of previous M-dwarf surveys that found very low detection rates and in the context of detection rates for sun-like type stars. I conclude that it is likely that previous telescopes could not detect M-dwarf discs due to their lower sensitivities and shorter wavelengths of observation, and that when ALMA is used M-dwarfs are not found to have a significantly different population to earlier type stars. I also examine the context of the much higher detection rate of debris discs around F-type stars in the BPMG [Pawellek et al., 2021] and raise that it is possible that either whatever mechanism boosts the detection rate for F-types in the BPMG does not apply to M-dwarfs, or that the BPMG detection rate is indeed boosted and thus the low field M-dwarf disc detection rate of the DEBRIS survey [Sibthorpe et al., 2018] could be a physical effect and not due to the instrumentation used. I also compare my detection rate to the predictions of Luppe et al. [2020] and find them consistent, placing more credence to the scenario that M-dwarf discs are similar to earlier types, but with the small number statistics of the sample I am unable to differentiate between their different disc scaling relationships.

Finally I examine that radii of the detected discs in the context of the ALMA resolved greater debris disc sample. I find the upper limit for the disc of GJ 2006 A to be reasonable, but that a  $\lesssim 10$  AU radius for an AT Mic A disc would be unusually small. I do identify several caveats in that conclusion, ultimately concluding that such a radius limit cannot be ruled a significant outlier in this under-sampled parameter space.

### 6.3 Summary

In summary, my work has significantly expanded the realm of mm-wave imaged M-dwarf debris discs. The resolved debris discs of Fomalhaut C and GSC 07396-00759 I have found

to be both not significantly divergent in properties from and just as interesting as the debris discs of earlier type stars. The ALMA survey of BPMG M-dwarfs has both detected new M-dwarf debris discs and taken a large stride in demonstrating that M-dwarf debris discs are not significantly less common than earlier type discs but have simply required longer wavelength and more sensitive observations to uncover them. I have taken the next steps in filling in the late-type star mm-wave observed parameter space and my work will be directly built upon when expanding this growing field.

## 6.4 Future work

The work presented in this thesis has provided plenty of avenues for short term follow-up science. Firstly, higher resolution ALMA observations will be able to properly characterise and explore the newly found debris disc around GJ 2006 A. Further ALMA observations will also be able to explore the intriguing AT Mic system. Any observations of the AT Mic system will naturally observe both stars due to their close separation on the sky, and thus new observations will simultaneously be able to i) discover whether or not there indeed is a significant excess flux around AT Mic B, which if found would likely constitute a debris disc and would raise the detection rate of the BPMG M-dwarf sample and significantly raise the completeness adjusted detection rate; and ii) characterise the circumstellar disc of AT Mic A. If both stars of the AT Mic close binary possess debris discs (in addition to their distant companion AU Mic) this system would be extraordinary.

High resolution follow up observations of GSC 07396-00759 would be able to replicate the unparalleled-for-M-dwarf-discs in-depth study of AU Mic, observations that resolve the scale height of the disc will be able to find limits on the size and mass of stirring bodies within the disc as Daley et al. [2019] did for AU Mic. Such observations would also be able to explore limits on the planetary architecture of the system and would be significantly able to confirm or reject whether or not any brightness asymmetry exists and whether or not a warp is present at mm-wavelengths.

The Luppe et al. [2020] theoretical M-dwarf disc samples were derived from the DEBRIS field star population; a more tailored comparative sample could be devised from observed young moving group samples that would better constrain whether the BPMG M-dwarf detection rate derives from a higher detection rate within young moving groups or a from a higher detection rate with the use of ALMA.

The BPMG observations of Chapter 5 could also be more widely examined for mm-flares. I only examined the observations with near-significant/significant flux levels at the stellar locations, but every star could be examined for flares to expand the work being performed in the M-dwarf mm-flare field [MacGregor et al., 2018b, 2020, 2021; Howard

et al., 2022].

## 6.5 Future prospects

Beyond the immediate future the field of M-dwarf debris discs only has room to grow as more ALMA observations and surveys are performed, finding new discs and further contextualising the sample. New telescopes and instruments are also in the works that will both deepen and widen our ability to investigate these elusive objects. A next-generation far-infrared space based telescope would be sensitive enough to detect and potentially image these discs at shorter wavelengths, increasing the available photometry to explore the spectral energy distributions and thus grain properties of these discs and allowing for the properties of these discs to be as well studied as those of earlier type discs. A future *Space Infrared Telescope for Cosmology and Astrophysics* [SPICA Roelfsema et al., 2018]-like instrument could fulfill this role, as could the *Origins Space Telescope* [OST Leisawitz et al., 2018, 2021], that would possess up to two orders of magnitude greater sensitivity than Herschel. A space based interferometer like the *Space Interferometer for Cosmic Evolution* [SPICE Leisawitz et al., 2007] would also be an order of magnitude more sensitive than Herschel at a wide range of far-infrared wavelengths.

On the ground, a large single-dish radio telescope like the *Atacama Large Aperture Submillimeter Telescope* [AtLAST Holland et al., 2019; Ramasawmy et al., 2022] would further push our sensitivity at long-wavelengths with ALMA-adjacent resolution to observe the dimmest discs expected around low-luminosity M-dwarf hosts. A new wave of ground-based interferometers are in development, not only is ALMA itself continuing to be upgraded [Huang et al., 2016; Fuller et al., 2016] but telescopes like the *next-generation VLA* [ngVLA; Selina et al., 2018] will be able to push sensitivity at mm-wavelengths to observe the coldest discs expected around low-luminosity M-dwarf hosts.

Ultimately, the driving force for future advancements will be increasing telescope sensitivity, and decades hence sensitivity will still be the limiting factor on our ability to perform surveys like the ALMA BPMG M-dwarf survey across a wide range of stellar ages and at greater distances.

As these instruments and more expand our ability to study M-dwarf discs, and as research into early type discs and the progenitor protoplanetary discs simultaneously develops, our understanding of planetary systems across all stars, as well as our understanding of our own, will reach currently unforeseeable heights that likely come with unexpected views.

# Bibliography

- B. Acke, M. Min, C. Dominik, B. Vandenbussche, B. Sibthorpe, C. Waelkens, G. Olofsson, P. Degroote, K. Smolders, E. Pantin, M. J. Barlow, J. A. D. L. Blommaert, A. Brandeker, W. De Meester, W. R. F. Dent, K. Exter, J. Di Francesco, M. Fridlund, W. K. Gear, A. M. Glauser, J. S. Greaves, P. M. Harvey, Th. Henning, M. R. Hogerheijde, W. S. Holland, R. Huygen, R. J. Ivison, C. Jean, R. Liseau, D. A. Naylor, G. L. Pilbratt, E. T. Polehampton, S. Regibo, P. Royer, A. Sicilia-Aguilar, and B. M. Swinyard. Herschel images of Fomalhaut. An extrasolar Kuiper belt at the height of its dynamical activity. *A&A*, 540:A125, Apr 2012. doi: 10.1051/0004-6361/201118581.
- C. Adam, J. Olofsson, R. G. van Holstein, A. Bayo, J. Milli, A. Boccaletti, Q. Kral, C. Ginski, Th. Henning, M. Montesinos, N. Pawellek, A. Zurlo, M. Langlois, A. Delboulb , A. Pavlov, J. Ramos, L. Weber, F. Wildi, F. Rigal, and J. F. Sauvage. Characterizing the morphology of the debris disk around the low-mass star GSC 07396-00759. *A&A*, 653: A88, September 2021. doi: 10.1051/0004-6361/202140740.
- Fred C. Adams, David Hollenbach, Gregory Laughlin, and Uma Gorti. Photoevaporation of Circumstellar Disks Due to External Far-Ultraviolet Radiation in Stellar Aggregates. *ApJ*, 611(1):360–379, Aug 2004. doi: 10.1086/421989.
- W. S. Adams, M. L. Humason, and A. H. Joy. Observations of Faint Spectra. *PASP*, 39 (231):365–369, October 1927. doi: 10.1086/123777.
- Richard Alexander. The Dispersal of Protoplanetary Disks around Binary Stars. *ApJ*, 757 (2):L29, October 2012. doi: 10.1088/2041-8205/757/2/L29.
- F. J. Alonso-Floriano, J. A. Caballero, M. Cort s-Contreras, E. Solano, and D. Montes. Reaching the boundary between stellar kinematic groups and very wide binaries. III. Sixteen new stars and eight new wide systems in the  $\beta$  Pictoris moving group. *A&A*, 583: A85, November 2015. doi: 10.1051/0004-6361/201526795.
- Guillem Anglada, Pedro J. Amado, Jose L. Ortiz, Jos  F. G mez, Enrique Mac as, Antxon Alberdi, Mayra Osorio, Jos  L. G mez, Itziar de Gregorio-Monsalvo, Miguel A. P rez-

Torres, Guillem Anglada-Escudé, Zaira M. Berdiñas, James S. Jenkins, Izaskun Jimenez-Serra, Luisa M. Lara, Maria J. López-González, Manuel López-Puertas, Nicolas Morales, Ignasi Ribas, Anita M. S. Richards, Cristina Rodríguez-López, and Eloy Rodriguez. ALMA Discovery of Dust Belts around Proxima Centauri. *ApJ*, 850(1):L6, November 2017. doi: 10.3847/2041-8213/aa978b.

M. Aravena, R. Decarli, F. Walter, E. Da Cunha, F. E. Bauer, C. L. Carilli, E. Daddi, D. Elbaz, R. J. Ivison, D. A. Riechers, I. Smail, A. M. Swinbank, A. Weiss, T. Anguita, R. J. Assef, E. Bell, F. Bertoldi, R. Bacon, R. Bouwens, P. Cortes, P. Cox, J. González-López, J. Hodge, E. Ibar, H. Inami, L. Infante, A. Karim, O. Le Le Fèvre, B. Magnelli, K. Ota, G. Popping, K. Sheth, P. van der Werf, and J. Wagg. The ALMA Spectroscopic Survey in the Hubble Ultra Deep Field: Continuum Number Counts, Resolved 1.2 mm Extragalactic Background, and Properties of the Faintest Dusty Star-forming Galaxies. *ApJ*, 833(1):68, December 2016. doi: 10.3847/1538-4357/833/1/68.

D. R. Ardila, S. H. Lubow, D. A. Golimowski, J. E. Krist, M. Clampin, H. C. Ford, G. F. Hartig, G. D. Illingworth, F. Bartko, N. Benítez, J. P. Blakeslee, R. J. Bouwens, L. D. Bradley, T. J. Broadhurst, R. A. Brown, C. J. Burrows, E. S. Cheng, N. J. G. Cross, P. D. Feldman, M. Franx, T. Goto, C. Gronwall, B. Holden, N. Homeier, L. Infante, R. A. Kimble, M. P. Lesser, A. R. Martel, F. Menanteau, G. R. Meurer, G. K. Miley, M. Postman, M. Sirianni, W. B. Sparks, H. D. Tran, Z. I. Tsvetanov, R. L. White, W. Zheng, and A. W. Zirm. A Dynamical Simulation of the Debris Disk around HD 141569A. *ApJ*, 627(2): 986–1000, Jul 2005. doi: 10.1086/430395.

Jessica A. Arnold, Alycia J. Weinberger, Gorden Videen, and Evgenij S. Zubko. The Effect of Dust Composition and Shape on Radiation-pressure Forces and Blowout Sizes of Particles in Debris Disks. *AJ*, 157(4):157, April 2019. doi: 10.3847/1538-3881/ab095e.

Erik Asphaug. Impact Origin of the Moon? *Annual Review of Earth and Planetary Sciences*, 42:551–578, May 2014. doi: 10.1146/annurev-earth-050212-124057.

J. C. Augereau and H. Beust. On the AU Microscopii debris disk. Density profiles, grain properties, and dust dynamics. *A&A*, 455(3):987–999, September 2006. doi: 10.1051/0004-6361:20054250.

J. C. Augereau, A. M. Lagrange, D. Mouillet, J. C. B. Papaloizou, and P. A. Grorod. On the HR 4796 A circumstellar disk. *A&A*, 348:557–569, August 1999.

J. C. Augereau, R. P. Nelson, A. M. Lagrange, J. C. B. Papaloizou, and D. Mouillet. Dynamical modeling of large scale asymmetries in the beta Pictoris dust disk. *A&A*, 370: 447–455, May 2001. doi: 10.1051/0004-6361:20010199.

- H. H. Aumann, F. C. Gillett, C. A. Beichman, T. de Jong, J. R. Houck, F. J. Low, G. Neugebauer, R. G. Walker, and P. R. Wesselius. Discovery of a shell around alpha Lyrae. *ApJ*, 278:L23–L27, March 1984. doi: 10.1086/184214.
- D. Backman, M. Marengo, K. Stapelfeldt, K. Su, D. Wilner, C. D. Dowell, D. Watson, J. Stansberry, G. Rieke, T. Megeath, G. Fazio, and M. Werner. Epsilon Eridani’s Planetary Debris Disk: Structure and Dynamics Based on Spitzer and Caltech Submillimeter Observatory Observations. *ApJ*, 690(2):1522–1538, January 2009. doi: 10.1088/0004-637X/690/2/1522.
- Dana E. Backman and Francesco Paresce. Main-Sequence Stars with Circumstellar Solid Material - the VEGA Phenomenon. In Eugene H. Levy and Jonathan I. Lunine, editors, *Protostars and Planets III*, page 1253, January 1993.
- C. A. L. Bailer-Jones, J. Rybizki, M. Fouesneau, M. Demleitner, and R. Andrae. VizieR Online Data Catalog: Distances to 1.47 billion stars in Gaia EDR3 (Bailer-Jones+, 2021). *VizieR Online Data Catalog*, art. I/352, February 2021.
- A Bayo, J Olofsson, L Matrà, J C Beamín, J Gallardo, I de Gregorio Monsalvo, M Booth, C Zamora, D Iglesias, Th Henning, M R Schreiber, and C Cáceres. Sub-millimetre non-contaminated detection of the disc around TWA 7 by ALMA. *Monthly Notices of the Royal Astronomical Society*, 486(4):5552–5557, 05 2019. ISSN 0035-8711. doi: 10.1093/mnras/stz1133. URL <https://doi.org/10.1093/mnras/stz1133>.
- Cameron P. M. Bell, Eric E. Mamajek, and Tim Naylor. A self-consistent, absolute isochronal age scale for young moving groups in the solar neighbourhood. *MNRAS*, 454(1):593–614, November 2015. doi: 10.1093/mnras/stv1981.
- Michael J. S. Belton. Dynamics of Interplanetary Dust. *Science*, 151(3706):35–44, January 1966. doi: 10.1126/science.151.3706.35.
- Gurtina Besla and Yanqin Wu. Formation of narrow dust rings in circumstellar debris disks. *The Astrophysical Journal*, 655(1):528–540, jan 2007. doi: 10.1086/509495. URL <https://doi.org/10.1086%2F509495>.
- J. L. Beuzit, A. Vigan, D. Mouillet, K. Dohlen, R. Gratton, A. Boccaletti, J. F. Sauvage, H. M. Schmid, M. Langlois, C. Petit, A. Baruffolo, M. Feldt, J. Milli, Z. Wahhaj, L. Abe, U. Anselmi, J. Antichi, R. Barette, J. Baudrand, P. Baudoz, A. Bazzon, P. Bernardi, P. Blanchard, R. Brast, P. Bruno, T. Buey, M. Carillet, M. Carle, E. Cascone, F. Chapron, J. Charton, G. Chauvin, R. Claudi, A. Costille, V. De Caprio, J. de Boer, A. Delboulbé, S. Desidera, C. Dominik, M. Downing, O. Dupuis, C. Fabron, D. Fantinel, G. Farisato,

P. Feautrier, E. Fedrigo, T. Fusco, P. Gigan, C. Ginski, J. Girard, E. Giro, D. Gisler, L. Gluck, C. Gry, T. Henning, N. Hubin, E. Hugot, S. Incorvaia, M. Jaquet, M. Kasper, E. Lagadec, A. M. Lagrange, H. Le Coroller, D. Le Mignant, B. Le Ruyet, G. Lessio, J. L. Lizon, M. Llored, L. Lundin, F. Madec, Y. Magnard, M. Marteaude, P. Martinez, D. Maurel, F. Ménard, D. Mesa, O. Möller-Nilsson, T. Moulin, C. Moutou, A. Origné, J. Parisot, A. Pavlov, D. Perret, J. Pragt, P. Puget, P. Rabou, J. Ramos, J. M. Reess, F. Rigal, S. Rochat, R. Roelfsema, G. Rousset, A. Roux, M. Saisse, B. Salasnich, E. Santambrogio, S. Scuderi, D. Segransan, A. Sevin, R. Siebenmorgen, C. Soenke, E. Stadler, M. Suarez, D. Tiphène, M. Turatto, S. Udry, F. Vakili, L. B. F. M. Waters, L. Weber, F. Wildi, G. Zins, and A. Zurlo. SPHERE: the exoplanet imager for the Very Large Telescope. *A&A*, 631: A155, November 2019a. doi: 10.1051/0004-6361/201935251.

J. L. Beuzit, A. Vigan, D. Mouillet, K. Dohlen, R. Gratton, A. Boccaletti, J. F. Sauvage, H. M. Schmid, M. Langlois, C. Petit, A. Baruffolo, M. Feldt, J. Milli, Z. Wahhaj, L. Abe, U. Anselmi, J. Antichi, R. Barette, J. Baudrand, P. Baudoz, A. Bazzon, P. Bernardi, P. Blanchard, R. Brast, P. Bruno, T. Buey, M. Carbillet, M. Carle, E. Cascone, F. Chapron, J. Charton, G. Chauvin, R. Claudi, A. Costille, V. De Caprio, J. de Boer, A. Delboulbé, S. Desidera, C. Dominik, M. Downing, O. Dupuis, C. Fabron, D. Fantinel, G. Farisato, P. Feautrier, E. Fedrigo, T. Fusco, P. Gigan, C. Ginski, J. Girard, E. Giro, D. Gisler, L. Gluck, C. Gry, T. Henning, N. Hubin, E. Hugot, S. Incorvaia, M. Jaquet, M. Kasper, E. Lagadec, A. M. Lagrange, H. Le Coroller, D. Le Mignant, B. Le Ruyet, G. Lessio, J. L. Lizon, M. Llored, L. Lundin, F. Madec, Y. Magnard, M. Marteaude, P. Martinez, D. Maurel, F. Ménard, D. Mesa, O. Möller-Nilsson, T. Moulin, C. Moutou, A. Origné, J. Parisot, A. Pavlov, D. Perret, J. Pragt, P. Puget, P. Rabou, J. Ramos, J. M. Reess, F. Rigal, S. Rochat, R. Roelfsema, G. Rousset, A. Roux, M. Saisse, B. Salasnich, E. Santambrogio, S. Scuderi, D. Segransan, A. Sevin, R. Siebenmorgen, C. Soenke, E. Stadler, M. Suarez, D. Tiphène, M. Turatto, S. Udry, F. Vakili, L. B. F. M. Waters, L. Weber, F. Wildi, G. Zins, and A. Zurlo. SPHERE: the exoplanet imager for the Very Large Telescope. *A&A*, 631: A155, Nov 2019b. doi: 10.1051/0004-6361/201935251.

Jean-Luc Beuzit, Markus Feldt, Kjetil Dohlen, David Mouillet, Pascal Puget, Francois Wildi, Lyu Abe, Jacopo Antichi, Andrea Baruffolo, Pierre Baudoz, Anthony Boccaletti, Marcel Carbillet, Julien Charton, Riccardo Claudi, Mark Downing, Christophe Fabron, Philippe Feautrier, Enrico Fedrigo, Thierry Fusco, Jean-Luc Gach, Raffaele Gratton, Thomas Henning, Norbert Hubin, Franco Joos, Markus Kasper, Maud Langlois, Rainer Lenzen, Claire Moutou, Alexey Pavlov, Cyril Petit, Johan Pragt, Patrick Rabou, Florence Rigal, Ronald Roelfsema, Gérard Rousset, Michel Saisse, Hans-Martin Schmid, Eric Stadler, Christian Thalmann, Massimo Turatto, Stéphane Udry, Farrokh Vakili, and Rens



Waters. SPHERE: a 'Planet Finder' instrument for the VLT. In Ian S. McLean and Mark M. Casali, editors, *Ground-based and Airborne Instrumentation for Astronomy II*, volume 7014 of *Society of Photo-Optical Instrumentation Engineers (SPIE) Conference Series*, page 701418, July 2008. doi: 10.1117/12.790120.

A. S. Binks and R. D. Jeffries. Spectroscopic confirmation of M-dwarf candidate members of the Beta Pictoris and AB Doradus Moving Groups. *MNRAS*, 455(3):3345–3358, January 2016. doi: 10.1093/mnras/stv2431.

A. S. Binks and R. D. Jeffries. A WISE-based search for debris discs amongst M dwarfs in nearby, young, moving groups. *MNRAS*, 469(1):579–593, July 2017. doi: 10.1093/mnras/stx838.

A. Boccaletti, E. Sezestre, A. M. Lagrange, P. Thébault, R. Gratton, M. Langlois, C. Thalmann, M. Janson, P. Delorme, J. C. Augereau, G. Schneider, J. Milli, C. Grady, J. Debes, Q. Kral, J. Olofsson, J. Carson, A. L. Maire, T. Henning, J. Wisniewski, J. Schlieder, C. Dominik, S. Desidera, C. Ginski, D. Hines, F. Ménard, D. Mouillet, N. Pawellek, A. Vigan, E. Lagadec, H. Avenhaus, J. L. Beuzit, B. Biller, M. Bonavita, M. Bonnefoy, W. Brandner, F. Cantalloube, G. Chauvin, A. Cheetham, M. Cudel, C. Gry, S. Daemgen, M. Feldt, R. Galicher, J. Girard, J. Hagelberg, P. Janin-Potiron, M. Kasper, H. Le Coroller, D. Mesa, S. Peretti, C. Perrot, M. Samland, E. Sissa, F. Wildi, A. Zurlo, S. Rochat, E. Stadler, L. Gluck, A. Origné, M. Llored, P. Baudoz, G. Rousset, P. Martinez, and F. Rigal. Observations of fast-moving features in the debris disk of AU Mic on a three-year timescale: Confirmation and new discoveries. *A&A*, 614:A52, June 2018. doi: 10.1051/0004-6361/201732462.

Anthony Boccaletti, Christian Thalmann, Anne-Marie Lagrange, Markus Janson, Jean-Charles Augereau, Glenn Schneider, Julien Milli, Carol Grady, John Debes, Maud Langlois, David Mouillet, Thomas Henning, Carsten Dominik, Anne-Lise Maire, Jean-Luc Beuzit, Joseph Carson, Kjetil Dohlen, Natalia Engler, Markus Feldt, Thierry Fusco, Christian Ginski, Julien H. Girard, Dean Hines, Markus Kasper, Dimitri Mawet, François Ménard, Michael R. Meyer, Claire Moutou, Johan Olofsson, Timothy Rodigas, Jean-Francois Sauvage, Joshua Schlieder, Hans Martin Schmid, Massimo Turatto, Stephane Udry, Farrokh Vakili, Arthur Vigan, Zahed Wahhaj, and John Wisniewski. Fast-moving features in the debris disk around AU Microscopii. *Nature*, 526(7572):230–232, October 2015. doi: 10.1038/nature15705.

M. Bocchio, S. Bianchi, and A. Abergel. Deep herschel pacs point spread functions. *A&A*, 591:A117, 2016. doi: 10.1051/0004-6361/201628665. URL <https://doi.org/10.1051/0004-6361/201628665>.

- Craig F. Bohren and Donald R. Huffman. *Absorption and scattering of light by small particles*. 1983.
- A. C. Boley, M. J. Payne, S. Corder, W. R. F. Dent, E. B. Ford, and M. Shabram. Constraining the planetary system of fomalhaut using high-resolution alma observations. *The Astrophysical Journal*, 750(1):L21, Apr 2012. ISSN 2041-8213. doi: 10.1088/2041-8205/750/1/L21. URL <http://dx.doi.org/10.1088/2041-8205/750/1/L21>.
- X. Bonfils, X. Delfosse, S. Udry, T. Forveille, M. Mayor, C. Perrier, F. Bouchy, M. Gillon, C. Lovis, F. Pepe, D. Queloz, N. C. Santos, D. Ségransan, and J. L. Bertaux. The HARPS search for southern extra-solar planets. XXXI. The M-dwarf sample. *A&A*, 549:A109, Jan 2013. doi: 10.1051/0004-6361/201014704.
- A. Bonsor, J. C. Augereau, and P. Thébault. Scattering of small bodies by planets: a potential origin for exozodiacal dust? *A&A*, 548:A104, December 2012. doi: 10.1051/0004-6361/201220005.
- Amy Bonsor, Grant M. Kennedy, Justin R. Crepp, John A. Johnson, Mark C. Wyatt, Bruce Sibthorpe, and Kate Y. L. Su. Spatially resolved images of dust belt(s) around the planet-hosting subgiant  $\kappa$  CrB. *MNRAS*, 431(4):3025–3035, June 2013. doi: 10.1093/mnras/stt367.
- Amy Bonsor, Grant M. Kennedy, Mark C. Wyatt, John A. Johnson, and Bruce Sibthorpe. Herschel observations of debris discs orbiting planet-hosting subgiants. *MNRAS*, 437(4): 3288–3297, February 2014. doi: 10.1093/mnras/stt2128.
- Mark Booth, Grant Kennedy, Bruce Sibthorpe, Brenda C. Matthews, Mark C. Wyatt, Gaspar Duchene, J. J. Kavelaars, David Rodriguez, Jane S. Greaves, Alice Koning, Laura Vican, George H. Rieke, Kate Y. L. Su, Amaya Moro-Martín, and Paul Kalas. Resolved debris discs around A stars in the Herschel DEBRIS survey. *Monthly Notices of the Royal Astronomical Society*, 428(2):1263–1280, 10 2012. ISSN 0035-8711. doi: 10.1093/mnras/sts117. URL <https://doi.org/10.1093/mnras/sts117>.
- Mark Booth, William R. F. Dent, Andrés Jordán, Jean-François Lestrade, Antonio S. Hales, Mark C. Wyatt, Simon Casassus, Steve Ertel, Jane S. Greaves, Grant M. Kennedy, Luca Matrà, Jean-Charles Augereau, and Eric Villard. The Northern arc of  $\epsilon$  Eridani’s Debris Ring as seen by ALMA. *Monthly Notices of the Royal Astronomical Society*, 469(3):3200–3212, 05 2017. ISSN 0035-8711. doi: 10.1093/mnras/stx1072. URL <https://doi.org/10.1093/mnras/stx1072>.
- A. P. Boss. Giant planet formation by gravitational instability. *Science*, 276:1836–1839, January 1997. doi: 10.1126/science.276.5320.1836.

- William F. Bottke and Marc D. Norman. The Late Heavy Bombardment. *Annual Review of Earth and Planetary Sciences*, 45(1):619–647, August 2017. doi: 10.1146/annurev-earth-063016-020131.
- D. S. Briggs. High Fidelity Interferometric Imaging: Robust Weighting and NNLS Deconvolution. In *American Astronomical Society Meeting Abstracts*, volume 187 of *American Astronomical Society Meeting Abstracts*, page 112.02, December 1995.
- Daniel S. Briggs, Frederic R. Schwab, and Richard A. Sramek. Imaging. In G. B. Taylor, C. L. Carilli, and R. A. Perley, editors, *Synthesis Imaging in Radio Astronomy II*, volume 180 of *Astronomical Society of the Pacific Conference Series*, page 127, January 1999.
- Garett Brown and Hanno Rein. On the long-term stability of the Solar system in the presence of weak perturbations from stellar flybys. *MNRAS*, 515(4):5942–5950, October 2022. doi: 10.1093/mnras/stac1763.
- G. Bryden, C. A. Beichman, J. M. Carpenter, G. H. Rieke, K. R. Stapelfeldt, M. W. Werner, A. M. Tanner, S. M. Lawler, M. C. Wyatt, D. E. Trilling, K. Y. L. Su, M. Blaylock, and J. A. Stansberry. Planets and Debris Disks: Results from a Spitzer/MIPS Search for Infrared Excess. *ApJ*, 705(2):1226–1236, November 2009. doi: 10.1088/0004-637X/705/2/1226.
- Adam J. Burgasser, J. Davy Kirkpatrick, I. Neill Reid, Michael E. Brown, Cherie L. Miskey, and John E. Gizis. Binarity in Brown Dwarfs: T Dwarf Binaries Discovered with the Hubble Space Telescope Wide Field Planetary Camera 2. *ApJ*, 586(1):512–526, March 2003. doi: 10.1086/346263.
- J. A. Burns, P. L. Lamy, and S. Soter. Radiation forces on small particles in the solar system. *Icarus*, 40(1):1–48, October 1979. doi: 10.1016/0019-1035(79)90050-2.
- J. A. Caballero. Reaching the boundary between stellar kinematic groups and very wide binaries. The Washington double stars with the widest angular separations. *A&A*, 507(1): 251–259, November 2009. doi: 10.1051/0004-6361/200912596.
- A. Campo Bagatin, A. Cellino, D. R. Davis, P. Farinella, and P. Paolicchi. Wavy size distributions for collisional systems with a small-size cutoff. *Planet. Space Sci.*, 42(12): 1079–1092, December 1994. doi: 10.1016/0032-0633(94)90008-6.
- Caitlin M. Casey, Desika Narayanan, and Asantha Cooray. Dusty star-forming galaxies at high redshift. *Phys. Rep.*, 541(2):45–161, August 2014. doi: 10.1016/j.physrep.2014.02.009.

- G. Cataldi, A. Brandeker, G. Olofsson, C. H. Chen, W. R. F. Dent, I. Kamp, A. Roberge, and B. Vandenbussche. Constraints on the gas content of the fomalhaut debris belt - can gas-dust interactions explain the belt's morphology? *A&A*, 574:L1, 2015. doi: 10.1051/0004-6361/201425322. URL <https://doi.org/10.1051/0004-6361/201425322>.
- M. Chavez-Dagostino, E. Bertone, F. Cruz-Saenz de Miera, J. P. Marshall, G. W. Wilson, D. Sánchez-Argüelles, D. H. Hughes, G. Kennedy, O. Vega, V. De la Luz, W. R. F. Dent, C. Eiroa, A. I. Gómez-Ruiz, J. S. Greaves, S. Lizano, R. López-Valdivia, E. Mamajek, A. Montaña, M. Olmedo, I. Rodríguez-Montoya, F. P. Schloerb, Min S. Yun, J. A. Zavala, and M. Zeballos. Early science with the Large Millimetre Telescope: Deep LMT/AzTEC millimetre observations of  $\epsilon$  Eridani and its surroundings. *MNRAS*, 462(3):2285–2294, November 2016. doi: 10.1093/mnras/stw1363.
- Christine H. Chen, Tushar Mittal, Marc Kuchner, William J. Forrest, Carey M. Lisse, P. Manoj, Benjamin A. Sargent, and Dan M. Watson. The Spitzer Infrared Spectrograph Debris Disk Catalog. I. Continuum Analysis of Unresolved Targets. *ApJS*, 211(2):25, April 2014. doi: 10.1088/0067-0049/211/2/25.
- E. Chiang, E. Kite, P. Kalas, J. R. Graham, and M. Clampin. Fomalhaut's Debris Disk and Planet: Constraining the Mass of Fomalhaut b from disk Morphology. *ApJ*, 693(1):734–749, March 2009. doi: 10.1088/0004-637X/693/1/734.
- Eugene Chiang and Jeffrey Fung. Stellar Winds and Dust Avalanches in the AU Mic Debris Disk. *ApJ*, 848(1):4, October 2017. doi: 10.3847/1538-4357/aa89e6.
- É. Choquet, J. Milli, Z. Wahhaj, R. Soummer, A. Roberge, J.-C. Augereau, M. Booth, O. Absil, A. Boccaletti, C. H. Chen, J. H. Debes, C. del Burgo, W. R. F. Dent, S. Ertel, J. H. Girard, E. Gofas-Salas, D. A. Golimowski, C. A. Gómez González, J. Brendan Hagan, P. Hibon, D. C. Hines, G. M. Kennedy, A.-M. Lagrange, L. Matrà, D. Mawet, D. Mouillet, M. N'Diaye, M. D. Perrin, C. Pinte, L. Pueyo, A. Rajan, G. Schneider, S. Wolff, and M. Wyatt. First Scattered-light Images of the Gas-rich Debris Disk around 49 Ceti. *ApJ*, 834:L12, January 2017. doi: 10.3847/2041-8213/834/2/L12.
- É. Choquet, G. Bryden, M. D. Perrin, R. Soummer, J.-C. Augereau, C. H. Chen, J. H. Debes, E. Gofas-Salas, J. B. Hagan, D. C. Hines, D. Mawet, F. Morales, L. Pueyo, A. Rajan, B. Ren, G. Schneider, C. C. Stark, and S. Wolff. HD 104860 and HD 192758: Two debris disks newly imaged in scattered light with the Hubble space telescope. *The Astrophysical Journal*, 854(1):53, feb 2018. doi: 10.3847/1538-4357/aaa892. URL <https://doi.org/10.3847/1538-4357/aaa892>.

- Élodie Choquet, Marshall D. Perrin, Christine H. Chen, Rémi Soummer, Laurent Pueyo, James B. Hagan, Elena Gofas-Salas, Abhijith Rajan, David A. Golimowski, Dean C. Hines, Glenn Schneider, Johan Mazoyer, Jean-Charles Augereau, John Debes, Christopher C. Stark, Schuyler Wolff, Mamadou N'Diaye, and Kevin Hsiao. First Images of Debris Disks around TWA 7, TWA 25, HD 35650, and HD 377. *ApJ*, 817(1):L2, January 2016. doi: 10.3847/2041-8205/817/1/L2.
- Aurélien Crida. Minimum Mass Solar Nebulae and Planetary Migration. *ApJ*, 698(1): 606–614, June 2009. doi: 10.1088/0004-637X/698/1/606.
- Patrick F. Cronin-Coltsmann, Grant M. Kennedy, Paul Kalas, Julien Milli, Cathie J. Clarke, Gaspard Duchêne, Jane Greaves, Samantha M. Lawler, Jean-François Lestrade, Brenda C. Matthews, Andrew Shannon, and Mark C. Wyatt. ALMA imaging of the M-dwarf Fomalhaut C’s debris disc. *MNRAS*, 504(3):4497–4510, July 2021. doi: 10.1093/mnras/stab1237.
- Patrick F. Cronin-Coltsmann, Grant M. Kennedy, Christian Adam, Quentin Kral, Jean-François Lestrade, Sebastian Marino, Luca Matrà, Simon J. Murphy, Johan Olofsson, and Mark C. Wyatt. ALMA’s view of the M-dwarf GSC 07396-00759’s edge-on debris disc: AU Mic’s coeval twin. *MNRAS*, 512(4):4752–4764, June 2022. doi: 10.1093/mnras/stac536.
- Katie A. Crotts, Brenda C. Matthews, Thomas M. Esposito, Gaspard Duchêne, Paul Kalas, Christine H. Chen, Pauline Arriaga, Maxwell A. Millar-Blanchaer, John H. Debes, Zachary H. Draper, Michael P. Fitzgerald, Justin Hom, Meredith A. MacGregor, Johan Mazoyer, Jennifer Patience, Malena Rice, Alycia J. Weinberger, David J. Wilner, and Schuyler Wolff. A Deep Polarimetric Study of the Asymmetrical Debris Disk HD 106906. *ApJ*, 915(1):58, July 2021. doi: 10.3847/1538-4357/abff5c.
- Katie A. Crotts, Zachary H. Draper, Brenda C. Matthews, Gaspard Duchêne, Thomas M. Esposito, David Wilner, Johan Mazoyer, Deborah Padgett, Paul Kalas, and Karl Stapelfeldt. A Multiwavelength Study of the Highly Asymmetrical Debris Disk around HD 111520. *ApJ*, 932(1):23, June 2022. doi: 10.3847/1538-4357/ac6c86.
- Thayne Currie, John Debes, Timothy J. Rodigas, Adam Burrows, Yoichi Itoh, Misato Fukagawa, Scott J. Kenyon, Marc Kuchner, and Soko Matsumura. DIRECT IMAGING CONFIRMATION AND CHARACTERIZATION OF a DUST-ENSHROUDED CANDIDATE EXOPLANET ORBITING FOMALHAUT. *The Astrophysical Journal*, 760(2):L32, nov 2012. doi: 10.1088/2041-8205/760/2/L32. URL <https://doi.org/10.1088/2041-8205/760/2/L32>.

- Thayne Currie, Ryan Cloutier, John H. Debes, Scott J. Kenyon, and Denise Kaisler. A deep keck/nirc2 search for thermal emission from planetary companions orbiting fomalhaut. *The Astrophysical Journal*, 777(1):L6, Oct 2013. ISSN 2041-8213. doi: 10.1088/2041-8205/777/1/L6. URL <http://dx.doi.org/10.1088/2041-8205/777/1/L6>.
- R. M. Cutri and et al. VizieR Online Data Catalog: WISE All-Sky Data Release (Cutri+ 2012). *VizieR Online Data Catalog*, art. II/311, April 2012.
- R. M. Cutri, M. F. Skrutskie, S. van Dyk, C. A. Beichman, J. M. Carpenter, T. Chester, L. Cambresy, T. Evans, J. Fowler, J. Gizis, E. Howard, J. Huchra, T. Jarrett, E. L. Kopan, J. D. Kirkpatrick, R. M. Light, K. A. Marsh, H. McCallon, S. Schneider, R. Stiening, M. Sykes, M. Weinberg, W. A. Wheaton, S. Wheelock, and N. Zacarias. VizieR Online Data Catalog: 2MASS All-Sky Catalog of Point Sources (Cutri+ 2003). *VizieR Online Data Catalog*, art. II/246, Jun 2003.
- R. M. Cutri, E. L. Wright, T. Conrow, J. Bauer, D. Benford, H. Brandenburg, J. Dailey, P. R. M. Eisenhardt, T. Evans, S. Fajardo-Acosta, J. Fowler, C. Gelino, C. Grillmair, M. Harbut, D. Hoffman, T. Jarrett, J. D. Kirkpatrick, D. Leisawitz, W. Liu, A. Mainzer, K. Marsh, F. Masci, H. McCallon, D. Padgett, M. E. Ressler, D. Royer, M. F. Skrutskie, S. A. Stanford, P. L. Wyatt, D. Tholen, C. W. Tsai, S. Wachter, S. L. Wheelock, L. Yan, R. Alles, R. Beck, T. Grav, J. Masiero, B. McCollum, P. McGehee, M. Papin, and M. Wittman. Explanatory Supplement to the WISE All-Sky Data Release Products. Explanatory Supplement to the WISE All-Sky Data Release Products, March 2012.
- R. M. Cutri, E. L. Wright, T. Conrow, J. W. Fowler, P. R. M. Eisenhardt, C. Grillmair, J. D. Kirkpatrick, F. Masci, H. L. McCallon, S. L. Wheelock, S. Fajardo-Acosta, L. Yan, D. Benford, M. Harbut, T. Jarrett, S. Lake, D. Leisawitz, M. E. Ressler, S. A. Stanford, C. W. Tsai, F. Liu, G. Helou, A. Mainzer, D. Gettns, A. Gonzalez, D. Hoffman, K. A. Marsh, D. Padgett, M. F. Skrutskie, R. Beck, M. Papin, and M. Wittman. VizieR Online Data Catalog: AllWISE Data Release (Cutri+ 2013). *VizieR Online Data Catalog*, art. II/328, February 2021.
- Cail Daley, A. Meredith Hughes, Evan S. Carter, Kevin Flaherty, Zachary Lambros, Margaret Pan, Hilke Schlichting, Eugene Chiang, Mark Wyatt, David Wilner, Sean Andrews, and John Carpenter. The Mass of Stirring Bodies in the AU Mic Debris Disk Inferred from Resolved Vertical Structure. *ApJ*, 875(2):87, April 2019. doi: 10.3847/1538-4357/ab1074.
- Robert J. De Rosa and Paul Kalas. A Near-coplanar Stellar Flyby of the Planet Host Star HD 106906. *AJ*, 157(3):125, Mar 2019. doi: 10.3847/1538-3881/ab0109.

- Rafael Ribeiro de Sousa, Alessandro Morbidelli, Sean N. Raymond, Andre Izidoro, Rodney Gomes, and Ernesto Vieira Neto. Dynamical evidence for an early giant planet instability. *Icarus*, 339:113605, March 2020. doi: 10.1016/j.icarus.2019.113605.
- J. H. Debes, M. Kilic, F. Faedi, E. L. Shkolnik, M. Lopez-Morales, A. J. Weinberger, C. Slesnick, and R. G. West. Detection of Weak Circumstellar Gas around the DAZ White Dwarf WD 1124-293: Evidence for the Accretion of Multiple Asteroids. *ApJ*, 754(1):59, July 2012. doi: 10.1088/0004-637X/754/1/59.
- John H. Debes and Steinn Sigurdsson. Are There Unstable Planetary Systems around White Dwarfs? *ApJ*, 572(1):556–565, June 2002. doi: 10.1086/340291.
- John H. Debes, Alycia J. Weinberger, and Marc J. Kuchner. Interstellar Medium Sculpting of the HD 32297 Debris Disk. *ApJ*, 702(1):318–326, September 2009. doi: 10.1088/0004-637X/702/1/318.
- Greet Decin, C Dominik, LBFM Waters, and C Waelkens. Age dependence of the vega phenomenon: observations. *The Astrophysical Journal*, 598(1):636, 2003.
- D. Defrère, P. M. Hinz, A. J. Skemer, G. M. Kennedy, V. P. Bailey, W. F. Hoffmann, B. Mennesson, R. Millan-Gabet, W. C. Danchi, O. Absil, P. Arbo, C. Beichman, G. Brusa, G. Bryden, E. C. Downey, O. Durney, S. Esposito, A. Gaspar, P. Grenz, C. Haniff, J. M. Hill, J. Lebreton, J. M. Leisenring, J. R. Males, L. Marion, T. J. McMahon, M. Montoya, K. M. Morzinski, E. Pinna, A. Puglisi, G. Rieke, A. Roberge, E. Serabyn, R. Sosa, K. Stapelfeldt, K. Su, V. Vaitheeswaran, A. Vaz, A. J. Weinberger, and M. C. Wyatt. First-light LBT Nulling Interferometric Observations: Warm Exozodiacal Dust Resolved within a Few AU of  $\eta$  Crv. *ApJ*, 799(1):42, January 2015. doi: 10.1088/0004-637X/799/1/42.
- X. Delfosse, T. Forveille, J. L. Beuzit, S. Udry, M. Mayor, and C. Perrier. New neighbours. I. 13 new companions to nearby M dwarfs. *A&A*, 344:897–910, April 1999.
- W. R. F. Dent, M. C. Wyatt, A. Roberge, J. C. Augereau, S. Casassus, S. Corder, J. S. Greaves, I. de Gregorio-Monsalvo, A. Hales, A. P. Jackson, A. Meredith Hughes, A. M. Lagrange, B. Matthews, and D. Wilner. Molecular Gas Clumps from the Destruction of Icy Bodies in the  $\beta$  Pictoris Debris Disk. *Science*, 343(6178):1490–1492, March 2014. doi: 10.1126/science.1248726.
- S. J. Desch. Mass Distribution and Planet Formation in the Solar Nebula. *ApJ*, 671(1):878–893, December 2007. doi: 10.1086/522825.
- K. Dohlen, M. Langlois, M. Saisse, L. Hill, A. Origine, M. Jacquet, C. Fabron, J.-C. Blanc, M. Llored, M. Carle, C. Moutou, A. Vigan, A. Boccaletti, M. Carillet, D. Mouillet,

and J.-L. Beuzit. The infra-red dual imaging and spectrograph for SPHERE: design and performance. In *Society of Photo-Optical Instrumentation Engineers (SPIE) Conference Series*, volume 7014 of *Society of Photo-Optical Instrumentation Engineers (SPIE) Conference Series*, August 2008. doi: 10.1117/12.789786.

J. S. Dohnanyi. Collisional Model of Asteroids and Their Debris. *J. Geophys. Res.*, 74: 2531–2554, May 1969. doi: 10.1029/JB074i010p02531.

C. Dominik and G. Decin. Age Dependence of the Vega Phenomenon: Theory. *ApJ*, 598 (1):626–635, November 2003. doi: 10.1086/379169.

V. D’Orazi, R. Gratton, S. Desidera, H. Avenhaus, D. Mesa, T. Stolker, E. Giro, S. Benatti, H. Jang-Condell, E. Rigliaco, E. Sissa, T. Scatolin, M. Benisty, T. Bhowmik, A. Boccaletti, M. Bonnefoy, W. Brandner, E. Buenzli, G. Chauvin, S. Daemgen, M. Damasso, M. Feldt, R. Galicher, J. Girard, M. Janson, J. Hagelberg, D. Mouillet, Q. Kral, J. Lannier, A. M. Lagrange, M. Langlois, A. L. Maire, F. Menard, O. Moeller-Nilsson, C. Perrot, S. Peretti, P. Rabou, J. Ramos, L. Rodet, R. Roelfsema, A. Roux, G. Salter, J. E. Schlieder, T. Schmidt, J. Szulagyi, C. Thalmann, P. Thebault, G. van der Plas, A. Vigan, and A. Zurlo. Mapping of shadows cast on a protoplanetary disk by a close binary system. *Nature Astronomy*, 3:167–172, November 2019. doi: 10.1038/s41550-018-0626-6.

B. T. Draine and H. M. Lee. Optical Properties of Interstellar Graphite and Silicate Grains. *ApJ*, 285:89, October 1984. doi: 10.1086/162480.

Courtney D. Dressing and David Charbonneau. The Occurrence of Potentially Habitable Planets Orbiting M Dwarfs Estimated from the Full Kepler Dataset and an Empirical Measurement of the Detection Sensitivity. *ApJ*, 807(1):45, Jul 2015. doi: 10.1088/0004-637X/807/1/45.

C. Ducourant, R. Teixeira, P. A. B. Galli, J. F. Le Campion, A. Krone-Martins, B. Zuckerman, G. Chauvin, and I. Song. The TW Hydrae association: trigonometric parallaxes and kinematic analysis. *A&A*, 563:A121, March 2014. doi: 10.1051/0004-6361/201322075.

C. Eiroa, J. P. Marshall, A. Mora, B. Montesinos, O. Absil, J. Ch. Augereau, A. Bayo, G. Bryden, W. Danchi, C. del Burgo, S. Ertel, M. Fridlund, A. M. Heras, A. V. Krivov, R. Launhardt, R. Liseau, T. Löhne, J. Maldonado, G. L. Pilbratt, A. Roberge, J. Rodmann, J. Sanz-Forcada, E. Solano, K. Stapelfeldt, P. Thébault, S. Wolf, D. Ardila, M. Arévalo, C. Beichmann, V. Faramaz, B. M. González-García, R. Gutiérrez, J. Lebreton, R. Martínez-Arnáiz, G. Meeus, D. Montes, G. Olofsson, K. Y. L. Su, G. J. White, D. Barado, M. Fukagawa, E. Grün, I. Kamp, R. Lorente, A. Morbidelli, S. Müller, H. Mutschke,



T. Nakagawa, I. Ribas, and H. Walker. DUst around NEarby Stars. The survey observational results. *A&A*, 555:A11, July 2013. doi: 10.1051/0004-6361/201321050.

Thomas M. Esposito, Michael P. Fitzgerald, James R. Graham, Paul Kalas, Eve J. Lee, Eugene Chiang, Gaspard Duchêne, Jason Wang, Maxwell A. Millar-Blanchaer, Eric Nielsen, S. Mark Ammons, Sebastian Bruzzone, Robert J. De Rosa, Zachary H. Draper, Bruce Macintosh, Franck Marchis, Stanimir A. Metchev, Marshall Perrin, Laurent Pueyo, Abhijith Rajan, Fredrik T. Rantakyö, David Vega, and Schuyler Wolff. Bringing “The Moth” to Light: A Planet-sculpting Scenario for the HD 61005 Debris Disk. *AJ*, 152(4): 85, October 2016. doi: 10.3847/0004-6256/152/4/85.

Thomas M. Esposito, Paul Kalas, Michael P. Fitzgerald, Maxwell A. Millar-Blanchaer, Gaspard Duchêne, Jennifer Patience, Justin Hom, Marshall D. Perrin, Robert J. De Rosa, Eugene Chiang, Ian Czekala, Bruce Macintosh, James R. Graham, Megan Ansdell, Pauline Arriaga, Sebastian Bruzzone, Joanna Bulger, Christine H. Chen, Tara Cotten, Ruobing Dong, Zachary H. Draper, Katherine B. Follette, Li-Wei Hung, Ronald Lopez, Brenda C. Matthews, Johan Mazoyer, Stan Metchev, Julien Rameau, Bin Ren, Malena Rice, Inseok Song, Kevin Stahl, Jason Wang, Schuyler Wolff, Ben Zuckerman, S. Mark Ammons, Vanessa P. Bailey, Travis Barman, Jeffrey Chilcote, Rene Doyon, Benjamin L. Gerard, Stephen J. Goodsell, Alexandra Z. Greenbaum, Pascale Hibon, Sasha Hinkley, Patrick Ingraham, Quinn Konopacky, Jérôme Maire, Franck Marchis, Mark S. Marley, Christian Marois, Eric L. Nielsen, Rebecca Oppenheimer, David Palmer, Lisa Poyneer, Laurent Pueyo, Abhijith Rajan, Fredrik T. Rantakyö, Jean-Baptiste Ruffio, Dmitry Savransky, Adam C. Schneider, Anand Sivaramakrishnan, Rémi Soummer, Sandrine Thomas, and Kimberly Ward-Duong. Debris Disk Results from the Gemini Planet Imager Exoplanet Survey’s Polarimetric Imaging Campaign. *AJ*, 160(1):24, July 2020. doi: 10.3847/1538-3881/ab9199.

Peter Faber and Alice C. Quillen. The total number of giant planets in debris discs with central clearings. *MNRAS*, 382(4):1823–1828, December 2007. doi: 10.1111/j.1365-2966.2007.12490.x.

V. Faramaz, H. Beust, J.-C. Augereau, P. Kalas, and J. R. Graham. Insights on the dynamical history of the fomalhaut system - investigating the fomypothesis. *A&A*, 573:A87, 2015. doi: 10.1051/0004-6361/201424691. URL <https://doi.org/10.1051/0004-6361/201424691>.

Virginie Faramaz, Sebastian Marino, Mark Booth, Luca Matrà, Eric E. Mamajek, Geoffrey Bryden, Karl R. Stapelfeldt, Simon Casassus, Jorge Cuadra, Antonio S. Hales, and Alice

Zurlo. A Detailed Characterization of HR 8799’s Debris Disk with ALMA in Band 7. *AJ*, 161(6):271, June 2021. doi: 10.3847/1538-3881/abf4e0.

G. G. Fazio, J. L. Hora, L. E. Allen, M. L. N. Ashby, P. Barmby, L. K. Deutsch, J. S. Huang, S. Kleiner, M. Marengo, S. T. Megeath, G. J. Melnick, M. A. Pahre, B. M. Patten, J. Polizotti, H. A. Smith, R. S. Taylor, Z. Wang, S. P. Willner, W. F. Hoffmann, J. L. Pipher, W. J. Forrest, C. W. McMurty, C. R. McCreight, M. E. McKelvey, R. E. McMurray, D. G. Koch, S. H. Moseley, R. G. Arendt, J. E. Mentzell, C. T. Marx, P. Losch, P. Mayman, W. Eichhorn, D. Krebs, M. Jhabvala, D. Y. Gezari, D. J. Fixsen, J. Flores, K. Shakoorzadeh, R. Jungo, C. Hakun, L. Workman, G. Karpatis, R. Kichak, R. Whitley, S. Mann, E. V. Tollestrup, P. Eisenhardt, D. Stern, V. Gorjian, B. Bhattacharya, S. Carey, B. O. Nelson, W. J. Glaccum, M. Lacy, P. J. Lowrance, S. Laine, W. T. Reach, J. A. Stauffer, J. A. Surace, G. Wilson, E. L. Wright, A. Hoffman, G. Domingo, and M. Cohen. The Infrared Array Camera (IRAC) for the Spitzer Space Telescope. *ApJS*, 154(1):10–17, September 2004. doi: 10.1086/422843.

F Feng and H R A Jones. Understanding Fomalhaut as a Cooper pair. *Monthly Notices of the Royal Astronomical Society*, 474(4):4412–4420, 12 2017. ISSN 0035-8711. doi: 10.1093/mnras/stx3088. URL <https://doi.org/10.1093/mnras/stx3088>.

R. Ferlet, L. M. Hobbs, and A. Vidal-Madjar. The beta Pictoris circumstellar disk. V. Time variations of the Ca II-K line. *A&A*, 185:267–270, October 1987.

F. Feroz, M. P. Hobson, and M. Bridges. MULTINEST: an efficient and robust Bayesian inference tool for cosmology and particle physics. *MNRAS*, 398(4):1601–1614, October 2009. doi: 10.1111/j.1365-2966.2009.14548.x.

Thomas A. Fleming, Juergen H. M. M. Schmitt, and Mark S. Giampapa. Correlations of Coronal X-Ray Emission with Activity, Mass, and Age of the Nearby K and M Dwarfs. *ApJ*, 450:401, September 1995. doi: 10.1086/176150.

Daniel Foreman-Mackey, David W. Hogg, Dustin Lang, and Jonathan Goodman. emcee: The MCMC Hammer. *PASP*, 125(925):306, Mar 2013. doi: 10.1086/670067.

G. A. Fuller, A. Avison, M. Beltran, V. Casasola, P. Caselli, C. Cicone, F. Costagliola, C. De Breuck, L. Hunt, I. Jimenez-Serra, R. Laing, S. Longmore, M. Massardi, T. Mroczkowski, R. Paladino, S. Ramstedt, A. Richards, L. Testi, D. Vergani, S. Viti, and J. Wagg. The Science Case for ALMA Band 2 and Band 2+3. *arXiv e-prints*, art. arXiv:1602.02414, February 2016.

Gaia Collaboration, T. Prusti, J. H. J. de Bruijne, A. G. A. Brown, A. Vallenari, C. Babusiaux, C. A. L. Bailer-Jones, U. Bastian, M. Biermann, D. W. Evans, L. Eyer, F. Jansen, C. Jordi,

S. A. Klioner, U. Lammers, L. Lindegren, X. Luri, F. Mignard, D. J. Milligan, C. Panem, V. Poinsignon, D. Pourbaix, S. Randich, G. Sarri, P. Sartoretti, H. I. Siddiqui, C. Soubiran, V. Valette, F. van Leeuwen, N. A. Walton, C. Aerts, F. Arenou, M. Cropper, R. Drimmel, E. Høg, D. Katz, M. G. Lattanzi, W. O'Mullane, E. K. Grebel, A. D. Holland, C. Huc, X. Passot, L. Bramante, C. Cacciari, J. Castañeda, L. Chaoul, N. Cheek, F. De Angeli, C. Fabricius, R. Guerra, J. Hernández, A. Jean-Antoine-Piccolo, E. Masana, R. Messineo, N. Mowlavi, K. Nienartowicz, D. Ordóñez-Blanco, P. Panuzzo, J. Portell, P. J. Richards, M. Riello, G. M. Seabroke, P. Tanga, F. Thévenin, J. Torra, S. G. Els, G. Gracia-Abril, G. Comoretto, M. Garcia-Reinaldos, T. Lock, E. Mercier, M. Altmann, R. Andrae, T. L. Astraatmadja, I. Bellas-Velidis, K. Benson, J. Berthier, R. Blomme, G. Busso, B. Carry, A. Cellino, G. Clementini, S. Cowell, O. Creevey, J. Cuypers, M. Davidson, J. De Ridder, A. de Torres, L. Delchambre, A. Dell'Oro, C. Ducourant, Y. Frémat, M. García-Torres, E. Gosset, J. L. Halbwachs, N. C. Hambly, D. L. Harrison, M. Hauser, D. Hestroffer, S. T. Hodgkin, H. E. Huckle, A. Hutton, G. Jasiewicz, S. Jordan, M. Kontizas, A. J. Korn, A. C. Lanzafame, M. Manteiga, A. Moitinho, K. Muinonen, J. Osinde, E. Pancino, T. Pauwels, J. M. Petit, A. Recio-Blanco, A. C. Robin, L. M. Sarro, C. Siopis, M. Smith, K. W. Smith, A. Sozzetti, W. Thuillot, W. van Reeve, Y. Viala, U. Abbas, A. Abreu Aramburu, S. Accart, J. J. Aguado, P. M. Allan, W. Allasia, G. Altavilla, M. A. Álvarez, J. Alves, R. I. Anderson, A. H. Andrei, E. Anglada Varela, E. Antiche, T. Antoja, S. Antón, B. Arcay, A. Atzei, L. Ayache, N. Bach, S. G. Baker, L. Balaguer-Núñez, C. Barache, C. Barata, A. Barbier, F. Barblan, M. Baroni, D. Barrado y Navascués, M. Barros, M. A. Barstow, U. Becciani, M. Bellazzini, G. Bellei, A. Bello García, V. Belokurov, P. Bendjoya, A. Berihuete, L. Bianchi, O. Bienaymé, F. Billebaud, N. Blagorodnova, S. Blanco-Cuaresma, T. Boch, A. Bombrun, R. Borrachero, S. Bouquillon, G. Bourda, H. Bouy, A. Bragaglia, M. A. Breddels, N. Brouillet, T. Brüsemeister, B. Bucciarelli, F. Budnik, P. Burgess, R. Burgon, A. Burlacu, D. Busonero, R. Buzzi, E. Caffau, J. Cambras, H. Campbell, R. Cancelliere, T. Cantat-Gaudin, T. Carlucci, J. M. Carrasco, M. Castellani, P. Charlot, J. Charnas, P. Charvet, F. Chassat, A. Chiavassa, M. Clotet, G. Cocozza, R. S. Collins, P. Collins, G. Costigan, F. Crifo, N. J. G. Cross, M. Crosta, C. Crowley, C. Dafonte, Y. Damerdj, A. Dapergolas, P. David, M. David, P. De Cat, F. de Felice, P. de Laverny, F. De Luise, R. De March, D. de Martino, R. de Souza, J. Debosscher, E. del Pozo, M. Delbo, A. Delgado, H. E. Delgado, F. di Marco, P. Di Matteo, S. Diakite, E. Distefano, C. Dolding, S. Dos Anjos, P. Drazinos, J. Durán, Y. Dzigian, E. Ecale, B. Edvardsson, H. Enke, M. Erdmann, D. Escolar, M. Espina, N. W. Evans, G. Eynard Bontemps, C. Fabre, M. Fabrizio, S. Faigler, A. J. Falcão, M. Farràs Casas, F. Faye, L. Federici, G. Fedorets, J. Fernández-Hernández, P. Fernique, A. Fienga, F. Figueras, F. Filippi, K. Findeisen, A. Fonti, M. Fouesneau, E. Fraile, M. Fraser, J. Fuchs, R. Furnell, M. Gai,

S. Galleti, L. Galluccio, D. Garabato, F. García-Sedano, P. Garé, A. Garofalo, N. Garalda, P. Gavras, J. Gerssen, R. Geyer, G. Gilmore, S. Girona, G. Giuffrida, M. Gomes, A. González-Marcos, J. González-Núñez, J. J. González-Vidal, M. Granvik, A. Guerrier, P. Guillout, J. Guiraud, A. Gúrpide, R. Gutiérrez-Sánchez, L. P. Guy, R. Haignon, D. Hatzidimitriou, M. Haywood, U. Heiter, A. Helmi, D. Hobbs, W. Hofmann, B. Holl, G. Holland, J. A. S. Hunt, A. Hypki, V. Icardi, M. Irwin, G. Jevardat de Fombelle, P. Jofré, P. G. Jonker, A. Jorissen, F. Julbe, A. Karampelas, A. Kochoska, R. Kohley, K. Kolenberg, E. Kontizas, S. E. Koposov, G. Kordopatis, P. Koubsky, A. Kowalczyk, A. Krone-Martins, M. Kudryashova, I. Kull, R. K. Bachchan, F. Lacoste-Seris, A. F. Lanza, J. B. Lavigne, C. Le Poncin-Lafitte, Y. Lebreton, T. Lebzelter, S. Leccia, N. Leclerc, I. Lecoeur-Taïbi, V. Lemaitre, H. Lenhardt, F. Leroux, S. Liao, E. Licata, H. E. P. Lindstrøm, T. A. Lister, E. Livanou, A. Lobel, W. Löffler, M. López, A. Lopez-Lozano, D. Lorenz, T. Loureiro, I. MacDonald, T. Magalhães Fernandes, S. Managau, R. G. Mann, G. Mantelet, O. Marchal, J. M. Marchant, M. Marconi, J. Marie, S. Marinoni, P. M. Marrese, G. Marschalkó, D. J. Marshall, J. M. Martín-Fleitas, M. Martino, N. Mary, G. Matijević, T. Mazeh, P. J. McMillan, S. Messina, A. Mestre, D. Michalik, N. R. Millar, B. M. H. Miranda, D. Molina, R. Molinaro, M. Molinaro, L. Molnár, M. Moniez, P. Montegriffo, D. Monteiro, R. Mor, A. Mora, R. Morbidelli, T. Morel, S. Morgenthaler, T. Morley, D. Morris, A. F. Mulone, T. Muraveva, I. Musella, J. Narbonne, G. Nelemans, L. Nicastro, L. Noval, C. Ordénovic, J. Ordieres-Meré, P. Osborne, C. Pagani, I. Pagano, F. Pailler, H. Palacin, L. Palaversa, P. Parsons, T. Paulsen, M. Pecoraro, R. Pedrosa, H. Pentikäinen, J. Pereira, B. Pichon, A. M. Piersimoni, F. X. Pineau, E. Plachy, G. Plum, E. Poujoulet, A. Prša, L. Pulone, S. Ragaini, S. Rago, N. Rambaux, M. Ramos-Lerate, P. Ranalli, G. Rauw, A. Read, S. Regibo, F. Renk, C. Reylé, R. A. Ribeiro, L. Rimoldini, V. Ripepi, A. Riva, G. Rixon, M. Roelens, M. Romero-Gómez, N. Rowell, F. Royer, A. Rudolph, L. Ruiz-Dern, G. Sadowski, T. Sagristà Sellés, J. Sahlmann, J. Salgado, E. Salguero, M. Sarasso, H. Savietto, A. Schnorhk, M. Schultheis, E. Sciacca, M. Segol, J. C. Segovia, D. Segransan, E. Serpell, I. C. Shih, R. Smareglia, R. L. Smart, C. Smith, E. Solano, F. Solitro, R. Sordo, S. Soria Nieto, J. Souchay, A. Spagna, F. Spoto, U. Stampa, I. A. Steele, H. Steidelmüller, C. A. Stephenson, H. Stoev, F. F. Suess, M. Süveges, J. Surdej, L. Szabados, E. Szegedi-Elek, D. Tapiador, F. Taris, G. Tauran, M. B. Taylor, R. Teixeira, D. Terrett, B. Tingley, S. C. Trager, C. Turon, A. Ulla, E. Utrilla, G. Valentini, A. van Elteren, E. Van Hemelryck, M. van Leeuwen, M. Varadi, A. Vecchiato, J. Veljanoski, T. Via, D. Vicente, S. Vogt, H. Voss, V. Votruba, S. Voutsinas, G. Walmsley, M. Weiler, K. Weingrill, D. Werner, T. Wevers, G. Whitehead, Ł. Wyrzykowski, A. Yoldas, M. Žerjal, S. Zucker, C. Zurbach, T. Zwitter, A. Alecu, M. Allen, C. Allende Prieto, A. Amorim, G. Anglada-Escudé, V. Arsenijevic, S. Azaz, P. Balm, M. Beck, H. H. Bernstein, L. Bigot,

A. Bijaoui, C. Blasco, M. Bonfigli, G. Bono, S. Boudreault, A. Bressan, S. Brown, P. M. Brunet, P. Bunclark, R. Buonanno, A. G. Butkevich, C. Carret, C. Carrion, L. Chemin, F. Chéreau, L. Corcione, E. Darmigny, K. S. de Boer, P. de Teodoro, P. T. de Zeeuw, C. Delle Luche, C. D. Domingues, P. Dubath, F. Fodor, B. Frézouls, A. Fries, D. Fustes, D. Fyfe, E. Gallardo, J. Gallegos, D. Gardiol, M. Gebran, A. Gomboc, A. Gómez, E. Grux, A. Gueguen, A. Heyrovsky, J. Hoar, G. Iannicola, Y. Isasi Parache, A. M. Janotto, E. Joliet, A. Jonckheere, R. Keil, D. W. Kim, P. Klagyivik, J. Klar, J. Knude, O. Kochukhov, I. Kolka, J. Kos, A. Kutka, V. Lainey, D. LeBouquin, C. Liu, D. Loreggia, V. V. Makarov, M. G. Marseille, C. Martayan, O. Martinez-Rubi, B. Massart, F. Meynadier, S. Mignot, U. Munari, A. T. Nguyen, T. Nordlander, P. Ocvirk, K. S. O’Flaherty, A. Olias Sanz, P. Ortiz, J. Osorio, D. Oszkiewicz, A. Ouzounis, M. Palmer, P. Park, E. Pasquato, C. Peltzer, J. Peralta, F. Péturaud, T. Pieniluoma, E. Pigozzi, J. Poels, G. Prat, T. Prod’homme, F. Raison, J. M. Rebordao, D. Risquez, B. Rocca-Volmerange, S. Rosen, M. I. Ruiz-Fuertes, F. Russo, S. Sembay, I. Serraller Vizcaino, A. Short, A. Siebert, H. Silva, D. Sinachopoulos, E. Slezak, M. Soffel, D. Sosnowska, V. Straižys, M. ter Linden, D. Terrell, S. Theil, C. Tiede, L. Troisi, P. Tsalmantza, D. Tur, M. Vaccari, F. Vachier, P. Valles, W. Van Hamme, L. Veltz, J. Virtanen, J. M. Wallut, R. Wichmann, M. I. Wilkinson, H. Ziaee pour, and S. Zschocke. The Gaia mission. *A&A*, 595:A1, Nov 2016. doi: 10.1051/0004-6361/201629272.

Gaia Collaboration, A. G. A. Brown, A. Vallenari, T. Prusti, J. H. J. de Bruijne, C. Babusiaux, C. A. L. Bailer-Jones, M. Biermann, D. W. Evans, L. Eyer, F. Jansen, C. Jordi, S. A. Klioner, U. Lammers, L. Lindegren, X. Luri, F. Mignard, C. Panem, D. Pourbaix, S. Randich, P. Sartoretti, H. I. Siddiqui, C. Soubiran, F. van Leeuwen, N. A. Walton, F. Arenou, U. Bastian, M. Cropper, R. Drimmel, D. Katz, M. G. Lattanzi, J. Bakker, C. Cacciari, J. Castañeda, L. Chaoul, N. Cheek, F. De Angeli, C. Fabricius, R. Guerra, B. Holl, E. Masana, R. Messineo, N. Mowlavi, K. Nienartowicz, P. Panuzzo, J. Portell, M. Riello, G. M. Seabroke, P. Tanga, F. Thévenin, G. Gracia-Abril, G. Comoretto, M. Garcia-Reinaldos, D. Teyssier, M. Altmann, R. Andrae, M. Audard, I. Bellas-Velidis, K. Benson, J. Berthier, R. Blomme, P. Burgess, G. Busso, B. Carry, A. Cellino, G. Clementini, M. Clotet, O. Creevey, M. Davidson, J. De Ridder, L. Delchambre, A. Dell’Oro, C. Ducourant, J. Fernández-Hernández, M. Fouesneau, Y. Frémat, L. Galuccio, M. García-Torres, J. González-Núñez, J. J. González-Vidal, E. Gosset, L. P. Guy, J. L. Halbwachs, N. C. Hambly, D. L. Harrison, J. Hernández, D. Hestroffer, S. T. Hodgkin, A. Hutton, G. Jasiewicz, A. Jean-Antoine-Piccolo, S. Jordan, A. J. Korn, A. Krone-Martins, A. C. Lanzafame, T. Lebzelter, W. Löffler, M. Manteiga, P. M. Marrese, J. M. Martín-Fleitas, A. Moitinho, A. Mora, K. Muinonen, J. Osinde, E. Pancino, T. Pauwels, J. M. Petit, A. Recio-Blanco, P. J. Richards, L. Rimoldini, A. C.

Robin, L. M. Sarro, C. Siopis, M. Smith, A. Sozzetti, M. Süveges, J. Torra, W. van Reeve, U. Abbas, A. Abreu Aramburu, S. Accart, C. Aerts, G. Altavilla, M. A. Álvarez, R. Alvarez, J. Alves, R. I. Anderson, A. H. Andrei, E. Anglada Varela, E. Antiche, T. Antoja, B. Arcay, T. L. Astraatmadja, N. Bach, S. G. Baker, L. Balaguer-Núñez, P. Balm, C. Barache, C. Barata, D. Barbato, F. Barblan, P. S. Barklem, D. Barrado, M. Barros, M. A. Barstow, S. Bartholomé Muñoz, J. L. Bassilana, U. Becciani, M. Bellazzini, A. Berihuete, S. Bertone, L. Bianchi, O. Bienaymé, S. Blanco-Cuaresma, T. Boch, C. Boeche, A. Bombrun, R. Borrachero, D. Bossini, S. Bouquillon, G. Bourda, A. Braglia, L. Bramante, M. A. Breddels, A. Bressan, N. Brouillet, T. Brüsemeister, E. Brugaletta, B. Bucciarelli, A. Burlacu, D. Busonero, A. G. Butkevich, R. Buzzi, E. Caffau, R. Cancelliere, G. Cannizzaro, T. Cantat-Gaudin, R. Carballo, T. Carlucci, J. M. Carrasco, L. Casamiquela, M. Castellani, A. Castro-Ginard, P. Charlot, L. Chemin, A. Chiavassa, G. Cocozza, G. Costigan, S. Cowell, F. Crifo, M. Crosta, C. Crowley, J. Cuypers, C. D'Amico, Y. Damerdj, A. Dapergolas, P. David, M. David, P. de Laverny, F. De Luise, R. De March, D. de Martino, R. de Souza, A. de Torres, J. Debosscher, E. del Pozo, M. Delbo, A. Delgado, H. E. Delgado, P. Di Matteo, S. Diakite, C. Diener, E. Distefano, C. Doldring, P. Drazinos, J. Durán, B. Edvardsson, H. Enke, K. Eriksson, P. Esquej, G. Eynard Bontemps, C. Fabre, M. Fabrizio, S. Faigler, A. J. Falcão, M. Farràs Casas, L. Federici, G. Fedorets, P. Fernique, F. Figueras, F. Filippi, K. Findeisen, A. Fonti, E. Fraile, M. Fraser, B. Frézouls, M. Gai, S. Galletti, D. Garabato, F. García-Sedano, A. Garofalo, N. Garralda, A. Gavel, P. Gavras, J. Gerssen, R. Geyer, P. Giacobbe, G. Gilmore, S. Girona, G. Giuffrida, F. Glass, M. Gomes, M. Granvik, A. Gueguen, A. Guerrier, J. Guiraud, R. Gutiérrez-Sánchez, R. Haigner, D. Hatzidimitriou, M. Hauser, M. Haywood, U. Heiter, A. Helmi, J. Heu, T. Hilger, D. Hobbs, W. Hofmann, G. Holland, H. E. Huckle, A. Hypki, V. Icardi, K. Janßen, G. Jevardat de Fombelle, P. G. Jonker, Á. L. Juhász, F. Julbe, A. Karampelas, A. Kewley, J. Klar, A. Kochoska, R. Kohley, K. Kolenberg, M. Kontizas, E. Kontizas, S. E. Koposov, G. Kordopatis, Z. Kostrzewa-Rutkowska, P. Koubsky, S. Lambert, A. F. Lanza, Y. Lasne, J. B. Lavigne, Y. Le Fustec, C. Le Poncin-Lafitte, Y. Lebreton, S. Leccia, N. Leclerc, I. Lecoœur-Taïbi, H. Lenhardt, F. Leroux, S. Liao, E. Licata, H. E. P. Lindstrøm, T. A. Lister, E. Livanou, A. Lobel, M. López, S. Managau, R. G. Mann, G. Mantelet, O. Marchal, J. M. Marchant, M. Marconi, S. Marinoni, G. Marschall, D. J. Marshall, M. Martino, G. Marton, N. Mary, D. Massari, G. Matijević, T. Mazeh, P. J. McMillan, S. Messina, D. Michalik, N. R. Millar, D. Molina, R. Molinaro, L. Molnár, P. Montegriffo, R. Mor, R. Morbidelli, T. Morel, D. Morris, A. F. Mulone, T. Muraveva, I. Musella, G. Nelemans, L. Nicastro, L. Noval, W. O'Mullane, C. Ordénovic, D. Ordóñez-Blanco, P. Osborne, C. Pagani, I. Pagano, F. Pailler, H. Palacin, L. Palaversa, A. Panahi, M. Pawlak, A. M. Piersimoni, F. X. Pineau,

E. Plachy, G. Plum, E. Poggio, E. Poujoulet, A. Prša, L. Pulone, E. Racero, S. Ragaini, N. Rambaux, M. Ramos-Lerate, S. Regibo, C. Reylé, F. Riclet, V. Ripepi, A. Riva, A. Rivard, G. Rixon, T. Roegiers, M. Roelens, M. Romero-Gómez, N. Rowell, F. Royer, L. Ruiz-Dern, G. Sadowski, T. Sagristà Sellés, J. Sahlmann, J. Salgado, E. Salguero, N. Sanna, T. Santana-Ros, M. Sarasso, H. Saviotto, M. Schultheis, E. Sciacca, M. Segol, J. C. Segovia, D. Ségransan, I. C. Shih, L. Siltala, A. F. Silva, R. L. Smart, K. W. Smith, E. Solano, F. Solitro, R. Sordo, S. Soria Nieto, J. Souchay, A. Spagna, F. Spoto, U. Stampa, I. A. Steele, H. Steidelmüller, C. A. Stephenson, H. Stoev, F. F. Suess, J. Surdej, L. Szabados, E. Szegedi-Elek, D. Tapiador, F. Taris, G. Tauran, M. B. Taylor, R. Teixeira, D. Terrett, P. Teyssandier, W. Thuillot, A. Titarenko, F. Torra Clotet, C. Turon, A. Ulla, E. Utrilla, S. Uzzi, M. Vaillant, G. Valentini, V. Valette, A. van Elteren, E. Van Hemelryck, M. van Leeuwen, M. Vaschetto, A. Vecchiato, J. Veljanoski, Y. Viala, D. Vicente, S. Vogt, C. von Essen, H. Voss, V. Votruba, S. Voutsinas, G. Walmsley, M. Weiler, O. Wertz, T. Wevers, Ł. Wyrzykowski, A. Yoldas, M. Žerjal, H. Ziaeeepour, J. Zorec, S. Zschocke, S. Zucker, C. Zurbach, and T. Zwitter. Gaia Data Release 2. Summary of the contents and survey properties. *A&A*, 616:A1, August 2018. doi: 10.1051/0004-6361/201833051.

Gaia Collaboration, A. G. A. Brown, A. Vallenari, T. Prusti, J. H. J. de Bruijne, C. Babusi-  
aux, M. Biermann, O. L. Creevey, D. W. Evans, L. Eyer, A. Hutton, F. Jansen, C. Jordi,  
S. A. Klioner, U. Lammers, L. Lindegren, X. Luri, F. Mignard, C. Panem, D. Pourbaix,  
S. Randich, P. Sartoretti, C. Soubiran, N. A. Walton, F. Arenou, C. A. L. Bailer-Jones,  
U. Bastian, M. Cropper, R. Drimmel, D. Katz, M. G. Lattanzi, F. van Leeuwen, J. Bakker,  
C. Cacciari, J. Castañeda, F. De Angeli, C. Ducourant, C. Fabricius, M. Fouesneau,  
Y. Frémat, R. Guerra, A. Guerrier, J. Guiraud, A. Jean-Antoine Piccolo, E. Masana,  
R. Messineo, N. Mowlavi, C. Nicolas, K. Nienartowicz, F. Pailler, P. Panuzzo, F. Riclet,  
W. Roux, G. M. Seabroke, R. Sordo, P. Tanga, F. Thévenin, G. Gracia-Abril, J. Portell,  
D. Teyssier, M. Altmann, R. Andrae, I. Bellas-Velidis, K. Benson, J. Berthier, R. Blomme,  
E. Brugaletta, P. W. Burgess, G. Busso, B. Carry, A. Cellino, N. Cheek, G. Clementini,  
Y. Damerdj, M. Davidson, L. Delchambre, A. Dell’Oro, J. Fernández-Hernández, L. Gal-  
luccio, P. García-Lario, M. Garcia-Reinaldos, J. González-Núñez, E. Gosset, R. Haigron,  
J. L. Halbwachs, N. C. Hambly, D. L. Harrison, D. Hatzidimitriou, U. Heiter, J. Hernán-  
dez, D. Hestroffer, S. T. Hodgkin, B. Holl, K. Janßen, G. Jevardat de Fombelle, S. Jordan,  
A. Krone-Martins, A. C. Lanzafame, W. Löffler, A. Lorca, M. Manteiga, O. Marchal, P. M.  
Marrese, A. Moitinho, A. Mora, K. Muinonen, P. Osborne, E. Pancino, T. Pauwels, J. M.  
Petit, A. Recio-Blanco, P. J. Richards, M. Riello, L. Rimoldini, A. C. Robin, T. Roegiers,  
J. Rybizki, L. M. Sarro, C. Siopis, M. Smith, A. Sozzetti, A. Ulla, E. Utrilla, M. van  
Leeuwen, W. van Reeve, U. Abbas, A. Abreu Aramburu, S. Accart, C. Aerts, J. J. Aguado,  
M. Ajaj, G. Altavilla, M. A. Álvarez, J. Álvarez Cid-Fuentes, J. Alves, R. I. Anderson,

E. Anglada Varela, T. Antoja, M. Audard, D. Baines, S. G. Baker, L. Balaguer-Núñez, E. Balbinot, Z. Balog, C. Barache, D. Barbato, M. Barros, M. A. Barstow, S. Bartolomé, J. L. Bassilana, N. Bauchet, A. Baudesson-Stella, U. Becciani, M. Bellazzini, M. Bernet, S. Bertone, L. Bianchi, S. Blanco-Cuaresma, T. Boch, A. Bombrun, D. Bossini, S. Bouquillon, A. Bragaglia, L. Bramante, E. Breedt, A. Bressan, N. Brouillet, B. Bucciarelli, A. Burlacu, D. Busonero, A. G. Butkevich, R. Buzzzi, E. Caffau, R. Cancelliere, H. Cánovas, T. Cantat-Gaudin, R. Carballo, T. Carlucci, M. I. Carnerero, J. M. Carrasco, L. Casamiquela, M. Castellani, A. Castro-Ginard, P. Castro Sampil, L. Chaoul, P. Charlot, L. Chemin, A. Chiavassa, M. R. L. Cioni, G. Comoretto, W. J. Cooper, T. Cornez, S. Cowell, F. Crifo, M. Crosta, C. Crowley, C. Dafonte, A. Dapergolas, M. David, P. David, P. de Laverny, F. De Luise, R. De March, J. De Ridder, R. de Souza, P. de Teodoro, A. de Torres, E. F. del Peloso, E. del Pozo, M. Delbo, A. Delgado, H. E. Delgado, J. B. Delisle, P. Di Matteo, S. Diakite, C. Diener, E. Distefano, C. Dolding, D. Eappachen, B. Edvardsson, H. Enke, P. Esquej, C. Fabre, M. Fabrizio, S. Faigler, G. Fedorets, P. Fernique, A. Fienga, F. Figueras, C. Fouron, F. Frangkoudi, E. Fraile, F. Franke, M. Gai, D. Garabato, A. Garcia-Gutierrez, M. García-Torres, A. Garofalo, P. Gavras, E. Gerlach, R. Geyer, P. Giacobbe, G. Gilmore, S. Girona, G. Giuffrida, R. Gomel, A. Gomez, I. Gonzalez-Santamaria, J. J. González-Vidal, M. Granvik, R. Gutiérrez-Sánchez, L. P. Guy, M. Hauser, M. Haywood, A. Helmi, S. L. Hidalgo, T. Hilger, N. Hładczuk, D. Hobbs, G. Holland, H. E. Huckle, G. Jasiewicz, P. G. Jonker, J. Juaristi Campillo, F. Julbe, L. Karbevaska, P. Kervella, S. Khanna, A. Kochoska, M. Kontizas, G. Kordopatis, A. J. Korn, Z. Kostrzewa-Rutkowska, K. Kruszyńska, S. Lambert, A. F. Lanza, Y. Lasne, J. F. Le Campion, Y. Le Fustec, Y. Lebreton, T. Lebzelter, S. Leccia, N. Leclerc, I. Lecoœur-Taibi, S. Liao, E. Licata, E. P. Lindstrøm, T. A. Lister, E. Livanou, A. Lobel, P. Madrero Pardo, S. Managau, R. G. Mann, J. M. Marchant, M. Marconi, M. M. S. Marcos Santos, S. Marinoni, F. Marocco, D. J. Marshall, L. Martin Polo, J. M. Martín-Fleitas, A. Masip, D. Massari, A. Mastrobuono-Battisti, T. Mazeh, P. J. McMillan, S. Messina, D. Michalik, N. R. Millar, A. Mints, D. Molina, R. Molinaro, L. Molnár, P. Montegriffo, R. Mor, R. Morbidelli, T. Morel, D. Morris, A. F. Mulone, D. Munoz, T. Muraveva, C. P. Murphy, I. Musella, L. Noval, C. Ordénovic, G. Orrù, J. Osinde, C. Pagani, I. Pagano, L. Palaversa, P. A. Palicio, A. Panahi, M. Pawlak, X. Peñalosa Esteller, A. Penttilä, A. M. Piersimoni, F. X. Pineau, E. Plachy, G. Plum, E. Poggio, E. Poretti, E. Poujoulet, A. Prša, L. Pulone, E. Racero, S. Ragaini, M. Rainer, C. M. Raiteri, N. Rambaux, P. Ramos, M. Ramos-Lerate, P. Re Fiorentin, S. Regibo, C. Reylé, V. Ripepi, A. Riva, G. Rixon, N. Robichon, C. Robin, M. Roelens, L. Rohrbasser, M. Romero-Gómez, N. Rowell, F. Royer, K. A. Rybicki, G. Sadowski, A. Sagristà Sellés, J. Sahlmann, J. Salgado, E. Salguero, N. Samaras, V. Sanchez Gimenez, N. Sanna, R. Santoveña, M. Sarasso, M. Schultheis, E. Sciacca,



M. Segol, J. C. Segovia, D. Ségransan, D. Semeux, S. Shahaf, H. I. Siddiqui, A. Siebert, L. Siltala, E. Slezak, R. L. Smart, E. Solano, F. Solitro, D. Souami, J. Souchay, A. Spagna, F. Spoto, I. A. Steele, H. Steidelmüller, C. A. Stephenson, M. Süveges, L. Szabados, E. Szegedi-Elek, F. Taris, G. Tauran, M. B. Taylor, R. Teixeira, W. Thuillot, N. Tonello, F. Torra, J. Torra, C. Turon, N. Unger, M. Vaillant, E. van Dillen, O. Vanel, A. Vecchiato, Y. Viala, D. Vicente, S. Voutsinas, M. Weiler, T. Wevers, Ł. Wyrzykowski, A. Yoldas, P. Yvard, H. Zhao, J. Zorec, S. Zucker, C. Zurbach, and T. Zwitter. Gaia Early Data Release 3. Summary of the contents and survey properties. *A&A*, 649:A1, May 2021. doi: 10.1051/0004-6361/202039657.

Gaia Collaboration, A. Vallenari, A. G. A. Brown, T. Prusti, J. H. J. de Bruijne, F. Arenou, C. Babusiaux, M. Biermann, O. L. Creevey, C. Ducourant, D. W. Evans, L. Eyer, R. Guerra, A. Hutton, C. Jordi, S. A. Klioner, U. L. Lammers, L. Lindegren, X. Luri, F. Mignard, C. Panem, D. Pourbaix, S. Randich, P. Sartoretti, C. Soubiran, P. Tanga, N. A. Walton, C. A. L. Bailer-Jones, U. Bastian, R. Drimmel, F. Jansen, D. Katz, M. G. Lattanzi, F. van Leeuwen, J. Bakker, C. Cacciari, J. Castañeda, F. De Angeli, C. Fabricius, M. Fouesneau, Y. Frémat, L. Galluccio, A. Guerrier, U. Heiter, E. Masana, R. Messineo, N. Mowlavi, C. Nicolas, K. Nienartowicz, F. Pailler, P. Panuzzo, F. Riclet, W. Roux, G. M. Seabroke, R. Sordoørcit, F. Thévenin, G. Gracia-Abril, J. Portell, D. Teyssier, M. Altmann, R. Andrae, M. Audard, I. Bellas-Velidis, K. Benson, J. Berthier, R. Blomme, P. W. Burgess, D. Busonero, G. Busso, H. Cánovas, B. Carry, A. Cellino, N. Cheek, G. Clementini, Y. Damerdj, M. Davidson, P. de Teodoro, M. Nuñez Campos, L. Delchambre, A. Dell’Oro, P. Esquej, J. Fernández-Hernández, E. Fraile, D. Garabato, P. García-Lario, E. Gosset, R. Haigron, J. L. Halbwachs, N. C. Hambly, D. L. Harrison, J. Hernández, D. Hestroffer, S. T. Hodgkin, B. Holl, K. Janßen, G. Jevardat de Fombelle, S. Jordan, A. Krone-Martins, A. C. Lanzafame, W. Löffler, O. Marchal, P. M. Marrese, A. Moitinho, K. Muinonen, P. Osborne, E. Pancino, T. Pauwels, A. Recio-Blanco, C. Reylé, M. Riello, L. Rimoldini, T. Roegiers, J. Rybizki, L. M. Sarro, C. Siopis, M. Smith, A. Sozzetti, E. Utrilla, M. van Leeuwen, U. Abbas, P. Ábrahám, A. Abreu Aramburu, C. Aerts, J. J. Aguado, M. Ajaj, F. Aldea-Montero, G. Altavilla, M. A. Álvarez, J. Alves, F. Anders, R. I. Anderson, E. Anglada Varela, T. Antoja, D. Baines, S. G. Baker, L. Balaguer-Núñez, E. Balbinot, Z. Balog, C. Barache, D. Barbato, M. Barros, M. A. Barstow, S. Bartolomé, J. L. Bassilana, N. Bauchet, U. Becciani, M. Bellazzini, A. Berihuete, M. Bernet, S. Bertone, L. Bianchi, A. Binnenfeld, S. Blanco-Cuaresma, A. Blazere, T. Boch, A. Bombrun, D. Bossini, S. Bouquillon, A. Bragaglia, L. Bramante, E. Breedt, A. Bressan, N. Brouillet, E. Brugaletta, B. Bucciarelli, A. Burlacu, A. G. Butkevich, R. Buzzi, E. Caffau, R. Cancelliere, T. Cantat-Gaudin, R. Carballo, T. Carlucci, M. I. Carnerero, J. M. Carrasco, L. Casamiquela, M. Castellani, A. Castro-Ginard, L. Chaoul, P. Charlot,

L. Chemin, V. Chiaramida, A. Chiavassa, N. Chornay, G. Comoretto, G. Contursi, W. J. Cooper, T. Cornez, S. Cowell, F. Crifo, M. Cropper, M. Crosta, C. Crowley, C. Dafonte, A. Dapergolas, M. David, P. David, P. de Laverny, F. De Luise, R. De March, J. De Ridder, R. de Souza, A. de Torres, E. F. del Peloso, E. del Pozo, M. Delbo, A. Delgado, J. B. Delisle, C. Demouchy, T. E. Dharmawardena, P. Di Matteo, S. Diakite, C. Diener, E. Distefano, C. Dolding, B. Edvardsson, H. Enke, C. Fabre, M. Fabrizio, S. Faigler, G. Fedorets, P. Fernique, A. Fienga, F. Figueras, Y. Fournier, C. Fouron, F. Fragkoudi, M. Gai, A. Garcia-Gutierrez, M. Garcia-Reinaldos, M. García-Torres, A. Garofalo, A. Gavel, P. Gavras, E. Gerlach, R. Geyer, P. Giacobbe, G. Gilmore, S. Girona, G. Giuffrida, R. Gomel, A. Gomez, J. González-Núñez, I. González-Santamaría, J. J. González-Vidal, M. Granvik, P. Guillout, J. Guiraud, R. Gutiérrez-Sánchez, L. P. Guy, D. Hatzidimitriou, M. Hauser, M. Haywood, A. Helmer, A. Helmi, M. H. Sarmiento, S. L. Hidalgo, T. Hilger, N. Hładczuk, D. Hobbs, G. Holland, H. E. Huckle, K. Jardine, G. Jasiewicz, A. Jean-Antoine Piccolo, Ó. Jiménez-Arranz, A. Jorissen, J. Juaristi Campillo, F. Julbe, L. Karbevská, P. Kervella, S. Khanna, M. Kontizas, G. Kordopatis, A. J. Korn, Á. Kóspál, Z. Kostrzewa-Rutkowska, K. Kruszyńska, M. Kun, P. Laizeau, S. Lambert, A. F. Lanza, Y. Lasne, J. F. Le Campion, Y. Lebreton, T. Lebzelter, S. Leccia, N. Leclerc, I. Lecoeur-Taibi, S. Liao, E. L. Licata, H. E. P. Lindstrøm, T. A. Lister, E. Livanou, A. Lobel, A. Lorca, C. Loup, P. Madrero Pardo, A. Magdaleno Romeo, S. Managau, R. G. Mann, M. Mantega, J. M. Marchant, M. Marconi, J. Marcos, M. M. S. Marcos Santos, D. Marín Pina, S. Marinoni, F. Marocco, D. J. Marshall, L. Martin Polo, J. M. Martín-Fleitas, G. Marton, N. Mary, A. Masip, D. Massari, A. Mastrobuono-Battisti, T. Mazeh, P. J. McMillan, S. Messina, D. Michalik, N. R. Millar, A. Mints, D. Molina, R. Molinaro, L. Molnár, G. Monari, M. Monguió, P. Montegriffo, A. Montero, R. Mor, A. Mora, R. Morbidelli, T. Morel, D. Morris, T. Muraveva, C. P. Murphy, I. Musella, Z. Nagy, L. Noval, F. Ocaña, A. Ogden, C. Ordenovic, J. O. Osinde, C. Pagani, I. Pagano, L. Palaversa, P. A. Palicio, L. Pallas-Quintela, A. Panahi, S. Payne-Wardenaar, X. Peñalosa Esteller, A. Penttilä, B. Pichon, A. M. Piersimoni, F. X. Pineau, E. Plachy, G. Plum, E. Poggio, A. Prša, L. Pulone, E. Racero, S. Ragaini, M. Rainer, C. M. Raiteri, N. Rambaux, P. Ramos, M. Ramos-Lerate, P. Re Fiorentin, S. Regibo, P. J. Richards, C. Rios Diaz, V. Ripepi, A. Riva, H. W. Rix, G. Rixon, N. Robichon, A. C. Robin, C. Robin, M. Roelens, H. R. O. Rogues, L. Rohrbasser, M. Romero-Gómez, N. Rowell, F. Royer, D. Ruz Mieres, K. A. Rybicki, G. Sadowski, A. Sáez Núñez, A. Sagristà Sellés, J. Sahlmann, E. Salguero, N. Samaras, V. Sanchez Gimenez, N. Sanna, R. Santoveña, M. Sarasso, M. Schultheis, E. Sciacca, M. Segol, J. C. Segovia, D. Ségransan, D. Semeux, S. Shahaf, H. I. Siddiqui, A. Siebert, L. Siltala, A. Silvelo, E. Slezak, I. Slezak, R. L. Smart, O. N. Snaith, E. Solano, F. Solitto, D. Souami, J. Souchay, A. Spagna, L. Spina, F. Spoto, I. A. Steele,

H. Steidelmüller, C. A. Stephenson, M. Süveges, J. Surdej, L. Szabados, E. Szegedi-Elek, F. Taris, M. B. Taylo, R. Teixeira, L. Tolomei, N. Tonello, F. Torra, J. Torra, G. Torralba Elipe, M. Trabucchi, A. T. Tsounis, C. Turon, A. Ulla, N. Unger, M. V. Vaillant, E. van Dillen, W. van Reeve, O. Vanel, A. Vecchiato, Y. Viala, D. Vicente, S. Voutsinas, M. Weiler, T. Wevers, L. Wyrzykowski, A. Yoldas, P. Yvard, H. Zhao, J. Zorec, S. Zucker, and T. Zwitter. Gaia Data Release 3: Summary of the content and survey properties. *arXiv e-prints*, art. arXiv:2208.00211, July 2022.

B. T. Gänsicke, A. Aungwerojwit, T. R. Marsh, V. S. Dhillon, D. I. Sahman, Dimitri Veras, J. Farihi, P. Chote, R. Ashley, S. Arjyotha, S. Rattanasoon, S. P. Littlefair, D. Pollacco, and M. R. Burleigh. High-speed Photometry of the Disintegrating Planetesimals at WD1145+017: Evidence for Rapid Dynamical Evolution. *ApJ*, 818(1):L7, February 2016. doi: 10.3847/2041-8205/818/1/L7.

B. L. Gary, S. Rappaport, T. G. Kaye, R. Alonso, and F. J. Hambschs. WD 1145+017 photometric observations during eight months of high activity. *MNRAS*, 465(3):3267–3280, March 2017. doi: 10.1093/mnras/stw2921.

A. Gáspár, D. Psaltis, G. H. Rieke, and F. Özel. Modeling Collisional Cascades in Debris Disks: Steep Dust-size Distributions. *ApJ*, 754:74, July 2012.

András Gáspár and George H. Rieke. New hst data and modeling reveal a massive planetesimal collision around fomalhaut. *Proceedings of the National Academy of Sciences*, 117(18):9712–9722, Apr 2020. ISSN 1091-6490. doi: 10.1073/pnas.1912506117. URL <http://dx.doi.org/10.1073/pnas.1912506117>.

III Gautier, Thomas N., G. H. Rieke, John Stansberry, Geoffrey C. Bryden, Karl R. Stapelfeldt, Michael W. Werner, Charles A. Beichman, Christine Chen, Kate Su, David Trilling, Brian M. Patten, and Thomas L. Roellig. Far-Infrared Properties of M Dwarfs. *ApJ*, 667(1):527–536, September 2007. doi: 10.1086/520667.

D. A. Golimowski, D. R. Ardila, J. E. Krist, M. Clampin, H. C. Ford, G. D. Illingworth, F. Bartko, N. Benítez, J. P. Blakeslee, R. J. Bouwens, L. D. Bradley, T. J. Broadhurst, R. A. Brown, C. J. Burrows, E. S. Cheng, N. J. G. Cross, R. Demarco, P. D. Feldman, M. Franx, T. Goto, C. Gronwall, G. F. Hartig, B. P. Holden, N. L. Homeier, L. Infante, M. J. Jee, R. A. Kimble, M. P. Lesser, A. R. Martel, S. Mei, F. Menanteau, G. R. Meurer, G. K. Miley, V. Motta, M. Postman, P. Rosati, M. Sirianni, W. B. Sparks, H. D. Tran, Z. I. Tsvetanov, R. L. White, W. Zheng, and A. W. Zirm. Hubble Space Telescope ACS Multiband Coronagraphic Imaging of the Debris Disk around  $\beta$  Pictoris. *AJ*, 131(6): 3109–3130, June 2006. doi: 10.1086/503801.

- D. A. Golimowski, J. E. Krist, K. R. Stapelfeldt, C. H. Chen, D. R. Ardila, G. Bryden, M. Clampin, H. C. Ford, G. D. Illingworth, P. Plavchan, G. H. Rieke, and K. Y. L. Su. Hubble and Spitzer Space Telescope Observations of the Debris Disk around the nearby K Dwarf HD 92945. *AJ*, 142(1):30, Jul 2011. doi: 10.1088/0004-6256/142/1/30.
- R. Gomes, H. F. Levison, K. Tsiganis, and A. Morbidelli. Origin of the cataclysmic Late Heavy Bombardment period of the terrestrial planets. *Nature*, 435(7041):466–469, May 2005. doi: 10.1038/nature03676.
- C. A. Grady, J. P. Wisniewski, G. Schneider, A. Boccaletti, A. Gaspar, J. H. Debes, D. C. Hines, C. C. Stark, C. Thalmann, A. M. Lagrange, J. C. Augereau, E. Sezestre, J. Milli, Th. Henning, and M. J. Kuchner. The Eroding Disk of AU Mic. *ApJ*, 889(1):L21, January 2020. doi: 10.3847/2041-8213/ab65bb.
- James R. Graham, K. Matthews, G. Neugebauer, and B. T. Soifer. The Infrared Excess of G29–38: A Brown Dwarf or Dust? *ApJ*, 357:216, July 1990. doi: 10.1086/168907.
- James R. Graham, Paul G. Kalas, and Brenda C. Matthews. The Signature of Primordial Grain Growth in the Polarized Light of the AU Microscopii Debris Disk. *ApJ*, 654(1): 595–605, January 2007. doi: 10.1086/509318.
- J. S. Greaves, W. S. Holland, M. C. Wyatt, W. R. F. Dent, E. I. Robson, I. M. Coulson, T. Jenness, G. H. Moriarty-Schieven, G. R. Davis, H. M. Butner, W. K. Gear, C. Dominik, and H. J. Walker. Structure in the  $\epsilon$  Eridani Debris Disk. *ApJ*, 619(2):L187–L190, February 2005. doi: 10.1086/428348.
- M. J. Griffin, A. Abergel, A. Abreu, P. A. R. Ade, P. André, J. L. Augueres, T. Babbedge, Y. Bae, T. Baillie, J. P. Baluteau, M. J. Barlow, G. Bendo, D. Benielli, J. J. Bock, P. Bonhomme, D. Brisbin, C. Brockley-Blatt, M. Caldwell, C. Cara, N. Castro-Rodriguez, R. Cerulli, P. Chaniel, S. Chen, E. Clark, D. L. Clements, L. Clerc, J. Coker, D. Communal, L. Conversi, P. Cox, D. Crumb, C. Cunningham, F. Daly, G. R. Davis, P. de Antoni, J. Delderfield, N. Devin, A. di Giorgio, I. Didschuns, K. Dohlen, M. Donati, A. Dowell, C. D. Dowell, L. Duband, L. Dumaye, R. J. Emery, M. Ferlet, D. Ferrand, J. Fontignie, M. Fox, A. Franceschini, M. Frerking, T. Fulton, J. Garcia, R. Gastaud, W. K. Gear, J. Glenn, A. Goizel, D. K. Griffin, T. Grundy, S. Guest, L. Guillemet, P. C. Hargrave, M. Harwit, P. Hastings, E. Hatziminaoglou, M. Herman, B. Hinde, V. Hristov, M. Huang, P. Imhof, K. J. Isaak, U. Israelsson, R. J. Ivison, D. Jennings, B. Kiernan, K. J. King, A. E. Lange, W. Latter, G. Laurent, P. Laurent, S. J. Leeks, E. Lellouch, L. Levenson, B. Li, J. Li, J. Lilienthal, T. Lim, S. J. Liu, N. Lu, S. Madden, G. Mainetti, P. Marliani, D. McKay, K. Mercier, S. Molinari, H. Morris, H. Moseley,

J. Mulder, M. Mur, D. A. Naylor, H. Nguyen, B. O’Halloran, S. Oliver, G. Olofsson, H. G. Olofsson, R. Orfei, M. J. Page, I. Pain, P. Panuzzo, A. Papageorgiou, G. Parks, P. Parr-Burman, A. Pearce, C. Pearson, I. Pérez-Fournon, F. Pinsard, G. Pisano, J. Podosek, M. Pohlen, E. T. Polehampton, D. Pouliquen, D. Rigopoulou, D. Rizzo, I. G. Roseboom, H. Roussel, M. Rowan-Robinson, B. Rownd, P. Saraceno, M. Sauvage, R. Savage, G. Savini, E. Sawyer, C. Scharnberg, D. Schmitt, N. Schneider, B. Schulz, A. Schwartz, R. Shafer, D. L. Shupe, B. Sibthorpe, S. Sidher, A. Smith, A. J. Smith, D. Smith, L. Spencer, B. Stobie, R. Sudiwala, K. Sukhatme, C. Surace, J. A. Stevens, B. M. Swinyard, M. Trichas, T. Tourette, H. Triou, S. Tseng, C. Tucker, A. Turner, M. Vaccari, I. Valtchanov, L. Vigroux, E. Virique, G. Voellmer, H. Walker, R. Ward, T. Waskett, M. Weilert, R. Wesson, G. J. White, N. Whitehouse, C. D. Wilson, B. Winter, A. L. Woodcraft, G. S. Wright, C. K. Xu, A. Zavagno, M. Zemcov, L. Zhang, and E. Zonca. The Herschel-SPIRE instrument and its in-flight performance. *A&A*, 518:L3, July 2010. doi: 10.1051/0004-6361/201014519.

M. A. T. Groenewegen. The Cepheid period-luminosity-metallicity relation based on Gaia DR2 data. *A&A*, 619:A8, November 2018. doi: 10.1051/0004-6361/201833478.

H. J. Habing. Circumstellar envelopes and Asymptotic Giant Branch stars. *A&ARv*, 7(2): 97–207, January 1996. doi: 10.1007/PL00013287.

Joseph M Hahn and Renu Malhotra. Neptune’s migration into a stirred-up kuiper belt: A detailed comparison of simulations to observations. *The Astronomical Journal*, 130(5): 2392, 2005.

John H. D. Harrison, Amy Bonsor, and Nikku Madhusudhan. Polluted white dwarfs: constraints on the origin and geology of exoplanetary material. *MNRAS*, 479(3):3814–3841, September 2018. doi: 10.1093/mnras/sty1700.

C. Hayashi. Structure of the Solar Nebula, Growth and Decay of Magnetic Fields and Effects of Magnetic and Turbulent Viscosities on the Nebula. *Progress of Theoretical Physics Supplement*, 70:35–53, January 1981. doi: 10.1143/PTPS.70.35.

Sara R. Heap, Don J. Lindler, Thierry M. Lanz, Robert H. Cornett, Ivan Hubeny, S. P. Maran, and Bruce Woodgate. Space Telescope Imaging Spectrograph Coronagraphic Observations of  $\beta$  Pictoris. *ApJ*, 539(1):435–444, August 2000. doi: 10.1086/309188.

Kevin Heng and Matej Malik. Debris discs around M stars: non-existence versus non-detection. *MNRAS*, 432(3):2562–2572, July 2013. doi: 10.1093/mnras/stt615.

Sasha Hinkley, Elisabeth C. Matthews, Charlène Lefevre, Jean-Francois Lestrade, Grant Kennedy, Dimitri Mawet, Karl R. Stapelfeldt, Shrishmoy Ray, Eric Mamajek, Brendan P.

Bowler, David Wilner, Jonathan Williams, Megan Ansdell, Mark Wyatt, Alexis Lau, Mark W. Phillips, Jorge Fernandez, Jonathan Gagné, Emma Bubb, Ben J. Sutcliffe, Thomas J. G. Wilson, Brenda Matthews, Henry Ngo, Danielle Piskorz, Justin R. Crepp, Erica Gonzalez, Andrew W. Mann, and Gregory Mace. Discovery of an Edge-on Circumstellar Debris Disk around BD+45° 598: A Newly Identified Member of the  $\beta$  Pictoris Moving Group. *ApJ*, 912(2):115, May 2021. doi: 10.3847/1538-4357/abec6e.

J. A. Högbom. Aperture Synthesis with a Non-Regular Distribution of Interferometer Baselines. *A&AS*, 15:417, June 1974.

W. S. Holland, D. Bintley, E. L. Chapin, A. Chrysostomou, G. R. Davis, J. T. Dempsey, W. D. Duncan, M. Fich, P. Friberg, M. Halpern, K. D. Irwin, T. Jenness, B. D. Kelly, M. J. MacIntosh, E. I. Robson, D. Scott, P. A. R. Ade, E. Atad-Ettdgui, D. S. Berry, S. C. Craig, X. Gao, A. G. Gibb, G. C. Hilton, M. I. Hollister, J. B. Kycia, D. W. Lunney, H. McGregor, D. Montgomery, W. Parkes, R. P. J. Tilanus, J. N. Ullom, C. A. Walther, A. J. Walton, A. L. Woodcraft, M. Amiri, D. Atkinson, B. Burger, T. Chuter, I. M. Coulson, W. B. Doriese, C. Dunare, F. Economou, M. D. Niemack, H. A. L. Parsons, C. D. Reintsema, B. Sibthorpe, I. Smail, R. Sudiwala, and H. S. Thomas. SCUBA-2: the 10 000 pixel bolometer camera on the James Clerk Maxwell Telescope. *MNRAS*, 430(4): 2513–2533, April 2013. doi: 10.1093/mnras/sts612.

Wayne Holland, Mark Booth, William Dent, Gaspard Duchene, Pamela Klaassen, Jean-Francois Lestrade, Jonathan Marshall, and Brenda Matthews. Debris disks: Exploring the environment and evolution of planetary systems. *Astro2020: Decadal Survey on Astronomy and Astrophysics*, 2020:80, May 2019.

Wayne S. Holland, Brenda C. Matthews, Grant M. Kennedy, Jane S. Greaves, Mark C. Wyatt, Mark Booth, Pierre Bastien, Geoff Bryden, Harold Butner, Christine H. Chen, Antonio Chrysostomou, Claire L. Davies, William R. F. Dent, James Di Francesco, Gaspard Duchêne, Andy G. Gibb, Per Friberg, Rob J. Ivison, Tim Jenness, JJ Kavelaars, Samantha Lawler, Jean-François Lestrade, Jonathan P. Marshall, Amaya Moro-Martin, Olja Panić, Neil Phillips, Stephen Serjeant, Gerald H. Schieven, Bruce Sibthorpe, Laura Vican, Derek Ward-Thompson, Paul van der Werf, Glenn J. White, David Wilner, and Ben Zuckerman. SONS: The JCMT legacy survey of debris discs in the submillimetre. *MNRAS*, 470(3):3606–3663, Sep 2017. doi: 10.1093/mnras/stx1378.

M. A. Hollands, B. T. Gänsicke, and D. Koester. Cool DZ white dwarfs II: compositions and evolution of old remnant planetary systems. *MNRAS*, 477(1):93–111, June 2018. doi: 10.1093/mnras/sty592.

- J. R. Houck, T. L. Roellig, J. van Cleve, W. J. Forrest, T. Herter, C. R. Lawrence, K. Matthews, H. J. Reitsema, B. T. Soifer, D. M. Watson, D. Weedman, M. Huisjen, J. Troeltzsch, D. J. Barry, J. Bernard-Salas, C. E. Blacken, B. R. Brandl, V. Charmandaris, D. Devost, G. E. Gull, P. Hall, C. P. Henderson, S. J. U. Higdon, B. E. Pirger, J. Schoenwald, G. C. Sloan, K. I. Uchida, P. N. Appleton, L. Armus, M. J. Burgdorf, S. B. Fajardo-Acosta, C. J. Grillmair, J. G. Ingalls, P. W. Morris, and H. I. Teplitz. The Infrared Spectrograph (IRS) on the Spitzer Space Telescope. *ApJS*, 154(1):18–24, September 2004. doi: 10.1086/423134.
- Ward S. Howard, Meredith A. MacGregor, Rachel Osten, Jan Forbrich, Steven R. Cranmer, Isaiah Tristan, Alycia J. Weinberger, Allison Youngblood, Thomas Barclay, R. O. Parke Loyd, Evgenya L. Shkolnik, Andrew Zic, and David J. Wilner. The Mouse that Squeaked: A small flare from Proxima Cen observed in the millimeter, optical, and soft X-ray with Chandra and ALMA. *arXiv e-prints*, art. arXiv:2209.05490, September 2022.
- Yau De (Ted) Huang, Oscar Morata, Patrick Michel Koch, Ciska Kemper, Yuh-Jing Hwang, Chau-Ching Chiong, Paul Ho, You-Hua Chu, Chi-Den Huang, Ching-Tang Liu, Fang-Chia Hsieh, Yen-Hsiang Tseng, Shou-Hsien Weng, Chin-Ting Ho, Po-Han Chiang, Hsiao-Ling Wu, Chih-Cheng Chang, Shou-Ting Jian, Chien-Feng Lee, Yi-Wei Lee, Satoru Iguchi, Shin’ichiro Asayama, Daisuke Iono, Alvaro Gonzalez, John Effland, Kamaljeet Saini, Marian Pospieszalski, Doug Henke, Keith Yeung, Ricardo Finger, Valeria Tapia, and Nicolas Reyes. The Atacama Large Millimeter/sub-millimeter Array band-1 receiver. In George Z. Angeli and Philippe Dierickx, editors, *Modeling, Systems Engineering, and Project Management for Astronomy VI*, volume 9911 of *Society of Photo-Optical Instrumentation Engineers (SPIE) Conference Series*, page 99111V, August 2016. doi: 10.1117/12.2232193.
- A. Meredith Hughes, Gaspard Duchene, and Brenda C. Matthews. Debris disks: Structure, composition, and variability. *Annual Review of Astronomy and Astrophysics*, 56(1):541–591, Sep 2018. ISSN 1545-4282. doi: 10.1146/annurev-astro-081817-052035. URL <http://dx.doi.org/10.1146/annurev-astro-081817-052035>.
- Satoru Iguchi, Koh-Ichiro Morita, Masahiro Sugimoto, Baltasar Vila Vilaró, Masao Saito, Tetsuo Hasegawa, Ryohei Kawabe, Ken’ichi Tatematsu, Seiichi Sakamoto, Hitoshi Kiuchi, Sachiko K. Okumura, George Kosugi, Junji Inatani, Shigehisa Takakuwa, Daisuke Iono, Takeshi Kamazaki, Ryusuke Ogasawara, and Masato Ishiguro. The Atacama Compact Array (ACA). *PASJ*, 61(1):1–12, February 2009. doi: 10.1093/pasj/61.1.1.
- Alan P. Jackson, Mark C. Wyatt, Amy Bonsor, and Dimitri Veras. Debris from giant impacts between planetary embryos at large orbital radii. *MNRAS*, 440(4):3757–3777, June 2014. doi: 10.1093/mnras/stu476.

- Markus Janson, Joseph C. Carson, David Lafrenière, David S. Spiegel, John R. Bent, and Palmer Wong. Infrared Non-detection of Fomalhaut b: Implications for the Planet Interpretation. *ApJ*, 747(2):116, March 2012. doi: 10.1088/0004-637X/747/2/116.
- D. Jewitt and J. Luu. Discovery of the candidate Kuiper belt object 1992 QB<sub>1</sub>. *Nature*, 362 (6422):730–732, April 1993. doi: 10.1038/362730a0.
- Lucie Jílková, Adrian S. Hamers, Michael Hammer, and Simon Portegies Zwart. Mass transfer between debris discs during close stellar encounters. *MNRAS*, 457(4):4218–4235, Apr 2016. doi: 10.1093/mnras/stw264.
- John Asher Johnson, Geoffrey W. Marcy, Debra A. Fischer, Jason T. Wright, Sabine Reffert, Julia M. Kregenow, Peter K. G. Williams, and Kathryn M. G. Peek. Retired A Stars and Their Companions. II. Jovian Planets Orbiting  $\kappa$  CrB and HD 167042. *ApJ*, 675(1): 784–789, March 2008. doi: 10.1086/526453.
- M. Jura. A Tidally Disrupted Asteroid around the White Dwarf G29-38. *ApJ*, 584(2): L91–L94, February 2003. doi: 10.1086/374036.
- Nathan A. Kaib, Ethan B. White, and André Izidoro. Simulations of the Fomalhaut system within its local galactic environment. *Monthly Notices of the Royal Astronomical Society*, 473(1):470–491, 09 2017. ISSN 0035-8711. doi: 10.1093/mnras/stx2456. URL <https://doi.org/10.1093/mnras/stx2456>.
- Paul Kalas, Michael C. Liu, and Brenda C. Matthews. Discovery of a Large Dust Disk Around the Nearby Star AU Microscopii. *Science*, 303(5666):1990–1992, March 2004. doi: 10.1126/science.1093420.
- Paul Kalas, James R. Graham, and Mark Clampin. A planetary system as the origin of structure in fomalhaut’s dust belt. *Nature*, 435(7045):1067, 2005.
- Paul Kalas, James R. Graham, Eugene Chiang, Michael P. Fitzgerald, Mark Clampin, Edwin S. Kite, Karl Stapelfeldt, Christian Marois, and John Krist. Optical images of an exosolar planet 25 light-years from earth. *Science*, 322(5906):1345–1348, 2008. ISSN 0036-8075. doi: 10.1126/science.1166609. URL <https://science.sciencemag.org/content/322/5906/1345>.
- Paul Kalas, James R. Graham, Michael P. Fitzgerald, and Mark Clampin. STIS CORONAGRAPHIC IMAGING OF FOMALHAUT: MAIN BELT STRUCTURE AND THE ORBIT OF FOMALHAUTb. *The Astrophysical Journal*, 775(1):56, sep 2013. doi: 10.1088/0004-637x/775/1/56. URL <https://doi.org/10.1088%2F0004-637x%2F775%2F1%2F56>.



- Paul G. Kalas, Abhijith Rajan, Jason J. Wang, Maxwell A. Millar-Blanchaer, Gaspard Duchene, Christine Chen, Michael P. Fitzgerald, Ruobing Dong, James R. Graham, Jennifer Patience, Bruce Macintosh, Ruth Murray-Clay, Brenda Matthews, Julien Rameau, Christian Marois, Jeffrey Chilcote, Robert J. De Rosa, René Doyon, Zachary H. Draper, Samantha Lawler, S. Mark Ammons, Pauline Arriaga, Joanna Bulger, Tara Cotten, Katherine B. Follette, Stephen Goodsell, Alexandra Greenbaum, Pascale Hibon, Sasha Hinkley, Li-Wei Hung, Patrick Ingraham, Quinn Konapacky, David Lafreniere, James E. Larkin, Douglas Long, Jérôme Maire, Franck Marchis, Stan Metchev, Katie M. Morzinski, Eric L. Nielsen, Rebecca Oppenheimer, Marshall D. Perrin, Laurent Pueyo, Fredrik T. Rantakyö, Jean-Baptiste Ruffio, Leslie Saddlemyer, Dmitry Savransky, Adam C. Schneider, Anand Sivaramakrishnan, Rémi Soummer, Inseok Song, Sandrine Thomas, Gautam Vasisht, Kimberly Ward-Duong, Sloane J. Wiktorowicz, and Schuyler G. Wolff. Direct Imaging of an Asymmetric Debris Disk in the HD 106906 Planetary System. *ApJ*, 814(1):32, November 2015. doi: 10.1088/0004-637X/814/1/32.
- Markus Kasper, Dániel Apai, Kevin Wagner, and Massimo Robberto. Discovery of an Edge-on Debris Disk with a Dust Ring and an Outer Disk Wing-tilt Asymmetry. *ApJ*, 812(2):L33, October 2015. doi: 10.1088/2041-8205/812/2/L33.
- Robert E. Kass and Adrian E. Raftery. Bayes factors. *Journal of the American Statistical Association*, 90(430):773–795, 1995. doi: 10.1080/01621459.1995.10476572. URL <https://www.tandfonline.com/doi/abs/10.1080/01621459.1995.10476572>.
- J. H. Kastner, G. G. Sacco, R. Montez, D. P. Huenemoerder, H. Shi, E. Alecian, C. Argiroffi, M. Audard, J. Bouvier, F. Damiani, J. F. Donati, S. G. Gregory, M. Güdel, G. A. J. Hussain, A. Maggio, and T. Montmerle. GSC 07396-00759 = V4046 Sgr C[D]: A Wide-separation Companion to the Close T Tauri Binary System V4046 Sgr AB. *ApJ*, 740(1):L17, October 2011. doi: 10.1088/2041-8205/740/1/L17.
- Joel H. Kastner, C. Qi, D. A. Dickson-Vandervelde, P. Hily-Blant, T. Forveille, S. Andrews, U. Gorti, K. Öberg, and D. Wilner. A Subarcsecond ALMA Molecular Line Imaging Survey of the Circumbinary, Protoplanetary Disk Orbiting V4046 Sgr. *ApJ*, 863(1):106, August 2018. doi: 10.3847/1538-4357/aacff7.
- G. M. Kennedy and M. C. Wyatt. Collisional evolution of irregular satellite swarms: detectable dust around solar system and extrasolar planets. *Monthly Notices of the Royal Astronomical Society*, 412(4):2137–2153, Feb 2011. ISSN 0035-8711. doi: 10.1111/j.1365-2966.2010.18041.x. URL <http://dx.doi.org/10.1111/j.1365-2966.2010.18041.x>.

- G. M. Kennedy and M. C. Wyatt. Do two-temperature debris discs have multiple belts? *MNRAS*, 444(4):3164–3182, November 2014. doi: 10.1093/mnras/stu1665.
- G. M. Kennedy, M. C. Wyatt, P. Kalas, G. Duchene, B. Sibthorpe, J.-F. Lestrade, B. C. Matthews, and J. Greaves. Discovery of the Fomalhaut C debris disc. *Monthly Notices of the Royal Astronomical Society: Letters*, 438(1):L96–L100, 12 2013. ISSN 1745-3925. doi: 10.1093/mnrasl/slt168. URL <https://doi.org/10.1093/mnrasl/slt168>.
- G M Kennedy, G Bryden, D Ardila, C Eiroa, J-F Lestrade, J P Marshall, B C Matthews, A Moro-Martin, and M C Wyatt. Kuiper belt analogues in nearby m-type planet-host systems. *Monthly Notices of the Royal Astronomical Society*, 476(4):4584–4591, Feb 2018a. ISSN 1365-2966. doi: 10.1093/mnras/sty492. URL <http://dx.doi.org/10.1093/mnras/sty492>.
- Grant M. Kennedy. The unexpected narrowness of eccentric debris rings: a sign of eccentricity during the protoplanetary disc phase. *Royal Society Open Science*, 7(6):200063, June 2020. doi: 10.1098/rsos.200063.
- Grant M Kennedy, Sebastian Marino, Luca Matrà, Olja Panić, David Wilner, Mark C Wyatt, and Ben Yelverton. Alma observations of the narrow hr 4796a debris ring. *Monthly Notices of the Royal Astronomical Society*, 475(4):4924–4938, Jan 2018b. ISSN 1365-2966. doi: 10.1093/mnras/sty135. URL <http://dx.doi.org/10.1093/mnras/sty135>.
- Matthew A. Kenworthy, Tiffany Meshkat, Sascha P. Quanz, Julien H. Girard, Michael R. Meyer, and Markus Kasper. Coronagraphic observations of fomalhaut at solar system scales. *The Astrophysical Journal*, 764(1):7, Jan 2013. ISSN 1538-4357. doi: 10.1088/0004-637x/764/1/7. URL <http://dx.doi.org/10.1088/0004-637x/764/1/7>.
- Scott J. Kenyon and Benjamin C. Bromley. Gravitational Stirring in Planetary Debris Disks. *AJ*, 121(1):538–551, January 2001. doi: 10.1086/318019.
- Scott J. Kenyon and Benjamin C. Bromley. Collisional cascades in planetesimal disks. i. stellar flybys. *The Astronomical Journal*, 123(3):1757–1775, Mar 2002. ISSN 1538-3881. doi: 10.1086/338850. URL <http://dx.doi.org/10.1086/338850>.
- Scott J. Kenyon and Benjamin C. Bromley. Detecting the Dusty Debris of Terrestrial Planet Formation. *ApJ*, 602(2):L133–L136, February 2004a. doi: 10.1086/382693.
- Scott J. Kenyon and Benjamin C. Bromley. The Size Distribution of Kuiper Belt Objects. *AJ*, 128(4):1916–1926, October 2004b. doi: 10.1086/423697.
- Scott J. Kenyon and Benjamin C. Bromley. Prospects for Detection of Catastrophic Collisions in Debris Disks. *AJ*, 130(1):269–279, July 2005. doi: 10.1086/430461.

- Scott J. Kenyon and Benjamin C. Bromley. Terrestrial Planet Formation. I. The Transition from Oligarchic Growth to Chaotic Growth. *AJ*, 131(3):1837–1850, March 2006. doi: 10.1086/499807.
- Scott J. Kenyon and Benjamin C. Bromley. Variations on Debris Disks: Icy Planet Formation at 30-150 AU for 1-3  $M_{\odot}$  Main-Sequence Stars. *ApJS*, 179(2):451–483, December 2008. doi: 10.1086/591794.
- Scott J. Kenyon, Thayne Currie, and Benjamin C. Bromley. Fomalhaut b as a cloud of dust: Testing aspects of planet formation theory. *The Astrophysical Journal*, 786(1):70, Apr 2014. ISSN 1538-4357. doi: 10.1088/0004-637x/786/1/70. URL <http://dx.doi.org/10.1088/0004-637X/786/1/70>.
- Pierre Kervella, Frédéric Arenou, François Mignard, and Frédéric Thévenin. Stellar and substellar companions of nearby stars from Gaia DR2. Binarity from proper motion anomaly. *A&A*, 623:A72, March 2019. doi: 10.1051/0004-6361/201834371.
- Hubert Klahr and DNC Lin. Dust distribution in gas disks. ii. self-induced ring formation through a clumping instability. *The Astrophysical Journal*, 632(2):1113, 2005.
- H. Kobayashi, H. Kimura, S. i. Watanabe, T. Yamamoto, and S. Müller. Sublimation temperature of circumstellar dust particles and its importance for dust ring formation. *Earth, Planets and Space*, 63(10):1067–1075, October 2011. doi: 10.5047/eps.2011.03.012.
- Hiroshi Kobayashi, Sei-ichiro Watanabe, Hiroshi Kimura, and Tetsuo Yamamoto. Dust ring formation due to ice sublimation of radially drifting dust particles under the Poynting Robertson effect in debris disks. *Icarus*, 195(2):871–881, June 2008. doi: 10.1016/j.icarus.2008.02.005.
- Hiroshi Kobayashi, Sei-ichiro Watanabe, Hiroshi Kimura, and Tetsuo Yamamoto. Dust ring formation due to sublimation of dust grains drifting radially inward by the Poynting-Robertson drag: An analytical model. *Icarus*, 201(1):395–405, May 2009. doi: 10.1016/j.icarus.2009.01.002.
- D. W. Koerner, S. Kim, D. E. Trilling, H. Larson, A. Coter, K. R. Stapelfeldt, Z. Wahhaj, S. Fajardo-Acosta, D. Padgett, and D. Backman. New Debris Disk Candidates Around 49 Nearby Stars. *ApJ*, 710(1):L26–L29, February 2010. doi: 10.1088/2041-8205/710/1/L26.
- Ágnes Kóspál, David R. Ardila, Attila Moór, and Péter Ábrahám. On the Relationship Between Debris Disks and Planets. *ApJ*, 700(2):L73–L77, August 2009. doi: 10.1088/0004-637X/700/2/L73.

- Q. Kral, P. Thébault, J. C. Augereau, A. Boccaletti, and S. Charnoz. Signatures of massive collisions in debris discs. A self-consistent numerical model. *A&A*, 573:A39, January 2015. doi: 10.1051/0004-6361/201424309.
- Q. Kral, M. Wyatt, R. F. Carswell, J. E. Pringle, L. Matrà, and A. Juhász. A self-consistent model for the evolution of the gas produced in the debris disc of  $\beta$  Pictoris. *MNRAS*, 461(1):845–858, September 2016. doi: 10.1093/mnras/stw1361.
- Quentin Kral, Sebastian Marino, Mark C. Wyatt, Mihkel Kama, and Luca Matrà. Imaging [CI] around HD 131835: reinterpreting young debris discs with protoplanetary disc levels of CO gas as shielded secondary discs. *MNRAS*, 489(4):3670–3691, November 2019. doi: 10.1093/mnras/sty2923.
- John E. Krist, Karl R. Stapelfeldt, Geoffrey Bryden, George H. Rieke, K. Y. L. Su, Christine H. Chen, Charles A. Beichman, Dean C. Hines, Luisa M. Rebull, Angelle Tanner, David E. Trilling, Mark Clampin, and András Gáspár. HST and Spitzer Observations of the HD 207129 Debris Ring. *AJ*, 140(4):1051–1061, Oct 2010. doi: 10.1088/0004-6256/140/4/1051.
- A. V. Krivov, T. Löhne, and M. Sremčević. Dust distributions in debris disks: effects of gravity, radiation pressure and collisions. *A&A*, 455(2):509–519, August 2006. doi: 10.1051/0004-6361:20064907.
- Alexander V. Krivov and Mark Booth. Self-stirring of debris discs by planetesimals formed by pebble concentration. *MNRAS*, 479(3):3300–3307, September 2018. doi: 10.1093/mnras/sty1607.
- Alexander V. Krivov and Mark C. Wyatt. Solution to the debris disc mass problem: planetesimals are born small? *MNRAS*, 500(1):718–735, January 2021. doi: 10.1093/mnras/staa2385.
- Alexander V. Krivov, Sebastian Müller, Torsten Löhne, and Harald Mutschke. Collisional and Thermal Emission Models of Debris Disks: Toward Planetesimal Population Properties. *ApJ*, 687(1):608–622, Nov 2008. doi: 10.1086/591507.
- A. M. Lagrange, M. Kasper, A. Boccaletti, G. Chauvin, D. Gratadour, T. Fusco, D. Ehrenreich, D. Apai, D. Mouillet, and D. Rouan. Constraining the orbit of the possible companion to  $\beta$  Pictoris. New deep imaging observations. *A&A*, 506(2):927–934, November 2009. doi: 10.1051/0004-6361/200912098.

- G. Laibe, J. F. Gonzalez, and S. T. Maddison. Revisiting the “radial-drift barrier” of planet formation and its relevance in observed protoplanetary discs. *A&A*, 537:A61, January 2012. doi: 10.1051/0004-6361/201015349.
- Ari Laor and Bruce T. Draine. Spectroscopic Constraints on the Properties of Dust in Active Galactic Nuclei. *ApJ*, 402:441, January 1993. doi: 10.1086/172149.
- S. M. Lawler, S. Greenstreet, and B. Gladman. Fomalhaut b as a dust cloud: Frequent collisions within the fomalhaut disk. *The Astrophysical Journal*, 802(2):L20, Apr 2015. ISSN 2041-8213. doi: 10.1088/2041-8205/802/2/L20. URL <http://dx.doi.org/10.1088/2041-8205/802/2/L20>.
- Léna Le Roy, Kathrin Altwegg, Hans Balsiger, Jean-Jacques Berthelier, Andre Bieler, Christelle Briois, Ursina Calmonte, Michael R. Combi, Johan De Keyser, Frederik Dhooghe, Björn Fiethe, Stephen A. Fuselier, Sébastien Gasc, Tamas I. Gombosi, Myrtha Hässig, Annette Jäckel, Martin Rubin, and Chia-Yu Tzou. Inventory of the volatiles on comet 67P/Churyumov-Gerasimenko from Rosetta/ROSINA. *A&A*, 583:A1, November 2015. doi: 10.1051/0004-6361/201526450.
- Glenn Ledrew. The Real Starry Sky. *J. R. Astron. Soc. Canada*, 95:32, February 2001.
- Eve J. Lee and Eugene Chiang. A Primer on Unifying Debris Disk Morphologies. *ApJ*, 827(2):125, August 2016. doi: 10.3847/0004-637X/827/2/125.
- D. Leisawitz, E. Amatuucci, R. Carter, M. DiPirro, A. Flores, J. Staguhn, C. Wu, L. Allen, J. Arenberg, L. Armus, C. Battersby, J. Bauer, R. Bell, P. Beltran, D. Benford, E. Bergin, C. M. Bradford, D. Bradley, D. Burgarella, S. Carey, D. Chi, A. Cooray, J. Corsetti, E. De Beck, K. Denis, L. Dewell, M. East, S. Edgington, K. Ennico, L. Fantano, G. Feller, D. Folta, J. Fortney, J. Generie, M. Gerin, Z. Granger, G. Harpole, K. Harvey, F. Helmich, L. Hilliard, J. Howard, M. Jacoby, A. Jamil, T. Kataria, S. Knight, P. Knollenberg, P. Lightsey, S. Lipsky, E. Mamajek, G. Martins, M. Meixner, G. Melnick, S. Milam, T. Mooney, S. H. Moseley, D. Narayanan, S. Neff, T. Nguyen, A. Nordt, J. Olson, D. Padgett, M. Petach, S. Petro, J. Pohner, K. Pontoppidan, A. Pope, D. Ramsbacher, T. Roellig, I. Sakon, C. Sandin, K. Sandstrom, D. Scott, K. Sheth, J. Steeves, K. Stevenson, L. Stokowski, E. Stoneking, K. Su, K. Tajdaran, S. Tompkins, J. Vieira, C. Webster, M. Wiedner, E. L. Wright, and J. Zmuidzinas. The Origins Space Telescope: mission concept overview. In Makenzie Lystrup, Howard A. MacEwen, Giovanni G. Fazio, Natalie Batalha, Nicholas Siegler, and Edward C. Tong, editors, *Space Telescopes and Instrumentation 2018: Optical, Infrared, and Millimeter Wave*, volume 10698 of *Society of Photo-Optical Instrumentation Engineers (SPIE) Conference Series*, page 1069815, July 2018. doi: 10.1117/12.2313823.

David Leisawitz, Charles Baker, Amy Barger, Dominic Benford, Andrew Blain, Rob Boyle, Richard Broderick, Jason Budinoff, John Carpenter, Richard Caverly, Phil Chen, Steve Cooley, Christine Cottingham, Julie Crooke, Dave DiPietro, Mike DiPirro, Michael Femiano, Art Ferrer, Jacqueline Fischer, Jonathan P. Gardner, Lou Hallock, Kenny Harris, Kate Hartman, Martin Harwit, Lynne Hillenbrand, Tupper Hyde, Drew Jones, Jim Kellogg, Alan Kogut, Marc Kuchner, Bill Lawson, Javier Lecha, Maria Lecha, Amy Mainzer, Jim Mannion, Anthony Martino, Paul Mason, John Mather, Gibran McDonald, Rick Mills, Lee Mundy, Stan Ollendorf, Joe Pellicciotti, Dave Quinn, Kirk Rhee, Stephen Rinehart, Tim Sauerwine, Robert Silverberg, Terry Smith, Gordon Stacey, H. Philip Stahl, Johannes Staguhn, Steve Tompkins, June Tveekrem, Sheila Wall, and Mark Wilson. The space infrared interferometric telescope (SPIRIT): High-resolution imaging and spectroscopy in the far-infrared. *Advances in Space Research*, 40(5):689–703, January 2007. doi: 10.1016/j.asr.2007.05.081.

David Leisawitz, Edward Amatucci, Lynn Allen, Jonathan Arenberg, Lee Armus, Cara Battersby, James Bauer, Bobby G. Beaman, Ray Bell, Porfirio Beltran, Dominic Benford, Edward Bergin, Jeffrey Bolognese, Charles M. Bradford, Damon Bradley, Denis Burgarella, Sean Carey, Ruth Carter, J. D. (Danny) Chi, Asantha Cooray, James Corsetti, Thomas D’Asto, Elvire De Beck, Kevin Denis, Christopher Derkacz, Larry Dewell, Michael DiPirro, Cleland P. Earle, Matthew East, Samantha Edgington, Kimberly Ennico, Louis Fantano, Greg Feller, David Folta, Jonathan Fortney, Benjamin J. Gavares, Joseph Generie, Maryvonne Gerin, Zachary Granger, Thomas P. Greene, Alex Griffiths, George Harpole, Keith Harvey, Frank Helmich, Lawrence Hilliard, Joseph Howard, Michael Jacoby, Anisa Jamil, Tracee Jamison, Lisa Kaltenegger, Tiffany Kataria, John S. Knight, Perry Knollenberg, Charles Lawrence, Paul Lightsey, Sarah Lipsy, Eric Mamajek, Gregory Martins, John C. Mather, Margaret Meixner, Gary Melnick, Stefanie Milam, Ted Mooney, Samuel H. Moseley, Desika Narayanan, Susan Neff, Thanh Nguyen, Alison Nordt, Jeffrey Olson, Deborah Padgett, Michael Petach, Susanna Petro, John Pohner, Klaus Pontoppidan, Alexandra Pope, Daniel Ramspacker, Alison Rao, Thomas Roellig, Itsuki Sakon, Carly Sandin, Karin Sandstrom, Douglas Scott, Len Seals, Kartik Sheth, Lawrence M. Sokolsky, Johannes Staguhn, John Steeves, Kevin Stevenson, Eric Stoneking, Kate Su, Kiarash Tajdaran, Steven Tompkins, Joaquin Vieira, Cassandra Webster, Martina C. Wiedner, Edward L. Wright, Chi Wu, and Jonas Zmuidzinas. Origins Space Telescope: baseline mission concept. *Journal of Astronomical Telescopes, Instruments, and Systems*, 7:011002, January 2021. doi: 10.1117/1.JATIS.7.1.011002.

Sébastien Lépine and Michal Simon. Nearby Young Stars Selected by Proper Motion. I.

Four New Members of the  $\beta$  Pictoris Moving Group From The Tycho-2 Catalog. *AJ*, 137 (3):3632–3645, March 2009. doi: 10.1088/0004-6256/137/3/3632.

J. F. Lestrade, E. Morey, A. Lassus, and N. Phou. Stripping a debris disk by close stellar encounters in an open stellar cluster. *A&A*, 532:A120, Aug 2011. doi: 10.1051/0004-6361/201014730.

J.-F. Lestrade, B. C. Matthews, B. Sibthorpe, G. M. Kennedy, M. C. Wyatt, G. Bryden, J. S. Greaves, E. Thilliez, A. Moro-Martín, M. Booth, and et al. A debris disk around the planet hosting m-star gj 581 spatially resolved with herschel. *Astronomy & Astrophysics*, 548:A86, Nov 2012. ISSN 1432-0746. doi: 10.1051/0004-6361/201220325. URL <http://dx.doi.org/10.1051/0004-6361/201220325>.

A. Li and J. M. Greenberg. A unified model of interstellar dust. *A&A*, 323:566–584, July 1997.

Aigen Li and J. Mayo Greenberg. A comet dust model for the beta Pictoris disk. *A&A*, 331: 291–313, March 1998.

Jeremy Lim and Stephen M. White. Limits to Mass Outflows from Late-Type Dwarf Stars. *ApJ*, 462:L91, May 1996. doi: 10.1086/310038.

L. Lindegren, J. Hernández, A. Bombrun, S. Klioner, U. Bastian, M. Ramos-Lerate, A. de Torres, H. Steidelmüller, C. Stephenson, D. Hobbs, U. Lammers, M. Biermann, R. Geyer, T. Hilger, D. Michalik, U. Stampá, P. J. McMillan, J. Castañeda, M. Clotet, G. Comoretto, M. Davidson, C. Fabricius, G. Gracia, N. C. Hambly, A. Hutton, A. Mora, J. Portell, F. van Leeuwen, U. Abbas, A. Abreu, M. Altmann, A. Andrei, E. Anglada, L. Balaguer-Núñez, C. Barache, U. Becciani, S. Bertone, L. Bianchi, S. Bouquillon, G. Bourda, T. Brüsemeister, B. Bucciarelli, D. Busonero, R. Buzzi, R. Cancelliere, T. Carlucci, P. Charlot, N. Cheek, M. Crosta, C. Crowley, J. de Bruijne, F. de Felice, R. Drimmel, P. Esquej, A. Fienga, E. Fraile, M. Gai, N. Garralda, J. J. González-Vidal, R. Guerra, M. Hauser, W. Hofmann, B. Holl, S. Jordan, M. G. Lattanzi, H. Lenhardt, S. Liao, E. Licata, T. Lister, W. Löffler, J. Marchant, J. M. Martin-Fleitas, R. Messineo, F. Mignard, R. Morbidelli, E. Poggio, A. Riva, N. Rowell, E. Salguero, M. Sarasso, E. Sciacca, H. Siddiqui, R. L. Smart, A. Spagna, I. Steele, F. Taris, J. Torra, A. van Elteren, W. van Reeve, and A. Vecchiato. Gaia Data Release 2. The astrometric solution. *A&A*, 616:A2, August 2018. doi: 10.1051/0004-6361/201832727.

T. Löhne, J. C. Augereau, S. Ertel, J. P. Marshall, C. Eiroa, A. Mora, O. Absil, K. Stapelfeldt, P. Thébault, A. Bayo, C. Del Burgo, W. Danchi, A. V. Krivov, J. Lebreton, G. Letawe, P. Magain, J. Maldonado, B. Montesinos, G. L. Pilbratt, G. J. White, and S. Wolf.

Modelling the huge, Herschel-resolved debris ring around HD 207129. *A&A*, 537:A110, January 2012. doi: 10.1051/0004-6361/201117731.

Torsten Löhne, Alexander V. Krivov, and Jens Rodmann. Long-Term Collisional Evolution of Debris Disks. *ApJ*, 673(2):1123–1137, February 2008. doi: 10.1086/524840.

Patricia Luppe, Alexander V. Krivov, Mark Booth, and Jean-François Lestrade. Observability of dusty debris discs around M-stars. *MNRAS*, 499(3):3932–3942, December 2020. doi: 10.1093/mnras/staa2608.

W. Lyra and M. Kuchner. Formation of sharp eccentric rings in debris disks with gas but without planets. *Nature*, 499(7457):184–187, Jul 2013. ISSN 1476-4687. doi: 10.1038/nature12281. URL <http://dx.doi.org/10.1038/nature12281>.

A. Meredith MacGregor, Rachel A. Osten, and A. Meredith Hughes. Properties of M Dwarf Flares at Millimeter Wavelengths. *ApJ*, 891(1):80, March 2020. doi: 10.3847/1538-4357/ab711d.

Meredith A. MacGregor, David J. Wilner, Katherine A. Rosenfeld, Sean M. Andrews, Brenda Matthews, A. Meredith Hughes, Mark Booth, Eugene Chiang, James R. Graham, Paul Kalas, Grant Kennedy, and Bruce Sibthorpe. Millimeter Emission Structure in the First ALMA Image of the AU Mic Debris Disk. *ApJ*, 762(2):L21, January 2013. doi: 10.1088/2041-8205/762/2/L21.

Meredith A. MacGregor, David J. Wilner, Claire Chandler, Luca Ricci, Sarah T. Maddison, Steven R. Cranmer, Sean M. Andrews, A. Meredith Hughes, and Amy Steele. Constraints on Planetesimal Collision Models in Debris Disks. *ApJ*, 823(2):79, June 2016. doi: 10.3847/0004-637X/823/2/79.

Meredith A. MacGregor, Luca Matrà, Paul Kalas, David J. Wilner, Margaret Pan, Grant M. Kennedy, Mark C. Wyatt, Gaspard Duchene, A. Meredith Hughes, George H. Rieke, Mark Clampin, Michael P. Fitzgerald, James R. Graham, Wayne S. Holland, Olja Panić, Andrew Shannon, and Kate Su. A complete ALMA map of the fomalhaut debris disk. *The Astrophysical Journal*, 842(1):8, jun 2017. doi: 10.3847/1538-4357/aa71ae. URL <https://doi.org/10.3847/1538-4357/aa71ae>.

Meredith A. MacGregor, Alycia J. Weinberger, A. Meredith Hughes, D. J. Wilner, Thayne Currie, John H. Debes, Jessica K. Donaldson, Seth Redfield, Aki Roberge, and Glenn Schneider. ALMA Detection of Extended Millimeter Halos in the HD 32297 and HD 61005 Debris Disks. *ApJ*, 869(1):75, December 2018a. doi: 10.3847/1538-4357/aaec71.



- Meredith A. MacGregor, Alycia J. Weinberger, David J. Wilner, Adam F. Kowalski, and Steven R. Cranmer. Detection of a Millimeter Flare from Proxima Centauri. *ApJ*, 855 (1):L2, March 2018b. doi: 10.3847/2041-8213/aaad6b.
- Meredith A. MacGregor, Alycia J. Weinberger, R. O. Parke Loyd, Evgenya Shkolnik, Thomas Barclay, Ward S. Howard, Andrew Zic, Rachel A. Osten, Steven R. Cranmer, Adam F. Kowalski, Emil Lenc, Allison Youngblood, Anna Estes, David J. Wilner, Jan Forbrich, Anna Hughes, Nicholas M. Law, Tara Murphy, Aaron Boley, and Jaymie Matthews. Discovery of an Extremely Short Duration Flare from Proxima Centauri Using Millimeter through Far-ultraviolet Observations. *ApJ*, 911(2):L25, April 2021. doi: 10.3847/2041-8213/abf14c.
- Meredith A. MacGregor, Spencer A. Hurt, Christopher C. Stark, Ward S. Howard, Alycia J. Weinberger, Bin Ren, Glenn Schneider, Elodie Choquet, and Dmitri Mawet. ALMA Images the Eccentric HD 53143 Debris Disk. *ApJ*, 933(1):L1, July 2022. doi: 10.3847/2041-8213/ac7729.
- Bruce A. Macintosh, James R. Graham, David W. Palmer, René Doyon, Jennifer Dunn, Donald T. Gavel, James Larkin, Ben Oppenheimer, Les Saddlemyer, Anand Sivaramakrishnan, J. Kent Wallace, Brian Bauman, Darren A. Erickson, Christian Marois, Lisa A. Poyneer, and Remi Soummer. The Gemini Planet Imager: from science to design to construction. In Norbert Hubin, Claire E. Max, and Peter L. Wizinowich, editors, *Adaptive Optics Systems*, volume 7015 of *Society of Photo-Optical Instrumentation Engineers (SPIE) Conference Series*, page 701518, July 2008. doi: 10.1117/12.788083.
- A. Mainzer, J. Bauer, T. Grav, J. Masiero, R. M. Cutri, J. Dailey, P. Eisenhardt, R. S. McMillan, E. Wright, R. Walker, R. Jedicke, T. Spahr, D. Tholen, R. Alles, R. Beck, H. Brandenburg, T. Conrow, T. Evans, J. Fowler, T. Jarrett, K. Marsh, F. Masci, H. McCallon, S. Wheelock, M. Wittman, P. Wyatt, E. DeBaun, G. Elliott, D. Elsbury, IV Gautier, T., S. Gomillion, D. Leisawitz, C. Maleszewski, M. Micheli, and A. Wilkins. Preliminary Results from NEOWISE: An Enhancement to the Wide-field Infrared Survey Explorer for Solar System Science. *ApJ*, 731(1):53, April 2011. doi: 10.1088/0004-637X/731/1/53.
- A. Mainzer, J. Bauer, R. M. Cutri, T. Grav, J. Masiero, R. Beck, P. Clarkson, T. Conrow, J. Dailey, P. Eisenhardt, B. Fabinsky, S. Fajardo-Acosta, J. Fowler, C. Gelino, C. Grillmair, I. Heinrichsen, M. Kendall, J. Davy Kirkpatrick, F. Liu, F. Masci, H. McCallon, C. R. Nugent, M. Papin, E. Rice, D. Royer, T. Ryan, P. Sevilla, S. Sonnett, R. Stevenson, D. B. Thompson, S. Wheelock, D. Wiemer, M. Wittman, E. Wright, and L. Yan. Initial Performance of the NEOWISE Reactivation Mission. *ApJ*, 792(1):30, September 2014. doi: 10.1088/0004-637X/792/1/30.

- Renu Malhotra. Resonant Kuiper belt objects: a review. *Geoscience Letters*, 6(1):12, December 2019. doi: 10.1186/s40562-019-0142-2.
- O. Yu. Malkov, V. S. Tamazian, J. A. Docobo, and D. A. Chulkov. Dynamical masses of a selected sample of orbital binaries. *A&A*, 546:A69, October 2012. doi: 10.1051/0004-6361/201219774.
- Lison Malo, René Doyon, David Lafrenière, Étienne Artigau, Jonathan Gagné, Frédérique Baron, and Adric Riedel. Bayesian Analysis to Identify New Star Candidates in Nearby Young Stellar Kinematic Groups. *ApJ*, 762(2):88, January 2013. doi: 10.1088/0004-637X/762/2/88.
- Lison Malo, Étienne Artigau, René Doyon, David Lafrenière, Loïc Albert, and Jonathan Gagné. BANYAN. III. Radial Velocity, Rotation, and X-Ray Emission of Low-mass Star Candidates in Nearby Young Kinematic Groups. *ApJ*, 788(1):81, June 2014. doi: 10.1088/0004-637X/788/1/81.
- Eric E. Mamajek, Jennifer L. Bartlett, Andreas Seifahrt, Todd J. Henry, Sergio B. Dieterich, John C. Lurie, Matthew A. Kenworthy, Wei-Chun Jao, Adric R. Riedel, John P. Subasavage, Jennifer G. Winters, Charlie T. Finch, Philip A. Ianna, and Jacob Bean. THE SOLAR NEIGHBORHOOD. XXX. FOMALHAUT c. *The Astrophysical Journal*, 146(6):154, nov 2013. doi: 10.1088/0004-6256/146/6/154. URL <https://doi.org/10.1088/0004-6256/146/6/154>.
- H. L. Maness, P. Kalas, K. M. G. Peek, E. I. Chiang, K. Scherer, M. P. Fitzgerald, James R. Graham, D. C. Hines, G. Schneider, and S. A. Metchev. Hubble Space Telescope Optical Imaging of the Eroding Debris Disk HD 61005. *ApJ*, 707(2):1098–1114, December 2009. doi: 10.1088/0004-637X/707/2/1098.
- Christopher J. Manser, Erik Dennihy, Boris T. Gänsicke, John H. Debes, Nicola P. Gentile Fusillo, J. J. Hermes, Mark Hollands, Paula Izquierdo, B. C. Kaiser, T. R. Marsh, Joshua S. Reding, Pablo Rodríguez-Gil, Dimitri Veras, and David J. Wilson. Velocity-imaging the rapidly precessing planetary disc around the white dwarf HE 1349-2305 using Doppler tomography. *MNRAS*, 508(4):5657–5670, December 2021. doi: 10.1093/mnras/stab2948.
- U. Marboeuf, A. Bonsor, and J. C. Augereau. Extrasolar comets: The origin of dust in exozodiacal disks? *Planet. Space Sci.*, 133:47–62, November 2016. doi: 10.1016/j.pss.2016.03.014.
- S. Marino, L. Matrà, C. Stark, M. C. Wyatt, S. Casassus, G. Kennedy, D. Rodriguez, B. Zuckerman, S. Perez, W. R. F. Dent, M. Kuchner, A. M. Hughes, G. Schneider,

- A. Steele, A. Roberge, J. Donaldson, and E. Nesvold. Exocometary gas in the HD 181327 debris ring. *MNRAS*, 460(3):2933–2944, August 2016. doi: 10.1093/mnras/stw1216.
- Sebastian Marino. Constraining planetesimal stirring: how sharp are debris disc edges? *MNRAS*, 503(4):5100–5114, May 2021. doi: 10.1093/mnras/stab771.
- C. Marois, D. Lafrenière, R. Doyon, B. Macintosh, and D. Nadeau. Angular Differential Imaging: A Powerful High-Contrast Imaging Technique. *ApJ*, 641:556–564, April 2006. doi: 10.1086/500401.
- Christian Marois, Bruce Macintosh, Travis Barman, B. Zuckerman, Inseok Song, Jennifer Patience, David Lafrenière, and René Doyon. Direct Imaging of Multiple Planets Orbiting the Star HR 8799. *Science*, 322(5906):1348, November 2008. doi: 10.1126/science.1166585.
- Christian Marois, B. Zuckerman, Quinn M. Konopacky, Bruce Macintosh, and Travis Barman. Images of a fourth planet orbiting HR 8799. *Nature*, 468(7327):1080–1083, December 2010. doi: 10.1038/nature09684.
- K. A. Marsh, T. Velusamy, C. D. Dowell, K. Grogan, and C. A. Beichman. Image of Fomalhaut Dust Ring at 350 Microns: The Relative Column Density Map Shows Pericenter-Apocenter Asymmetry. *ApJ*, 620(1):L47–L50, February 2005. doi: 10.1086/428401.
- J. P. Marshall, J. Milli, É. Choquet, C. del Burgo, G. M. Kennedy, L. Matrà, S. Ertel, and A. Boccaletti. Comprehensive Analysis of HD 105, A Young Solar System Analog. *ApJ*, 869(1):10, Dec 2018. doi: 10.3847/1538-4357/aaec6a.
- Rafael Martinez-Brunner, Simon Casassus, Sebastián Pérez, Antonio Hales, Philipp Weber, Miguel Cárcamo, Carla Arce-Tord, Lucas Cieza, Antonio Garufi, Sebastián Marino, and Alice Zurlo. High-resolution ALMA observations of V4046 Sgr: a circumbinary disc with a thin ring. *MNRAS*, 510(1):1248–1257, February 2022. doi: 10.1093/mnras/stab3440.
- L. Matrà, O. Panić, M. C. Wyatt, and W. R. F. Dent. CO mass upper limits in the Fomalhaut ring – the importance of NLTE excitation in debris discs and future prospects with ALMA. *Monthly Notices of the Royal Astronomical Society*, 447(4):3936–3947, 01 2015. ISSN 0035-8711. doi: 10.1093/mnras/stu2619. URL <https://doi.org/10.1093/mnras/stu2619>.
- L. Matrà, M. A. MacGregor, P. Kalas, M. C. Wyatt, G. M. Kennedy, D. J. Wilner, G. Duchene, A. M. Hughes, M. Pan, A. Shannon, M. Clampin, M. P. Fitzgerald, J. R. Graham, W. S. Holland, O. Panić, and K. Y. L. Su. Detection of exocometary CO within the 440 myr old fomalhaut belt: A similar CO+CO<sub>2</sub> ice abundance in exocomets and solar system comets.

*The Astrophysical Journal*, 842(1):9, jun 2017. doi: 10.3847/1538-4357/aa71b4. URL <https://doi.org/10.3847/1538-4357/aa71b4>.

- L. Matrà, S. Marino, G. M. Kennedy, M. C. Wyatt, K. I. Öberg, and D. J. Wilner. An Empirical Planetesimal Belt Radius-Stellar Luminosity Relation. *ApJ*, 859(1):72, May 2018. doi: 10.3847/1538-4357/aabcc4.
- L. Matrà, K. I. Öberg, D. J. Wilner, J. Olofsson, and A. Bayo. On the Ubiquity and Stellar Luminosity Dependence of Exocometary CO Gas: Detection around M Dwarf TWA 7. *AJ*, 157(3):117, March 2019a. doi: 10.3847/1538-3881/aaff5b.
- L. Matrà, M. C. Wyatt, D. J. Wilner, W. R. F. Dent, S. Marino, G. M. Kennedy, and J. Milli. Kuiper Belt-like Hot and Cold Populations of Planetesimal Inclinations in the  $\beta$  Pictoris Belt Revealed by ALMA. *AJ*, 157(4):135, April 2019b. doi: 10.3847/1538-3881/ab06c0.
- Luca Matrà, William R. F. Dent, David J. Wilner, Sebastián Marino, Mark C. Wyatt, Jonathan P. Marshall, Kate Y. L. Su, Miguel Chavez, Antonio Hales, A. Meredith Hughes, Jane S. Greaves, and Stuart A. Corder. Dust Populations in the Iconic Vega Planetary System Resolved by ALMA. *ApJ*, 898(2):146, August 2020. doi: 10.3847/1538-4357/aba0a4.
- B. C. Matthews, A. V. Krivov, M. C. Wyatt, G. Bryden, and C. Eiroa. Observations, Modeling, and Theory of Debris Disks. In Henrik Beuther, Ralf S. Klessen, Cornelis P. Dullemond, and Thomas Henning, editors, *Protostars and Planets VI*, page 521, January 2014. doi: 10.2458/azu\_uapress\_9780816531240-ch023.
- Brenda C. Matthews, Grant Kennedy, Bruce Sibthorpe, Wayne Holland, Mark Booth, Paul Kalas, Meredith MacGregor, David Wilner, Bart Vandenbussche, Göran Olofsson, Joris Blommaert, Alexis Brandeker, W. R. F. Dent, Bernard L. de Vries, James Di Francesco, Malcolm Fridlund, James R. Graham, Jane Greaves, Ana M. Heras, Michiel Hogerheijde, R. J. Ivison, Eric Pantin, and Göran L. Pilbratt. The AU Mic Debris Disk: Far-infrared and Submillimeter Resolved Imaging. *ApJ*, 811(2):100, October 2015. doi: 10.1088/0004-637X/811/2/100.
- Elisabeth Matthews, Sasha Hinkley, Arthur Vigan, Grant Kennedy, Aaron Rizzuto, Karl Stapelfeldt, Dimitri Mawet, Mark Booth, Christine Chen, and Hannah Jang-Condell. The First Scattered-light Image of the Debris Disk around the Sco-Cen Target HD 129590. *ApJ*, 843(1):L12, July 2017. doi: 10.3847/2041-8213/aa7943.
- J. Mazoyer, A. Boccaletti, J. C. Augereau, A. M. Lagrange, R. Galicher, and P. Baudoz. Is the HD 15115 inner disk really asymmetrical? *A&A*, 569:A29, September 2014. doi: 10.1051/0004-6361/201424479.

- J. P. McMullin, B. Waters, D. Schiebel, W. Young, and K. Golap. *Astronomical Society of the Pacific Conference Series Vol. 376, Astronomical Data Analysis Software and Systems XVI*, page 127, 2007.
- S. Messina, A. C. Lanzafame, L. Malo, S. Desidera, A. Buccino, L. Zhang, S. Artemenko, M. Millward, and F. J. Hambsch. The  $\beta$  Pictoris association low-mass members: Membership assessment, rotation period distribution, and dependence on multiplicity. *A&A*, 607:A3, October 2017. doi: 10.1051/0004-6361/201730444.
- Sergio Messina, Giuseppe Leto, and Isabella Pagano. The triple system AT Mic AB + AU Mic in the  $\beta$  Pictoris association. *Ap&SS*, 361(9):291, September 2016. doi: 10.1007/s10509-016-2886-x.
- J. Milli, D. Mouillet, A.-M. Lagrange, A. Boccaletti, D. Mawet, G. Chauvin, and M. Bonnefoy. Impact of angular differential imaging on circumstellar disk images. *A&A*, 545: A111, September 2012. doi: 10.1051/0004-6361/201219687.
- J. Milli, A. Vigan, D. Mouillet, A. M. Lagrange, J. C. Augereau, C. Pinte, D. Mawet, H. M. Schmid, A. Boccaletti, L. Matrà, Q. Kral, S. Ertel, G. Chauvin, A. Bazzon, F. Ménard, J. L. Beuzit, C. Thalmann, C. Dominik, M. Feldt, T. Henning, M. Min, J. H. Girard, R. Galicher, M. Bonnefoy, T. Fusco, J. de Boer, M. Janson, A. L. Maire, D. Mesa, J. E. Schlieder, and SPHERE Consortium. Near-infrared scattered light properties of the HR 4796 A dust ring. A measured scattering phase function from  $13.6^\circ$  to  $166.6^\circ$ . *A&A*, 599: A108, March 2017. doi: 10.1051/0004-6361/201527838.
- N. Miret-Roig, P. A. B. Galli, W. Brandner, H. Bouy, D. Barrado, J. Olivares, T. Antoja, M. Romero-Gómez, F. Figueras, and J. Lillo-Box. Dynamical traceback age of the  $\beta$  Pictoris moving group. *A&A*, 642:A179, October 2020. doi: 10.1051/0004-6361/202038765.
- B. Montesinos, C. Eiroa, A. V. Krivov, J. P. Marshall, G. L. Pilbratt, R. Liseau, A. Mora, J. Maldonado, S. Wolf, S. Ertel, A. Bayo, J. C. Augereau, A. M. Heras, M. Fridlund, W. C. Danchi, E. Solano, F. Kirchschrager, C. del Burgo, and D. Montes. Incidence of debris discs around FGK stars in the solar neighbourhood. *A&A*, 593:A51, September 2016. doi: 10.1051/0004-6361/201628329.
- Michèle Moons. Review of the dynamics in the Kirkwood gaps. *Celestial Mechanics and Dynamical Astronomy*, 65(1-2):175–204, March 1996. doi: 10.1007/BF00048446.
- A. Moór, Gy. M. Szabó, L. L. Kiss, Cs. Kiss, P. Ábrahám, J. Szulágyi, Á. Kóspál, and T. Szalai. Unveiling new members in five nearby young moving groups. *MNRAS*, 435(2): 1376–1388, October 2013. doi: 10.1093/mnras/stt1381.

- Attila Moór, Nicole Pawellek, Péter Ábrahám, Ágnes Kóspál, Krisztián Vida, András Pál, Anne Dutrey, Emmanuel Di Folco, A. Meredith Hughes, Quentin Kral, and Ilaria Pascucci. The Big Sibling of AU Mic: A Cold Dust-rich Debris Disk around CP-72 2713 in the  $\beta$  Pic Moving Group. *AJ*, 159(6):288, June 2020. doi: 10.3847/1538-3881/ab8f98.
- Attila Moór, Péter Ábrahám, Gyula Szabó, Krisztián Vida, Gianni Cataldi, Alíz Derekas, Thomas Henning, Karen Kinemuchi, Ágnes Kóspál, József Kovács, András Pál, Paula Sarkis, Bálint Seli, Zsófia M. Szabó, and Katalin Takáts. A New Sample of Warm Extreme Debris Disks from the ALLWISE Catalog. *ApJ*, 910(1):27, March 2021. doi: 10.3847/1538-4357/abdc26.
- M. Moshir, G. Kopan, T. Conrow, H. McCallon, P. Hacking, D. Gregorich, G. Rohrbach, M. Melnyk, W. Rice, L. Fullmer, J. White, and T. Chester. The IRAS Faint Source Catalog, Version 2. In *Bulletin of the American Astronomical Society*, volume 22, page 1325, September 1990.
- D. Mouillet, J. D. Larwood, J. C. B. Papaloizou, and A. M. Lagrange. A planet on an inclined orbit as an explanation of the warp in the beta Pictoris disc. *MNRAS*, 292(4): 896–904, December 1997. doi: 10.1093/mnras/292.4.896.
- T. Mukai and T. Yamamoto. A Model of the Circumsolar Dust Cloud. *PASJ*, 31:585–596, January 1979.
- T. Mukai, T. Yamamoto, H. Hasegawa, A. Fujiwara, and C. Koike. On the Circumsolar Grain Materials. *PASJ*, 26:445, January 1974.
- Gijs D. Mulders, Ilaria Pascucci, and Dániel Apai. A Stellar-mass-dependent Drop in Planet Occurrence Rates. *ApJ*, 798(2):112, Jan 2015. doi: 10.1088/0004-637X/798/2/112.
- D. J. Mullan, J. G. Doyle, R. O. Redman, and M. Mathioudakis. Limits on Detectability of Mass Loss from Cool Dwarfs. *ApJ*, 397:225, September 1992. doi: 10.1086/171781.
- Hiroshi Murakami, Hajime Baba, Peter Barthel, David L. Clements, Martin Cohen, Yasuo Doi, Keigo Enya, Elysandra Figueredo, Naofumi Fujishiro, Hideaki Fujiwara, Mikio Fujiwara, Pedro Garcia-Lario, Tomotsugu Goto, Sunao Hasegawa, Yasunori Hibi, Takanori Hirao, Norihisa Hiromoto, Seung Soo Hong, Koji Imai, Miho Ishigaki, Masateru Ishiguro, Daisuke Ishihara, Yoshifusa Ita, Woong-Seob Jeong, Kyung Sook Jeong, Hidehiro Kaneda, Hirokazu Kataza, Mitsunobu Kawada, Toshihide Kawai, Akiko Kawamura, Martin F. Kessler, Do Kester, Tsuneo Kii, Dong Chan Kim, Woojung Kim, Hisato Kobayashi, Bon Chul Koo, Suk Minn Kwon, Hyung Mok Lee, Rosario Lorente, Sin’itirou Mak-iuti, Hideo Matsuhara, Toshio Matsumoto, Hiroshi Matsuo, Shuji Matsuura, Thomas G.

Müller, Noriko Murakami, Hirohisa Nagata, Takao Nakagawa, Takahiro Naoi, Masanao Narita, Manabu Noda, Sang Hoon Oh, Akira Ohnishi, Youichi Ohyama, Yoko Okada, Haruyuki Okuda, Sebastian Oliver, Takashi Onaka, Takafumi Ootsubo, Shinki Oyabu, Soojong Pak, Yong-Sun Park, Chris P. Pearson, Michael Rowan-Robinson, Toshinobu Saito, Itsuki Sakon, Alberto Salama, Shinji Sato, Richard S. Savage, Stephen Serjeant, Hiroshi Shibai, Mai Shirahata, Jungjoo Sohn, Toyoaki Suzuki, Toshinobu Takagi, Hidenori Takahashi, Toshihiko Tanabé, Tsutomu T. Takeuchi, Satoshi Takita, Matthew Thomson, Kazunori Uemizu, Munetaka Ueno, Fumihiko Usui, Eva Verdugo, Takehiko Wada, Lingyu Wang, Toyoki Watabe, Hidenori Watarai, Glenn J. White, Issei Yamamura, Chisato Yamauchi, and Akiko Yasuda. The Infrared Astronomical Mission AKARI\*. *PASJ*, 59:S369–S376, October 2007. doi: 10.1093/pasj/59.sp2.S369.

Alexander J. Mustill and Mark C. Wyatt. Debris disc stirring by secular perturbations from giant planets. *MNRAS*, 399(3):1403–1414, November 2009. doi: 10.1111/j.1365-2966.2009.15360.x.

Joan R. Najita, Sean M. Andrews, and James Muzerolle. Demographics of transition discs in Ophiuchus and Taurus. *MNRAS*, 450(4):3559–3567, July 2015. doi: 10.1093/mnras/stv839.

G. Neugebauer, H. J. Habing, R. van Duinen, H. H. Aumann, B. Baud, C. A. Beichman, D. A. Beintema, N. Boggess, P. E. Clegg, T. de Jong, J. P. Emerson, T. N. Gautier, F. C. Gillett, S. Harris, M. G. Hauser, J. R. Houck, R. E. Jennings, F. J. Low, P. L. Marsden, G. Miley, F. M. Olton, S. R. Pottasch, E. Raimond, M. Rowan-Robinson, B. T. Soifer, R. G. Walker, P. R. Wesselius, and E. Young. The Infrared Astronomical Satellite (IRAS) mission. *ApJ*, 278:L1–L6, March 1984. doi: 10.1086/184209.

Eric L. Nielsen, Robert J. De Rosa, Jason Wang, Julien Rameau, Inseok Song, James R. Graham, Bruce Macintosh, Mark Ammons, Vanessa P. Bailey, Travis S. Barman, Joanna Bulger, Jeffrey K. Chilcote, Tara Cotten, Rene Doyon, Gaspard Duchêne, Michael P. Fitzgerald, Katherine B. Follette, Alexandra Z. Greenbaum, Pascale Hibon, Li-Wei Hung, Patrick Ingraham, Paul Kalas, Quinn M. Konopacky, James E. Larkin, Jérôme Maire, Franck Marchis, Mark S. Marley, Christian Marois, Stanimir Metchev, Maxwell A. Millar-Blanchaer, Rebecca Oppenheimer, David W. Palmer, Jenny Patience, Marshall D. Perrin, Lisa A. Poyneer, Laurent Pueyo, Abhijith Rajan, Fredrik T. Rantakyö, Dmitry Savransky, Adam C. Schneider, Anand Sivaramakrishnan, Remi Soummer, Sandrine Thomas, J. Kent Wallace, Kimberly Ward-Duong, Sloane J. Wiktorowicz, and Schuyler G. Wolff. Dynamical Mass Measurement of the Young Spectroscopic Binary V343 Normae

AaAb Resolved With the Gemini Planet Imager. *AJ*, 152(6):175, December 2016. doi: 10.3847/0004-6256/152/6/175.

Brodie J. Norfolk, Sarah T. Maddison, Jonathan P. Marshall, Grant M. Kennedy, Gaspard Duchêne, David J. Wilner, Christophe Pinte, Attila Moór, Brenda Matthews, Péter Ábrahám, Ágnes Kóspál, and Nienke van der Marel. Four new planetesimals around typical and pre-main-sequence stars (PLATYPUS) debris discs at 8.8 mm. *MNRAS*, 507(3):3139–3147, November 2021. doi: 10.1093/mnras/stab1901.

Karin I. Öberg, Chunhua Qi, Jeffrey K. J. Fogel, Edwin A. Bergin, Sean M. Andrews, Catherine Espaillat, David J. Wilner, Ilaria Pascucci, and Joel H. Kastner. Disk Imaging Survey of Chemistry with SMA. II. Southern Sky Protoplanetary Disk Data and Full Sample Statistics. *ApJ*, 734(2):98, June 2011. doi: 10.1088/0004-637X/734/2/98.

David P. O’Brien and Richard Greenberg. Steady-state size distributions for collisional populations: analytical solution with size-dependent strength. *Icarus*, 164(2):334–345, August 2003. doi: 10.1016/S0019-1035(03)00145-3.

J. Olofsson, A. Juhász, Th. Henning, H. Mutschke, A. Tamanai, A. Moór, and P. Ábrahám. Transient dust in warm debris disks. Detection of Fe-rich olivine grains. *A&A*, 542:A90, June 2012. doi: 10.1051/0004-6361/201118735.

J. Olofsson, M. Samland, H. Avenhaus, C. Caceres, Th. Henning, A. Moór, J. Milli, H. Canovas, S. P. Quanz, M. R. Schreiber, J. C. Augereau, A. Bayo, A. Bazzon, J. L. Beuzit, A. Boccaletti, E. Buenzli, S. Casassus, G. Chauvin, C. Dominik, S. Desidera, M. Feldt, R. Gratton, M. Janson, A. M. Lagrange, M. Langlois, J. Lannier, A. L. Maire, D. Mesa, C. Pinte, D. Rouan, G. Salter, C. Thalmann, and A. Vigan. Azimuthal asymmetries in the debris disk around HD 61005. A massive collision of planetesimals? *A&A*, 591:A108, June 2016. doi: 10.1051/0004-6361/201628196.

J. Olofsson, R. G. van Holstein, A. Boccaletti, M. Janson, P. Thébault, R. Gratton, C. Lazzoni, Q. Kral, A. Bayo, H. Canovas, C. Caceres, C. Ginski, C. Pinte, R. Asensio-Torres, G. Chauvin, S. Desidera, Th. Henning, M. Langlois, J. Milli, J. E. Schlieder, M. R. Schreiber, J. C. Augereau, M. Bonnefoy, E. Buenzli, W. Brandner, S. Durkan, N. Engler, M. Feldt, N. Godoy, C. Grady, J. Hagelberg, A. M. Lagrange, J. Lannier, R. Ligi, A. L. Maire, D. Mawet, F. Ménard, D. Mesa, D. Mouillet, S. Peretti, C. Perrot, G. Salter, T. Schmidt, E. Sissa, C. Thalmann, A. Vigan, L. Abe, P. Feautrier, D. Le Mignant, T. Moulin, A. Pavlov, P. Rabou, G. Rousset, and A. Roux. Resolving faint structures in the debris disk around TWA 7. Tentative detections of an outer belt, a spiral arm, and a dusty cloud. *A&A*, 617:A109, September 2018. doi: 10.1051/0004-6361/201832583.



- J. Olofsson, P. Thébault, G. M. Kennedy, and A. Bayo. The halo around HD 32297:  $\mu\text{m}$ -sized cometary dust. *A&A*, 664:A122, August 2022. doi: 10.1051/0004-6361/202243794.
- Rachel Osten, Mario Livio, Steve Lubow, J. E. Pringle, David Soderblom, and Jeff Valenti. Coronal Mass Ejections as a Mechanism for Producing IR Variability in Debris Disks. *ApJ*, 765(2):L44, March 2013. doi: 10.1088/2041-8205/765/2/L44.
- Rene D. Oudmaijer, W. E. C. J. van der Veen, L. B. F. M. Waters, N. R. Trams, C. Waelkens, and E. Engelsman. SAO stars with infrared excess in the IRAS Point Source Catalog. *A&AS*, 96:625–643, December 1992.
- James E. Owen. The Origin and Evolution of Transition Discs: Successes, Problems, and Open Questions. *Publ. Astron. Soc. Australia*, 33:e005, February 2016. doi: 10.1017/pasa.2016.2.
- Margaret Pan and Hilke E. Schlichting. Self-consistent Size and Velocity Distributions of Collisional Cascades. *ApJ*, 747(2):113, March 2012. doi: 10.1088/0004-637X/747/2/113.
- Margaret Pan, Erika R. Nesvold, and Marc J. Kuchner. Apocenter Glow in Eccentric Debris Disks: Implications for Fomalhaut and  $\epsilon$  Eridani. *ApJ*, 832(1):81, November 2016. doi: 10.3847/0004-637X/832/1/81.
- Nicole Pawellek, Alexander V. Krivov, Jonathan P. Marshall, Benjamin Montesinos, Péter Ábrahám, Attila Moór, Geoffrey Bryden, and Carlos Eiroa. Disk Radii and Grain Sizes in Herschel-resolved Debris Disks. *ApJ*, 792(1):65, Sep 2014. doi: 10.1088/0004-637X/792/1/65.
- Nicole Pawellek, Mark Wyatt, Luca Matrà, Grant Kennedy, and Ben Yelverton. A  $\sim 75$  per cent occurrence rate of debris discs around F stars in the  $\beta$  Pic moving group. *MNRAS*, 502(4):5390–5416, April 2021. doi: 10.1093/mnras/stab269.
- Tim D. Pearce, Ralf Launhardt, Robert Ostermann, Grant M. Kennedy, Mario Gennaro, Mark Booth, Alexander V. Krivov, Gabriele Cugno, Thomas K. Henning, Andreas Quirrenbach, Arianna Musso Barucci, Elisabeth C. Matthews, Henrik L. Ruh, and Jordan M. Stone. Planet populations inferred from debris discs. Insights from 178 debris systems in the ISPY, LEECH, and LStEN planet-hunting surveys. *A&A*, 659:A135, March 2022. doi: 10.1051/0004-6361/202142720.
- Mark J. Pecaut and Eric E. Mamajek. Intrinsic Colors, Temperatures, and Bolometric Corrections of Pre-main-sequence Stars. *ApJS*, 208(1):9, September 2013. doi: 10.1088/0067-0049/208/1/9.

- Jean-Marc Petit, Alessandro Morbidelli, and John Chambers. The Primordial Excitation and Clearing of the Asteroid Belt. *Icarus*, 153(2):338–347, October 2001. doi: 10.1006/icar.2001.6702.
- G. L. Pilbratt, J. R. Riedinger, T. Passvogel, G. Crone, D. Doyle, U. Gageur, A. M. Heras, C. Jewell, L. Metcalfe, S. Ott, and M. Schmidt. Herschel Space Observatory. An ESA facility for far-infrared and submillimetre astronomy. *A&A*, 518:L1, July 2010. doi: 10.1051/0004-6361/201014759.
- Peter Plavchan, M. Jura, and S. J. Lipsky. Where Are the M Dwarf Disks Older Than 10 Million Years? *ApJ*, 631(2):1161–1169, Oct 2005. doi: 10.1086/432568.
- Peter Plavchan, M. W. Werner, C. H. Chen, K. R. Stapelfeldt, K. Y. L. Su, J. R. Stauffer, and I. Song. New Debris Disks Around Young, Low-Mass Stars Discovered with the Spitzer Space Telescope. *ApJ*, 698(2):1068–1094, June 2009. doi: 10.1088/0004-637X/698/2/1068.
- A. Poglitsch, C. Waelkens, N. Geis, H. Feuchtgruber, B. Vandenbussche, L. Rodriguez, O. Krause, E. Renotte, C. van Hoof, P. Saraceno, J. Cepa, F. Kerschbaum, P. Agnès, B. Ali, B. Altieri, P. Andreani, J. L. Augeres, Z. Balog, L. Barl, O. H. Bauer, N. Belbachir, M. Benedettini, N. Billot, O. Boulade, H. Bischof, J. Blommaert, E. Callut, C. Cara, R. Cerulli, D. Cesarsky, A. Contursi, Y. Creten, W. De Meester, V. Doublier, E. Doumayrou, L. Duband, K. Exter, R. Genzel, J. M. Gillis, U. Grözinger, T. Henning, J. Herreros, R. Huygen, M. Inguscio, G. Jakob, C. Jamar, C. Jean, J. de Jong, R. Katterloher, C. Kiss, U. Klaas, D. Lemke, D. Lutz, S. Madden, B. Marquet, J. Martignac, A. Mazy, P. Merken, F. Montfort, L. Morbidelli, T. Müller, M. Nielbock, K. Okumura, R. Orfei, R. Ottensamer, S. Pezzuto, P. Popesso, J. Putzeys, S. Regibo, V. Reveret, P. Royer, M. Sauvage, J. Schreiber, J. Stegmaier, D. Schmitt, J. Schubert, E. Sturm, M. Thiel, G. Tofani, R. Vavrek, M. Wetzstein, E. Wieprecht, and E. Wiezorrek. The Photodetector Array Camera and Spectrometer (PACS) on the Herschel Space Observatory. *A&A*, 518:L2, July 2010. doi: 10.1051/0004-6361/201014535.
- Gergö Poppinga, Fabian Walter, Peter Behroozi, Jorge González-López, Christopher C. Hayward, Rachel S. Somerville, Paul van der Werf, Manuel Aravena, Roberto J. Assef, Leindert Boogaard, Franz E. Bauer, Paulo C. Cortes, Pierre Cox, Tanio Díaz-Santos, Roberto Decarli, Maximilien Franco, Rob Ivison, Dominik Riechers, Hans-Walter Rix, and Axel Weiss. The ALMA Spectroscopic Survey in the HUDF: A Model to Explain Observed 1.1 and 0.85 mm Dust Continuum Number Counts. *ApJ*, 891(2):135, March 2020. doi: 10.3847/1538-4357/ab76c0.

- J. H. Poynting. Radiation in the Solar System: Its Effect on Temperature and Its Pressure on Small Bodies. *Philosophical Transactions of the Royal Society of London Series A*, 202: 525–552, January 1904. doi: 10.1098/rsta.1904.0012.
- Alice C. Quillen. Predictions for a planet just inside Fomalhaut’s eccentric ring. *MNRAS*, 372(1):L14–L18, October 2006. doi: 10.1111/j.1745-3933.2006.00216.x.
- Roman R. Rafikov. Metal Accretion onto White Dwarfs Caused by Poynting-Robertson Drag on their Debris Disks. *ApJ*, 732(1):L3, May 2011. doi: 10.1088/2041-8205/732/1/L3.
- Joanna Ramasawmy, Pamela D. Klaassen, Claudia Cicone, Tony K. Mroczkowski, Chian-Chou Chen, Thomas Cornish, Elisabete Lima da Cunha, Evanthia Hatziminaoglou, Doug Johnstone, Daizhong Liu, Yvette Perrott, Alice Schimek, Thomas Stanke, and Sven Wedemeyer. The Atacama Large Aperture Submillimeter Telescope: Key science drivers. *arXiv e-prints*, art. arXiv:2207.03914, July 2022.
- J. Rameau, G. Chauvin, A. M. Lagrange, A. Boccaletti, S. P. Quanz, M. Bonnefoy, J. H. Girard, P. Delorme, S. Desidera, H. Klahr, C. Mordasini, C. Dumas, and M. Bonavita. Discovery of a Probable 4-5 Jupiter-mass Exoplanet to HD 95086 by Direct Imaging. *ApJ*, 772(2):L15, August 2013a. doi: 10.1088/2041-8205/772/2/L15.
- J. Rameau, G. Chauvin, A. M. Lagrange, T. Meshkat, A. Boccaletti, S. P. Quanz, T. Currie, D. Mawet, J. H. Girard, M. Bonnefoy, and M. Kenworthy. Confirmation of the Planet around HD 95086 by Direct Imaging. *ApJ*, 779(2):L26, December 2013b. doi: 10.1088/2041-8205/779/2/L26.
- Valerie A. Rapson, Benjamin Sargent, G. Germano Sacco, Joel H. Kastner, David Wilner, Katherine Rosenfeld, Sean Andrews, Gregory Herczeg, and Nienke van der Marel. A Combined Spitzer and Herschel Infrared Study of Gas and Dust in the Circumbinary Disk Orbiting V4046 Sgr. *ApJ*, 810(1):62, September 2015. doi: 10.1088/0004-637X/810/1/62.
- S. N. Raymond and A. Bonsor. Vega’s hot dust from icy planetesimals scattered inwards by an outward-migrating planetary system. *MNRAS*, 442:L18–L22, July 2014. doi: 10.1093/mnras/lu048.
- Sean N. Raymond and Alessandro Morbidelli. Planet Formation: Key Mechanisms and Global Models. In Katia Biazzo, Valerio Bozza, Luigi Mancini, and Alessandro Sozzetti, editors, *Demographics of Exoplanetary Systems, Lecture Notes of the 3rd Advanced School on Exoplanetary Science*, volume 466 of *Astrophysics and Space Science Library*, pages 3–82, January 2022. doi: 10.1007/978-3-030-88124-5\_1.

- L. M. Rebull, K. R. Stapelfeldt, M. W. Werner, V. G. Mannings, C. Chen, J. R. Stauffer, P. S. Smith, I. Song, D. Hines, and F. J. Low. Spitzer MIPS Observations of Stars in the  $\beta$  Pictoris Moving Group. *ApJ*, 681(2):1484–1504, July 2008. doi: 10.1086/588182.
- R. Reche, H. Beust, and J. C. Augereau. Investigating the flyby scenario for the HD 141569 system. *A&A*, 493(2):661–669, Jan 2009. doi: 10.1051/0004-6361/200810419.
- M. Reidemeister, A. V. Krivov, C. C. Stark, J. C. Augereau, T. Löhne, and S. Müller. The cold origin of the warm dust around  $\epsilon$  Eridani. *A&A*, 527:A57, Mar 2011. doi: 10.1051/0004-6361/201015328.
- Bo Reipurth and Seppo Mikkola. Formation of the widest binary stars from dynamical unfolding of triple systems. *Nature*, 492(7428):221–224, Dec 2012. ISSN 1476-4687. doi: 10.1038/nature11662. URL <http://dx.doi.org/10.1038/nature11662>.
- Bin Ren, Élodie Choquet, Marshall D. Perrin, Dimitri Mawet, Christine H. Chen, Julien Milli, John H. Debes, Isabel Rebolledo, Christopher C. Stark, J. Brendan Hagan, Dean C. Hines, Maxwell A. Millar-Blanchaer, Laurent Pueyo, Aki Roberge, Glenn Schneider, Eugene Serabyn, Rémi Soummer, and Schuyler G. Wolff. A Layered Debris Disk around M Star TWA 7 in Scattered Light. *ApJ*, 914(2):95, June 2021. doi: 10.3847/1538-4357/ac03b9.
- Joseph H. Rhee, Inseok Song, B. Zuckerman, and Michael McElwain. Characterization of Dusty Debris Disks: The IRAS and Hipparcos Catalogs. *ApJ*, 660(2):1556–1571, May 2007. doi: 10.1086/509912.
- G. H. Rieke, E. T. Young, C. W. Engelbracht, D. M. Kelly, F. J. Low, E. E. Haller, J. W. Beeman, K. D. Gordon, J. A. Stansberry, K. A. Misselt, J. Cadien, J. E. Morrison, G. Rivlis, W. B. Latter, A. Noriega-Crespo, D. L. Padgett, K. R. Stapelfeldt, D. C. Hines, E. Egami, J. Muzerolle, A. Alonso-Herrero, M. Blaylock, H. Dole, J. L. Hinz, E. Le Floch, C. Papovich, P. G. Pérez-González, P. S. Smith, K. Y. L. Su, L. Bennett, D. T. Frayer, D. Henderson, N. Lu, F. Masci, M. Pesenson, L. Rebull, J. Rho, J. Keene, S. Stolovy, S. Wachter, W. Wheaton, M. W. Werner, and P. L. Richards. The Multiband Imaging Photometer for Spitzer (MIPS). *ApJS*, 154(1):25–29, September 2004. doi: 10.1086/422717.
- George H Rieke, KYL Su, JA Stansberry, D Trilling, G Bryden, J Muzerolle, B White, Nadiya Gorlova, ET Young, CA Beichman, et al. Decay of planetary debris disks. *The Astrophysical Journal*, 620(2):1010, 2005.

- Jessica K. Rigley and Mark C. Wyatt. Dust size and spatial distributions in debris discs: predictions for exozodiacal dust dragged in from an exo-Kuiper belt. *MNRAS*, 497(1): 1143–1165, September 2020. doi: 10.1093/mnras/staa2029.
- H. P. Robertson. Dynamical effects of radiation in the solar system. *MNRAS*, 97:423, April 1937. doi: 10.1093/mnras/97.6.423.
- L. Rodet, H. Beust, M. Bonnefoy, A. M. Lagrange, P. A. B. Galli, C. Ducourant, and R. Teixeira. Origin of the wide-orbit circumbinary giant planet HD 106906. A dynamical scenario and its impact on the disk. *A&A*, 602:A12, Jun 2017. doi: 10.1051/0004-6361/201630269.
- L. Rodet, H. Beust, M. Bonnefoy, R. J. De Rosa, P. Kalas, and A. M. Lagrange. ODEA: Orbital Dynamics in a complex Evolving Architecture. Application to the planetary system HD 106906. *A&A*, 631:A139, Nov 2019. doi: 10.1051/0004-6361/201935728.
- Timothy J. Rodigas, Christopher C. Stark, Alycia Weinberger, John H. Debes, Philip M. Hinz, Laird Close, Christine Chen, Paul S. Smith, Jared R. Males, Andrew J. Skemer, Alfio Puglisi, Katherine B. Follette, Katie Morzinski, Ya-Lin Wu, Runa Briguglio, Simone Esposito, Enrico Pinna, Armando Riccardi, Glenn Schneider, and Marco Xompero. On the Morphology and Chemical Composition of the HR 4796A Debris Disk. *ApJ*, 798(2): 96, January 2015. doi: 10.1088/0004-637X/798/2/96.
- David R. Rodriguez and B. Zuckerman. BINARIES AMONG DEBRIS DISK STARS. *The Astrophysical Journal*, 745(2):147, jan 2012. doi: 10.1088/0004-637x/745/2/147. URL <https://doi.org/10.1088/0004-637x/745/2/147>.
- David R. Rodriguez, Gaspard Duchêne, Henry Tom, Grant M. Kennedy, Brenda Matthews, Jane Greaves, and Harold Butner. Stellar multiplicity and debris discs: an unbiased sample. *MNRAS*, 449(3):3160–3170, May 2015. doi: 10.1093/mnras/stv483.
- P. R. Roelfsema, H. Shibai, L. Armus, D. Arrazola, M. Audard, M. D. Audley, C. M. Bradford, I. Charles, P. Dieleman, Y. Doi, L. Duband, M. Eggens, J. Evers, I. Funaki, J. R. Gao, M. Giard, A. di Giorgio, L. M. González Fernández, M. Griffin, F. P. Helmich, R. Hijmering, R. Huisman, D. Ishihara, N. Isobe, B. Jackson, H. Jacobs, W. Jellema, I. Kamp, H. Kaneda, M. Kawada, F. Kemper, F. Kerschbaum, P. Khosropanah, K. Kohno, P. P. Kooijman, O. Krause, J. van der Kuur, J. Kwon, W. M. Laauwen, G. de Lange, B. Larsson, D. van Loon, S. C. Madden, H. Matsuhara, F. Najarro, T. Nakagawa, D. Naylor, H. Ogawa, T. Onaka, S. Oyabu, A. Poglitsch, V. Reveret, L. Rodriguez, L. Spinoglio, I. Sakon, Y. Sato, K. Shinozaki, R. Shipman, H. Sugita, T. Suzuki, F. F. S. van der Tak, J. Torres Redondo, T. Wada, S. Y. Wang, C. K. Wafelbakker, H. van Weers, S. Withington,

- B. Vandenbussche, T. Yamada, and I. Yamamura. SPICA-A Large Cryogenic Infrared Space Telescope: Unveiling the Obscured Universe. *Publ. Astron. Soc. Australia*, 35: e030, August 2018. doi: 10.1017/pasa.2018.15.
- Katherine A. Rosenfeld, Sean M. Andrews, David J. Wilner, J. H. Kastner, and M. K. McClure. The Structure of the Evolved Circumbinary Disk around V4046 Sgr. *ApJ*, 775(2):136, October 2013. doi: 10.1088/0004-637X/775/2/136.
- Shoko Sai, Yoichi Itoh, Misato Fukagawa, Hiroshi Shibai, and Takahiro Sumi. Near-infrared image of the debris disk around HD 15115. *PASJ*, 67(2):20, April 2015. doi: 10.1093/pasj/psu152.
- Edward F. Schlafly, Aaron M. Meisner, and Gregory M. Green. The unWISE Catalog: Two Billion Infrared Sources from Five Years of WISE Imaging. *ApJS*, 240(2):30, February 2019. doi: 10.3847/1538-4365/aafbea.
- Joshua E. Schlieder, Sébastien Lépine, and Michal Simon.  $\beta$  Pictoris and AB Doradus Moving Groups: Likely New Low-mass Members. *AJ*, 140(1):119–128, July 2010. doi: 10.1088/0004-6256/140/1/119.
- Glenn Schneider, Carol A. Grady, Dean C. Hines, Christopher C. Stark, John H. Debes, Joe Carson, Marc J. Kuchner, Marshall D. Perrin, Alycia J. Weinberger, John P. Wisniewski, Murray D. Silverstone, Hannah Jang-Condell, Thomas Henning, Bruce E. Woodgate, Eugene Serabyn, Amaya Moro-Martin, Motohide Tamura, Phillip M. Hinz, and Timothy J. Rodigas. Probing for Exoplanets Hiding in Dusty Debris Disks: Disk Imaging, Characterization, and Exploration with HST/STIS Multi-roll Coronagraphy. *AJ*, 148(4): 59, October 2014. doi: 10.1088/0004-6256/148/4/59.
- Gideon Schwarz. Estimating the dimension of a model. *Ann. Statist.*, 6(2):461–464, 03 1978. doi: 10.1214/aos/1176344136. URL <https://doi.org/10.1214/aos/1176344136>.
- R. J. Selina, E. J. Murphy, M. McKinnon, A. Beasley, B. Butler, C. Carilli, B. Clark, S. Durand, A. Erickson, W. Grammer, R. Hiriart, J. Jackson, B. Kent, B. Mason, M. Morgan, O. Y. Ojeda, V. Rosero, W. Shillue, S. Sturgis, and D. Urbain. The ngVLA Reference Design. In Eric Murphy, editor, *Science with a Next Generation Very Large Array*, volume 517 of *Astronomical Society of the Pacific Conference Series*, page 15, December 2018.
- Aldo G. Sepulveda, Luca Matrà, Grant M. Kennedy, Carlos del Burgo, Karin I. Öberg, David J. Wilner, Sebastián Marino, Mark Booth, John M. Carpenter, Claire L. Davies, William R. F. Dent, Steve Ertel, Jean-Francois Lestrade, Jonathan P. Marshall, Julien Milli, Mark C. Wyatt, Meredith A. MacGregor, and Brenda C. Matthews. The REASONS

- Survey: Resolved Millimeter Observations of a Large Debris Disk around the Nearby F Star HD 170773. *ApJ*, 881(1):84, Aug 2019. doi: 10.3847/1538-4357/ab2b98.
- É. Sezestre, J. C. Augereau, A. Boccaletti, and P. Thébault. Expelled grains from an unseen parent body around AU Microscopii. *A&A*, 607:A65, November 2017. doi: 10.1051/0004-6361/201731061.
- É. Sezestre, J. C. Augereau, and P. Thébault. Hot exozodiacal dust: an exocometary origin? *A&A*, 626:A2, June 2019. doi: 10.1051/0004-6361/201935250.
- Andrew Shannon, Cathie Clarke, and Mark Wyatt. Dancing with the stars: formation of the Fomalhaut triple system and its effect on the debris discs. *Monthly Notices of the Royal Astronomical Society*, 442(1):142–147, 06 2014. ISSN 0035-8711. doi: 10.1093/mnras/stu846. URL <https://doi.org/10.1093/mnras/stu846>.
- Ed J. Shaya and Rob P. Olling. Very Wide Binaries and Other Comoving Stellar Companions: A Bayesian Analysis of the Hipparcos Catalogue. *ApJS*, 192(1):2, January 2011. doi: 10.1088/0067-0049/192/1/2.
- Evgenya L. Shkolnik, Guillem Anglada-Escudé, Michael C. Liu, Brendan P. Bowler, Alycia J. Weinberger, Alan P. Boss, I. Neill Reid, and Motohide Tamura. Identifying the Young Low-mass Stars within 25 pc. II. Distances, Kinematics, and Group Membership. *ApJ*, 758(1):56, October 2012. doi: 10.1088/0004-637X/758/1/56.
- Evgenya L. Shkolnik, Katelyn N. Allers, Adam L. Kraus, Michael C. Liu, and Laura Flagg. All-sky Co-moving Recovery Of Nearby Young Members (ACRONYM). II. The  $\beta$  Pictoris Moving Group. *AJ*, 154(2):69, August 2017. doi: 10.3847/1538-3881/aa77fa.
- B. Sibthorpe, G. M. Kennedy, M. C. Wyatt, J. F. Lestrade, J. S. Greaves, B. C. Matthews, and G. Duchêne. Analysis of the Herschel DEBRIS Sun-like star sample. *MNRAS*, 475(3):3046–3064, April 2018. doi: 10.1093/mnras/stx3188.
- E. Sissa, J. Olofsson, A. Vigan, J. C. Augereau, V. D’Orazi, S. Desidera, R. Gratton, M. Langlois, E. Rigliaco, A. Boccaletti, Q. Kral, C. Lazzoni, D. Mesa, S. Messina, E. Sezestre, P. Thébault, A. Zurlo, T. Bhowmik, M. Bonnefoy, G. Chauvin, M. Feldt, J. Hagelberg, A. M. Lagrange, M. Janson, A. L. Maire, F. Ménard, J. Schlieder, T. Schmidt, J. Szulágyi, E. Stadler, D. Maurel, A. Delboulbé, P. Feautrier, J. Ramos, and F. Rigal. New disk discovered with VLT/SPHERE around the M star GSC 07396-00759. *A&A*, 613:L6, May 2018. doi: 10.1051/0004-6361/201832740.
- M. F. Skrutskie, R. M. Cutri, R. Stiening, M. D. Weinberg, S. Schneider, J. M. Carpenter, C. Beichman, R. Capps, T. Chester, J. Elias, J. Huchra, J. Liebert, C. Lonsdale, D. G.

- Monet, S. Price, P. Seitzer, T. Jarrett, J. D. Kirkpatrick, J. E. Gizis, E. Howard, T. Evans, J. Fowler, L. Fullmer, R. Hurt, R. Light, E. L. Kopan, K. A. Marsh, H. L. McCallon, R. Tam, S. Van Dyk, and S. Wheelock. The Two Micron All Sky Survey (2MASS). *AJ*, 131(2):1163–1183, February 2006. doi: 10.1086/498708.
- K. R. Stapelfeldt, E. K. Holmes, C. Chen, G. H. Rieke, K. Y. L. Su, D. C. Hines, M. W. Werner, C. A. Beichman, M. Jura, D. L. Padgett, J. A. Stansberry, G. Bendo, J. Cadien, M. Marengo, T. Thompson, T. Velusamy, C. Backus, M. Blaylock, E. Egami, C. W. Engelbracht, D. T. Frayer, K. D. Gordon, J. Keene, W. B. Latter, T. Megeath, K. Misselt, J. E. Morrison, J. Muzerolle, A. Noriega-Crespo, J. Van Cleve, and E. T. Young. First Look at the Fomalhaut Debris Disk with the Spitzer Space Telescope. *ApJS*, 154(1): 458–462, September 2004. doi: 10.1086/423135.
- H. C. Stempels and G. F. Gahm. The close T Tauri binary V 4046 Sagittarii. *A&A*, 421: 1159–1168, July 2004. doi: 10.1051/0004-6361:20034502.
- Paul A. Strøm, Dennis Bodewits, Matthew M. Knight, Flavien Kiefer, Geraint H. Jones, Quentin Kral, Luca Matrà, Eva Bodman, Maria Teresa Capria, Ilse Cleeves, Alan Fitzsimmons, Nader Haghighipour, John H. D. Harrison, Daniela Iglesias, Mihkel Kama, Harold Linnartz, Liton Majumdar, Ernst J. W. de Mooij, Stefanie N. Milam, Cyrielle Opitom, Isabel Rebolledo, Laura K. Rogers, Colin Snodgrass, Clara Sousa-Silva, Siyi Xu, Zhong-Yi Lin, and Sebastian Zieba. Exocomets from a Solar System Perspective. *PASP*, 132(1016):101001, October 2020. doi: 10.1088/1538-3873/aba6a0.
- Linda E. Strubbe and Eugene I. Chiang. Dust Dynamics, Surface Brightness Profiles, and Thermal Spectra of Debris Disks: The Case of AU Microscopii. *ApJ*, 648(1):652–665, September 2006. doi: 10.1086/505736.
- K. Y. L. Su, G. H. Rieke, K. A. Misselt, J. A. Stansberry, A. Moro-Martin, K. R. Stapelfeldt, M. W. Werner, D. E. Trilling, G. J. Bendo, K. D. Gordon, D. C. Hines, M. C. Wyatt, W. S. Holland, M. Marengo, S. T. Megeath, and G. G. Fazio. The Vega Debris Disk: A Surprise from Spitzer. *ApJ*, 628(1):487–500, July 2005. doi: 10.1086/430819.
- K. Y. L. Su, G. H. Rieke, J. A. Stansberry, G. Bryden, K. R. Stapelfeldt, D. E. Trilling, J. Muzerolle, C. A. Beichman, A. Moro-Martin, D. C. Hines, and M. W. Werner. Debris Disk Evolution around A Stars. *ApJ*, 653(1):675–689, December 2006. doi: 10.1086/508649.
- K. Y. L. Su, G. H. Rieke, K. R. Stapelfeldt, R. Malhotra, G. Bryden, P. S. Smith, K. A. Misselt, A. Moro-Martin, and J. P. Williams. The Debris Disk Around HR 8799. *ApJ*, 705(1):314–327, November 2009. doi: 10.1088/0004-637X/705/1/314.



- Kate Y. L. Su, George H. Rieke, Renu Malhotra, Karl R. Stapelfeldt, A. Meredith Hughes, Amy Bonsor, David J. Wilner, Zoltan Balog, Dan M. Watson, Michael W. Werner, and Karl A. Misselt. Asteroid Belts in Debris Disk Twins: Vega and Fomalhaut. *ApJ*, 763(2): 118, February 2013. doi: 10.1088/0004-637X/763/2/118.
- Kate Y. L. Su, Alan P. Jackson, András Gáspár, George H. Rieke, Ruobing Dong, Johan Olofsson, G. M. Kennedy, Zoë M. Leinhardt, Renu Malhotra, Michael Hammer, Huan Y. A. Meng, W. Rujopakarn, Joseph E. Rodriguez, Joshua Pepper, D. E. Reichart, David James, and Keivan G. Stassun. Extreme Debris Disk Variability: Exploring the Diverse Outcomes of Large Asteroid Impacts During the Era of Terrestrial Planet Formation. *AJ*, 157(5):202, May 2019. doi: 10.3847/1538-3881/ab1260.
- Devin Sullivan, David J. Wilner, Luca Matrà, Mark C. Wyatt, Sean M. Andrews, Meredith A. MacGregor, and Brenda Matthews. An ALMA 1.3 millimeter Search for Debris Disks around Solar-type Stars in the Pleiades. *AJ*, 164(3):100, September 2022. doi: 10.3847/1538-3881/ac80c5.
- D. Tamayo. Consequences of an eccentric orbit for fomalhaut b. *Monthly Notices of the Royal Astronomical Society*, 438(4):3577–3586, Jan 2014. ISSN 0035-8711. doi: 10.1093/mnras/stt2473. URL <http://dx.doi.org/10.1093/mnras/stt2473>.
- Hidekazu Tanaka, Satoshi Inaba, and Kiyoshi Nakazawa. Steady-State Size Distribution for the Self-Similar Collision Cascade. *Icarus*, 123(2):450–455, October 1996. doi: 10.1006/icar.1996.0170.
- Angelle Tanner, Peter Plavchan, Geoff Bryden, Grant Kennedy, Luca Matrá, Patrick Cronin-Coltsmann, Patrick Lowrance, Todd Henry, Basmah Riaz, John E. Gizis, Adric Riedel, and Elodie Choquet. Herschel Observations of Disks around Late-type Stars. *PASP*, 132(1014):084401, August 2020. doi: 10.1088/1538-3873/ab895f.
- M. Tazzari, F. Beaujean, and L. Testi. GALARIO: a GPU accelerated library for analysing radio interferometer observations. *MNRAS*, 476:4527–4542, June 2018. doi: 10.1093/mnras/sty409.
- Charles M. Telesco, R. Scott Fisher, Mark C. Wyatt, Stanley F. Dermott, Thomas J. J. Kehoe, Steven Novotny, Naibi Mariñas, James T. Radomski, Christopher Packham, James De Buizer, and Thomas L. Hayward. Mid-infrared images of  $\beta$  Pictoris and the possible role of planetesimal collisions in the central disk. *Nature*, 433(7022):133–136, January 2005. doi: 10.1038/nature03255.
- P. Thébault. Vertical structure of debris discs. *A&A*, 505(3):1269–1276, October 2009. doi: 10.1051/0004-6361/200912396.

- P. Thébault and Y. Wu. Outer edges of debris discs. How sharp is sharp? *A&A*, 481(3): 713–724, April 2008. doi: 10.1051/0004-6361:20079133.
- A. R. Thompson, B. G. Clark, C. M. Wade, and P. J. Napier. The Very Large Array. *ApJS*, 44:151–167, October 1980. doi: 10.1086/190688.
- N. D. Thureau, J. S. Greaves, B. C. Matthews, G. Kennedy, N. Phillips, M. Booth, G. Duchêne, J. Horner, D. R. Rodriguez, B. Sibthorpe, and M. C. Wyatt. An unbiased study of debris discs around A-type stars with Herschel. *MNRAS*, 445(3):2558–2573, December 2014. doi: 10.1093/mnras/stu1864.
- C. A. O. Torres, G. R. Quast, L. da Silva, R. de La Reza, C. H. F. Melo, and M. Sterzik. Search for associations containing young stars (SACY). I. Sample and searching method. *A&A*, 460(3):695–708, December 2006. doi: 10.1051/0004-6361:20065602.
- D. E. Trilling, G. Bryden, C. A. Beichman, G. H. Rieke, K. Y. L. Su, J. A. Stansberry, M. Blaylock, K. R. Stapelfeldt, J. W. Beeman, and E. E. Haller. Debris Disks around Sun-like Stars. *ApJ*, 674(2):1086–1105, February 2008. doi: 10.1086/525514.
- P. H. van Cittert. Die Wahrscheinliche Schwingungsverteilung in Einer von Einer Lichtquelle Direkt Oder Mittels Einer Linse Beleuchteten Ebene. *Physica*, 1(1):201–210, January 1934. doi: 10.1016/S0031-8914(34)90026-4.
- G. H. J. van den Oord and J. G. Doyle. Constraints on mass loss from dMe stars: theory and observations. *A&A*, 319:578–588, March 1997.
- R. van Lieshout, C. Dominik, M. Kama, and M. Min. Near-infrared emission from sublimating dust in collisionally active debris disks. *A&A*, 571:A51, November 2014. doi: 10.1051/0004-6361/201322090.
- Andrew Vanderburg, John Asher Johnson, Saul Rappaport, Allyson Bieryla, Jonathan Irwin, John Arban Lewis, David Kipping, Warren R. Brown, Patrick Dufour, David R. Ciardi, Ruth Angus, Laura Schaefer, David W. Latham, David Charbonneau, Charles Beichman, Jason Eastman, Nate McCrady, Robert A. Wittenmyer, and Jason T. Wright. A disintegrating minor planet transiting a white dwarf. *Nature*, 526(7574):546–549, October 2015. doi: 10.1038/nature15527.
- Dimitri Veras, Zoë M. Leinhardt, Amy Bonsor, and Boris T. Gänsicke. Formation of planetary debris discs around white dwarfs - I. Tidal disruption of an extremely eccentric asteroid. *MNRAS*, 445(3):2244–2255, December 2014. doi: 10.1093/mnras/stu1871.

- Dimitri Veras, Siegfried Eggl, and Boris T. Gänsicke. The orbital evolution of asteroids, pebbles and planets from giant branch stellar radiation and winds. *MNRAS*, 451(3): 2814–2834, August 2015. doi: 10.1093/mnras/stv1047.
- Vilenius, E., Kiss, C., Mommert, M., Müller, T., Santos-Sanz, P., Pal, A., Stansberry, J., Mueller, M., Peixinho, N., Fornasier, S., Lellouch, E., Delsanti, A., Thirouin, A., Ortiz, J. L., Duffard, R., Perna, D., Szalai, N., Protopapa, S., Henry, F., Hestroffer, D., Rengel, M., Dotto, E., and Hartogh, P. "tnos are cool": A survey of the trans-neptunian region - vi. herschel/pacs observations and thermal modeling of 19 classical kuiper belt objects. *A&A*, 541:A94, 2012. doi: 10.1051/0004-6361/201118743. URL <https://doi.org/10.1051/0004-6361/201118743>.
- Z. Wahhaj, J. Milli, G. Kennedy, S. Ertel, L. Matra, A. Boccaletti, C. del Burgo, M. Wyatt, C. Pinte, A. M. Lagrange, O. Absil, E. Choquet, C. Gomez Gonzalez, H. Kobayashii, D. Mawet, D. Mouillet, L. Pueyo, W. R. F. Dent, J.-C. Augereau, and J. Girard. The SHARDDS survey: first resolved image of the HD114082 debris disk in Lower Centaurus Crux with SPHERE. *A&A*, 596:L4, November 2016. doi: 10.1051/0004-6361/201321887.
- Jason J. Wang, James R. Graham, Laurent Pueyo, Eric L. Nielsen, Max Millar-Blanchaer, Robert J. De Rosa, Paul Kalas, S. Mark Ammons, Joanna Bulger, Andrew Cardwell, Christine Chen, Eugene Chiang, Jeffrey K. Chilcote, René Doyon, Zachary H. Draper, Gaspard Duchêne, Thomas M. Esposito, Michael P. Fitzgerald, Stephen J. Goodsell, Alexandra Z. Greenbaum, Markus Hartung, Pascale Hibon, Sasha Hinkley, Li-Wei Hung, Patrick Ingraham, James E. Larkin, Bruce Macintosh, Jerome Maire, Franck Marchis, Christian Marois, Brenda C. Matthews, Katie M. Morzinski, Rebecca Oppenheimer, Jenny Patience, Marshall D. Perrin, Abhijith Rajan, Fredrik T. Rantakyö, Naru Sadakuni, Andrew Serio, Anand Sivaramakrishnan, Rémi Soummer, Sandrine Thomas, Kimberly Ward-Duong, Sloane J. Wiktorowicz, and Schuyler G. Wolff. Gemini Planet Imager Observations of the AU Microscopii Debris Disk: Asymmetries within One Arcsecond. *ApJ*, 811(2):L19, October 2015. doi: 10.1088/2041-8205/811/2/L19.
- Bradford J. Wargelin and Jeremy J. Drake. Observability of Stellar Winds from Late-Type Dwarfs via Charge Exchange X-Ray Emission. *ApJ*, 546(1):L57–L60, January 2001. doi: 10.1086/318066.
- Bradford J. Wargelin and Jeremy J. Drake. Stringent X-Ray Constraints on Mass Loss from Proxima Centauri. *ApJ*, 578(1):503–514, October 2002. doi: 10.1086/342270.
- S. J. Weidenschilling. The Distribution of Mass in the Planetary System and Solar Nebula. *Ap&SS*, 51(1):153–158, September 1977. doi: 10.1007/BF00642464.

- AJ Weinberger, EE Becklin, G Schneider, BA Smith, PJ Lowrance, MD Silverstone, B Zuckerman, and RJ Terile. The circumstellar disk of hd 141569 imaged with nicmos. *The Astrophysical Journal Letters*, 525(1):L53, 1999.
- M. Wenger, F. Ochsenbein, D. Egret, P. Dubois, F. Bonnarel, S. Borde, F. Genova, G. Jasiewicz, S. Laloë, S. Lesteven, and R. Monier. The SIMBAD astronomical database. The CDS reference database for astronomical objects. *A&AS*, 143:9–22, April 2000. doi: 10.1051/aas:2000332.
- M. W. Werner, T. L. Roellig, F. J. Low, G. H. Rieke, M. Rieke, W. F. Hoffmann, E. Young, J. R. Houck, B. Brandl, G. G. Fazio, J. L. Hora, R. D. Gehrz, G. Helou, B. T. Soifer, J. Stauffer, J. Keene, P. Eisenhardt, D. Gallagher, T. N. Gautier, W. Irace, C. R. Lawrence, L. Simmons, J. E. Van Cleve, M. Jura, E. L. Wright, and D. P. Cruikshank. The Spitzer Space Telescope Mission. *ApJS*, 154(1):1–9, September 2004. doi: 10.1086/422992.
- Jacob Aaron White, AC Boley, WRF Dent, EB Ford, and S Corder. 1.3-mm alma observations of the fomalhaut debris system. *Monthly Notices of the Royal Astronomical Society*, 466(4):4201–4210, 2017.
- Jonathan P. Williams and Lucas A. Cieza. Protoplanetary Disks and Their Evolution. *ARA&A*, 49(1):67–117, September 2011. doi: 10.1146/annurev-astro-081710-102548.
- Jonathan P. Williams, Joan Najita, Michael C. Liu, Sandrine Bottinelli, John M. Carpenter, Lynne A. Hillenbrand, Michael R. Meyer, and David R. Soderblom. Detection of Cool Dust around the G2 V Star HD 107146. *ApJ*, 604(1):414–419, March 2004. doi: 10.1086/381721.
- David J. Wilner, Sean M. Andrews, Meredith A. MacGregor, and A. Meredith Hughes. A Resolved Millimeter Emission Belt in the AU Mic Debris Disk. *ApJ*, 749(2):L27, April 2012. doi: 10.1088/2041-8205/749/2/L27.
- John P. Wisniewski, Adam F. Kowalski, James R. A. Davenport, Glenn Schneider, Carol A. Grady, Leslie Hebb, Kellen D. Lawson, Jean-Charles Augereau, Anthony Boccaletti, Alexander Brown, John H. Debes, Andras Gaspar, Thomas K. Henning, Dean C. Hines, Marc J. Kuchner, Anne-Marie Lagrange, Julien Milli, Elie Sevestre, Christopher C. Stark, and Christian Thalmann. High-fidelity Imaging of the Inner AU Mic Debris Disk: Evidence of Differential Wind Sculpting? *ApJ*, 883(1):L8, September 2019. doi: 10.3847/2041-8213/ab40bf.
- Brian E. Wood, Jeffrey L. Linsky, Hans-Reinhard Müller, and Gary P. Zank. Observational Estimates for the Mass-Loss Rates of  $\alpha$  Centauri and Proxima Centauri Using Hubble

Space Telescope Ly $\alpha$  Spectra. *ApJ*, 547(1):L49–L52, January 2001. doi: 10.1086/318888.

Brian E. Wood, Hans-Reinhard Müller, Gary P. Zank, and Jeffrey L. Linsky. Measured Mass-Loss Rates of Solar-like Stars as a Function of Age and Activity. *ApJ*, 574(1): 412–425, July 2002. doi: 10.1086/340797.

B. E. Woodgate, R. A. Kimble, C. W. Bowers, S. Kraemer, M. E. Kaiser, A. C. Danks, J. F. Grady, J. J. Loiacono, M. Brumfield, L. Feinberg, T. R. Gull, S. R. Heap, S. P. Maran, D. Lindler, D. Hood, W. Meyer, C. Vanhouten, V. Argabright, S. Franka, R. Bybee, D. Dorn, M. Bottema, R. Woodruff, D. Michika, J. Sullivan, J. Hetlinger, C. Ludtke, R. Stocker, A. Delamere, D. Rose, I. Becker, H. Garner, J. G. Timothy, M. Blouke, C. L. Joseph, G. Hartig, R. F. Green, E. B. Jenkins, J. L. Linsky, J. B. Hutchings, H. W. Moos, A. Boggess, F. Roesler, and D. Weistrop. The Space Telescope Imaging Spectrograph Design. *PASP*, 110(752):1183–1204, October 1998. doi: 10.1086/316243.

Alwyn Wootten and A. Richard Thompson. The Atacama Large Millimeter/Submillimeter Array. *IEEE Proceedings*, 97(8):1463–1471, August 2009. doi: 10.1109/JPROC.2009.2020572.

Edward L. Wright, Peter R. M. Eisenhardt, Amy K. Mainzer, Michael E. Ressler, Roc M. Cutri, Thomas Jarrett, J. Davy Kirkpatrick, Deborah Padgett, Robert S. McMillan, Michael Skrutskie, S. A. Stanford, Martin Cohen, Russell G. Walker, John C. Mather, David Leisawitz, III Gautier, Thomas N., Ian McLean, Dominic Benford, Carol J. Lonsdale, Andrew Blain, Bryan Mendez, William R. Irace, Valerie Duval, Fengchuan Liu, Don Royer, Ingolf Heinrichsen, Joan Howard, Mark Shannon, Martha Kendall, Amy L. Walsh, Mark Larsen, Joel G. Cardon, Scott Schick, Mark Schwalm, Mohamed Abid, Beth Fabinsky, Larry Naes, and Chao-Wei Tsai. The Wide-field Infrared Survey Explorer (WISE): Mission Description and Initial On-orbit Performance. *AJ*, 140(6):1868–1881, December 2010. doi: 10.1088/0004-6256/140/6/1868.

M. C. Wyatt. The insignificance of P-R drag in detectable extrasolar planetesimal belts. *A&A*, 433(3):1007–1012, April 2005a. doi: 10.1051/0004-6361:20042073.

M. C. Wyatt. Spiral structure when setting up pericentre glow: possible giant planets at hundreds of AU in the HD 141569 disk. *A&A*, 440(3):937–948, September 2005b. doi: 10.1051/0004-6361:20053391.

M. C. Wyatt. Evolution of debris disks. *ARA&A*, 46:339–383, Sep 2008. doi: 10.1146/annurev.astro.45.051806.110525.

- M. C. Wyatt and W. R. F. Dent. Collisional processes in extrasolar planetesimal discs - dust clumps in Fomalhaut's debris disc. *MNRAS*, 334(3):589–607, August 2002. doi: 10.1046/j.1365-8711.2002.05533.x.
- M. C. Wyatt, S. F. Dermott, C. M. Telesco, R. S. Fisher, K. Grogan, E. K. Holmes, and R. K. Piña. How Observations of Circumstellar Disk Asymmetries Can Reveal Hidden Planets: Pericenter Glow and Its Application to the HR 4796 Disk. *ApJ*, 527(2):918–944, Dec 1999. doi: 10.1086/308093.
- M. C. Wyatt, R. Smith, K. Y. L. Su, G. H. Rieke, J. S. Greaves, C. A. Beichman, and G. Bryden. Steady State Evolution of Debris Disks around A Stars. *ApJ*, 663(1):365–382, July 2007. doi: 10.1086/518404.
- M. C. Wyatt, C. J. Clarke, and M. Booth. Debris disk size distributions: steady state collisional evolution with poynting-robertson drag and other loss processes. *Celestial Mechanics and Dynamical Astronomy*, 111(1):1–28, Oct 2011. ISSN 1572-9478. doi: 10.1007/s10569-011-9345-3. URL <https://doi.org/10.1007/s10569-011-9345-3>.
- Ben Yelverton, Grant M. Kennedy, Kate Y. L. Su, and Mark C. Wyatt. A statistically significant lack of debris discs in medium separation binary systems. *MNRAS*, 488(3): 3588–3606, September 2019. doi: 10.1093/mnras/stz1927.
- Ben Yelverton, Grant M. Kennedy, and Kate Y. L. Su. No significant correlation between radial velocity planet presence and debris disc properties. *MNRAS*, 495(2):1943–1957, May 2020. doi: 10.1093/mnras/staa1316.
- Donald G. York, J. Adelman, Jr. Anderson, John E., Scott F. Anderson, James Annis, Neta A. Bahcall, J. A. Bakken, Robert Barkhouser, Steven Bastian, Eileen Berman, William N. Boroski, Steve Bracker, Charlie Briegel, John W. Briggs, J. Brinkmann, Robert Brunner, Scott Burles, Larry Carey, Michael A. Carr, Francisco J. Castander, Bing Chen, Patrick L. Colestock, A. J. Connolly, J. H. Crocker, István Csabai, Paul C. Czarapata, John Eric Davis, Mamoru Doi, Tom Dombeck, Daniel Eisenstein, Nancy Ellman, Brian R. Elms, Michael L. Evans, Xiaohui Fan, Glenn R. Federwitz, Larry Fiscelli, Scott Friedman, Joshua A. Frieman, Masataka Fukugita, Bruce Gillespie, James E. Gunn, Vijay K. Gurbani, Ernst de Haas, Merle Haldeman, Frederick H. Harris, J. Hayes, Timothy M. Heckman, G. S. Hennessy, Robert B. Hindsley, Scott Holm, Donald J. Holmgren, Chi-hao Huang, Charles Hull, Don Husby, Shin-Ichi Ichikawa, Takashi Ichikawa, Željko Ivezić, Stephen Kent, Rita S. J. Kim, E. Kinney, Mark Klaene, A. N. Kleinman, S. Kleinman, G. R. Knapp, John Korienek, Richard G. Kron, Peter Z. Kunszt, D. Q. Lamb, B. Lee, R. French Leger, Siriluk Limmongkol, Carl Lindenmeyer, Daniel C. Long, Craig Loomis,

Jon Loveday, Rich Lucinio, Robert H. Lupton, Bryan MacKinnon, Edward J. Mannery, P. M. Mantsch, Bruce Margon, Peregrine McGehee, Timothy A. McKay, Avery Meiksin, Aronne Merelli, David G. Monet, Jeffrey A. Munn, Vijay K. Narayanan, Thomas Nash, Eric Neilsen, Rich Neswold, Heidi Jo Newberg, R. C. Nichol, Tom Nicinski, Mario Nonino, Norio Okada, Sadanori Okamura, Jeremiah P. Ostriker, Russell Owen, A. George Pauls, John Peoples, R. L. Peterson, Donald Petravick, Jeffrey R. Pier, Adrian Pope, Ruth Pordes, Angela Prosapio, Ron Rechenmacher, Thomas R. Quinn, Gordon T. Richards, Michael W. Richmond, Claudio H. Rivetta, Constance M. Rockosi, Kurt Ruthmanskorfer, Dale Sandford, David J. Schlegel, Donald P. Schneider, Maki Sekiguchi, Gary Sergey, Kazuhiro Shimasaku, Walter A. Siegmund, Stephen Smee, J. Allyn Smith, S. Snedden, R. Stone, Chris Stoughton, Michael A. Strauss, Christopher Stubbs, Mark SubbaRao, Alexander S. Szalay, Istvan Szapudi, Gyula P. Szokoly, Anirudda R. Thakar, Christy Tremonti, Douglas L. Tucker, Alan Uomoto, Dan Vanden Berk, Michael S. Vogeley, Patrick Waddell, Shu-i. Wang, Masaru Watanabe, David H. Weinberg, Brian Yanny, Naoki Yasuda, and SDSS Collaboration. The Sloan Digital Sky Survey: Technical Summary. *AJ*, 120(3):1579–1587, September 2000. doi: 10.1086/301513.

Andrew N. Youdin and Jeremy Goodman. Streaming Instabilities in Protoplanetary Disks. *ApJ*, 620(1):459–469, February 2005. doi: 10.1086/426895.

F. Zernike. The concept of degree of coherence and its application to optical problems. *Physica*, 5(8):785–795, August 1938. doi: 10.1016/S0031-8914(38)80203-2.

S. Zieba, K. Zwintz, M. A. Kenworthy, and G. M. Kennedy. Transiting exocomets detected in broadband light by TESS in the  $\beta$  Pictoris system. *A&A*, 625:L13, May 2019. doi: 10.1051/0004-6361/201935552.

S. Zúñiga-Fernández, A. Bayo, P. Elliott, C. Zamora, G. Corvalán, X. Haubois, J. M. Corral-Santana, J. Olofsson, N. Huélamo, M. F. Sterzik, C. A. O. Torres, G. R. Quast, and C. H. F. Melo. Search for associations containing young stars (SACY). VIII. An updated census of spectroscopic binary systems exhibiting hints of non-universal multiplicity among their associations. *A&A*, 645:A30, January 2021. doi: 10.1051/0004-6361/202037830.

B. Zuckerman and E. E. Becklin. Excess infrared radiation from a white dwarf—an orbiting brown dwarf? *Nature*, 330(6144):138–140, November 1987. doi: 10.1038/330138a0.

B. Zuckerman, Inseok Song, M. S. Bessell, and R. A. Webb. The  $\beta$  Pictoris Moving Group. *ApJ*, 562(1):L87–L90, November 2001. doi: 10.1086/337968.